

## TABLE OF CONTENTS

<b>Table of Contents</b>	<b>i</b>
	<b>Page</b>
<b>Introduction</b>	<b>1</b>
<b>1 High energy nuclear physics</b>	<b>3</b>
1.1 The strong interaction . . . . .	3
1.1.1 The standard model . . . . .	3
1.1.2 Quantum chromodynamics . . . . .	5
1.1.3 Parton distribution functions . . . . .	10
1.1.4 QCD phase diagram . . . . .	13
1.2 Relativistic heavy-ion collisions . . . . .	14
1.2.1 History of heavy-ion accelerators . . . . .	15
1.2.2 Geometry of nucleus-nucleus collisions . . . . .	17
1.2.3 Evolution of heavy-ion collisions . . . . .	20
1.2.4 Experimental probes of the QGP . . . . .	21
<b>2 Experimental setup</b>	<b>35</b>
2.1 The Large Hadron Collider . . . . .	35
2.1.1 Accelerator complex . . . . .	36
2.1.2 Detectors . . . . .	37
2.1.3 Luminosity . . . . .	39
2.1.4 LHC schedule . . . . .	39
2.1.5 Heavy-ion schemes in 2015-2016 . . . . .	40
2.2 The Compact Muon Solenoid . . . . .	41
2.2.1 Subdetectors . . . . .	45
2.2.2 Trigger system . . . . .	53
2.2.3 Reconstruction . . . . .	60

---

**TABLE OF CONTENTS**


---

<b>3 W-boson production in proton-lead collisions</b>	<b>65</b>
3.1 Introduction . . . . .	65
3.1.1 A brief history of the weak theory . . . . .	66
3.1.2 The modern electroweak theory . . . . .	69
3.1.3 Production of W bosons in p-Pb and decay into muons . . . . .	71
3.1.4 Nuclear PDFs . . . . .	74
3.1.5 Experimental results at LHC . . . . .	80
3.2 Analysis . . . . .	84
3.2.1 Dataset . . . . .	84
3.2.2 Next-to-leading order simulations . . . . .	86
3.2.3 Event selection . . . . .	88
3.2.4 Correction for weak-boson transverse momentum . . . . .	93
3.2.5 Corrections for missing transverse momentum . . . . .	94
3.2.6 Signal efficiency . . . . .	105
3.2.7 Signal extraction . . . . .	114
3.2.8 Observables . . . . .	123
3.2.9 Systematic uncertainties . . . . .	126
3.3 Results . . . . .	136
3.3.1 W-boson production in p-Pb at 8.16 TeV . . . . .	136
3.3.2 Comparison with theoretical models . . . . .	140
<b>4 Charmonia</b>	<b>145</b>
4.1 Theory . . . . .	146
4.1.1 Charmonium hadronic production . . . . .	146
4.1.2 Cold nuclear matter effects . . . . .	146
4.1.3 Hot nuclear matter effects . . . . .	146
4.1.4 Experimental results in Pb-Pb collisions at LHC . . . . .	146
4.2 Analysis . . . . .	148
4.2.1 Dataset and simulated samples . . . . .	148
4.2.2 Event selection . . . . .	148
4.2.3 $J/\psi$ -meson yield extraction . . . . .	148
4.2.4 Signal acceptance and efficiency . . . . .	148
4.2.5 Systematic uncertainties . . . . .	148
4.3 Results . . . . .	149
<b>Conclusion</b>	<b>151</b>

---

TABLE OF CONTENTS

<b>A Results of the fits for the W boson analysis</b>	<b>153</b>
<b>Bibliography</b>	<b>157</b>
<b>List of Tables</b>	<b>175</b>
<b>List of Figures</b>	<b>177</b>



## INTRODUCTION

2 The progress made by the scientific community over the last century have pushed the  
 3 boundaries of our understanding of the subatomic world and have led to the formulation  
 4 of one the most successful theories of physics, the so-called Standard Model (SM) of  
 5 particle physics. Even though the SM framework is able to describe, with great accuracy,  
 6 the interactions and properties of most known particles, some fundamental phenomena  
 7 are still not fully understood, such as the phase states of matter or the evolution of  
 8 particles in a nuclear environment.

9 Under normal circumstances, the main constituents of matter, called partons (i.e.  
 10 quarks and gluons), are confined by the strong nuclear force into hadrons. However, at  
 11 high enough temperatures or densities, it is expected that matter undergoes a phase  
 12 transition to a state where quarks and gluons become asymptotically free, known as the  
 13 Quark Gluon Plasma (QGP). Such extreme state of matter is believed to have existed  
 14 during the creation of the Universe and to be part of the core of neutron stars. To  
 15 recreate the QGP in the laboratory, heavy ions are collided in accelerator facilities at  
 16 high energies. The QGP can be probed in heavy-ion experiments by measuring different  
 17 observables, such as the production yield of particles that interact strongly with the  
 18 QGP medium (e.g. quarkonia, jets, ...). In addition, the environment present in a nucleus  
 19 can also affect the production of particles produced in heavy-ion collisions, even in the  
 20 absence of QGP. The measurement of electroweak particles that do not interact with  
 21 the QGP medium (photons, Z and W bosons) allow to study the nuclear modification of  
 22 Parton Distribution Functions (PDF). The PDFs of nuclei are crucial inputs to theory  
 23 predictions for heavy-ion colliders and their precise determination with experimental  
 24 data is indispensable for calculations of the initial stage of nucleus-nucleus reactions.

25 Three analyses are presented in this thesis. The first one measure the production of W  
 26 bosons in p-Pb collisions at a center-of-mass energy per nucleon pair of  $\sqrt{s_{\text{NN}}} = 8.16 \text{ TeV}$ ,  
 27 with the goal to provide precise experimental constrains to the nuclear modifications of  
 28 the quark PDFs. I am the *contact person* of the analysis and have conducted all the work  
 29 except the tag-and-probe and the weak boson  $p_T$  corrections. I presented the preliminary

## TABLE OF CONTENTS

---

30 results at the Quark Matter [1] and ICHEP [2] conferences in 2018. The work is expected  
31 to be published in a peer-reviewed journal in the near future [3]. The second and third  
32 analyses probe quark deconfinement in the QGP by measuring the  $J/\psi$  and  $\psi(2S)$  (i.e.  
33 charmonium) production in Pb-Pb collisions at  $\sqrt{s_{NN}} = 5.02\text{ TeV}$ . My main contributions  
34 to the  $J/\psi$  and  $\psi(2S)$  analyses include the optimization of the muon kinematic selection,  
35 the signal extraction and the systematic uncertainties associated to the fitting. The  
36 results of the  $\psi(2S)$  and  $J/\psi$  analyses have been published in PRL [4] and EPJC [5],  
37 respectively, and I presented them at the Hot Quarks 2016 [6] and EPS-HEP 2017 [7]  
38 conferences.

39 The manuscript is organised as follows. The general concepts of the strong interac-  
40 tions and heavy-ion collisions are introduced in Chapter 1. A brief description of the  
41 main probes of the QGP concludes the chapter. Chapter 2 describes the experimental  
42 apparatus, where the operational conditions of the Large Hadron Collider and character-  
43 istics of the Compact Muon Solenoid detector are detailed. The chapter also describes the  
44 trigger and reconstruction algorithms employed to select and process the data. Chapter 3  
45 presents in details the samples generated, event selection, corrections to the missing  
46 transverse momentum, estimation of the muon efficiency, signal extraction, systematic  
47 uncertainties and results of the  $W$ -boson analysis, accompanied by a short introduction  
48 on electroweak physics. The charmonium analysis in Pb-Pb collisions is exposed in Chap-  
49 ter 4. The chapter contains details on the charmonium samples, the event selection, the  
50  $J/\psi$  efficiency estimation, the extraction of the  $J/\psi$  yields and the  $\psi(2S)/J/\psi$  ratios, the  
51 systematic uncertainties and the results, including a brief introduction to the physics of  
52 charmonia in heavy-ion collisions.

## HIGH ENERGY NUCLEAR PHYSICS

55 This chapter introduces some key concepts of high energy nuclear physics com-  
56 mon to the analysis of the production of W bosons and charmonia in heavy-ion  
57 collisions. The quantum field theory of the strong interactions is described in  
58 Section 1.1. The state of hot dense hadronic matter, known as the quark-gluon plasma,  
59 and the study of its properties in heavy-ion collisions are reviewed in Section 1.2.

### 60 1.1 The strong interaction

61 The strong interaction is one of the three fundamental interactions described by the  
62 standard model of particle physics introduced in Section 1.1.1. Its underlying theory is  
63 Quantum Chromodynamics (QCD) presented in Section 1.1.2. It binds quarks and gluons  
64 in hadrons, which are distributed inside the hadron as described by PDFs (Section 1.1.3).  
65 Depending on the temperature and density of the system, it is expected to exhibit a  
66 complex phase diagram (Section 1.1.4).

#### 67 1.1.1 The standard model

68 The standard model is a theoretical framework that describes the properties of elemen-  
69 tary particles and their interactions. The SM was developed during the 20th century  
70 through the collaborative effort of many physicists. According to the SM, the most ele-  
71 mentary particles are fermions and bosons. Fermions are particles with half-integer spin

72 which behave according to Fermi-Dirac statistics formulated by Enrico Fermi [8] and  
 73 Paul Dirac [9] in 1926. As a consequence, fermions are restricted by the Pauli exclusion  
 74 principle [10] which dictates that two or more fermions with the same quantum numbers  
 75 cannot occupy the same quantum state.

76 In addition, fermions can be classified as leptons or quarks. There are six leptons  
 77 arranged in three "generations": the electron ( $e^-$ ) and the electron neutrino ( $\nu_e$ ), the  
 78 muon ( $\mu^-$ ) and the muon neutrino ( $\nu_\mu$ ), and the tau ( $\tau^-$ ) and the tau neutrino ( $\nu_\tau$ ).  
 79 The neutrinos are electrically neutral and almost massless, while the other leptons  
 80 have negative electric charge ( $-1$ ) and sizeable masses. In the case of quarks, there are  
 81 six "flavours" paired also in three generations of increasing mass. The up and down  
 82 quarks belong to the first generation, while the more heavier quarks are included in the  
 83 second generation (charm and strange quarks) and third generation (top and bottom  
 84 quarks). The up (u), charm (c) and top (t) quarks have positive electric charge ( $+2/3$ )  
 85 while the down (d), strange (s) and bottom (b) quarks have negative electric charge  
 86 ( $-1/3$ ). Each quark also carry another quantum number called colour charge that can  
 87 have three different values labelled as red, green and blue. Moreover, each fermion has  
 88 an associated antiparticle with the same mass but with opposite charges. The positron  
 89 ( $e^+$ ) is the antiparticle of the electron, while the name of the rest of antiparticles simply  
 90 starts with the prefix "anti" (e.g. anti-quarks  $\bar{q}$ , anti-neutrinos  $\bar{\nu}$  or anti-leptons  $\ell^+$ ).

91 The interactions between fermions are described in the standard model by three  
 92 fundamental forces: electromagnetism, strong nuclear force and the weak nuclear force.  
 93 The gravitational force is currently not included in the SM but the effect of gravity at the  
 94 quantum level is too small to be observed. In the SM, each fundamental force is mediated  
 95 by the exchange of bosons, which are integer spin particles that follows the Bose-Einstein  
 96 statistics proposed in 1924 by Sateyndra Bose [11] and Albert Einstein [12].

97 The electromagnetic and the weak nuclear forces are described in the SM by the  
 98 electroweak theory. The electromagnetic interactions between particles with electric  
 99 charge are mediated by photons which are massless and chargeless spin one particles.  
 100 On the other hand, the weak interactions can act on all fermions but the strength of  
 101 the weak force is roughly  $10^{-4}$  times weaker than the electromagnetic force and  $10^{-6}$   
 102 times weaker than the strong nuclear force<sup>1</sup>. The weak interactions are mediated by  
 103 three massive vector bosons: the electrically charged  $W^\pm$  bosons<sup>2</sup> and the electrically  
 104 neutral Z boson. Processes involving neutrinos or the change of quark flavour are only

---

<sup>1</sup>The strength of the interactions is determined for two up quarks separated by a distance of  $3 \times 10^{-17}$  m.

<sup>2</sup>Since the W bosons are used to probe the nuclear PDF, the theory of the weak interaction is further described, together with the analysis in p-Pb collisions, in Chapter 3.

possible through the weak interactions. Last, the strong nuclear force is responsible for the interactions between colour charged particles (i.e. quarks) described by the theory of Quantum Chromodynamics (QCD). The strong interactions are mediated by spin one bosons called gluons which carry colour and anti-colour charge. Unlike the photon, gluons can interact with themselves leading to a strong attraction that confines the quarks in colourless configurations known as hadrons. Hadrons compose of three (anti-)quarks are called baryons while those made of a quark and an anti-quark are called mesons. Exotic hadrons containing four and five quarks have been recently observed by the Belle [13] and LHCb [14] collaborations, respectively.

The generation of mass of the elementary particles is explained in the SM by the Brout-Englert-Higgs (BEH) mechanism [15, 16]. The weak bosons and the fermions acquire their mass by interacting with the Higgs field. The stronger a particle couples to the Higgs field, the more massive it becomes. The quantum excitation of the Higgs field corresponds to a scalar boson, the so-called Higgs boson. The BEH mechanism was experimentally confirmed after the CMS [17] and ATLAS [18] collaborations announced the discovery of the Higgs boson in 2012. The basic properties of leptons, quarks and bosons of the SM are summarised in Table 1.1.

### 1.1.2 Quantum chromodynamics

The development of new experimental techniques, such as the synchrocyclotron and the bubble chamber, led to the discovery of many hadronic resonances starting from the late 1940s. In an attempt to organise these new hadrons, Murray Gell-Mann [20] and Yuval Ne’eman [21] proposed in 1961 the Eightfold Way classification. The Eightfold Way scheme managed to sort the hadrons into representations of the SU(3) group leading to the creation of the quark model. The quark model, developed in 1964 by Gell-Mann [22] and George Zweig [23], considered the hadrons as composite objects made of valence quarks and anti-quarks. Even though the quark model was successful at describing the properties of most hadrons known at the time, it had problems explaining the structure of the  $\Omega^-$  baryon. The  $\Omega^-$  baryon is made of three strange quarks with parallel spins but such configuration was forbidden by the Pauli exclusion principle. To solve the spin-statistics paradox, Oscar Greenberg [24] proposed that each quark also carried a 3-valued quantum number named the colour charge. The description of the strong interactions using the concept of colour charges was formally developed in the theory of QCD by Harald Fritzsch, Heinrich Leutwyler and Murray Gell-Mann [25] in 1973.

	Name	Symbol	Mass	Charge	Spin	Interactions
Quarks	1 <sup>st</sup> Up	u	2.2 MeV	2/3	1/2	All
	Down	d	4.7 MeV	-1/3	1/2	All
	2 <sup>nd</sup> Charm	c	1.28 GeV	2/3	1/2	All
	Strange	s	96 MeV	-1/3	1/2	All
	3 <sup>rd</sup> Top	t	173.5 GeV	2/3	1/2	All
	Bottom	b	4.18 GeV	-1/3	1/2	All
Leptons	1 <sup>st</sup> Electron	$e^-$	511 keV	-1	1/2	Electroweak
	Electron neutrino	$\nu_e$	<2 eV	0	1/2	Weak
	2 <sup>nd</sup> Muon	$\mu^-$	106 MeV	-1	1/2	Electroweak
	Muon neutrino	$\nu_\mu$	<2 eV	0	1/2	Weak
	3 <sup>rd</sup> Tau	$\tau^-$	1.78 GeV	-1	1/2	Electroweak
	Tau neutrino	$\nu_\tau$	<2 eV	0	1/2	Weak
Bosons	Photon	$\gamma$	$< 10^{-18}$ eV	0	1	Electromagnetic
	Gluon	g	0	0	1	Strong
	W boson	$W^\pm$	80.4 GeV	$\pm 1$	1	Electroweak
	Z boson	Z	91.2 GeV	0	1	Electroweak
	Higgs boson	H	125.1 GeV	0	0	BEH mechanism

Table 1.1: Basic properties of quarks, leptons and bosons from the SM. The table includes the mass, electric charge, spin and type of interactions of each particle. The values are taken from Ref. [19].

138        Quantum chromodynamics is a non-abelian quantum field theory with gauge symmetry group  $SU(3)$ , that describes the strong interactions between colour charged particles.  
 139        The primary objects of QCD are the quarks which carry one colour charge (e.g. green)  
 140        and the gluons which carry a colour and an anti-colour charge (e.g. red-antiblue). There  
 141        are eight different gluons which form an octet representation of  $SU(3)$ <sup>3</sup>. The Lagrangian  
 142        of QCD is:  
 143

$$L_{QCD} = \sum_f \bar{q}_{f,i} \left( i\gamma^\mu D_\mu^{i,j} - m_f \delta^{a,b} \right) q_{f,j} - \frac{1}{4} F_{\mu,\nu}^a F_a^{\mu,\nu} \quad (1.1)$$

144        where  $g_s$  is the strong gauge coupling constant, and  $\gamma^\mu$  are the Dirac  $\gamma$ -matrices. The  
 145         $q_{f,i}$  represents the Dirac spinor of a quark with flavour  $f$ , mass  $m_f$  and colour index  $i$   
 146        running from  $i = 1$  to 3. The QCD gauge covariant derivative  $D_\mu^{i,j}$  and the gluon field  
 147        strength tensor  $F_{\mu,\nu}^a$  are given by:

<sup>3</sup>The fully symmetric colour-anticolour combination is colourless and thus, can not mediate colour.

$$D_\mu^{i,j} = \delta^{i,j} \partial_\mu - i \frac{g_s}{2} \lambda_a^{i,j} G_\mu^a \quad (1.2)$$

$$F_{\mu,\nu}^a = \partial_\mu G_\nu^a - \partial_\nu G_\mu^a + g_s f_{bc}^a G_\mu^b G_\nu^c$$

148 where  $f_{bc}^a$  are the SU(3) structure constants,  $\lambda_a^{i,j}$  are the Gell-Mann matrices, and  $G_\mu^a$   
 149 is the vector field of a gluon with index  $a$  that runs from 1 to 8.

150 Expanding the terms in Eq. (1.1), one can derive three different types of vertices  
 151 representing the interaction between quarks and gluons, and the gluon self-interactions  
 152 as shown in Figure 1.1.

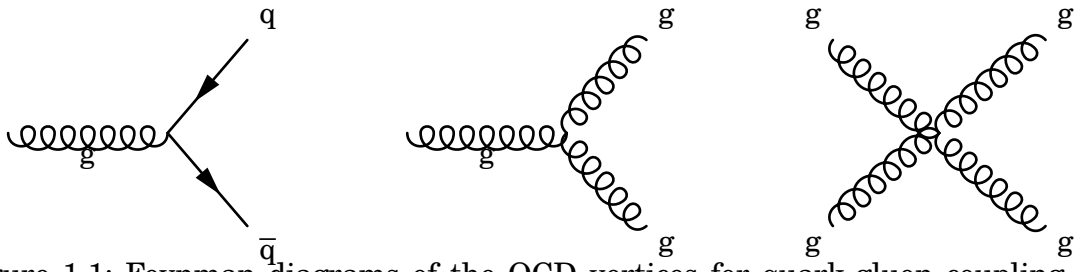


Figure 1.1: Feynman diagrams of the QCD vertices for quark-gluon coupling (left), triple-gluon self-coupling (middle) and quadri-gluon self-coupling (right).

### 153 1.1.2.1 Running coupling constant

154 In quantum field theory, physical quantities are calculated by performing a perturbative  
 155 expansion of the theory in terms of its coupling constant. The first order of the expansion  
 156 is called the leading order (LO). At higher orders, some of the terms contain loops (infinite  
 157 integrals) which diverge due to high momentum particles in the loop. The ultraviolet  
 158 (UV) divergences can be removed from the perturbation series by renormalising the  
 159 Lagrangian.

160 The renormalisation procedure consists in replacing the bare parameters of the La-  
 161 grangian by finite renormalised parameters, and then treat the divergences by applying a  
 162 regularisation scheme. There are many regularisation schemes but one of the most often  
 163 used is Minimal Subtraction (MS) based on dimensional regularisation. The MS scheme  
 164 consists in solving the loop integrals in  $d$  arbitrary spacetime dimensions introducing a  
 165 scale  $\mu$  in the process [26]. In order to keep the physical observables independent of the  
 166 renormalisation scale, the dependence of the renormalised parameters on the scale  $\mu$  is  
 167 fixed by renormalisation group equations (RGE) [26].

168 In the case of QCD, the strength of the strong interactions is parametrised by the  
 169 strong coupling constant  $\alpha_s = 4\pi g_s^2$ . The UV divergences in perturbative QCD (pQCD)  
 170 appears from loop diagrams like those shown in Figure 1.2.

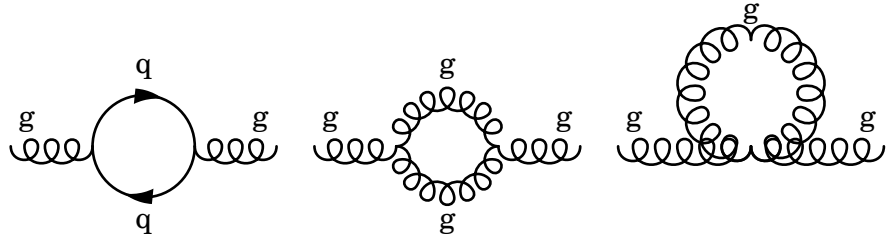


Figure 1.2: Feynman diagrams of 1-loop contributions to pQCD.

171 The renormalised strong coupling constant  $\alpha_s(\mu^2)$  satisfies the following RGE [19]:

$$\mu^2 \frac{d\alpha_s(\mu^2)}{d\mu^2} = \beta(\alpha_s) = -\alpha_s^2 (\beta_0 + \beta_1 \alpha_s + \dots) \quad (1.3)$$

172 where  $\beta_0 = 7/(4\pi)$  and  $\beta_1 = 13/(8\pi^2)$  are the 1-loop and the 2-loop coefficients of the  
 173  $\beta$ -function, respectively [19]. In the one-loop approximation,  $\alpha_s(\mu^2)$  can be expressed as:

$$\alpha_s(\mu^2) = \frac{1}{\beta_0 \ln\left(\frac{\mu^2}{\Lambda_{\text{QCD}}^2}\right)} \quad (1.4)$$

174 where  $\Lambda_{\text{QCD}} \approx 255$  MeV [27]<sup>4</sup> is the QCD Landau pole (i.e. the scale at which the  
 175 coupling becomes infinite). The factorisation scale  $\mu$  is generally associated to the energy  
 176 scale  $Q$  of a given process. This means that  $\alpha_s(\mu^2)$  is not really a constant but depends  
 177 on the energy scale, so it is also known as the QCD running coupling constant. Figure 1.3  
 178 presents the latest results on the measurement of  $\alpha_s(Q^2)$  as a function of the energy  
 179 scale  $Q$  [19].

### 180 1.1.2.2 Asymptotic freedom

181 One important consequence of the non-abelian nature of QCD is the asymptotic freedom  
 182 of colour charged particles discovered in 1973 by David Gross and Frank Wilczek [28],  
 183 and also by David Politzer [29]. As can be observe in Figure 1.3, the strength of the strong  
 184 nuclear force gets asymptotically reduced as the energy scale is increased. Perturbative

<sup>4</sup>Derived in the  $\overline{\text{MS}}$  scheme for 2 quark flavours.

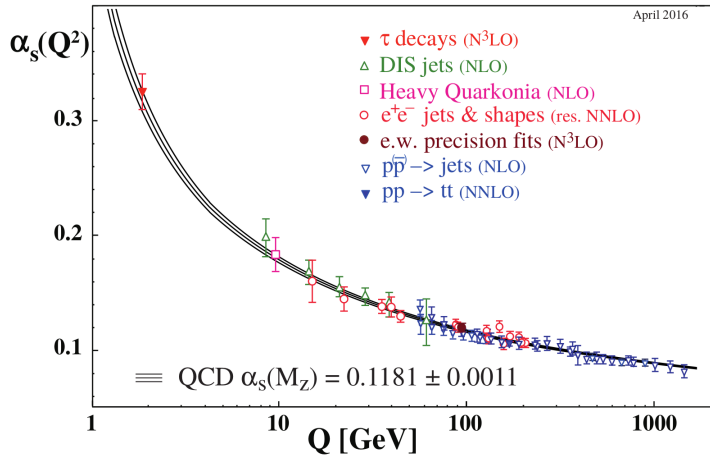


Figure 1.3: Summary of measurements of  $\alpha_s$  as a function of the energy scale  $Q$ . Figure taken from the PDG [19]

185 QCD can then be fully applied in the asymptotic free regime since the strong coupling  
 186 constant is small.

187 Considering the inverse relation between the wavelength of particles and their mo-  
 188 mentum (the de Broglie hypothesis [30]), asymptotic freedom implies that the strong  
 189 nuclear interactions between quarks gets weaker at larger momentum or at shorter dis-  
 190 tances. This phenomenon can be understood qualitatively as derived from the interaction  
 191 with the QCD vacuum. The presence of virtual quark-antiquark pairs from the vacuum  
 192 acts as colour dipoles reducing (screening) the strength of the colour charge field. In  
 193 addition, virtual gluons can couple to other gluons increasing (anti-screening) the net  
 194 effect of the colour charge seen at larger distances. Thus, there is an interplay between  
 195 quark-antiquark colour screening and gluon colour anti-screening, where the later effect  
 196 dominates in QCD.

### 197 1.1.2.3 Colour confinement

198 The fact that quarks and gluons have never been observed isolated in normal conditions is  
 199 due to another phenomenon of QCD called colour confinement. The intensity of the strong  
 200 nuclear force increases when the energy scale is reduced or the distance is increased as  
 201 seen in Figure 1.3. The large strong interactions between colour charged particles force  
 202 the quarks and gluons to be confined in hadrons. The divergent behaviour of  $\alpha_s$  at the  
 203 Landau pole shown in Eq. (1.4), is a consequence of the inability of pQCD to describe the  
 204 low energy regime, which becomes non-perturbative.

205 The strong nuclear force can be described qualitatively as a string. When a quark

206 and anti-quark gets separated, the gluon string that mediates their strong interaction  
 207 elongates, increasing the energy. The string eventually breaks when it becomes more  
 208 energetically favourable to create a light quark-antiquark pair, splitting the original me-  
 209 son into two mesons as shown in Figure 1.4. This leads to a process called hadronisation  
 210 where quarks and gluons produce a cascade of hadrons. The presence of colour charged  
 211 particles in high energy collisions can be measured experimentally using jets derived by  
 212 clustering the final state hadrons in narrow cones.

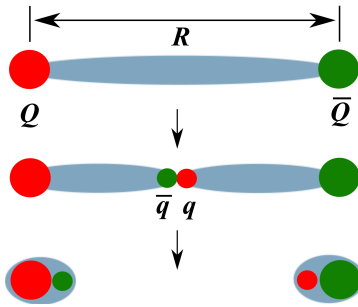


Figure 1.4: Sketch of the gluon string breaking between a quark  $Q$  and an anti-quark  $\bar{Q}$  due to  $q\bar{q}$  pair creation. Figure taken from Ref. [31].

### 213 1.1.3 Parton distribution functions

214 The production of particles in hadronic collisions depends on the evolution of the partons  
 215 (i.e. quarks and gluons) inside the hadrons and the parton momentum transfer during the  
 216 hard scattering. Since the strong coupling constant decreases with increasing momentum  
 217 scales, partons can be considered asymptotically free within the hadron during collisions  
 218 involving large momentum transfer. In this case, each parton carries a fraction of the total  
 219 momentum of the hadron, represented by the quantity called Bjorken  $x$  [32] (labelled  
 220 simply as  $x$ ), given by:

$$p_{parton} = x p_{proton} \quad (1.5)$$

221 The net quantum properties of hadrons, such as the electric or colour charge, are  
 222 derived from the valence quarks. The interaction between valence quarks is mediated  
 223 by the exchange of gluons. Gluons can also produce virtual quark-antiquark pairs and  
 224 other gluons through self interactions. The virtual quarks produced inside the hadrons  
 225 are called sea quarks. The gluons and sea quarks do not contribute to the net quantum  
 226 numbers of the hadron but they can contribute to its mass and they also play a key role  
 227 in the interaction of hadrons with other particles.

228 A convenient way of studying the partonic content of hadrons is through the parton  
 229 distribution functions. The PDF of a hadron represents the probability that a parton  
 230 carries a given fraction  $x$  of the total momentum of the hadron.

231 According to the QCD factorisation theorem [33], the cross section of a given hard  
 232 scattering process in hadronic collisions can be split in a partonic cross section times the  
 233 PDFs of each incoming hadron. On one hand, the partonic cross section can be derived  
 234 using perturbative QCD and does not depend on the colliding hadrons. On the other  
 235 hand, the PDFs can not be calculated from first principles due to the non-perturbative  
 236 nature of QCD, but they can be determined from global fits to experimental data since the  
 237 PDFs are independent of the initial scattering process (i.e. universal). The hadronic cross  
 238 section in a given final state can be expressed at LO, using the factorisation theorem, as:

$$\sigma_{h_1, h_2} = \sum_{f_1, f_2 = (q, \bar{q}, g)} \int_0^1 dx_1 dx_2 f_1^{h_1}(x_1, Q^2) f_2^{h_2}(x_2, Q^2) \hat{\sigma}_{f_1 f_2} \quad (1.6)$$

239 where  $Q^2$  is the momentum scale,  $f^{h_1}(x, Q^2)$  is the PDF of a given incoming hadron  
 240  $h_1$ , and  $\hat{\sigma}_{f_1 f_2}$  represents the partonic cross section of the scattering process between  
 241 partons  $f_1$  and  $f_2$ .

242 The  $Q^2$  dependence of the PDFs is described by the parton evolution equations  
 243 developed by Dokshitzer, Gribov, Lipatov, Altarelli and Parisi (DGLAP) [34–36]. In the  
 244 DGLAP formalism, the PDFs can be expressed in terms of kernels  $P_{q_1 q_2}$  (called splitting  
 245 functions), and the evolution equations of the parton densities can be written as:

$$\begin{aligned} \frac{d}{dt} q_i(x, t) &= \frac{\alpha_s(Q)}{2\pi} [q_i \circledast P_{qq} + g \circledast P_{qg}] \\ \frac{d}{dt} g(x, t) &= \frac{\alpha_s(Q)}{2\pi} \left[ \sum_i (q_i + \bar{q}_i) \circledast P_{gq} + g \circledast P_{gg} \right] \\ [q \circledast P] &= \int_x^1 dy \frac{q(y, t)}{y} \times P\left(\frac{x}{y}\right) \end{aligned} \quad (1.7)$$

246 where  $t = \log(Q^2/\mu_F^2)$ ,  $\mu_F$  is the factorisation scale (energy scale that separates the  
 247 PDFs from the partonic cross sections), and  $P_{q_1 q_2}$  represents the probability that a parton  
 248 of type  $q_1$  emits a parton of type  $q_2$ . In other words, the DGLAP evolution equations  
 249 state that the PDF of a given parton  $q$  at an  $x$  value is determined from the contribution  
 250 of all the partons at higher momentum fraction considering their probability of decaying  
 251 into the parton  $q$ .

252 From the definition of the PDFs, one can also formulate a set of structure functions  
 253 defined as:

$$F_2^P(x) = \sum_q e_q^2 f(x, Q^2) x \quad (1.8)$$

where  $e_q$  is the electric charge of a given quark flavour  $q$ . The structure functions were extensively measured in deep-inelastic scattering (DIS) collisions at the Hadron-Elektron-Ring-Anlage (HERA) accelerator. The DIS process consists in the inelastic scattering of electrons off protons as presented in Figure 1.5. In the DIS process, the momentum transferred from the electron to the proton is defined as  $Q^2 = -q^2 = -(k - k')^2$  and the corresponding Bjorken  $x$  fraction is  $x = Q^2/(2p \cdot q)$ , where all 4-momenta are defined in the figure.

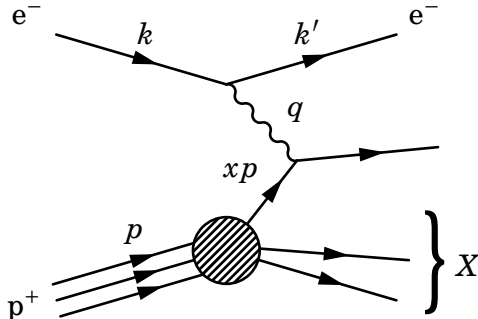


Figure 1.5: Feynman diagram of deep inelastic scattering of electrons against protons.

The measurements of the  $F_2$  structure function performed by the ZEUS collaboration [37] at HERA are shown in Figure 1.6. Even though DIS experiments were not able to probe the gluons directly, the DIS data showed that valence quarks only carry half of the proton momentum, the other half being carried by the gluons.

Another important process used to constrain PDFs is the Drell-Yan (DY) process or the production of W bosons. In the DY process, a quark from one hadron and an anti-quark from another hadron annihilate into a virtual photon ( $\gamma^*$ ) or a Z boson, which then decays to a particle-antiparticle pair as shown in Figure 1.7. The measurement of DY production can be used to constrain the quark PDFs in a wide range of momentum fraction  $x$  depending on the invariant mass of the dilepton pair. In addition, the measurement of the production of positive and negative charged W bosons in hadronic collisions is used to disentangle the flavour dependence of the quark PDFs. More details about the W boson production will be provided in Chapter 3, since the present thesis report a measurement of W bosons in p-Pb collisions that provide strong constraints on nuclear PDF.

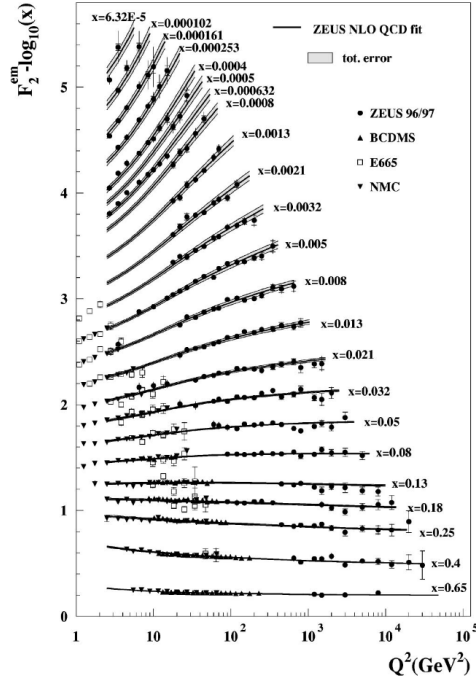


Figure 1.6: Next-to-leading order QCD fits to the ZEUS  $F_2$  structure function data from 1996, 1997 and proton fixed-target at HERA. The error bands of the fit represent the total experimental uncertainty from both correlated and uncorrelated sources. Figure taken from Ref. [37].

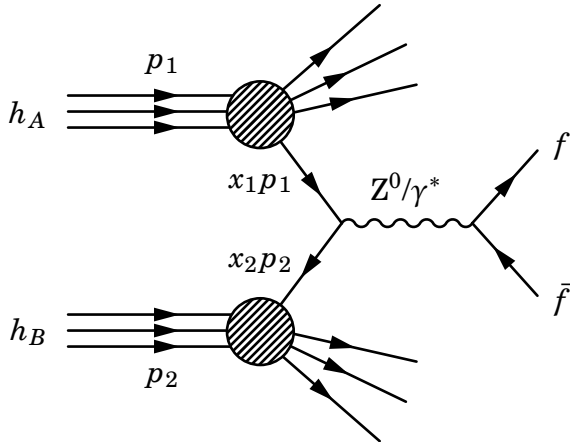


Figure 1.7: Feynman diagram of the Drell-Yan process.

#### 275 1.1.4 QCD phase diagram

276 The first attempt to describe the temperature evolution of matter at high energies  
 277 was performed by Rolf Hagedorn in 1965 [38]. Hagedorn considered matter at high

278 energies as a gas made of hadrons and he employed a thermodynamical bootstrap  
279 approach to describe the hadron gas. After studying the mass spectrum of all the hadron  
280 species measured at the time, Hagedorn realised that the density of hadron species  
281 grows exponentially until it diverges at a temperature of  $T_H \approx 158$  MeV, known as the  
282 Hagedorn temperature. Years later, with the advent of QCD, it was understood that the  
283 Hagedorn temperature described a transition from a hadron gas to a state of matter  
284 where quarks and gluons are asymptotically free called the quark-gluon plasma.

285 The description of the QCD phase transition turned out to be complicated because the  
286 critical temperature is close to the QCD scale  $\Lambda_{\text{QCD}} \approx 255$  MeV [27], where perturbative  
287 calculations are no longer reliable. An alternative method to study the non-perturbative  
288 regime of QCD consists of solving numerically the QCD field equations on a discrete  
289 space-time grid using a method called lattice QCD. Nowadays, lattice QCD is able to  
290 describe the evolution of matter at finite temperatures and low densities. A sketch of the  
291 QCD phase diagram in terms of the temperature  $T$  and the baryon chemical potential  
292  $\mu_B$ <sup>5</sup>. is shown in Figure 1.8.

293 Normal nuclear matter exists in nature at low temperatures and high  $\mu_B$  (900 MeV).  
294 At higher  $\mu_B$ , matter undergoes a phase transition to a degenerate gas of fermions,  
295 known as neutron gas, which is present in neutron stars. It is theorised that at even  
296 higher  $\mu_B$ , matter could reach a state of colour superconductivity where quarks bind  
297 together into Cooper pairs [40]. On the other hand, matter present at the beginning of  
298 the universe or produced in TeV-scale particle collisions has very low baryon chemical  
299 potential. Matter is described at low temperatures as a hadron gas and it becomes a  
300 QGP when the temperature exceeds some critical value. At low  $\mu_B$ , the phase transition  
301 between the hadron gas and the QGP has been established, using lattice QCD, to be a  
302 crossover where the two states coexist [41, 42].

## 303 **1.2 Relativistic heavy-ion collisions**

304 Heavy-ion colliders have become essential tools to explore the fundamental properties of  
305 matter. Collisions of nuclei are used to probe the phase transitions of QCD and to recreate  
306 the QGP in the laboratory. The QGP is believed to have existed at the beginning of the  
307 Universe and to be part of the core of some astrophysical objects such as neutron stars.  
308 The study of the QGP allows to test QCD in the most extreme regimes and provides an

---

<sup>5</sup>The baryon chemical potential can be viewed as a measure of the excess of matter over anti-matter and it is proportional to the baryon density.

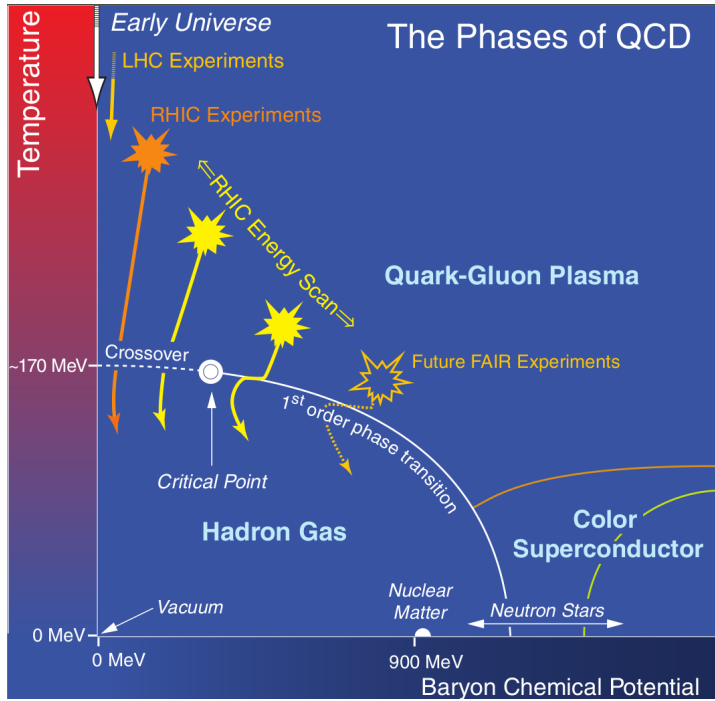


Figure 1.8: Sketch of the QCD phase diagram for nuclear matter. The solid lines show the phase boundaries and the solid circle represents the critical point. Figure taken from Ref. [39].

309 insight on the evolution of the Universe. Some of the primary research goals of the heavy-  
 310 ion physics programme is to understand the formation and properties of the QGP, and  
 311 how does matter interact with the nuclear medium. Nowadays, the experimental study of  
 312 ultra-relativistic (i.e. at energies above  $\sqrt{s_{NN}} > 10 \text{ GeV}$ ) heavy-ion collisions is performed  
 313 at the Brookhaven National Laboratory (BNL) and at the European Organization for  
 314 Nuclear Research (CERN).

### 315 1.2.1 History of heavy-ion accelerators

316 The interest in probing the QCD phase diagram in the laboratory arose in the 1970s  
 317 after Werner Scheid, Hans Müller and Walter Greiner predicted that nuclear matter  
 318 could be compressed in heavy-ion collisions at nucleus-nucleus energies larger than  
 319 100 MeV/nucleon [43]. The shock compression mechanism could reach matter densities  
 320 up to five times higher than the density of atomic nuclei ( $\rho_0 = 0.16 \text{ baryons/fm}^3$ ) [43].  
 321 Coinciding in time, the Lawrence Berkeley National Laboratory (LBNL) decided to  
 322 transform their proton synchrotron accelerator Bevatron into a heavy-ion experiment  
 323 called Bevalac. Heavy ions were produced in the Bevalac using the heavy-ion linear

324 accelerator SuperHILAC and then sent to the Bevatron, where the ions were further  
325 accelerated against a fixed target with energies of up to 2.6 GeV/nucleon [44]. The goal  
326 at the time was to investigate the equation of state (EoS) of hadronic matter at high  
327 densities. The understanding of the relation between the pressure and the energy density  
328 of dense matter was a key element needed to describe the dynamics of astrophysical  
329 objects such as neutron stars [45, 46].

330 The successful creation of compressed nuclear matter at the Bevatron motivated  
331 the construction of several heavy-ion accelerators at higher energies. The first one was  
332 the Alternating Gradient Synchrotron (AGS) particle accelerator at the Brookhaven  
333 National Laboratory (BNL). The AGS became the first facility in 1960 to accelerate  
334 protons to an energy of 33 GeV, which allowed to discover the muon neutrino in 1962  
335 and to observe the CP violation of the weak interactions in Kaon decays in 1964. An  
336 electrostatic accelerator called the Tandem Van de Graaf was built in 1970 to provide  
337 beams of ions to the AGS. The relativistic heavy-ion programme started at AGS in 1986  
338 and lasted for 12 years during which several experiments were performed (e.g. E802,  
339 E858, E866, E896 and E917). The AGS accelerated Si beams at 14.6 GeV/nucleon and  
340 Au beams at 11.1 GeV/nucleon, and collided them against different types of fixed targets  
341 (e.g. Al and Au).

342 In parallel, CERN built the Super Proton Synchrotron (SPS) in 1976. To study the QGP,  
343 CERN added an Electron-Cyclotron Resonance (ERC) ion source in 1986 which initially  
344 accelerated ions of oxygen and sulphur at 200 GeV/nucleon. A subsequent upgrade of  
345 the ion injector in 1994 allowed to accelerate up to an energy of 158 GeV/nucleon the Pb  
346 ions, which were collided against fixed targets located in two experimental halls: one in  
347 the SPS north area (NA) and the other in the SPS west area (WA). Several fixed target  
348 experiments were built at the SPS between 1986 and 2005. After years of analysing the  
349 Pb-Pb and Pb-Au fixed target collision data from SPS, CERN announced in 2000 that  
350 the combined results of the experiments NA44, NA45, NA49, NA50, NA52, WA97/NA57  
351 and WA98, provided a first evidence of the creation of a new state of matter consistent  
352 with the QGP [47].

353 In the meantime, the first nucleus-nucleus collider, known as the Relativistic Heavy  
354 Ion Collider (RHIC), started operations at the BNL in 2000. Two beams of Au are pre-  
355 accelerated at the AGS to an energy of 8.86 GeV/nucleon and then sent to RHIC where  
356 the Au beams were first collided at  $\sqrt{s_{NN}} = 130$  GeV, and later at 200 GeV. Other collision  
357 systems explored at RHIC include: p-p, p-Au, d-Au, Cu-Cu, Cu-Au and U-U [48]. There  
358 were four detectors at RHIC called BRAHMS, PHENIX, STAR, and PHOBOS. Currently,

359 only the STAR and PHENIX collaborations are still active, while PHOBOS ceased  
 360 operations in 2005 and BRAHMS in 2006. After four years of meticulously studying the  
 361 system produced in Au-Au collisions with the four detectors, RHIC finally announced  
 362 in 2005 the discovery of a strongly coupled QGP. Contrary to the expected gaseous  
 363 behaviour, the QGP observed at RHIC turned out to resemble more a liquid with very  
 364 little viscosity [49–52].

365 Currently, the largest heavy-ion collider is the Large Hadron Collider (LHC) at CERN,  
 366 whose construction finished in 2008. The SPS is used as injector to the LHC, accelerating  
 367 the Pb beams to energies of 1.38 TeV. The first nucleus-nucleus collisions at LHC took  
 368 place in 2010 using Pb beams at 2.76 TeV. Since then, the LHC has collided different  
 369 configurations involving ions, including p-Pb at 2.76 TeV (2013), Pb-Pb at 5.02 TeV  
 370 (2015), p-Pb at 8.16 TeV (2016), Xe-Xe at 5.44 TeV (2017), and at the end of 2018 LHC is  
 371 planning to provide a larger set of Pb-Pb collisions at 5.02 TeV. There are four detectors  
 372 at the LHC called ALICE, CMS, ATLAS and LHCb. The four experiments are nowadays  
 373 participating in the heavy-ion programme at LHC. Due to the large beam energies, the  
 374 LHC is an ideal collider to study the QGP at very high temperatures, where one expects  
 375 smaller QGP formation times and larger hot medium densities, compared to RHIC.

### 376 1.2.2 Geometry of nucleus-nucleus collisions

377 The number of particles produced in a nucleus-nucleus collision depends on the geometry  
 378 of the collision. Since nuclei are extended objects made of nucleons (i.e. protons and  
 379 neutrons), the number of nucleon-nucleon (NN) interactions increases the more head-  
 380 on or central is the collision. The nucleons that participate in the collision are called  
 381 participants while those that do not participate are referred to as spectators. The overlap  
 382 region of the collision depends on the impact parameter  $\vec{b}$ , which is the transverse  
 383 distance between the centres of the two colliding nuclei as shown in Figure 1.9.

384 The formation and characteristics of the QGP in nucleus-nucleus collisions depends  
 385 on the number of colliding nucleons. To study the dynamics of the nuclear medium, the  
 386 heavy-ion collisions are classified based on their centrality. The centrality  $c$  is defined as  
 387 the fraction of the total nucleus-nucleus inelastic cross section  $\sigma_{AB}^{\text{inel}}$  determined within  
 388 the area defined by the impact parameter  $b$ , and it is expressed as:

$$c = \frac{\pi b^2}{\sigma_{AB}^{\text{inel}}} \quad (1.9)$$

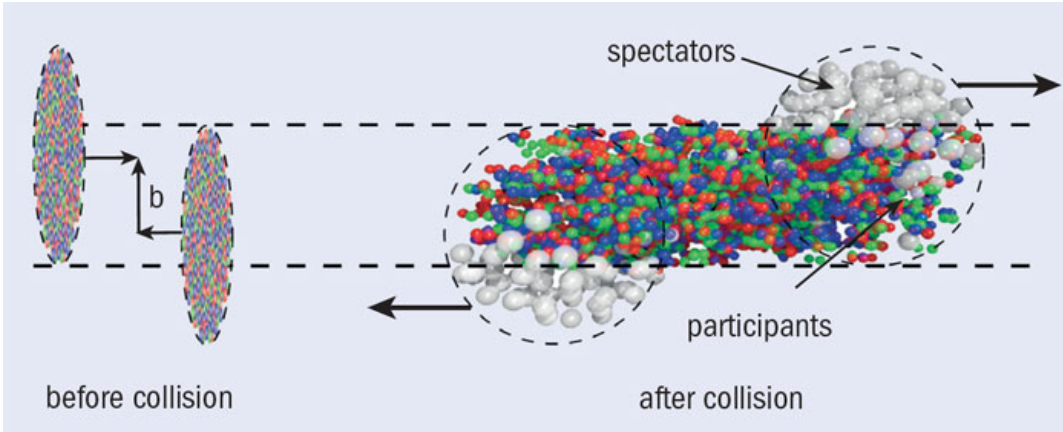


Figure 1.9: Illustration of two nucleus with impact parameter  $b$  before (left) and after (right) colliding. Figure taken from Ref. [39].

389     The collision centrality can be related to the number of participants  $N_{\text{part}}$  and the  
 390     number of binary nucleon-nucleon collisions  $N_{\text{coll}}$  using a Glauber model. The Glauber  
 391     model, developed in the 1950s by Roy Glauber, describes the collision between two nuclei  
 392     as a superposition of independent NN interactions [53].

393     There are two ways of implementing the Glauber model, the optical and the Monte  
 394     Carlo approaches. In the optical approach, the physical observables are computed using  
 395     the optical limit which assumes a continuous nucleon density distribution. On the  
 396     other hand, in the Monte Carlo approach, the two nuclei are simulated by distributing  
 397     the nucleons according to their nuclear density profile, and then the nucleus-nucleus  
 398     collisions are modelled, at random impact parameters, by computing the individual NN  
 399     collisions [53].

400     An example of a heavy-ion collision described by the optical Glauber model geometry  
 401     is shown in Figure 1.10. It represents the collision between a nucleus A with  $A$  nucleons  
 402     and a nucleus B with  $B$  nucleons.

403     The tube located at a distance  $\vec{s}$  from the center of the nucleus A overlaps the tube  
 404     located at a distance  $\vec{b} - \vec{s}$  from the center of the nucleus B. In this case, the nuclear  
 405     overlap function  $T_{AB}(b)$  is defined as:

$$T_{AB}(b) = \int d\vec{s}^2 T_A(\vec{s}) T_B(\vec{b} - \vec{s}) \quad (1.10)$$

406     where  $T_A$  and  $T_B$  are the nuclear thickness functions of the nucleus A and B, respec-  
 407     tively.

408     The nuclear thickness function is given by  $T(\vec{r}) = \int dz \rho(\vec{r}, z)$ , where  $\rho$  is the nuclear

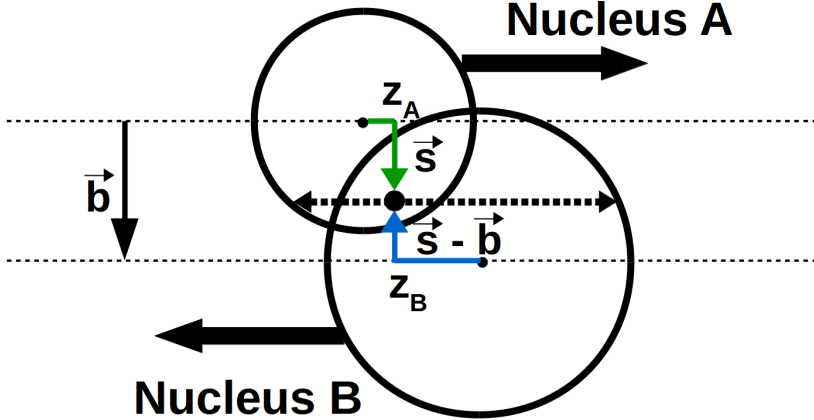


Figure 1.10: Schematic representation of the optical Glauber model geometry.

409 density distribution of a given nucleus, which is generally parametrised with a Wood-  
410 Saxon density profile [53]:

$$\rho(r) = \frac{\rho_0}{1 + \exp\left(\frac{r-r_0}{a}\right)} \quad (1.11)$$

411 where  $r$  is the distance to the center of the nucleus,  $a$  represents the width of the  
412 edge region of the nucleus called the skin depth,  $r_0$  is the mean radius of the nucleus  
413 and  $\rho_0$  is the nuclear density at the center of the nucleus. The average number of binary  
414 NN collisions  $\langle N_{\text{coll}} \rangle$  for a given impact parameter  $b$  is defined as:

$$\langle N_{\text{coll}}(b) \rangle = AB \cdot \langle T_{AB}(b) \rangle \cdot \sigma_{\text{nn}}^{\text{inel}} \quad (1.12)$$

415 where  $\sigma_{\text{nn}}^{\text{inel}}$  is the inelastic nucleon-nucleon cross section and  $\langle T_{AB}(b) \rangle$  is the average  
416 nuclear overlap function. Hence, the Glauber model provides a quantitative description  
417 of the geometry of the nuclear collision and can be used to estimate the variables ( $N_{\text{part}}$ ,  
418  $N_{\text{coll}}$  and  $T_{AB}$ ) for a given centrality class.

419 Experimentally, the impact parameter of the collision can not be determined directly.  
420 However, the distribution of the number of soft particles scales with  $N_{\text{part}}$ . As a result,  
421 one can classify the events in different centrality classes by binning the measured  
422 distribution of charged particles, so that each bin contain the same fraction of the  
423 total integral. The mean parameters  $\langle N_{\text{part}} \rangle$  and  $\langle N_{\text{coll}} \rangle$ , can be then derived, for each  
424 centrality class, by simulating the charged-particle distribution using a MC Glauber  
425 model. In addition, the collision centrality can sometimes be also inferred from the

426 number of spectators determined from the measurement of the transverse energy in the  
427 forward region.

428 **1.2.3 Evolution of heavy-ion collisions**

429 The evolution of a nucleus-nucleus collision undergoes several steps, starting from the  
430 collision of the nuclei to the final production of hadrons. Figure 1.11 illustrates the  
431 different processes that occur during a heavy-ion collision associated to the production of  
432 the QGP.

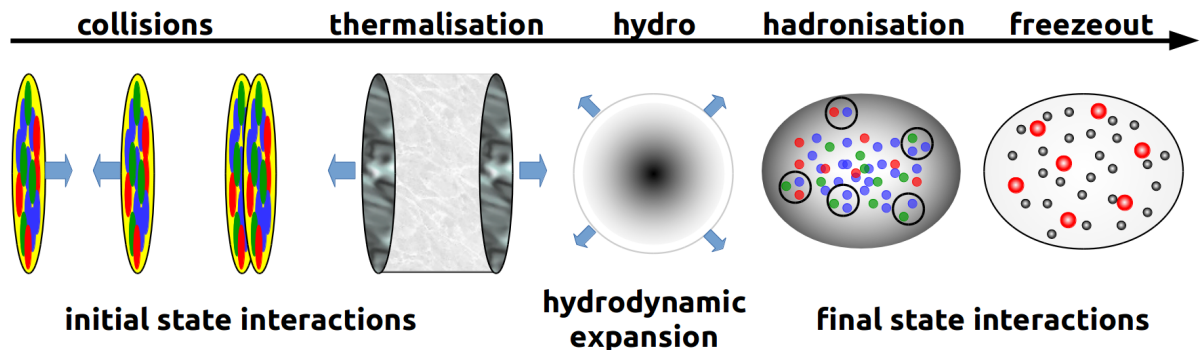


Figure 1.11: Sketch of the evolution of a relativistic heavy-ion collision.

433 1. Initial stage: At high energies, the two nuclei are Lorentz contracted along the  
434 axis of motion while approaching each other at almost the speed of light. As a  
435 consequence, the nucleons of each nuclei are also contracted increasing the number  
436 of gluons until it reaches the gluon saturation scale. The initial conditions can be  
437 described in various ways, depending on the physics to be addressed: the Glauber  
438 model or the effective theory called the Color Glass Condensate are often used.  
439 When the two nuclei collide, the partons inside the geometrical overlap region of  
440 the two nuclei undergo parton-parton interactions.

441

442 2. QGP formation and thermalisation: The parton-parton interactions quickly start  
443 producing new particles increasing the density of the system until a phase tran-  
444 sition is reached forming the QGP. After some time, the system reaches thermal  
445 equilibrium.

446

447 3. Hydrodynamical expansion: After reaching the thermal equilibrium, the system  
448 evolves as a nearly-perfect fluid. It first expands longitudinally along the beam  
449 direction and then it expands in all directions until the QGP cools down back to  
450 the critical temperature.

451

452 4. Hadronisation: The medium undergoes a second phase transition back to a hadronic  
453 gas where the partons recombine into hadrons. In this phase, the system keeps  
454 expanding via hadron-hadron interactions until the average path length of the  
455 hadrons is as large as the size of the system.

456

457 5. Freeze-out: The hadron gas experience first a chemical freeze-out when the in-  
458 elastic collisions between hadrons cease, fixing the composition of the particles.  
459 Subsequently, the system reaches a kinetic freeze-out when the elastic scattering  
460 between the hadrons also stop, fixing the kinematic distributions of the parti-  
461 cles. Subsequently, the particles escape the medium and are reconstructed in the  
462 detector.

#### 463 1.2.4 Experimental probes of the QGP

464 The QGP can not be directly measured experimentally, since once it is created it only  
465 exists for a very short amount of time. Nonetheless, the QGP can be studied indirectly  
466 by measuring how the particles and the system produced in the collision are modified by  
467 the presence of the QGP. There are many experimental *signatures* that has been used  
468 to asses the different properties of the QGP, such as the enhancement of the strange  
469 quark production, suppression of the quarkonium yields, attenuation of the energy of jets,  
470 anisotropies in the azimuthal distribution of particles, among others. The production  
471 mechanism of each experimental probe depends on the momentum scale of the process.  
472 Signatures produced in processes involving large momentum transfer are called hard  
473 probes while those produced at low momentum scales are called soft probes.

474 The majority of the particles produced in heavy-ion collisions are soft and constitute  
475 the bulk of the system. Soft probes are used to study the thermal and hydrodynamical  
476 evolution of the medium. The production yields of soft particles scales with  $N_{\text{part}}$ . The  
477 strange hadron yields and the elliptic flow are two examples of soft probes. On the  
478 other hand, hard probes are produced from the parton-parton hard scattering during  
479 the initial stage of the collision. Hard probes are ideal tools to study the structure of

480 the system since they are produced early in a well-controlled manner<sup>6</sup> and often living  
 481 through the QGP. The number of hard particles produced in the medium scales with  $N_{\text{coll}}$ .  
 482 Some important hard probes used to study the nuclear medium includes the electroweak  
 483 bosons, quarkonia and jets. The following subsections present a brief description on some  
 484 of the soft and hard probes of the QGP.

485 **1.2.4.1 Elliptic flow**

486 When the QGP is formed, it undergoes a collective expansion due to the large pressure  
 487 gradient produced by the multiple partonic interactions during the heavy-ion collision.  
 488 This collective expansion is known as flow. The magnitude of the flow tend to grow with  
 489 the number of parton-parton interactions and it depends on the initial conditions of the  
 490 collision. If the nucleus-nucleus collision is completely central ( $b = 0$ ) then the particles  
 491 develop a radial flow, but if the collision is non-central ( $b \neq 0$ ) then the spacial anisotropy  
 492 of the overlap region leads to an additional anisotropic flow as shown in Figure 1.12.

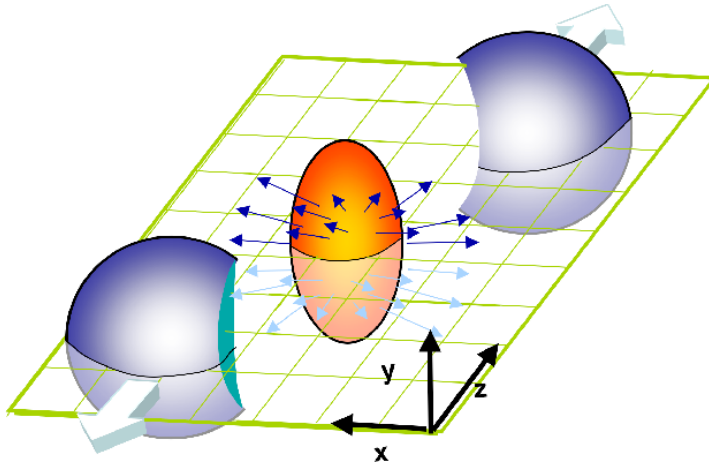


Figure 1.12: Sketch of the elliptic flow produced in non-central heavy-ion collisions.  
 Figure taken from Ref. [54].

493 Experimentally, the anisotropic flow can be determined from the Fourier decomposi-  
 494 tion of the particle azimuthal angle  $\phi$  distribution with respect to the reaction plane  
 495  $\psi_{RP}$  [55]:

$$\frac{d^3N}{d^3\vec{p}} = \frac{1}{2\pi} \frac{d^2N}{p_T dp_T dy} \left( 1 + 2 \sum_{n=1}^{\infty} v_n \cos[n(\phi - \psi_{RP})] \right) \quad (1.13)$$

---

<sup>6</sup>The production cross section of hard probes can be computed using the QCD factorisation theorem.

496 where the Fourier coefficient  $v_2$  measures the strength of the elliptic flow and the  
497 reaction plane is derived from the direction of the beam ( $z$ -axis) and the impact parameter  
498 ( $x$ -axis) as presented in Figure 1.12.

499 An alternative way to derive the flow coefficients is by computing the Fourier decom-  
500 position of the two-particle azimuthal distribution defined as [55]:

$$v_n \{2\}^2 = c_n \{2\} = \langle \cos[n(\phi_1 - \phi_2)] \rangle \quad (1.14)$$

501 where  $c_n \{2\}$  is called the two-particle cumulant and the brackets represent the  
502 average over all particles and events. The advantage of using particle correlations is that  
503 the Fourier coefficients do not depend on the reaction plane determination, but non-flow  
504 contributions (e.g. resonance decays or back-to-back jets) can affect the measurements.  
505 Correlating more than two particles, such as four-particle correlations, can reduce the  
506 impact of the non-flow effects.

507 The elliptic flow of the medium is sensitive to the equation of states of the QGP [55]  
508 and bulk viscosity [56]. Furthermore, relativistic hydrodynamic calculations [57] predicts  
509 that the elliptic flow of hadrons can approximately be expressed as  $v_2 \propto (p_T - \beta \cdot m_T)$ ,  
510 where  $\beta$  is the average flow velocity and  $m_T$  is the transverse mass of the hadron, which  
511 is defined as  $m_T^2 = m^2 + p_T^2$ . As a consequence, the elliptic flow is expected to show a mass  
512 ordering where the more massive hadrons would have lower  $v_2$  values compared to the  
513 lighter hadrons.

514 The low  $p_T$ -dependence of the elliptic flow of strange hadrons measured at RHIC in  
515 Au-Au collisions at  $\sqrt{s_{NN}} = 200$  GeV is presented in Figure 1.13. The measurement of  
516 the elliptic flow of  $\pi^\pm$  mesons,  $K_s^0$  mesons, antiprotons and  $\Lambda$  baryons (with masses of  
517 140, 495, 940 and 1,115 MeV, respectively), shows the expected mass ordering pattern.  
518 Moreover, the good agreement between the RHIC results and the predictions using  
519 relativistic hydrodynamics assuming that the fluid flow is non-viscous, supported the  
520 conclusion that the QGP behaves as a nearly ideal fluid [58].

521 At the start of the LHC, the CMS collaboration performed a measurement of the two-  
522 particle angular correlations in p-p collisions producing high number of particles (referred  
523 as high-multiplicity collisions). Figure 1.14 presents the two-particle  $\Delta\eta$ - $\Delta\phi$  correlation  
524 function measured by the CMS collaboration in p-p collisions at  $\sqrt{s} = 7$  TeV [59], where  
525  $\Delta\phi$  is the azimuthal angle difference between the two particles and  $\Delta\eta$  is the difference  
526 in their pseudorapidity. The results show a long-range structure ( $2.0 < \Delta\eta < 4.8$ ) of  
527 near-side ( $\Delta\phi \sim 0$ ) two-particle correlations, often called "ridge". The structure is seen  
528 for particles with  $1 \text{ GeV}/c < p_T < 3 \text{ GeV}/c$ , produced in high-multiplicity ( $N > 110$ ) p-p

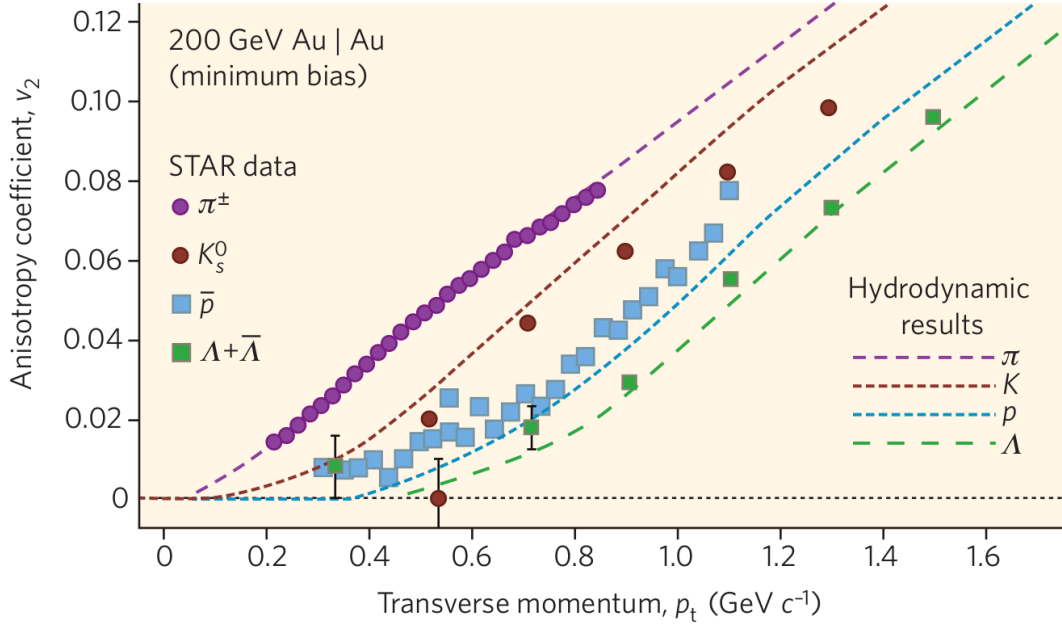


Figure 1.13: Elliptic flow distribution of as a function of transverse momentum for  $\pi^\pm$  mesons,  $K_s^0$  mesons, antiprotons and  $\Lambda$  baryons measured by STAR collaboration in Au-Au collisions at  $\sqrt{s_{\text{NN}}} = 200 \text{ GeV}$ . The results are compared with relativistic hydrodynamic calculations. Figure taken from Ref. [58].

529 collisions. A similar ridge-like structure had already been observed at RHIC in heavy-ion  
 530 collisions [60], which was understood as a result of the hydrodynamic expansion of the  
 531 QGP, but the phenomenon found in p-p collisions was completely unexpected at the time  
 532 and it is still not fully understood yet.

### 533 1.2.4.2 Strangeness enhancement

534 Strange quarks belongs to the second generation of quarks and are roughly 20-40 times  
 535 more massive than up and down quarks. The number of strange quarks involved in a  
 536 decay can be quantified through the quantum number called strangeness, which can take  
 537 values of  $+1$ ,  $-1$  and  $0$ , for strange quarks, strange anti-quarks, and the other quarks,  
 538 respectively. Strangeness is conserved in strong and electromagnetic interactions, while  
 539 it is not conserved in weak decays. In hadronic collisions, strange quark-antiquark  
 540 pairs ( $s\bar{s}$ ) are produced in parton-parton interactions via gluon fusion ( $gg \rightarrow s\bar{s}$ ) or quark  
 541 annihilation ( $q\bar{q} \rightarrow s\bar{s}$ ), and through gluon splitting ( $g \rightarrow s\bar{s}$ ) during the evolution of the  
 542 medium. The production of strange hadrons in proton-proton collisions is suppressed  
 543 relative to hadrons made of light quarks (i.e. pions), due to the higher mass of the strange

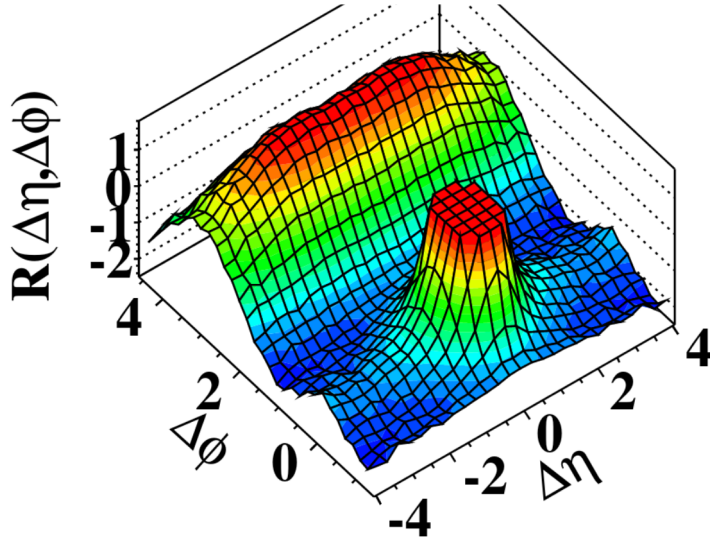


Figure 1.14: 3D display of the  $\Delta\eta$ - $\Delta\phi$  correlation function between two charged particles with  $1 \text{ GeV}/c < p_T < 3 \text{ GeV}/c$ , measured by the CMS collaboration in high multiplicity ( $N \geq 110$ ) p-p collisions at  $\sqrt{s} = 7 \text{ TeV}$ . Figure taken from Ref. [59].

544 quark.

545 In heavy-ion collisions, where the QGP is formed, it was proposed by Johann Rafelski  
 546 and Rolf Hagedorn [61] in 1980, that the enhancement of strangeness could serve as  
 547 a signature of the QGP. Due to the large gluon density and energy present in the hot  
 548 medium, the gluon fusion becomes the dominant production mode of strange-quark pairs  
 549 in the QGP. When the temperature of the QGP decreases and the partons hadronise,  
 550 the production of hadrons containing strange (anti-)quarks is enhanced relative to the  
 551 production of pions. Moreover, at high collision energies, the strange quarks can also bind  
 552 to charm and bottom quarks during hadronisation, producing many exotic hadrons (e.g.  
 553 strange D<sub>s</sub> or B<sub>s</sub> mesons) that would otherwise be rarely seen without the presence of  
 554 the QGP. In summary, one expects an overall increase of strange-quark pair production,  
 555 leading to an enhancement of the production of strange hadrons in central heavy-ion  
 556 collisions compared to proton-proton collisions [62].

557 The enhancement of strange hadrons has been observed at SPS [63, 64] and RHIC [65].  
 558 The production yields in heavy-ion collisions of strange hadrons measured at RHIC and  
 559 SPS are shown in Figure 1.15. The results show a clear enhancement of the production  
 560 of strange baryons in heavy-ion collisions relative to p-p (at RHIC) or p-Be (at SPS)  
 561 collisions, increasing for higher  $N_{\text{part}}$  (more central collisions) and strangeness content  
 562 ( $\Omega^-[\text{sss}] > \Xi^-[\text{dss}] > \Lambda[\text{uds}]$ ). This strangeness enhancement can be described using a

563 thermal model based on a grand canonical ensemble approach, suggesting the presence  
 564 of a hot medium [62].

565 Recently, the ALICE collaboration published in [66] the observation of enhanced  
 566 production of strange hadrons in high-multiplicity proton-proton collisions at  $\sqrt{s} =$   
 567 7 TeV, as presented in the right plot of Figure 1.15. The results at LHC show that the  
 568 enhancement of the strangeness production increases as a function of charged-particle  
 569 multiplicity from high-multiplicity p-p to p-Pb to Pb-Pb collisions. Therefore, further  
 570 studies of the mechanism of strangeness production at high multiplicities are necessary  
 571 to understand the evolution of small systems.

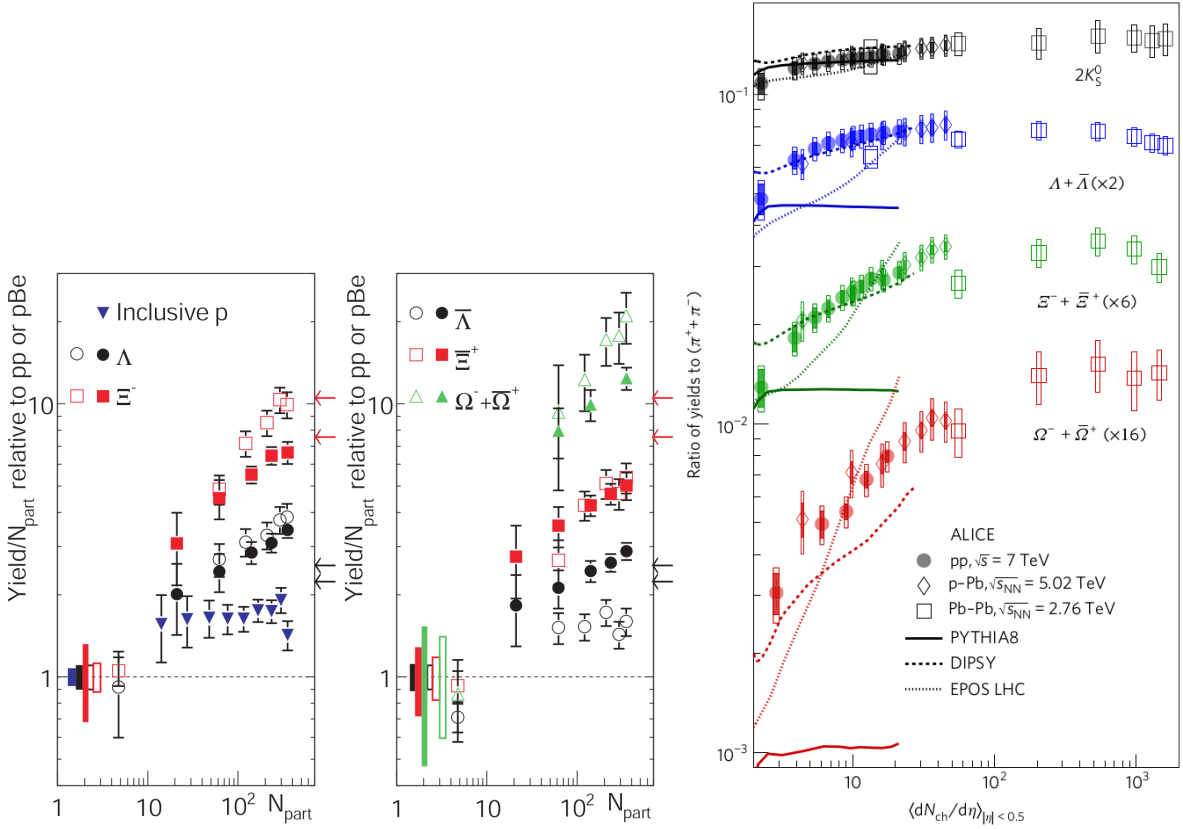


Figure 1.15: Left: Distribution of the yield of inclusive protons and strange baryons, measured by the STAR collaboration in Au-Au collisions at  $\sqrt{s_{\text{NN}}} = 200$  GeV (solid symbols) and by the NA57 collaboration in Pb-Pb collisions at  $\sqrt{s_{\text{NN}}} = 17.3$  GeV (empty symbols), relative to the corresponding yield in p-p (at RHIC) or p-Be (at SPS) collisions scaled by  $N_{\text{part}}$ . Figure from Ref. [65]. Right: Distribution of the  $p_T$ -integrated yield ratios of strange hadrons to pions as a function of the average charged-particle multiplicity measured in  $|\eta| < 0.5$  by the ALICE collaboration in p-p, p-Pb and Pb-Pb collisions at  $\sqrt{s} = 7$  TeV,  $\sqrt{s_{\text{NN}}} = 5.02$  TeV and  $\sqrt{s_{\text{NN}}} = 2.56$  TeV, respectively. Figure from Ref. [66].

572 **1.2.4.3 Jet quenching**

573 Energetic partons are produced in the hard scattering at the beginning of the collision.  
 574 These scattered partons fragment into other colour-charged particles, which then create  
 575 an ensemble of hadrons during the hadronisation process. The baryons and mesons  
 576 produced at the end of the collision tend to move along the same direction as the original  
 577 fragmented parton, forming a localised spray of particles called jet. The jets can be  
 578 reconstructed by clustering hadrons and other particles around a given direction using a  
 579 jet sequential recombination algorithm (e.g. anti- $k_t$  [67]).

580 In heavy-ion collisions, the hard partons lose energy when they traverse the hot  
 581 medium either by multiple scattering with the medium constituents or by medium-  
 582 induced gluon radiation. As a consequence, the energy of the jets is attenuated and the  
 583 jets are considered quenched by the medium. The phenomenon of jet quenching in the  
 584 QGP was first proposed in 1982 by James Bjorken. Bjorken suggested in [68] that the  
 585 observation of events with two jets, where one of the jets escape the QGP without loosing  
 586 energy while the other jet is fully quenched as shown in Figure 1.16, could be used as a  
 587 probe to determine the presence of the QGP.

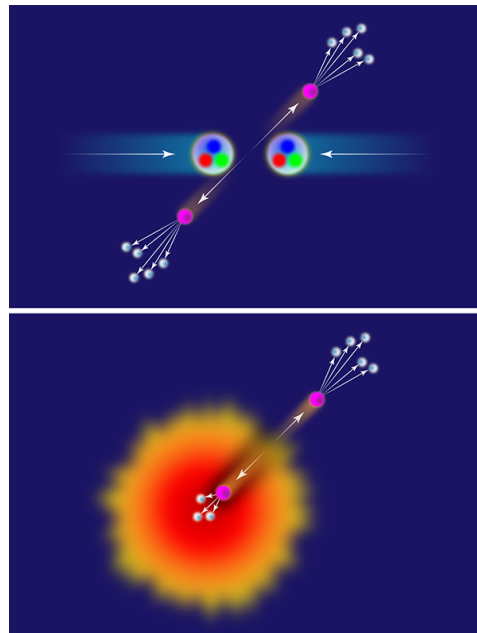


Figure 1.16: Sketch of the production mechanism of two jets in proton-proton (top) and heavy-ions (bottom) collisions. Figure taken from Ref. [69].

588 In order to quantify how the hot nuclear medium modifies the production of a given  
 589 particle, one can measure the nuclear modification factor  $R_{AA}$  defined as:

$$R_{AA} = \frac{N_{AA}}{\langle N_{coll} \rangle N_{pp}} \quad (1.15)$$

590 where  $N_{AA}$  is the yield of particles measured per nucleus-nucleus collision,  $N_{pp}$  is  
 591 the same yield measured per p-p collision, and  $\langle N_{coll} \rangle$  is the average number of binary  
 592 nucleon-nucleon collisions. Proton-proton collisions are used as a reference since most of  
 593 the events do not produce a QGP, even though it is not excluded that a hot medium could  
 594 be formed in the most rare and violent p-p collisions.

595 The first direct observation of jet quenching was determined at RHIC, where the  
 596 production of hadrons were found to be suppressed in central Au-Au collisions compared  
 597 to p-p collisions. Figure 1.17 shows the nuclear modification factor of direct photons<sup>7</sup>,  
 598 pions,  $\eta$  mesons, and charged hadrons measured at RHIC in central Au-Au collisions at  
 599  $\sqrt{s_{NN}} = 200 \text{ GeV}$ . The results show a strong suppression ( $R_{AA} \sim 0.2$ ) of the production of  
 600 hadrons consistent with parton energy loss in the QGP<sup>8</sup>. In addition, the  $R_{AA}$  of direct  
 601 photons is found to be consistent with unity (expected since photons do not interact  
 602 strongly), which serves as a sanity check of the  $N_{coll}$  scaling.

603 In the case of LHC, an enhanced dijet asymmetry was observed in Pb-Pb collisions  
 604 compared to proton-proton collisions. The dijet asymmetry is quantified by measuring the  
 605 jet energy imbalance between the two highest transverse energy jets with an azimuthal  
 606 angle separation of  $\Delta\phi = |\phi_1 - \phi_2| > \pi/2$ . The jet energy imbalance  $A_J$  is derived as:

$$A_J = \frac{E_{T1} - E_{T2}}{E_{T1} + E_{T2}} \quad (1.16)$$

607 where  $E_{T1}$  is the transverse energy of the most energetic jet among the pair of  
 608 jets. 1.18 presents the results, published by the ATLAS collaboration [72], of the dijet  
 609 asymmetry distribution and the azimuthal angle between the two jets in different bins  
 610 of centrality. The dijet asymmetry measured in Pb-Pb collisions at  $\sqrt{s_{NN}} = 2.76 \text{ TeV}$  are  
 611 compared to the measurements from p-p collisions at  $\sqrt{s} = 7 \text{ TeV}$  and the simulated  
 612 results derived using events from the Heavy Ion Jet INteraction Generator (HIJING)  
 613 superimposed with PYTHIA events. The LHC results show a significant dijet energy  
 614 imbalance in Pb-Pb collisions which increases with the centrality of the collision. The  
 615 missing jet energy was later found in the form of low-momentum particles emitted at  
 616 larger angles [73]. This dijet asymmetry is not seen in p-p collisions evidencing the  
 617 strong jet energy loss present in the QGP.

---

<sup>7</sup>Photons not originating from the decay of hadrons.

<sup>8</sup>At low  $p_T$ , extra thermal photons can be created by the medium providing insights on its average temperature [70].

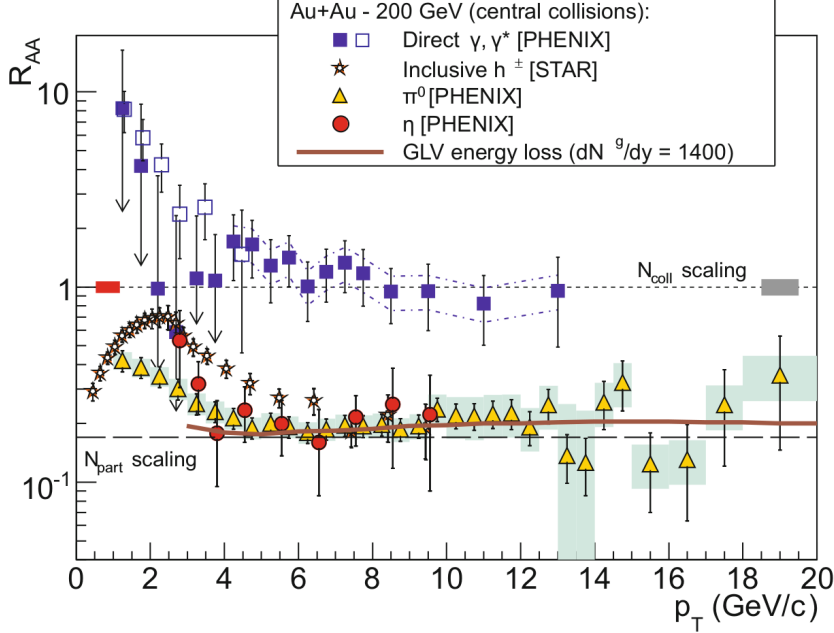


Figure 1.17: Distribution of the nuclear modification factor  $R_{AA}$  of direct photons, pions,  $\eta$  mesons and charged hadrons, measured at RHIC in central Au-Au collisions at  $\sqrt{s_{NN}} = 200$  GeV. Theoretical predictions of radiative parton energy loss are also included. Figure taken from Ref. [71].

#### 618 1.2.4.4 Quarkonium production

619 Quarkonia ( $Q\bar{Q}$ ) are mesons composed of a heavy quark and its own anti-quark. Quarko-  
 620 nia can be classified as charmonia or bottomonia if they are made of charm quarks or  
 621 bottom quarks, respectively. The first excited state of charmonia is called  $J/\psi$  meson while  
 622 for bottomonia is called  $\Upsilon(1S)$  meson. The properties of quarkonia are non-perturbative  
 623 but since the mass of the heavy quarks is comparable to the mass of the quarkonia, the  
 624 quarks move inside the quarkonia much slower than the speed of light. As a result, the  
 625 properties of quarkonia can be computed using an effective non-relativistic model. For  
 626 instance, one way to describe the binding of the quarks is by using a Cornell potential [74]  
 627 given by:

$$V_{Q\bar{Q}}(r) = -\frac{a}{r} + br \quad (1.17)$$

628 where  $r$  is the binding radius of the quarkonium,  $a$  is the coulombic interaction  
 629 coupling, and  $b$  is the string tension. By solving the Schrödinger equation for the  $Q\bar{Q}$   
 630 potential, one finds several higher excited states of charmonia (e.g.  $\psi(2S)$ ) and bottomonia

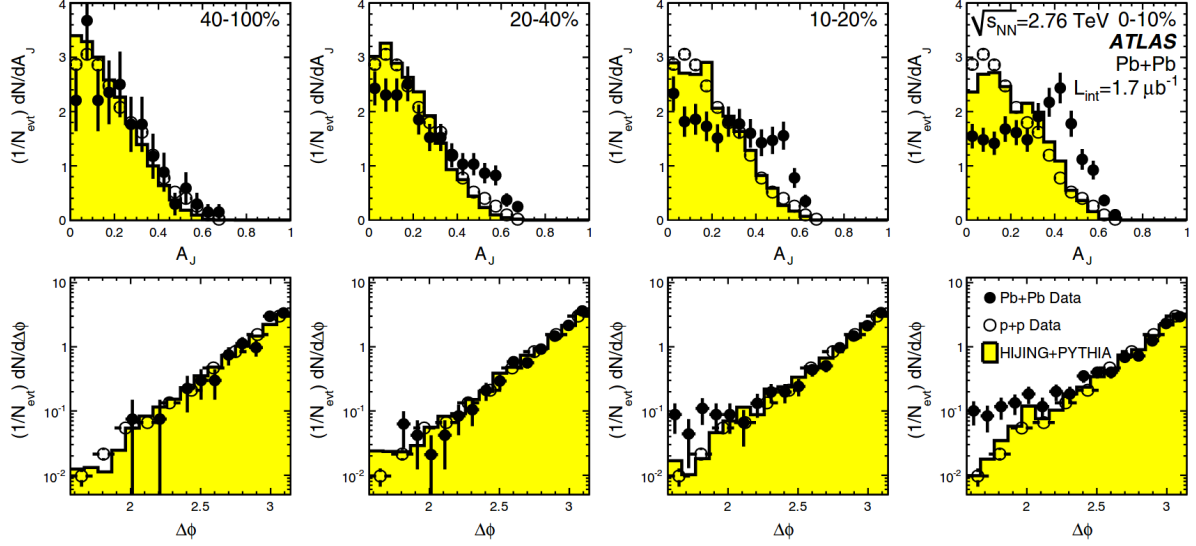


Figure 1.18: Dijet asymmetry measured by the ATLAS collaboration in lead-lead collisions at  $\sqrt{s_{NN}} = 2.76$  TeV (points) and proton-proton collisions at  $\sqrt{s} = 7$  TeV (open circles). The top panel shows the dijet asymmetry distributions and unquenched HIJING with superimposed PYTHIA dijets (solid yellow histograms), as a function of collision centrality. The bottom panel shows the distribution of the azimuthal angle between the two jets  $\Delta\phi$ , for data and HIJING+PYTHIA, also as a function of centrality. Figure taken from Ref. [72].

631 (e.g.  $\Upsilon(2S)$  and  $\Upsilon(3S)$ ), with lower binding energies and larger radius (i.e.  $r_{\Upsilon(1S)} < r_{\Upsilon(2S)} <$   
632  $r_{\Upsilon(3S)}$ ).

633 One of the first signatures suggested to probe the QGP was the suppression of  $J/\psi$   
634 meson production. In 1986, Tetsuo Matsui and Helmut Satz [75] proposed that the  
635  $J/\psi$  meson binding potential gets screened in the QGP due to the interactions with  
636 the free colour charged constituents of the hot medium. The Debye colour screening  
637 potential increases with the temperature of the medium until the binding potential can  
638 no longer hold the quarks together, and the quarkonium "melts". The binding potential  
639 of quarkonium states gets weaker for larger binding radius. As a result, the higher  
640 excited states of quarkonium are expected to be more dissociated at a given temperature  
641 compared to the ground state, leading to a sequential suppression of quarkonia.

642 The sequential suppression of bottomonium states has been observed at the LHC.  
643 Figure 1.19 shows the invariant mass distribution of dimuons measured by the CMS  
644 collaboration in Pb-Pb collisions at  $\sqrt{s_{NN}} = 5.02$  TeV [76]. The result is compared to the  
645 invariant mass distribution obtained by adding the bottomonium mass peaks extracted

646 from p-p collisions at  $\sqrt{s} = 5.02$  TeV on top of the Pb-Pb background and normalised  
 647 to the  $\Upsilon(1S)$  mass peak in Pb-Pb. The comparison shows a clear suppression pattern  
 648 where the  $\Upsilon(3S)$  meson is completely melted while part of the  $\Upsilon(2S)$  mass peak still  
 649 survives. In the case of the  $\Upsilon(1S)$  meson, the feed-down contributions from excited state  
 650 decays of  $\chi_b(nP) \rightarrow \Upsilon(1S)$  and  $\nu(nS) \rightarrow \Upsilon(1S)$ , can reach values up to 40% as measured  
 651 by the LHCb collaboration for  $p_T^\Upsilon > 6$  GeV/c [77]. As a result, it is not clear if the observed  
 652 suppression of the  $\Upsilon(1S)$  meson is due to deconfinement in the QGP or the dissociation  
 653 of the excited states that decays to the  $\Upsilon(1S)$  meson.

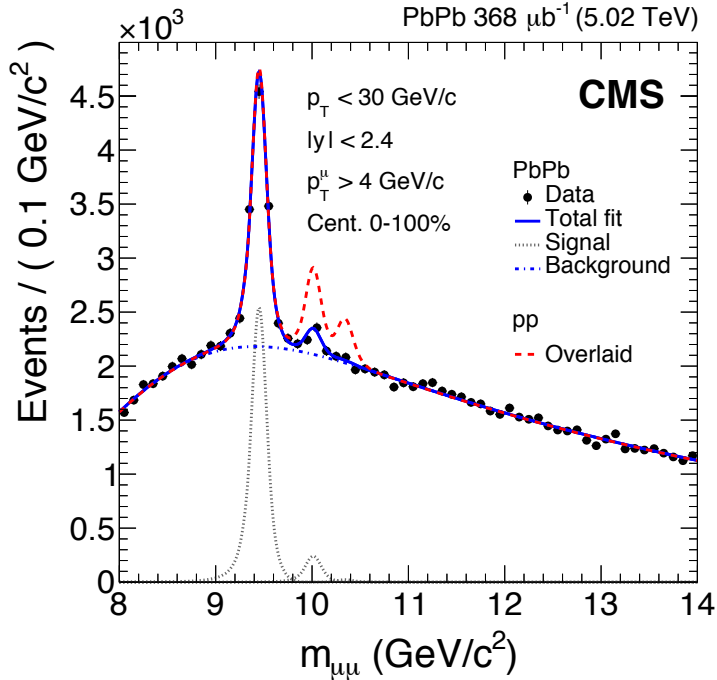


Figure 1.19: Dimuon invariant mass distribution measured by the CMS collaboration in Pb-Pb collisions at  $\sqrt{s_{NN}} = 5.02$  TeV. The total fit (solid blue line), the background component (dot-dashed blue line) and the individual  $\Upsilon(1S)$ ,  $\Upsilon(2S)$  and  $\Upsilon(3S)$  mass peaks (dotted gray lines) are shown. The dashed red line represents the p-p signal shapes added on top of the Pb-Pb background and normalised to the  $\Upsilon(1S)$  mass peak in Pb-Pb. Figure taken from Ref. [76].

654 The first evidence of  $J/\psi$ -meson anomalous suppression (i.e. beyond nuclear effects)  
 655 was observed in Pb-Pb collisions at 158 GeV/nucleon by the NA50 collaboration at  
 656 SPS [78]. The results at SPS showed that the  $J/\psi$ -meson cross section measured in  
 657 peripheral collisions was consistent with the expectations from nuclear absorption  
 658 while in central collisions it was more suppressed [79]. The measurement of the  $J/\psi$ -  
 659 meson production in Au-Au collisions at  $\sqrt{s_{NN}} = 200$  GeV at RHIC [80] showed a similar

660 level of suppression at mid-rapidity ( $|y| < 0.35$ ) compared to SPS, despite the higher  
661 energy density at RHIC. In addition, the production of  $J/\psi$  mesons at forward rapidity  
662 ( $1.2 < |y| < 2.2$ ) was found to be more suppressed than at mid-rapidity.

663 To understand the measurements of  $J/\psi$ -meson production at SPS and RHIC, two  
664 explanations were proposed. The first one suggested that, apart from the anomalous  
665 suppression, the  $J/\psi$  meson production could also be enhanced at RHIC energies. Ac-  
666 cording to [81], the  $J/\psi$  mesons could be regenerated in the most central collisions from  
667 the combination of initially uncorrelated charm quarks (i.e. not produced in the same  
668 hard scattering). The number of directly produced  $c\bar{c}$  pairs in central nucleus-nucleus  
669 collisions is expected to be small at SPS energies, but it can reach values around 10 (200)  
670 charm-quark pairs at RHIC (LHC) energies [82, 83]. The second explanation proposed  
671 that the production of  $J/\psi$  mesons at RHIC was mainly affected by an interplay between  
672 initial state effects (e.g. nuclear PDFs or CGC) and the dissociation of the excited states  
673 (e.g.  $\chi_c$  and  $\psi(2S)$ ) that contributes to the feed-down of the  $J/\psi$  meson.

674 The measurements of the  $J/\psi$ -meson production have also been performed at the  
675 LHC. The results of the  $J/\psi$ -meson nuclear modification factor measured by the ALICE  
676 collaboration in the 0% – 20% most central Pb-Pb collisions at  $\sqrt{s_{NN}} = 2.76 \text{ TeV}$  are  
677 compared in Figure 1.20 to the results measured by the PHENIX collaboration in the  
678 0% – 20% most central Au-Au collisions at  $\sqrt{s_{NN}} = 200 \text{ GeV}$ . The  $J/\psi R_{AA}$  measured at  
679 the LHC is larger than the one measured at RHIC at low  $J/\psi$  meson  $p_T$ , which can so far  
680 only be explained by the presence of regeneration.

#### 681 **1.2.4.5 Electroweak boson production**

682 Electroweak particles, such as W bosons and Z bosons, are produced in the parton-parton  
683 hard scattering and they do not interact strongly with the nuclear medium produced in  
684 the heavy-ion collisions. As a result, electroweak bosons are good probes of the initial  
685 stage of the proton-nucleus (p-A) and nucleus-nucleus (A-A) collisions, but they do not  
686 probe the QGP. The dominant production mode of electroweak bosons in heavy-ion  
687 collisions is via the annihilation of a light quark and anti-quark. The large momentum  
688 scales involved in the production of weak bosons allows to derive precise calculations of  
689 their partonic cross sections using pQCD.

690 The production yields of electroweak bosons in p-A or A-A collisions are affected by  
691 the mix of protons and neutrons in the colliding nucleus (isospin effect), and the depletion  
692 (shadowing) or enhancement (anti-shadowing) of the PDFs in the nucleus. Thus, the  
693 measurement of the electroweak boson production in heavy-ion collisions can be used

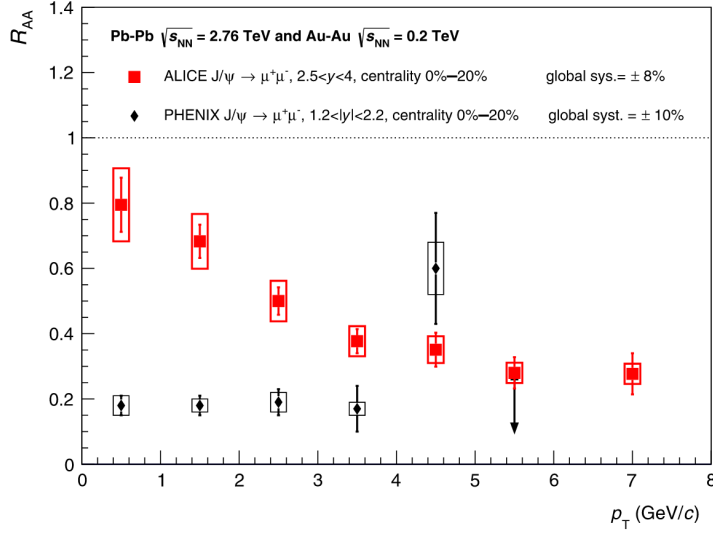


Figure 1.20: Nuclear modification factor of  $\text{J}/\psi$  meson as a function of transverse momentum measured by the ALICE collaboration in the 0% – 20% most central Pb-Pb collisions at  $\sqrt{s_{\text{NN}}} = 2.76 \text{ TeV}$  compared to results from the PHENIX collaboration measured in the 0% – 20% most central Au-Au collisions at  $\sqrt{s_{\text{NN}}} = 200 \text{ GeV}$ . Figure taken from Ref. [84].

694 to set constraints to the global fits of the nuclear PDFs. In the case of A-A collisions,  
 695 the measurement of the nuclear modification factor of Z bosons at the LHC in Pb-Pb  
 696 collisions at  $\sqrt{s_{\text{NN}}} = 2.56 \text{ TeV}$  [85], presented in Figure 1.21, shows that the production  
 697 of weak bosons is not modified by the hot nuclear medium and can then be used as  
 698 a *standard candle* to check, at first order, the binary scaling ( $R_{\text{AA}} = 1$ ) and indirectly  
 699 determine the centrality of the collision.

## 700 Summary

701 Our understanding of the QGP has expanded substantially since the last 20 years.  
 702 The first evidence of its existence was found at SPS, after studying the suppression  
 703 of  $\text{J}/\psi$  mesons and the strangeness enhancement in Pb-Pb collisions. Years after, the  
 704 first observation of the QGP was claimed at RHIC, supported by a vast amount of  
 705 experimental signatures such as jet quenching, charmonium suppression, strangeness  
 706 enhancement and collectivity. The QGP found at RHIC turns out to behave as a nearly  
 707 perfect dense fluid. The QGP was later also observed at the LHC, which has provided  
 708 further knowledge on the properties of the QGP at TeV energies. In addition, the LHC  
 709 experiments have also observed hints of the formation of a collective medium in small  
 710 systems such as high-multiplicity p-p collisions, which is still not fully understood.

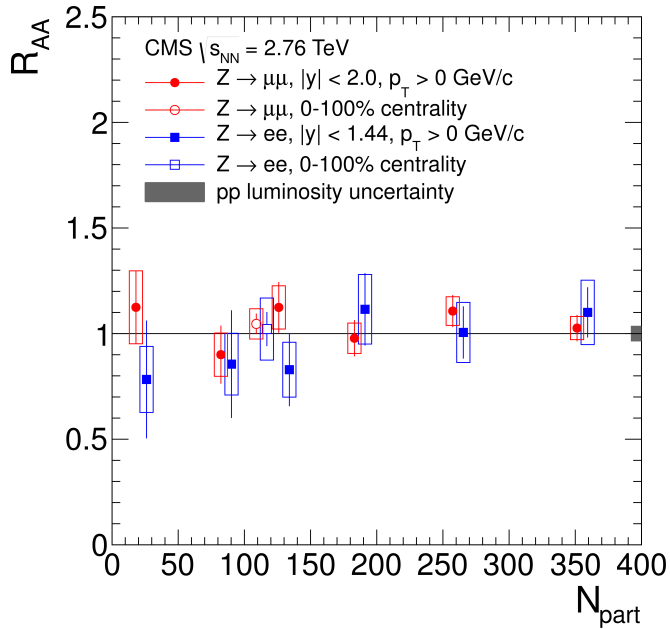


Figure 1.21: Nuclear modification factor  $R_{AA}$  of  $Z \rightarrow e^+e^-$  (blue squares) and  $Z \rightarrow \mu^+\mu^-$  (red circles) events as a function of  $N_{\text{part}}$  measured by the CMS collaboration in Pb-Pb collisions at  $\sqrt{s_{\text{NN}}} = 2.56 \text{ TeV}$ . The open points represent the centrality-integrated  $R_{AA}$  and the vertical lines (boxes) correspond to statistical (systematic) uncertainties. Figure taken from Ref. [85].

711     The production of  $J/\psi$  mesons in heavy-ion collisions has shown a rich phenomenology  
 712     and will be the main topic of Chapter 4, where the analysis of charmonia in Pb-Pb  
 713     collisions will be presented. These results provide new insights on the production of  
 714     non-prompt  $J/\psi$  mesons (i.e. from b-hadron decays) and  $\psi(2S)$  mesons, extending the  
 715     coverage to higher charmonium  $p_T$  ranges.

716     Electroweak bosons are sensitive probes of the initial state of the collision and  
 717     the measurement of their production in heavy-ion collisions can be used to constrain  
 718     the nuclear PDFs, which are crucial theoretical inputs for a better description of the  
 719     formation of the QGP. In Chapter 3, this thesis reports the first measurement of significant  
 720     nuclear modification of W-boson production.

721

722

## EXPERIMENTAL SETUP

723 This chapter provides a brief overview of the experimental setup employed to ac-  
724 quire the data used in this thesis. The data is derived from high energy collisions  
725 of protons and lead ions recorded by the Compact Muon Solenoid (CMS) detector.  
726 The Large Hadron Collider (LHC) and the settings of the particle collisions are described  
727 in Section 2.1. The main features of the CMS detector and its components are detailed in  
728 Section 2.2.

### 729 2.1 The Large Hadron Collider

730 The Large Hadron Collider is currently the largest and highest-energy particle accelera-  
731 tor in the world. It is installed in an underground tunnel of 26.7 km in circumference,  
732 located as deep as 175 m underground beneath the border between France and Switzer-  
733 land. The construction of the LHC was handled by CERN and took almost 30 years.  
734 The LHC is designed to accelerate and collide beams of protons or heavy ions (e.g Pb  
735 nuclei). Before being injected into the LHC, particles are accelerated through a chain of  
736 accelerators housed at CERN. Each accelerator boosts the energy of the particles and  
737 transfers them to the next machine. The accelerator complex for the LHC is presented  
738 in Section 2.1.1 and a short description of the LHC detectors is given in Section 2.1.2.  
739 The concept of luminosity is introduced in Section 2.1.3, and brief overview of the LHC  
740 schedule and heavy-ion schemes used during 2015-2016, are presented in Section 2.1.4  
741 and Section 2.1.5, respectively.

### 2.1.1 Accelerator complex

There are two main injection chains for the LHC, one optimised for protons and the other for Pb nuclei ( $Pb^{82+}$ ). Figure 2.1 shows a schematic diagram of the LHC injection chains for protons and Pb ions represented with red and blue arrows, respectively.

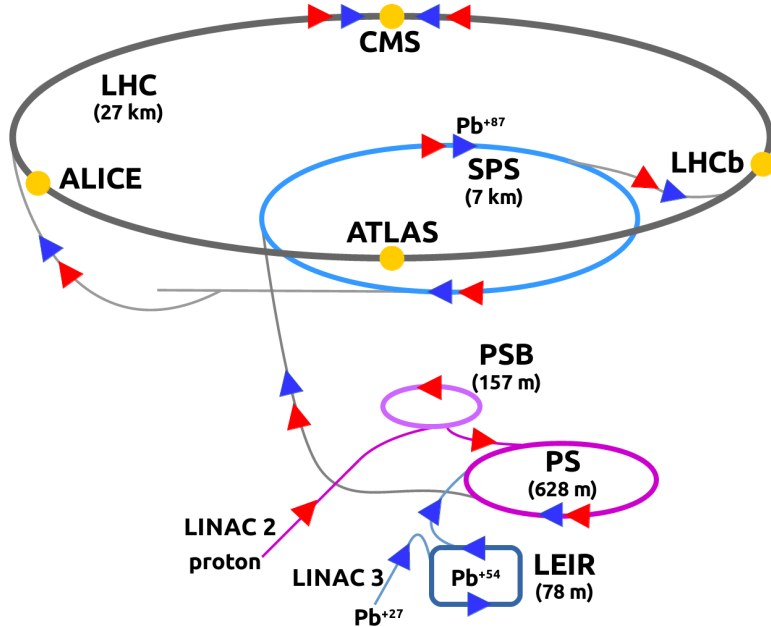


Figure 2.1: Schematic diagram of the LHC injection chain for protons and Pb nuclei. The proton and Pb ion trajectories are indicated with red and blue arrows, accordingly. The location of each LHC detector is also included.

Protons are extracted from a gas of hydrogen atoms by stripping off their electrons in a duoplasmatron, and are initially accelerated to an energy of 50 MeV with radio-frequency (RF) cavities in the linear accelerator Linac-2. Afterwards, they are sent to the Proton Synchrotron Booster (PSB), which is composed of four superimposed synchrotron rings that groups the protons into bunches and accelerates them to 1.4 GeV. Six proton bunches from the PSB are sequentially fed into the Proton Synchrotron (PS), where they are accelerated to 25 GeV and further splitted into 72 bunches separated in time by 25 ns. The proton beam is further accelerated to 450 GeV in the Super Proton Synchrotron (SPS) and alternately injected in the two LHC beam pipes, one beam pipe in the clockwise direction and the other in the counter-clockwise direction. Conventional electromagnets are used to keep the particles circulating in the PSB, PS and SPS accelerators.

The heavy-ion accelerator chain was initially designed in the 1990s for the SPS fixed-

target experiments and then upgraded in the 2000s for the LHC. The Electron Cyclotron Resonance Ion Source (ECRIS) is used to produce heavy ions. In the case of lead, a beam of  $\text{Pb}^{27+}$  ions with an energy of 2.5 keV/nucleon is extracted from the ECRIS every 200  $\mu\text{s}$ , and then accelerated to 250 keV/nucleon with a 100 MHz RF quadrupole (RFQ). The ion beam is sent afterwards to the linear accelerator Linac-3, which accelerates the Pb ions to 4.2 MeV/nucleon and transfers them to the Low Energy Ion Ring (LEIR). The  $\text{Pb}^{27+}$  ions are passed through a 0.3  $\mu\text{m}$ -thick carbon foil in the Linac-3–LEIR transfer line, stripping them to  $\text{Pb}^{54+}$  ions. The LEIR accelerates the  $\text{Pb}^{54+}$  ions to 72 MeV/nucleon and packs them in bunches using electron cooling. Every 3.6 s, the LEIR feeds two bunches into the PS ring and up to 16 bunches are accumulated, forming a batch, before being transferred to the SPS. The PS batch is compressed to a time interval of 100 ns, and accelerated to 5.9 GeV/nucleon. When the  $\text{Pb}^{54+}$  ions are sent to the SPS, they are fully stripped ( $\text{Pb}^{82+}$  ions) through an aluminium foil. The SPS accelerates up to twelve  $\text{Pb}^{82+}$  ion batches from the PS to 176.4 GeV/nucleon and then injects them into the LHC.

The LHC consists of eight straight sections called insertion regions (IR), connected by eight arc sections as shown in Figure 2.2. The size and trajectory of the particle beams are controlled, in each arc section of the LHC, with a series of superconducting magnets made of Niobium-Titanium and kept at a temperature of 1.9 K with superfluid Helium-4. Dipole magnets are used to bend the particles, while quadrupole magnets focus the beam. Moreover, each particle beam is accelerated in IR4 with eight RF superconducting cavities operated at 400 MHz. The LHC beam dumping system, employed to safely stop the particle beams, is located at IR6. In addition, to protect the LHC from beam losses and absorb the beam halo, a collimation system is installed at IR3 and IR7, dedicated for beam momentum and betatron cleaning, respectively. The other four insertion regions house each of the four main LHC detectors, where the beams are collided in their corresponding interaction point (IP).

### 2.1.2 Detectors

The four main detectors installed in the LHC ring are:

- A Large Ion Collider Experiment (ALICE) [87]: a particle detector located at IP2, specialised on the measurement of the properties of nuclear matter at high densities. The main interest of the ALICE collaboration is the study of the QGP and the different aspects of heavy-ion physics. The ALICE detector is divided in three sets of subdetectors: the global event detectors are used to characterise

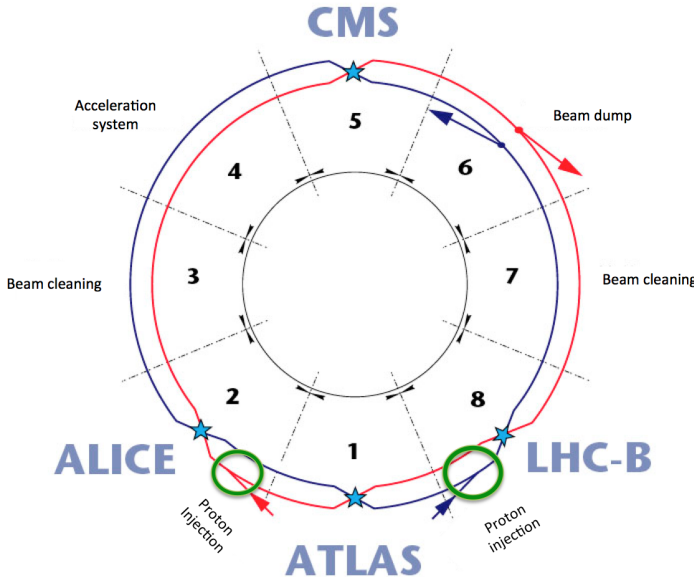


Figure 2.2: Schematic diagram of the LHC layout. Figure taken from Ref. [86].

791       the geometry of the collisions, the central barrel detectors can track charged  
792       particles down to low momentum and identify hadrons and electrons, and the  
793       muon spectrometer can reconstruct muons in the forward region.

- 794     • A Toroidal LHC ApparatuS (ATLAS) [88]: a general-purpose particle detector  
795       located at IP1, optimised for particle collisions at the highest rates and energies  
796       achieved in the LHC. It consists of a toroidal magnetic system, an inner tracker,  
797       an electromagnetic and hadronic calorimeter, and a muon spectrometer. It is able  
798       to measure the energy of electromagnetic particles and hadrons, determine the  
799       momentum of charged particles, reconstruct jets, and identify muons with high  
800       precision. The ATLAS collaboration is involved in different physic areas including  
801       the discovery of the Higgs boson, searches for physics beyond the SM, precision  
802       measurements of electroweak and top-quark properties, and heavy-ion physics.
- 803     • Compact Muon Solenoid (CMS) [89]: a multi-purpose particle detector located at  
804       IP5. It has a similar design as the ATLAS detector covering the same physics areas.  
805       The CMS detector and its inner components are detailed in Section 2.2.
- 806     • LHCb [90]: a single-arm forward spectrometer located at IP8, designed to precisely  
807       measure the decays of hadrons containing bottom quarks. It is able to distinguish

between the interaction point and the b-hadron decay vertex, perform particle identification, measure the energy of electrons, photons and hadrons, and reconstruct the trajectories of charged particles. The research programme of the LHCb experiment nowadays covers heavy-flavour, QCD, electroweak and heavy-ion physics. LHCb can also operate in fixed-target mode by injecting a small amount of a noble gas (e.g. helium) around its collision region inside the beam pipe.

### 2.1.3 Luminosity

The performance of the LHC can be characterised based on its delivered luminosity. The higher the luminosity of the collider, the more particle interactions occur when the beams are collided. The number of interactions per unit time  $dN/dt$ , produced in a given reaction, is proportional to the cross section  $\sigma_r$  of the corresponding process, as defined in:

$$\frac{dN}{dt} = \mathcal{L}\sigma_r \quad (2.1)$$

where  $\mathcal{L}$  represents the instantaneous luminosity of the particle collisions. In the case of circular beam profiles, the instantaneous luminosity depends on several factors:

$$\mathcal{L} = \frac{k_b N_{b,1} N_{b,2} f_{rev} \gamma}{4\pi \epsilon_n \beta^*} F \quad (2.2)$$

where  $k_b$  is the number of bunches collided,  $N_{b,1}$  and  $N_{b,2}$  are the number of particles per bunch in the two beams,  $f_{rev} = 11245$  Hz is the revolution frequency at the LHC,  $\epsilon_n$  is the normalised transverse beam emittance,  $\beta^*$  is the beta-function defined at the interaction point, and  $F$  is a geometric reduction factor due to the angle at which the two beams collide. The integrated luminosity is derived by integrating the instantaneous luminosity over a given period of time.

### 2.1.4 LHC schedule

The LHC started operations in 2008, and delivered collision data during its first running period (labelled as Run-1) until 2013, followed by a long shut-down (LS1) period of 2 years dedicated to upgrade the machine. The second period of LHC operations (Run-2) started on 2015 and will conclude at the end of 2018. During Run-1, the LHC performed proton-proton (p-p) collisions at a center-of-mass (CM) energy of  $\sqrt{s} = 2.36$  TeV in 2009, and p-p collisions at  $\sqrt{s} = 7$  TeV and lead-lead (Pb-Pb) collisions at a nucleon-nucleon CM

835 energy of  $\sqrt{s_{\text{NN}}} = 2.56 \text{ TeV}$  between 2010 and 2011. In addition, the LHC collided protons  
836 at  $\sqrt{s} = 8 \text{ TeV}$  in 2012, and proton-lead (p-Pb) at  $\sqrt{s_{\text{NN}}} = 5.02 \text{ TeV}$  in 2013. Afterwards,  
837 the Run-2 period started with p-p collisions at  $\sqrt{s} = 13 \text{ TeV}$  and Pb-Pb collisions at  
838  $\sqrt{s} = 5.02 \text{ TeV}$  in 2015, p-Pb collisions at  $\sqrt{s} = 8.16 \text{ TeV}$  in 2016, p-p collisions at  $\sqrt{s_{\text{NN}}} =$   
839  $5.02 \text{ TeV}$  in 2017, Xenon-Xenon (Xe-Xe) collisions at  $\sqrt{s_{\text{NN}}} = 5.16 \text{ TeV}$ , and will finish with  
840 Pb-Pb collisions at  $\sqrt{s_{\text{NN}}} = 5.02 \text{ TeV}$  at the end of 2018.

### 841 2.1.5 Heavy-ion schemes in 2015-2016

842 The LHC heavy-ion physics programme began in 2010, and has since then provided  
843 data from p-Pb and Pb-Pb collisions at various beam energies. The results presented in  
844 this thesis are based on heavy-ion data taken between 2015 and 2016. The charmonium  
845 analysis, detailed in Chapter 4, uses data from p-p and Pb-Pb collision at  $\sqrt{s_{\text{NN}}} = 5.02 \text{ TeV}$   
846 taken in 2015, while the W-boson analysis, described in Chapter 3, utilises p-Pb collision  
847 data recorded in 2016.

848 In 2015, the LHC programme dedicated to heavy-ion physics took place during four  
849 weeks between November and December. The first week was dedicated to p-p collisions at  
850  $\sqrt{s} = 5.02 \text{ TeV}$  to create a reference sample for the Pb-Pb collision data. Each proton beam  
851 was accelerated to 2.51 TeV. The number of proton bunches were initially 44 and was  
852 sequentially increased during the week to a maximum of 1825 bunches. The subsequent  
853 week, the LHC beam settings were modified to collide two beams of  $\text{Pb}^{82+}$  ions at  
854  $\sqrt{s_{\text{NN}}} = 5.02 \text{ TeV}$ . The LHC started accelerating ten Pb bunches to 2.51 TeV/nucleon, and  
855 then progressively increased the number of Pb bunches until it reached 518 at the end  
856 of the Pb-Pb data taking. The Pb beam lifetime was shorter than for protons due to the  
857 large ultraperipheral electromagnetic interactions between Pb ions, requiring to refill  
858 the beams more often. All experiments took Pb-Pb collision data, including LHCb for the  
859 first time [91]. The integrated luminosity of the Pb-Pb collision data is shown in the left  
860 plot of Figure 2.3.

861 The following year, asymmetric collisions of  $\text{Pb}^{82+}$  nuclei with protons were performed  
862 between November 7th and December 4th. Several beam configurations were imple-  
863 mented in 2016 to fulfil the interests of each experiment: ALICE requested p-Pb data  
864 at  $\sqrt{s_{\text{NN}}} = 5.02 \text{ TeV}$ , CMS and ATLAS asked for p-Pb data at  $\sqrt{s_{\text{NN}}} = 8.16 \text{ TeV}$  with an  
865 integrated luminosity of at least  $\mathcal{L} = 100 \text{ nb}^{-1}$ , and LHCb requested p-Pb collisions at  
866  $\sqrt{s_{\text{NN}}} = 8.16 \text{ TeV}$  complemented with a reversal of the beam direction. After careful plan-  
867 ning, the first ten days were dedicated to p-Pb collisions at  $\sqrt{s_{\text{NN}}} = 5.02 \text{ TeV}$  optimised  
868 for ALICE. Afterwards, the LHC spent two weeks on p-Pb collisions at  $\sqrt{s_{\text{NN}}} = 8.16 \text{ TeV}$ .

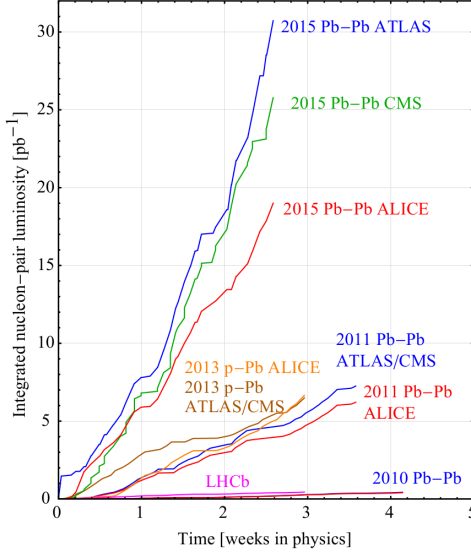


Figure 2.3: Integrated nucleon-pair luminosity delivered by the LHC to each experiment during Pb-Pb collisions at  $\sqrt{s_{NN}} = 5.02\text{ TeV}$ . The integrated luminosity of p-Pb collisions at  $\sqrt{s_{NN}} = 5.02\text{ TeV}$  and Pb-Pb collisions at  $\sqrt{s_{NN}} = 2.76\text{ TeV}$  are included for comparison. Figure taken from Ref. [91].

At the beginning of the p-Pb collisions at  $\sqrt{s_{NN}} = 8.16\text{ TeV}$ , the proton beam was composed of 702 bunches at 6.5 TeV moving in the clockwise direction, while the Pb beam was made of 548 bunches at 2.56 TeV/nucleon moving in the anti-clockwise direction, around the LHC rings. The LHC then proceeded to reverse the beam directions after the integrated luminosity accumulated in CMS and ATLAS reached half of the requested value ( $\sim 60\text{ nb}^{-1}$ ), and kept colliding 540 Pb bunches with 684 proton bunches during the last nine days. At the end of the heavy-ion data taking period, the LHC managed to deliver a total integrated luminosity of  $\mathcal{L} = 188\text{ nb}^{-1}$  of p-Pb data to the CMS experiment as shown in Figure 2.4. The beam settings used by LHC during the heavy-ion collision programme performed in 2015 and 2016 are summarised in Table 2.1.

## 2.2 The Compact Muon Solenoid

The CMS [89] is a multi-purpose particle detector housed in an underground cavern at IP5 of the LHC. The CMS experiment is integrated, at the time of writing this thesis, by an international collaboration of over 5600 members from around 215 institutes from 46 countries. The CMS is composed of a central barrel in the mid-rapidity region closed by two endcap disks, one on each side of the IP, forming a hermetic cylindrical detector.

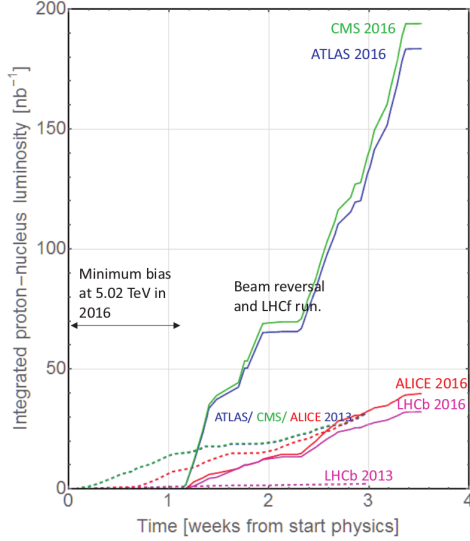


Figure 2.4: Integrated proton-nucleus luminosity delivered by the LHC to each experiment during p-Pb collisions at  $\sqrt{s_{NN}} = 8.16 \text{ TeV}$  (solid lines). The integrated luminosity of p-Pb collisions at  $\sqrt{s_{NN}} = 5.02 \text{ TeV}$  (dashed lines) is included for comparison. Figure taken from Ref. [92].

Variable	p-p 2015	Pb-Pb 2015	p-Pb 2016
Fill no.	4647	4720	5562
Collision energy $\sqrt{s_{NN}}$ [TeV]	5.02	5.02	8.16
Pb beam energy $E_{\text{Pb}}$ [TeV/nucleon]	-	2.51	2.56
Beam energy $E_p$ [TeV/proton]	2.56	6.37	6.5
Pb ions per bunch $N_b^{\text{Pb}}$ [ $10^8$ ]	-	2.0	2.1
Protons per bunch $N_b^p$ [ $10^{10}$ ]	10.1	-	2.7
No. of Pb bunches $k_b^{\text{Pb}}$	-	518	540
No. of proton bunches $k_b^p$	1825	-	684
No. of colliding bunches $k_c$	1813	491	513
$\beta^*$ [m]	4	0.8	0.6
Crossing angle [ $\mu\text{rad}$ ]	170	145	140
Pb beam emittance $\epsilon_n^{\text{Pb}}(x, y)$ [ $\mu\text{m}$ ]	-	2.1	1.6
Pb bunch length $\sigma_z^{\text{Pb}}$ [m]	-	0.09	0.9
CMS peak lumi. $\mathcal{L}^{\text{peak}}$ [ $10^{27} \text{ cm}^{-2} \text{ s}^{-1}$ ]	$3.4 \times 10^5$	3	869
CMS integrated lumi. $\mathcal{L}_{\text{int}}$ [ $\text{nb}^{-1}$ ]	28820	0.6	188

Table 2.1: LHC beam parameters during the highest luminosity physics fills. The luminosity values are averages for CMS. Information extracted from Ref. [93].

## 2.2. THE COMPACT MUON SOLENOID

The CMS detector consists of four main subdetector systems: the silicon tracker, the Electromagnetic CALorimeter (ECAL), the Hadronic CALorimeter (HCAL) and the muon chambers. A superconducting solenoid magnet placed in the barrel section generates a magnetic field of 3.8 T. The tracking system, the ECAL and the HCAL, are located within the solenoid volume, while the muon system is placed between the layers of the flux-return yoke, which confines the magnetic flux. A sectional view of the CMS detector including the number of channels per subdetector, in its 2016 configuration, is shown in Figure 2.5.

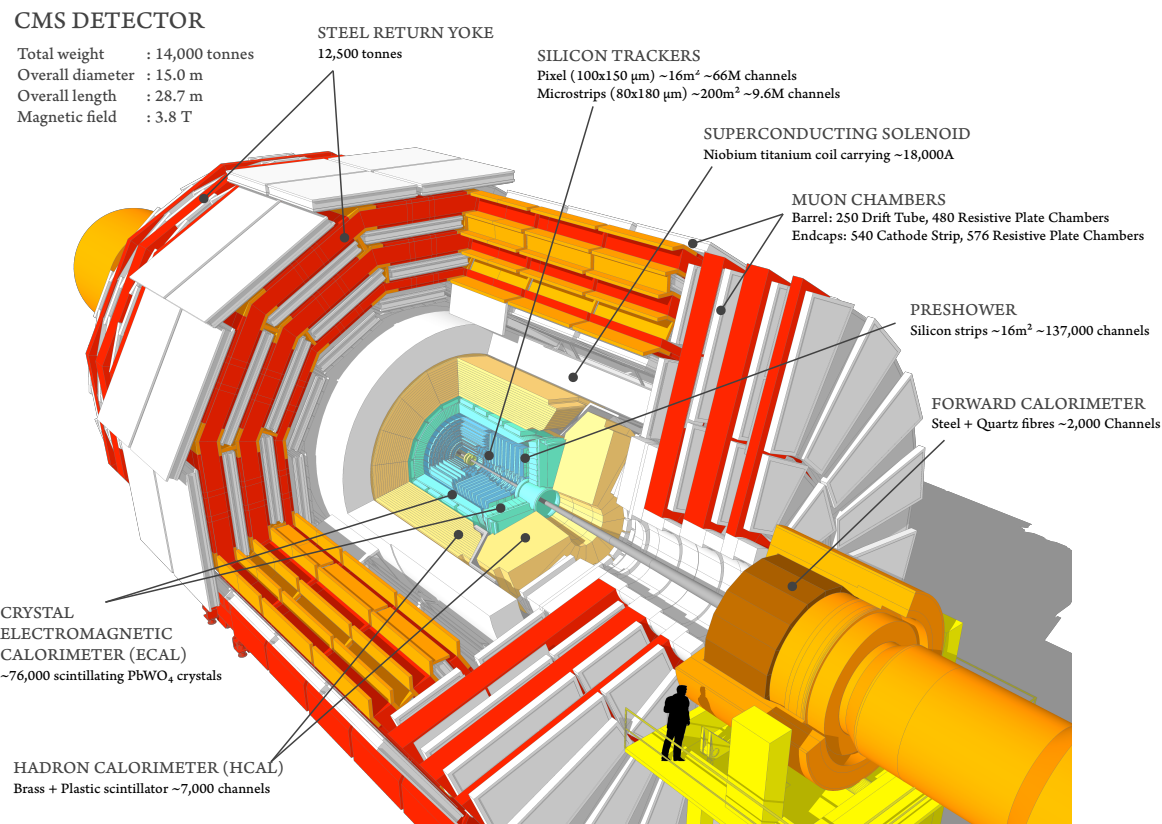


Figure 2.5: Cutaway view of the CMS detector in its configuration used during 2015 and 2016. Labels and basic details of each subdetector are included. [94]

One of the main components of the CMS detector is its superconducting solenoid magnet of 6 m internal diameter and 12.5 m length. The magnet produce a uniform magnetic field of 3.8 T in the central region by supplying an electric current of 18.1 kA through a four-layer winding coil made of NbTi wire. To be able to sustain the large electric currents, the solenoid coil is thermally insulated within a vacuum volume and

898 operated in superconducting mode at a temperature of 4.6 K with a thermal-siphon  
 899 cooling system fed with liquid helium. The flux of the magnetic field outside the barrel  
 900 is returned through a massive steel yoke of 10000 tons divided in five barrel wheels  
 901 and four endcap disks at each end. In case there is a major system fault or the magnet  
 902 suffers a superconducting-to-resistive transition (quench), the electric power source is  
 903 immediately disconnected and the stored magnetic energy is quickly discharged through  
 904 a 30 mΩ dump resistor placed outdoors.

905 The coordinate system of the CMS detector is centred at the interaction point. It  
 906 is oriented in such a way that the  $x$ -axis points radially inward to the centre of the  
 907 LHC ring while the  $y$ -axis points upward perpendicular to the LHC plane. The  $z$ -axis  
 908 is defined parallel to the beam. By convention, the positive  $z$ -direction is defined along  
 909 the counter-clockwise beam direction. For asymmetric collisions, such as p-Pb, it is  
 910 later reversed (if necessary) to match the proton-going direction, so that the "forward"  
 911 (low Bjorken-x) physics corresponds to the "forward" ( $\eta > 0$ ) part of the detector (see  
 912 Section 3.2.1).

913 The trajectory of particles measured at CMS is described in the coordinate system  
 914 displayed in Figure 2.6. The polar angle  $\theta$  is measured from the  $z$ -axis while the az-  
 915 imuthal angle  $\phi$  is measured from the  $x$ -axis in the  $x$ - $y$  plane, called the transverse  
 916 plane. The radial coordinate  $r$  is also measured in the transverse plane. The polar angle  
 917 is replaced by the pseudorapidity  $\eta$  which, for massless particles, matches the rapidity  
 918 and is Lorentz invariant under longitudinal boosts. The pseudorapidity is zero in the  
 919 transverse plane and approaches infinity towards the  $z$ -axis, according to:

$$\eta = -\ln \left[ \tan \left( \frac{\theta}{2} \right) \right] \quad (2.3)$$

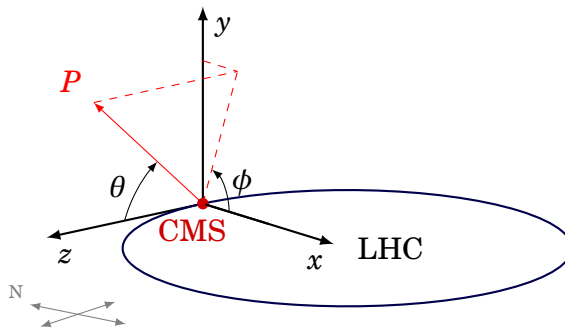


Figure 2.6: Schematic diagram of the coordinate system used in the CMS experiment.

920 The details of the original configuration of the CMS detector can be found in Ref. [89].  
921 After Run-1 was over, the CMS underwent several improvements as part of the planned  
922 upgrades for the LS1 shut-down period (2013-2014). The systems upgraded during LS1  
923 include the muon endcap stations, the hadron calorimeter, and the L1 trigger. In the  
924 case of the muon system, an additional disk of muon detectors was installed on the  
925 outermost part of each endcap section providing a fourth measurement in the forward  
926 region [95]. Moreover, the photosensors of the forward (outer-barrel) hadron calorimeter  
927 were replaced with multi-anode photomultiplier tubes (silicon photomultipliers), and the  
928 corresponding readout electronics were upgraded to handle the new sensors [96]. And  
929 finally, the framework and electronics of the L1 trigger system were completely changed  
930 to sustain the increasing interaction rate of the LHC beam collisions [97].

931 **2.2.1 Subdetectors**

932 The CMS detector [89] is composed of several subdetectors which provide a precise  
933 measurement of the trajectory and energy of the particles emitted from the LHC collisions.  
934 The superconducting solenoid volume contains the inner tracker close to the beam line  
935 followed radially outwards by the electromagnetic and hadronic calorimeters. The muon  
936 chambers are installed outside of the solenoid, interspersed with layers of the flux-return  
937 yoke. An electromagnetic preshower is installed in the endcaps complementing the ECAL  
938 to improve the identification of photons and electrons.

939 **2.2.1.1 Tracker**

940 The CMS tracking system is designed to measure the trajectory of charged particles and  
941 reconstruct the 3D vertex position of the primary interaction and the secondary decays.  
942 It is completely surrounded by the volume of the solenoid magnet in the barrel region,  
943 and has a diameter of 2.5 m and a length of 5.8 m, centred on the interaction point. The  
944 CMS tracker is made of a pixel detector and a silicon strip tracker. A schematic cross  
945 section of the CMS tracker is presented in Figure 2.7.

946 The pixel detector is made of 1440 pixel modules installed in the tracker section  
947 closest to the interaction region. It covers the pseudorapidity range  $|\eta| < 2.5$  with three  
948 Barrel Pixel (BPix) layers and two Forward Pixel (FPix) disks. The BPix layers are placed  
949 at a radii of 4.4 cm, 7.3 cm and 10.2 cm from the beam axis, while the FPix disks are  
950 located, on each side of the IP, at a longitudinal distance of  $z = \pm 34.5$  cm and  $z = \pm 46.5$  cm.  
951 The BPix (FPix) detectors contain 48 (18) million silicon pixels, each with a cell size of

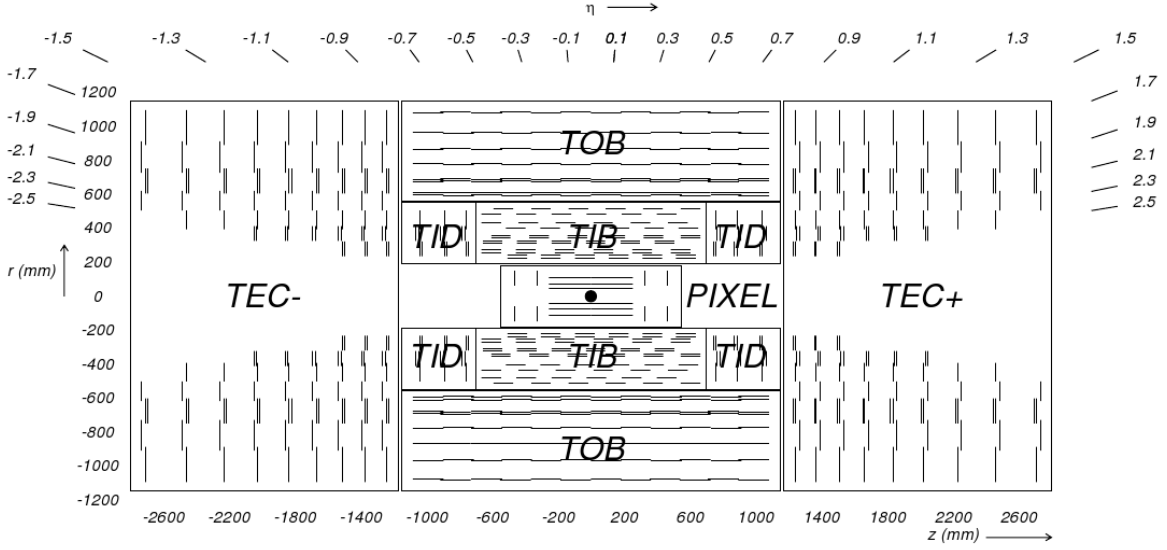


Figure 2.7: View of the CMS tracker in the  $r$ - $z$  plane. Each line represents a detector module. Figure taken from Ref. [89].

952  $100 \times 150 \mu\text{m}^2$ . The arrangement of the pixel detector modules in the forward)  
 953 region provides, over the full tracker coverage, three tracking hits per track and a  
 954 position resolution of 15-20 (15)  $\mu\text{m}$  in the  $z$ -coordinate.

955 The silicon-strip tracker contains 9.3 million strips divided in 24244 silicon sensors,  
 956 covering the region between the pixel detector and the ECAL. In the barrel region, the  
 957 strip tracker is composed of the Tracker Inner Barrel (TIB), made of four concentric  
 958 cylinders placed at a radius between 25.5 cm and 49.8 cm, and the Tracker Outer Barrel  
 959 (TOB), which consists of a wheel-like structure containing six cylinders with an inner  
 960 (outer) radius of 55.5 (116) cm. The pseudorapidity coverage of the strip tracker is  
 961 extended up to  $|\eta| = 2.5$  with three Tracker Inner Disks (TID) and nine Tracker EndCap  
 962 (TEC) disks, installed on each endcap section along  $80 \text{ cm} < |z| < 90 \text{ cm}$  and  $124 \text{ cm} < |z| <$   
 963  $282 \text{ cm}$ , accordingly. The strip detector modules used in the TIB, TID and inner four  
 964 TEC rings are made of one  $320 \mu\text{m}$ -thick sensor, while those used in the TOB and outer  
 965 five TEC rings are made of two  $500 \mu\text{m}$ -thick sensors. The strip pitch varies between  
 966  $80\text{-}120 \mu\text{m}$ ,  $100\text{-}141 \mu\text{m}$ ,  $122\text{-}183 \mu\text{m}$ , and  $97\text{-}184 \mu\text{m}$ , in the TIB, TID, TOB and TEC,  
 967 respectively. The strip tracker can achieve a position resolution in the TIB (TOB) of 23-35  
 968 ( $35\text{-}53$ )  $\mu\text{m}$  in the transverse plane and  $230$  ( $530$ )  $\mu\text{m}$  in the  $z$ -coordinate.

969 **2.2.1.2 Electromagnetic calorimeter**

970 The ECAL of the CMS is a hermetic homogeneous calorimeter composed of 75848 lead-  
 971 tungstate ( $\text{PbWO}_4$ ) crystals. The ECAL is designed to fully absorb and measure the  
 972 energy of electrons and photons. The  $\text{PbWO}_4$  material was chosen for its small Molière  
 973 radius (2.2 cm), a short radiation length (0.89 cm), and a high density ( $8.28 \text{ g cm}^{-3}$ ).  
 974 When a high-energy electron or photon interacts with the nuclei of the ECAL crystals, it  
 975 generates a cascade of electromagnetic particles ( $e^-$ ,  $e^+$  and  $\gamma$ ) and induces the emission  
 976 of blue scintillation light ( $\lambda \approx 420 \text{ nm}$ ), which is then measured in photodetectors. The  
 977 total amount of scintillation light produced is proportional to the energy deposited in  
 978 the crystals by the electrons and photons. In order to cope with the running conditions  
 979 of the LHC, the crystals are designed to have a fast response (25 ns), and be optically  
 980 transparent and radiation-hard.

981 The ECAL is installed between the silicon-strip tracker and the HCAL. It is divided  
 982 in a cylindrical-barrel section (EB) and two endcap rings (EE), one on each side of the  
 983 IP. The EB is made of 61200 crystals of 23 cm long, covering the pseudorapidity range  
 984  $|\eta| < 1.48$  with a granularity of 170-fold in  $\eta$  and 360-fold in  $\phi$ . The crystals are grouped  
 985 in modules of either 400 or 500 units, and four modules are assembled in so-called  
 986 supermodules. The EB has a total of 36 supermodules, each covering  $20^\circ$  in  $\phi$  with 1700  
 987 crystals. The scintillation light is measured in the EB with Avalanche PhotoDiodes  
 988 (APD), mounted in pairs on the back of each crystal. Each APD is operated, with a  
 989 high-voltage power supply system, at gain 50 and a voltage between 340-430 V. The  
 990 schematic layout and geometric view of the ECAL are shown in Figure 2.8.

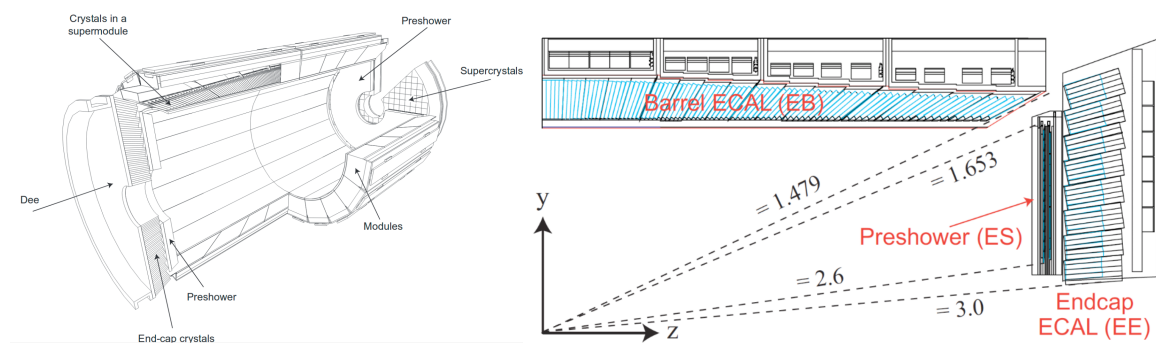


Figure 2.8: Schematic layout [89] (left) of the CMS electromagnetic calorimeter, and its corresponding one-quarter geometric view [98] (right).

991 The EE rings are installed at  $z = \pm 3.15 \text{ m}$ , extending the coverage of the ECAL up  
 992 to  $|\eta| = 3.0$ . The EE consists of 14648 crystals of 22 cm long, assembled in units of  $5 \times 5$

993 crystals known as SuperCrystals (SC). Each EE ring is divided in two halves, each  
994 containing 156 SCs. A single-stage photomultiplier called Vacuum PhotoTriodes (VPT),  
995 attached to the back of each EE crystal, is used to measure the scintillation photons. The  
996 VPT has a diameter of 25 mm, a quantum efficiency of 22% at a wavelength of 430 nm,  
997 and a gain of 10.2 at zero magnetic field.

998 An additional calorimeter called the Preshower detector is installed in the endcap  
999 rings between the tracker and the EE. The Preshower is an electromagnetic sampling  
1000 calorimeter of 20 cm thickness, optimised to identify photons from neutral pion decays.  
1001 It is composed of two layers of lead absorbers interleaved with 4300 silicon sensors  
1002 organised in 32 strips. Each silicon sensor has a thickness of 320  $\mu\text{m}$  and an active area  
1003 of  $63 \times 63 \text{ mm}^2$ . Incoming photons and electrons initiate an electromagnetic shower when  
1004 they interact with the lead absorbers. The energy deposited in the absorbers and the  
1005 transverse profile of the shower are measured in the silicon strips.

1006 The response of the crystals and the signal amplification of the APDs depend on  
1007 the operating temperature. As a result, a water flow cooling system is installed to  
1008 keep the crystals and sensors at a stable temperature of  $18.00 \pm 0.05^\circ\text{C}$ . Moreover, the  
1009 transparency of the crystals to scintillation light is affected by the radiation dose due  
1010 to the formation of colour centres which absorbs part of the light. The variation of the  
1011 crystal transparency is monitored using laser pulses introduced into the crystals at a  
1012 frequency of 80 Hz. The laser monitoring system uses two blue lasers ( $\lambda \approx 440 \text{ nm}$ ) to  
1013 track the radiation-induced transparency variations, which are then corrected for by  
1014 recalibrating the detector.

1015 The energy resolution of the ECAL is affected by several sources, such as the fluc-  
1016 tuations in the shower, crystal non-uniformities, calibration errors, and noise in the  
1017 photodetectors. The relative energy resolution of the ECAL is parametrised as a function  
1018 of the measured energy  $E$  via:

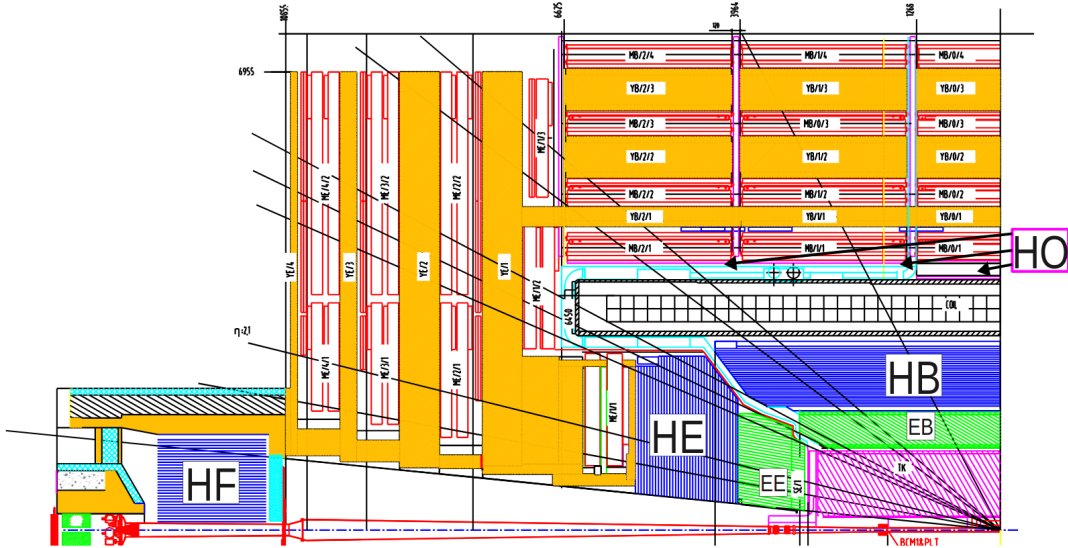
$$\left(\frac{\sigma_E}{E}\right)^2 = \left(\frac{2.8\%}{\sqrt{E/\text{GeV}}}\right)^2 + \left(\frac{12\%}{E/\text{GeV}}\right)^2 + (0.3\%) \quad (2.4)$$

1019 **2.2.1.3 Hadronic calorimeter**

1020 The HCAL is a hermetic sampling calorimeter made of 70000 plastic-scintillator tiles  
1021 interleaved with absorber plates. The goal of the HCAL is to completely absorb and  
1022 measure the energy of hadrons. When a hadron hits an absorber plate, it induces a  
1023 shower of particles through the successive absorber layers. The secondary particles

## 2.2. THE COMPACT MUON SOLENOID

produced in the cascade pass through the plastic tiles, located in between the absorbers, leading to the emission of scintillator light at a peak wavelength of  $\sim 440\text{ nm}$ . Photons generated on each tile are collected with WaveLength-Shifting (WLS) fibres fabricated in a double-clad configuration with a diameter of 0.94 mm. The WLS fibres shifts the scintillator light to the green spectrum (515 nm) and pass it to fibre-optic waveguides which then transfers the light to a phototransducer. The scintillator tiles are grouped in trays that are  $5^\circ$  wide in  $\phi$ . A geometric view of CMS, highlighting the different components of the HCAL, is presented in Figure 2.9.



trays. The HO has 2730 scintillator tiles of 10 mm thick organised in 422 trays, offering the same  $\Delta\eta \times \Delta\phi$  granularity as the HB. The HO uses a multipixel Geiger-mode APD, known as Silicon PhotoMultiplier (SiPM), to detect photons.

The coverage of the HCAL is extended in the forward region to  $|\eta| = 3$  with the Hadron-Endcap (HE) calorimeter and up to  $|\eta| = 5.2$  with the Hadron-Forward (HF) calorimeter. The HE is located in the endcap rings and its absorber is made of two 79 mm-thick plates of cartridge brass separated by 9 mm. The HE contains 20916 plastic tiles and has a  $\Delta\eta \times \Delta\phi$  granularity of  $0.17 \times 0.17$ . The HE also uses HPDs to measure the scintillator light.

The HF is divided in 36 wedges that are  $20^\circ$  wide in  $\phi$ , and its front face is located at  $z = \pm 11.2$  m, on each side of the IP. Since the HF experience a large energy deposit from the beam collisions, its design has been optimised to handle high levels of radiation. The HF absorber consists of a 1.7 m-depth cylindrical structure made of 5 mm-thick steel-grooved plates, while the HF active medium is composed of quartz fibres of polymer hard-cladding and fused-silica core. The signal consists of Cherenkov light generated when energetic charged particles from the shower traverse the quartz fibres. The Cherenkov light is measured by multi-anode PhotoMultiplier Tubes (PMT) shielded behind 40 cm of steel. The HF fibres are inserted in the absorber grooves along the beam line in two longitudinal segments. Long fibres are inserted over the full absorber depth while short fibres starts at a depth of 22 cm from the front face covering the back of the absorber. Since most of the energy of electrons and photons is deposited in the first 22 cm while hadrons are able to penetrate more in the HF absorber, the difference in energy measured in the long and short fibres is used to estimate the electromagnetic and hadronic components of the shower.

#### 2.2.1.4 Muon detectors

The CMS muon tracking system measures the momentum and charge of muons in the fiducial region  $|\eta| < 2.4$ . It is divided in four stations corresponding to four concentric cylinders in the barrel region and to four disks on each endcap section. Figure 2.10 shows a geometric view of one quadrant of the CMS muon system. The dense material of the calorimeters and the solenoid magnet absorbs most of the hadrons, electrons and photons, while energetic muons are able to reach the muon stations loosing only a small fraction of their energy. Muons are detected in CMS using three type of gaseous technologies: Drift Tubes (DT), Cathode Strip Chambers (CSC) and Resistive Plate Chambers (RPC).

The DT detectors are used in the barrel region of the muon system ( $|\eta| < 1.2$ ). A

## 2.2. THE COMPACT MUON SOLENOID

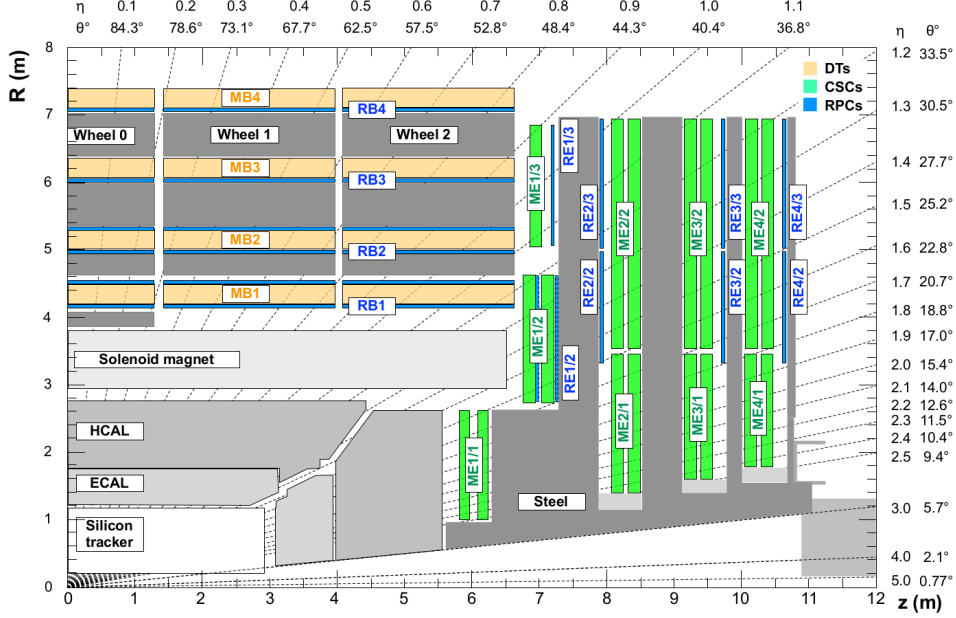


Figure 2.10: Geometric view of one quadrant the CMS detector in the  $r$ - $z$  plane. Each chamber of the muon system is shown in blue (RPC), green (CSC) and orange (DT). Figure taken from Ref. [99].

DT consists of a 50  $\mu\text{m}$ -diameter anode wire placed inside a rectangular tube connected to two cathode strips and filled with a gas mixture of 85% of Ar and 15% of CO<sub>2</sub>. The layout of a DT cell is displayed on the left of Figure 2.11. When a charged particle passes through a DT, it ionises the gas releasing electrons that are then detected in the anode wire. The DT system is composed of 172000 anode wires of 2.4 m length. There are four DT chambers in each of the five barrel wheels and twelve azimuthal sectors. In total, the fourth station contain 70 DT chambers and the first three stations contain 60 DT chambers each. Four layers, each containing up to 60 DTs, are grouped in units called SuperLayers (SL). The DT chambers of the three inner stations (outermost station) are made of three (two) SLs. The first and third SL, as shown on the right of Figure 2.11, have their anode wires installed parallel to the  $z$ -axis to measure the bending in the transverse plane, while the anode wires of the second SL are placed orthogonal to the beam line to measure the position in the  $z$ -coordinate. The SLs of the fourth station only have anode wires parallel to the  $z$ -axis. The SLs measure the position and angle of the track segments with a precision of 1.5 mm and 20 mrad, respectively.

Instead of DTs, the two endcap sections use 540 CSCs covering a pseudorapidity range  $0.9 < |\eta| < 2.4$ . The CSC system is designed to cope with the higher rate of particles and the large non-uniform magnetic field present in the forward region. A CSC is made

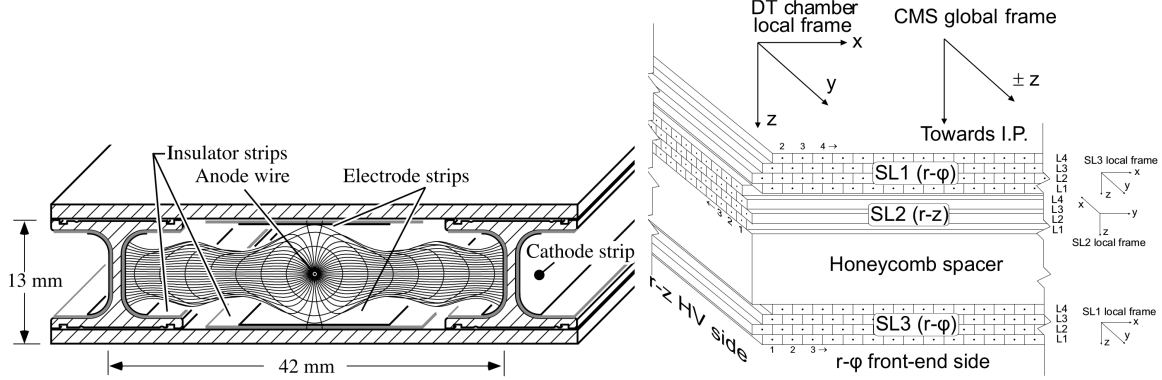


Figure 2.11: Schematic layout of a DT cell (left) and a DT chamber (right). Figures taken from [100].

of six anode wire planes crossed with seven cooper cathode strips within a gas mixture of 40% Ar, 50% CO<sub>2</sub>, and 10% CF<sub>4</sub>, forming a multiwire proportional chamber. The CSCs are operated at 3.6 kV with a gas gain of  $7 \times 10^4$ , and are organised in chambers installed perpendicular to the beam pipe. The CSC chambers are trapezoidal and cover either 10° or 20° in  $\phi$ , and they overlap providing contiguous coverage in  $\phi$ . The cathode strips are milled in panels along constant  $\Delta\phi$ -width and provide measurements in the transverse plane, while the anode wires are placed azimuthally and measure the pseudorapidity of muons. The CSC system has a total of 266112 cathode-strip and 210816 anode-wire read-out channels. A schematic layout of a CSC is shown in Figure 2.12.

To allow fast muon triggering, the barrel and endcap regions are complemented with RPC detectors. A RPC module consists of an anode plate parallel to a cathode plate, as shown in Figure 2.13. The RPC plates are separated by a gap filled with a gas mixture of 96.2% C<sub>2</sub>H<sub>2</sub>F<sub>4</sub>, 3.5% iC<sub>4</sub>H<sub>10</sub> and 0.3% SF<sub>6</sub>, and operated in avalanche mode with read-out strips in between. There are 480 (576) RPC chambers in the barrel (endcap) region. Each RPC chamber consists of two or three modules of up to 96 strips each. Each RPC strip covers 0.31° in  $\phi$ . The RPC chambers are organised in six coaxial cylinders in the barrel region and four rings in the endcaps, covering the pseudorapidity region up to  $|\eta| = 1.9$ . The innermost ring span 20° in  $\phi$  while the other rings span 10°. The RPC modules are optimised for fast muon triggering by detecting ionising events faster than the time interval between two bunch crossings (25 ns). They provide a good timing resolution but with a coarser spatial granularity compared to DTs and CSCs. The RPCs also allow to resolve ambiguities between tracks made from multiple hits in the muon chambers.

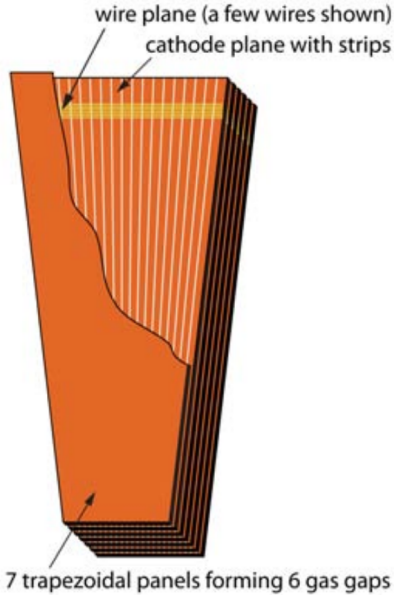


Figure 2.12: Schematic layout of a CSC. Figure taken from [89].

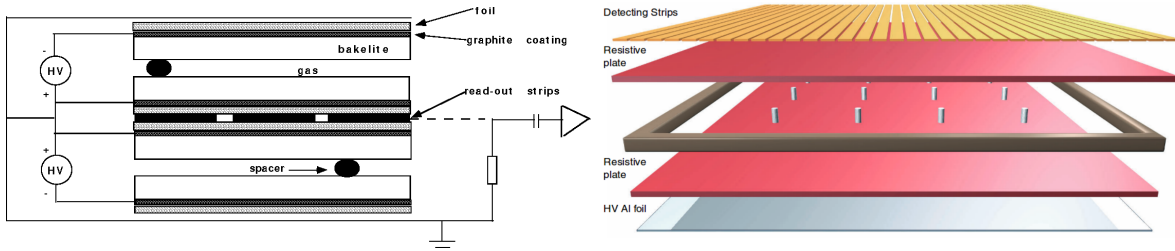


Figure 2.13: Cross section view (left) [101] and exploded view (right) [102] of a RPC module.

### 2.2.2 Trigger system

At LHC design conditions, the two beams crosses each IP every 25 ns, equivalent to a frequency of 40 MHz. Once a collision is recorded by CMS, all detector channels are read out and the data is sent to the CERN main computing farm, known as the Tier-0, to be further processed with the CMS SoftWare (CMSSW). However, the Tier-0 processing rate is limited by its CPU performance and storage capacity. As a result, the input rate of data transferred to the Tier-0 has to be kept below 1 kHz to avoid overflowing the computing centre.

To reach this goal, CMS has implemented a two-level trigger system designed to select events of interest for physics analysis. The first level, known as the Level-1 (L1) trigger, lowers the collision rate to an output rate of 100 kHz by filtering events using custom

hardware. The next trigger level, called the High Level Trigger (HLT), is performed in a cluster of computers located in the CMS experimental cavern. The HLT software algorithms further reduce the data rate down the limit required by the Tier-0.

2.2.2.1 **Level-1 trigger**

The L1 trigger system [103] is designed to handle the large collision rate of the LHC. To accomplish this goal, the L1 trigger is made of custom hardware modules optimised to process the events with a latency of less than 4  $\mu$ s. The L1 trigger is divided in two parts: the calorimeter and muon triggers.

The data from each subdetector are organised in units called Trigger Primitives (TP). The calorimeter TP are derived from the Trigger Towers (TT), each corresponding to a region of  $0.087 \times 0.087$  in  $\eta\phi$  (represents  $5 \times 5$  crystals in the ECAL). While for muons, a TP corresponds to a segment in either the DT or CSC systems. The information of the inner tracker is not used in the L1 trigger since the tracker data can not be currently read out within a bunch crossing time of 25 ns. As a result, the L1 calorimeter trigger cannot discriminate between electrons and photons. The output of the L1 muon and calorimeter triggers is combined in the L1 Global Trigger (GT), which then takes the final decision to either reject or accept the event.

The L1 trigger decision is determined according to a set of user-defined L1 trigger conditions. The L1 criteria are organised in a menu made of different algorithms which are programmed by the users and hard-coded in the firmware of a Field-Programmable Gate Array (FPGA). Some typical conditions used to define the L1 algorithms include setting a minimum  $p_T$  threshold or  $\eta$  range on the L1 objects, or requiring events to have a given amount of L1 candidates. If an event passes the conditions of at least one of the L1 algorithms, the whole CMS detector is read out and the data is then sent to the HLT computers. The L1 menu is updated several times during data taking, to adapt to the changes in the LHC beam conditions and physics requirements.

In order to reduce the contribution from cosmic muons and also suppresses pre-firing from the calorimeters caused by particles interacting in the photomultipliers, the events processed by the L1 trigger are required to be associated to a bunch crossing. The Beam Pick-up Timing eXperiment (BPTX) detectors, installed at a distance of  $z = \pm 175$  m on each side of the IP, are used to select valid bunch crossings by checking for a coincidence of the signals on each side.

The L1 system underwent, between 2014 and 2015, an extensive upgrade that included a complete replacement of the electronics and the data acquisition system. The

1164 previous L1 trigger, used during LHC Run-1 and 2015, is referred in this manuscript as  
 1165 the legacy L1 trigger, while the L1 trigger deployed before the pPb collision run in 2016,  
 1166 is called the upgraded L1 trigger.

1167 **Legacy L1 trigger.** The legacy L1 trigger [103] was used in CMS until the end of 2015,  
 1168 covering the entire LHC Run-1 and beginning of Run-2 data taking periods. The events  
 1169 from p-p and Pb-Pb collisions at  $\sqrt{s_{\text{NN}}} = 5.02 \text{ TeV}$ , in particular the data used for the  
 1170 charmonium analysis reported in Chapter 4, were selected using the legacy L1 trigger.  
 1171 Figure 2.14 shows a diagram of the legacy L1 trigger system.

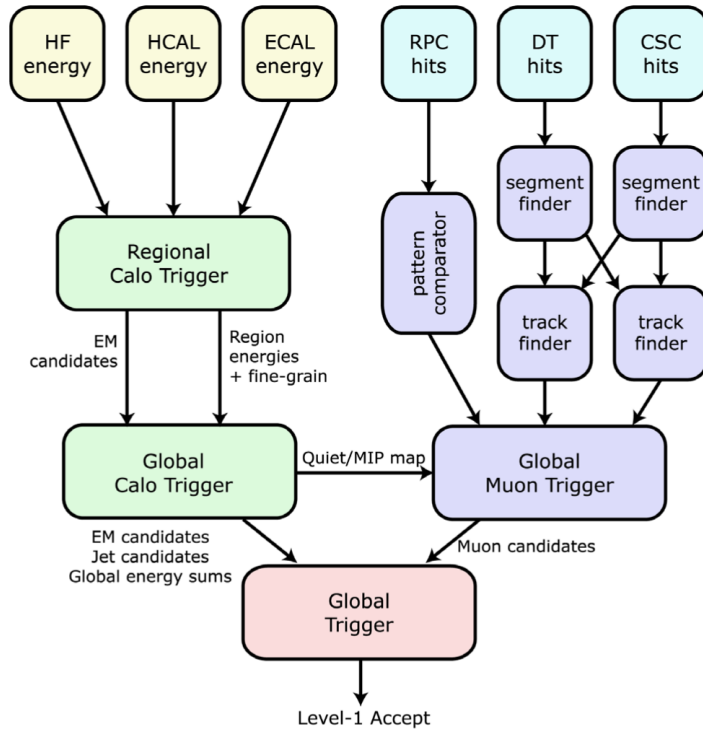


Figure 2.14: Diagram of the legacy L1 trigger of CMS. Figure taken from Ref. [104].

1172 In the legacy L1 trigger, the transverse energy  $E_T$  values are read out from each  
 1173 ECAL, HF and HCAL TT, and then sent to the Regional Calorimeter Trigger (RCT). The  
 1174 RCT processes the raw data and produces 72 electron-photon ( $e/\gamma$ ) candidates (identified  
 1175 as energy clusters mainly deposited in the ECAL), computes the  $E_T$  in the HF region  
 1176 and derives 396  $E_T$  sums of  $4 \times 4$  TT regions. The Global Calorimeter Trigger (GCT) then  
 1177 receives the objects from the RCT and reconstructs jets and hadronic tau decays based on  
 1178 the regional  $E_T$  sums, sorts the  $e/\gamma$  candidates according to their  $E_T$ , and computes global

1179 quantities such as the total  $E_T$ . Eight  $e/\gamma$  candidates, eight jets, four tau candidates, the  
1180 HF  $E_T$ , and the global quantities are then sent to the GT.

1181 The legacy L1 muon trigger follows a detector-based design. The DT and CSC hit  
1182 measurements are used by the front-end trigger electronics to reconstruct track segments  
1183 in each muon station. Regional track finders (TF), one for each muon subsystem, sort the  
1184 track segments and identify muons using pattern recognition algorithms. The hardware  
1185 modules of the DT (CSC) TFs consists of 72 (12) Versa Module Eurocard (VME) boards.  
1186 The muon momentum is estimated based on the bending of the track along the magnetic  
1187 field. The position of each muon detector hit is converted to  $\eta\text{-}\phi$  coordinates using lookup  
1188 tables derived from simulation. To cover the overlap region between the CSC and DT  
1189 muon systems, the information of their TFs is combined. The RPC hits are directly sent  
1190 to a pattern comparator trigger (PACT), which find muon candidates by comparing the  
1191 RPC measurements to predefined patterns. Each muon TF determines the  $\eta\text{-}\phi$  position  
1192 and the  $p_T$  of the muon candidates, and also assigns a quality value based on the position  
1193 and number of muon stations used to form the muon track.

1194 On every bunch crossing, the CSC and DT TFs transfer, each one, four muon can-  
1195 didates to the Global Muon Trigger (GMT), while the RPC trigger sends eight muon  
1196 candidates. The GMT then proceeds to merge the muon tracks if they have been identi-  
1197 fied by several muon subsystems, and assigns a three-bit quality code to the muon tracks  
1198 depending on the information provided by each TF. All muon candidates are ranked in  
1199 the GMT based on their quality code, and those with the same quality are then ranked  
1200 based on their  $p_T$ . The four highest ranked candidates are then transferred to the GT.  
1201 The quality bits assigned to the L1 muon candidates are:

- 1202 • **Bits 0 to 4:** Represent empty, halo or very low quality muon tracks. Not used for  
1203 physics.
- 1204 • **Bit 5:** Muon candidate found by the DT or CSC TFs, but not confirmed by the RPC  
1205 PACT.
- 1206 • **Bit 6:** Muon candidate found by the RPC PACT, but not confirmed by the DT or  
1207 CSC TFs.
- 1208 • **Bit 7:** Muon candidate detected by the DT or CSC TFs, and also by the RPC PACT.

1209 Finally, legacy GT takes the final L1 decision based on the information provided by  
1210 the GMT and the GCT. It is able to evaluate up to 128 L1 algorithms.

1211 **Upgraded L1 trigger.** The upgraded L1 trigger system [97], deployed in CMS at  
1212 the beginning of 2016, was used during the data taking period of p-Pb collisions at

1213  $\sqrt{s_{\text{NN}}} = 8.16 \text{ TeV}$ , and thus for the W-boson analysis reported in Chapter 3. A diagram of  
 1214 the upgraded L1 trigger system is shown in Figure 2.15.

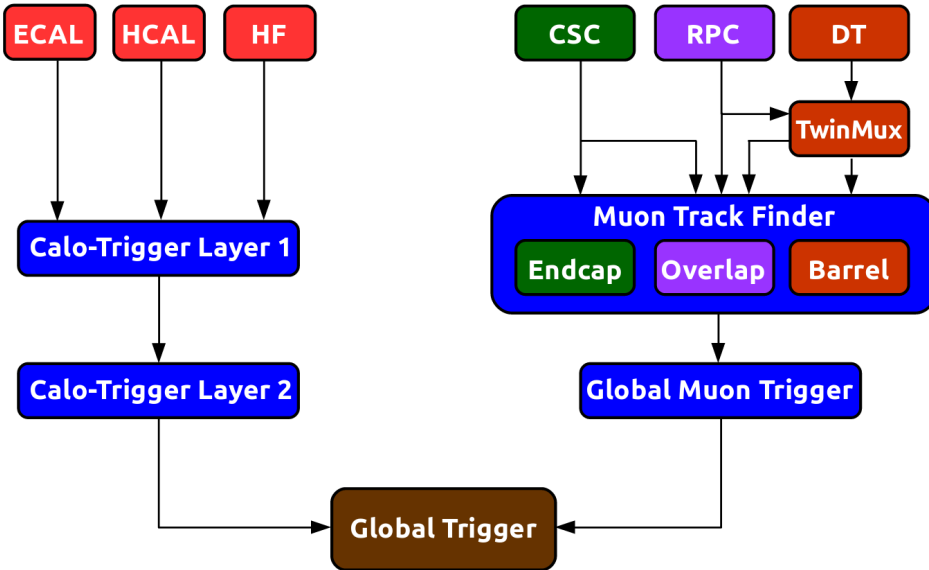


Figure 2.15: Diagram of the CMS L1 trigger used in 2016.

1215 The electronic system of the upgraded L1 trigger consists of Xilinx Virtex-7 FPGAs  
 1216 mounted on Advanced Mezzanine Cards (AMC), designed according to the micro Telecom-  
 1217 munications Computing Architecture ( $\mu$ TCA) standard. Compared to the VME standard  
 1218 employed in its predecessor, the  $\mu$ TCA standard provides higher scalability, flexibility  
 1219 and bandwidth. The communication links between the L1 boards were upgraded from  
 1220 copper serial links (limited to 1.2 Gb/s in the legacy L1 trigger) to high speed optical  
 1221 serial links capable of handling a bandwidth of up to 10 Gb/s.

1222 The upgraded L1 calorimeter [105] trigger is divided in two separate processing  
 1223 layers and its architecture follows a time-multiplexed trigger design (the data is splitted  
 1224 in bunch-crossing intervals instead of detector regions). The first layer (Layer-1) collects  
 1225 data from the calorimeter TTs with 36 trigger processor cards and then distributes all  
 1226 data for a given bunch crossing to one of the nine multi-purpose FPGAs of the second  
 1227 layer (Layer-2). The Layer-2 use the TT data to reconstruct  $e/\gamma$  candidates, jets, and taus  
 1228 (decaying to hadrons), and compute global energy quantities. Lookup tables are used to  
 1229 perform the shape pattern recognition and the energy calibration.

1230 In the case of the L1 muon trigger [106], its architecture is upgraded following a  
 1231 regional approach. The data from the different muon subsystems are combined at an  
 1232 earlier stage than in the legacy trigger, and L1 muon tracks are reconstructed in three

regions: barrel ( $|\eta| < 0.8$ ), overlap ( $0.8 < |\eta| < 1.25$ ), and endcap ( $1.25 < |\eta| < 2.4$ ). The Endcap-Muon TF (EMTF) is designed to process the information from the CSC and RPC modules, however it only received data from the CSC system during 2016 since the RPC concentrator card was still been commissioning. The Barrel-Muon TF (BMTF) builds muon candidates using RPC hits and DT segments reconstructed in the central region. The transition area ( $|\eta| \approx 1.04$ ) between the endcap and barrel sections is covered with the Overlap-Muon TF (OMTF), which takes into account the data from the three muon subsystems. The DT and RPC segments from the barrel region are collected by an intermediate layer called the TwinMux system, which concentrates data and distributes it to the BMTF and OMTF.

The upgraded GMT, referred as  $\mu$ GMT, receives up to 36 L1 muon candidates from each L1 muon TF. The  $\mu$ GMT sorts the muon tracks, removes duplicate muons found by different TFs and ranks the muon candidates by their  $p_T$  and track quality. The eight highest ranked L1 muon candidates are then sent to the GT. The information from the  $\mu$ GMT and the Layer-2 is used by the upgraded GT to evaluate up to 512 L1 algorithms and determine the final L1 decision.

#### 2.2.2.2 High level trigger

The HLT is executed on a processor farm composed of an array of multi-core computers running a Linux-based operating system known as Scientific Linux. During 2016, approximately 20000 cores were employed to run the HLT [107]. The HLT software is organised in readout, builder and filter units. The readout unit extracts the information from all CMS subsystems once an event passes the L1 trigger. The builder unit assembles the raw data provided by the readout unit to build detector segments, hits and clusters. The assembled data are subsequently sent to the filter unit which performs the reconstruction of physics objects and selects events for data analysis. The logic of the HLT reconstruction framework is similar to what is used in offline reconstruction but optimised to handle high input data rates ( $\leq 100\text{kHz}$ ).

The structure of the HLT algorithms is organised in a set of processing steps, called HLT path, that runs the reconstruction and selection of events. Each HLT path consists of a sequence of processing units that runs in a predefined order and selects events based on user-defined conditions, such as requiring the presence of muons with  $p_T$  larger than a given threshold. Once an event has been accepted by the HLT, the CMS data is kept temporarily on disk and eventually sent to the Tier-0 computing facility for further offline processing. The HLT output rate is constrained by the size of the event data and

1267 the Tier-0 processing power. The average data size of an event in p-p collisions is around  
1268 500 kb, while in central Pb-Pb collisions can reach values as large as 3 Mb due to the  
1269 higher particle multiplicity.

1270 For the analyses presented in this manuscript, the data was triggered requiring  
1271 the presence of identified muons. The reconstruction of muon candidates in the HLT is  
1272 performed in two steps. The first one, referred as the Level-2 (L2), reconstructs muon  
1273 tracks using data from the muon system only, while the next step, known as the Level-3  
1274 (L3), combines the information from both the inner tracker and the muon stations.

1275 **HLT L2 muon reconstruction.** The L2 muon algorithm starts by performing a local  
1276 reconstruction of the muon detectors to determine the hits on each muon chamber. The  
1277 CSC and DT hits are then combined to form segments, which are only kept if found near  
1278 a L1 muon candidate. The muon segments are then recursively fitted with a Kalman  
1279 Filter (KF) technique [108] to build the L2 muon tracks. Duplicate tracks are filtered by  
1280 removing L2 muon tracks that share hits. The KF fit is constrained to the position of the  
1281 IP to improved the  $p_T$  resolution of L2 muon candidates.

1282 **HLT L3 muon reconstruction.** The L3 muon reconstruction improves the momen-  
1283 tum resolution by combining the measurements from the inner tracker and the muon  
1284 chambers. The reconstruction of all tracks in the inner tracker (hereafter called tracker  
1285 tracks) cannot be done at HLT due to timing constrains. Instead, a regional tracking is  
1286 performed by only reconstructing tracker tracks close to the L2 muon candidates using  
1287 three different seeding algorithms. In the first case, the seeds are defined by extrapo-  
1288 lating the parameters (position and  $p_T$ ) of the L2 muon tracks to the outer surface of  
1289 the inner tracker. The second seeding procedure takes the extrapolated L2 muon tracks  
1290 and updates their parameters with the hit information from the outermost layers of  
1291 the silicon-strip tracker. And the third seeding algorithm uses segments from two pixel  
1292 hits measured in consecutive layers found in a narrow  $\eta$ - $\phi$  region around each L2 muon  
1293 track. Each seed is then used to build the tracker tracks with a KF fit. The reconstructed  
1294 tracker and L2 muon tracks are propagated to a common surface, and then matched by  
1295 comparing their goodness-of-fit  $\chi^2$ . If a L2 muon track and a tracker track is matched,  
1296 the hits of both tracks are then combined and refitted to form the L3 muon track.

### 2.2.3 Reconstruction

The aim of the CMS event reconstruction algorithms is to build and identify the physics objects generated during the collision by processing the raw data recorded by the CMS detector. The reconstruction algorithms are implemented in CMSSW framework. Once an event is selected by the HLT, the detector information is then transferred to the Tier-0 computing centre and processed with CMSSW. The reconstruction software starts by building the hits, segments and clusters, measured in each of the CMS subdetectors. Afterwards, it processes the detector information to form physics objects such as charged-particle tracks, muons, electrons, photons and jets. Global event quantities, like the missing transverse momentum ( $p_T^{\text{miss}}$ ), are computed by combining the information from the different reconstructed objects. Only the reconstruction of muons and the  $p_T^{\text{miss}}$  are described hereafter, since they are the only objects used in the W-boson and charmonium analyses presented in Chapter 3 and Chapter 4, respectively.

#### 2.2.3.1 Muon reconstruction

Muon candidates are reconstructed in CMS using the information from the inner tracker and the muon system. Tracks formed in the muon system only are called *standalone-muon* tracks, while those built in the inner tracker and matched to a hit in the muon system are referred to as *tracker-muon* tracks. *Global-muon* tracks are reconstructed by matching a tracker track with a standalone-muon track [109]. The three different types of muon tracks used in CMS are displayed in Figure 2.16.

**Standalone muons.** The standalone muon reconstruction starts with the formation of segments made from a linear interpolation of the position of hits measured in the DT or CSC layers. Each track segment has an associated state vector representing its position, direction and  $p_T$ . The state vector of the segments built in the innermost muon station is used to seed the muon track fit.

In the barrel region, tracks are built by fitting the DT segments with a KF algorithm [108], starting from the innermost muon chamber. Moreover, since the magnetic field in the endcap sections is not uniform, the hits of the CSC segments are used directly to perform the KF fit. The RPC hits are also included in the KF. In the case that no hits are found between muon layers, the state vector of the muon track is propagated to the next layer taking into account the magnetic field and the interaction of muons with the CMS detector material.

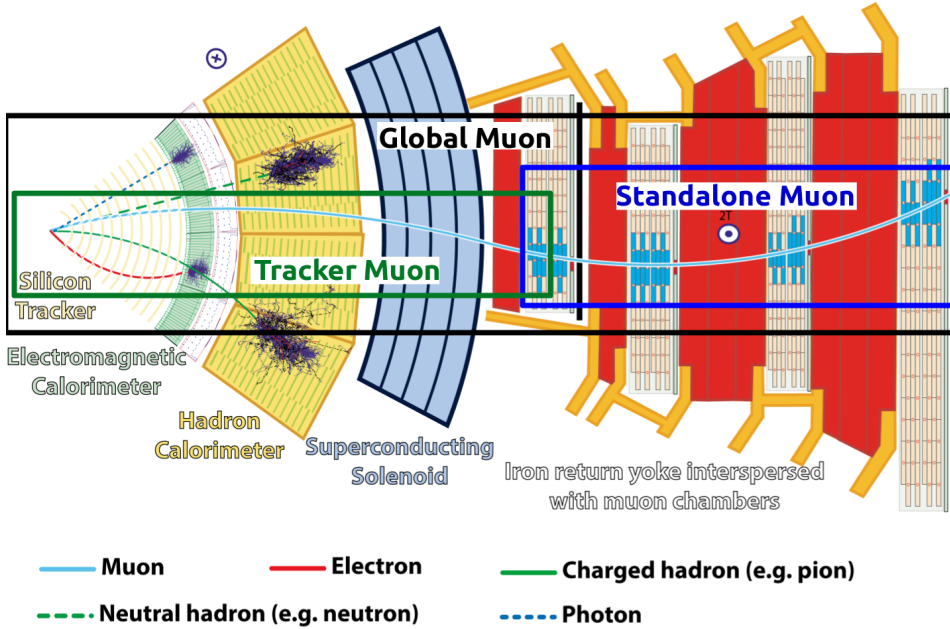


Figure 2.16: Cross section view of the CMS detector showing how particles interact in the CMS. The different types of muon tracks are indicated by boxes. Figure taken from Ref. [110].

1329        The track building procedure is iterated while progressing towards the outer muon  
 1330      chambers. The  $\chi^2$  value between the detector hits and the position of the track projected  
 1331      onto the muon chambers is computed in each step. The hits with large  $\chi^2$  values are  
 1332      excluded from the KF fit and the parameters of the track are updated accordingly. The  
 1333      track fit algorithm stops when it reaches the last muon station. Subsequently, the KF  
 1334      algorithm is performed backwards working from the outermost to the innermost muon  
 1335      chambers, completing the standalone-muon track. Finally, the standalone-muon tracks  
 1336      are extrapolated to the closest approach to the beam line and their position is required  
 1337      to be close to the IP.

1338      **Global muons.** The global muon reconstruction improves the momentum measure-  
 1339      ment by including the information from the inner tracker. The global muon tracking  
 1340      begins by propagating the standalone-muon tracks to the outer surface of the silicon-strip  
 1341      tracker, and a tracker layer consistent with the position of the propagated standalone  
 1342      muon then defines a common surface.

1343      Tracker-track segments are built from pairs (triplets), made of two (three), hits  
 1344      reconstructed in adjacent inner-tracker layers. These segments are then employed to seed

1345 an iterative KF combinatorial track finder. The sophisticated tracking procedure runs  
1346 ten different iterations. The first two iterations reconstruct low- $p_T$  and high- $p_T$  tracks  
1347 seeded with pixel-hit triplets. The third iteration uses pixel-hit triplets to reconstruct  
1348 tracks from secondary vertices displaced, within a radial distance  $R < 5$  cm, from the  
1349 primary vertex. The next iteration is meant to recover tracks with one or two missing  
1350 hits by seeding with pixel-hit pairs instead. The fifth iteration build displaced tracks  
1351 ( $R < 7$  cm) seeded by triplets from pixel and strip hits. The following two iterations  
1352 reconstruct very displaced tracks ( $R < 60$  cm) seeded by strip-hit triplets. The eighth  
1353 iteration aims to find tracks within the core of high- $p_T$  jets seeded by pairs of pixel and  
1354 strip hits. And the last two iterations build tracks seeded with hits and segments from  
1355 the muon chambers, to improve the muon reconstruction efficiency. The hits associated  
1356 to tracks formed in a given iteration are excluded in the subsequent iterations to avoid  
1357 duplicating tracks. The rate of mis-reconstructed tracks is kept low in each step by  
1358 applying a set of quality criteria on the goodness-of-fit  $\chi^2$  and the number of hits used,  
1359 and by requiring the tracks to be consistent with a charged-particle trajectory originating  
1360 from the primary vertex.

1361 The tracker track and the propagated standalone-muon track are matched in the  
1362 common surface according to their  $p_T$ , position and direction measured in the common  
1363 plane, and the hits from both tracks are then refitted to derive the ultimate global-muon  
1364 candidate. If multiple global-muon tracks are found for the same standalone muon, the  
1365 track with the best  $\chi^2$  fit value is kept.

1366 **Tracker muons.** The tracker-muon candidates are built by propagating all tracker  
1367 tracks with  $p_T > 0.5$  GeV/c and total momentum  $p > 2.5$  GeV/c, outward to the innermost  
1368 muon station. The propagated track is then considered a tracker-muon track if it matches,  
1369 along the transverse plane, at least one hit reconstructed in the inner muon chambers.

1370 **Tracking in Pb-Pb collisions.** A modified version of the tracker-track reconstruction  
1371 was employed during Pb-Pb collisions at  $\sqrt{s_{\text{NN}}} = 5.02$  TeV, to cope with the large number  
1372 of charged particles produced in central heavy-ion collisions. The tracking algorithm used  
1373 to build the tracker tracks consists of seven iterations and is called Regional Iterative  
1374 tracking (RegIt). Instead of using all pixel hits reconstructed in the inner tracker, RegIt  
1375 performs a regional track reconstruction using only those hits found in a  $\eta$ - $\phi$  area around  
1376 each standalone-muon track. The RegIt iterations follow the same logic as the standard  
1377 tracking, excluding the three iterations corresponding to low- $p_T$ , very displaced, and

1378 high- $p_T$  jet tracks. In each iteration, tracks made with RegIt are required to have a  
 1379  $p_T > 0.8 \text{ GeV}/c$  and at least eight hits, which is a tighter criteria compared to the standard  
 1380 track reconstruction.

1381 **2.2.3.2 Missing transverse momentum reconstruction**

1382 Since neutrinos cannot be detected, their presence is inferred from the overall particle  
 1383 momentum imbalance in the transverse plane, known as missing transverse momentum  
 1384 ( $p_T^{\text{miss}}$ ). The  $p_T^{\text{miss}}$  is defined as the magnitude of  $\vec{p}_T^{\text{miss}}$ , which represents the negative  
 1385 vector sum of the transverse momentum of all particles identified by CMS in an event,  
 1386 as described in:

$$\begin{aligned}\vec{p}_T^{\text{miss}} &= - \sum_{\text{particles}} \vec{p}_T \\ p_T^{\text{miss}} &= \left| \vec{p}_T^{\text{miss}} \right|\end{aligned}\tag{2.5}$$

1387 The Particle-Flow (PF) algorithm [111] is used to identify the particles produced in a  
 1388 given event. The PF algorithm is optimised to reconstruct stable particles by taking into  
 1389 account the information from all CMS subdetectors. The algorithm determines the mo-  
 1390 mentum of the reconstructed objects and classify them in five categories: electron, muon,  
 1391 photon, charged hadron and neutral hadron, as shown in Figure 2.16. The transverse  
 1392 momentum of all PF particles is used to compute the  $p_T^{\text{miss}}$ . The performance of the  $p_T^{\text{miss}}$   
 1393 reconstruction in p-p collision data has been documented in [112, 113].



## W-BOSON PRODUCTION IN PROTON-LEAD COLLISIONS

1396 This chapter reports the measurement of the production of W bosons in proton-  
1397 lead collisions at a nucleon-nucleon center-of-mass energy  $\sqrt{s_{\text{NN}}} = 8.16 \text{ TeV}$  with  
1398 the CMS detector. A brief introduction to the theory of electroweak interactions  
1399 and the W-boson production in p-Pb collisions is presented in Section 3.1. This section  
1400 concludes with a overview of the latest measurements of weak-boson production in  
1401 heavy-ion collisions at the LHC. The W-boson analysis is then described in detailed  
1402 in Section 3.2. In Section 3.3, the results of the W-boson analysis are presented and  
1403 compared to theoretical calculations based on PDFs.

### 3.1 Introduction

1404 This section provides a short introduction to the W-boson analysis. It starts with a  
1405 brief historical overview of the weak theory (Section 3.1.1) and continues with a short  
1406 description of the modern theory of electroweak interactions (Section 3.1.2). The process  
1407 of interest in this analysis,  $p\text{Pb} \rightarrow W \rightarrow \mu\nu_\mu$ , is detailed in Section 3.1.3. Section 3.1.4  
1408 introduces the nuclear PDFs and describes the most recent nuclear PDF sets. Finally,  
1409 Section 3.1.5 present some of the latest results on weak boson production in heavy-ion  
1410 collisions at the LHC.

**3.1.1 A brief history of the weak theory**

In the early 20th century, quantum mechanics was the standard framework of atomic physics but certain processes such as the  $\beta$  decay, discovered by Ernest Rutherford in 1899 [114], were not fully understood yet. At the time, the  $\beta$  decay was characterized by the process  $A_i \rightarrow A_f + e^-$ , where an initial nucleus  $A_i$  decays into another nucleus  $A_f$  emitting an electron during the process. In order to conserve energy, the electron is required to have a fixed kinetic energy, but James Chadwick observed in 1914 that the  $\beta$  rays produced a continuous energy spectrum [115, 116] in disagreement with what was expected. Another puzzle was the apparently wrong statistics of  $^{14}\text{Ni}$  ( $A = 14$ ,  $Z = 7$ ), which was thought at the time to be composed of 14 protons and 7 electrons (behaving as a fermion), but was experimentally proven to have spin 1. As a way to solve the problem of the continuous  $\beta$  decay spectrum and the statistics problem of nitrogen, Wolfgang Pauli proposed in 1930 the existence of a new particle [117, 118]. Pauli named his particle initially the neutron, but was later renamed to neutrino by Enrico Fermi after the discovery of a new heavy neutral particle by Chadwick in 1932 [119], that ended up solving the  $^{14}\text{Ni}$  statistics problem by explaining the nitrogen nucleus as made of 7 protons and 7 neutrons (even number of fermions). Pauli described the neutrino as a neutral fermion with mass close to zero and spin 1/2 capable of penetrating matter deeper than photons [117].

Enrico Fermi, after attending the 7th Solvay conference, where the discovery of the neutron and the neutrino hypothesis were presented, proposed a new theory to explain the  $\beta$  decay [120]. Fermi's theory defined the  $\beta$  decay as a process in which the neutron decays to a proton, emitting an electron and a neutrino. Fermi formulated his theory using an analogous approach as in Quantum Electrodynamics (QED), by proposing the following Lagrangian for  $\beta$  decay [121]:

$$L_\beta = G_F (\bar{u}_p \gamma_\mu u_n) (\bar{u}_e \gamma^\mu u_\nu) \quad (3.1)$$

where  $u$  is the Dirac spinor of each particle,  $\gamma_\mu$  is the Dirac matrix and  $G_F$  is the Fermi coupling constant. Fermi's theory of weak interactions assumed the same conservation rules as QED, including the symmetry under reflection in space [121]. A system that is invariant under reflections conserve a quantity called parity.

In the upcoming years, the physicists Tsung Dao Lee and Chen Ning Yang started to suspect that the weak interactions could violate parity conservation, after not finding any experimental evidence of its conservation so far [122]. In an attempt to test the

1444 conservation of parity in weak interactions, Lee and Yang proposed in 1956 to study  
1445 the  $\beta$  decays of Cobalt ( $^{60}\text{Co}$ ) and measure the projection of the momentum of electrons  
1446 along the spin axis of the Cobalt nucleus [122]. If the decay process conserves parity then  
1447 electrons would be produced in both directions: parallel and anti-parallel to the magnetic  
1448 field. The experiment to test the conservation of parity was realized by Chien-Shiung  
1449 Wu in 1957. The results of Wu's research showed that electrons were preferentially  
1450 produced in the opposite direction to the Cobalt spin [123], which meant that parity was  
1451 not conserved in weak interactions, and even maximally violated.

1452 Apart from parity, one can also associate a helicity to particles. The particle's helicity  
1453 is considered right-handed if the projection of the spin on the particle momentum is  
1454 aligned, and left-handed otherwise. In 1958, Goldhaber, Grodzins and Sunyar measured  
1455 the neutrino helicity at Brookhaven National Laboratory (BNL) and discovered that  
1456 neutrinos were always left-handed and anti-neutrinos were right-handed [124]. As a  
1457 consequence of the discovery of parity violation and the neutrino helicity, Robert Marshak  
1458 and George Sudarshan modified Fermi's weak theory and introduced an axial vector  
1459 term, giving rise to the V-A (vector-axial) theory of weak interactions [125]. Even though  
1460 parity (P) and charge conjugation (C) (transforms particles into their anti-particles)  
1461 were violated separately, it was then assumed that the combined CP operation was still  
1462 conserved by the weak interaction.

1463 The assumption of the conservation of CP did not last long. An experiment performed  
1464 at BNL by James Christenson, James Cronin, Val Fitch and René Turlay [126] in  
1465 1964 concluded that a small proportion of long-lived  $K_L$  meson ( $\text{CP} = -1$ ) was able to  
1466 decay to two pions ( $\text{CP} = +1$ ) violating CP in the process. To explain the CP violation  
1467 in weak theory, Makoto Kobayashi and Toshihide Maskawa [127] extended in 1973  
1468 the formulation of the Cabibbo angle to include three generation of quarks and a CP-  
1469 violating phase term. The Cabibbo angle was originally computed by Nicola Cabibbo [128]  
1470 to explain the different amplitudes observed between the up, down and strange quark  
1471 transitions. The charm quark was not yet discovered but was strongly hypothesized,  
1472 through the Glashow-Iliopoulos-Maiani (GIM) mechanism [129]. The Cabibbo, Kobayashi  
1473 and Maskawa (CKM) matrix supposed the existence of the charm, bottom and top quarks,  
1474 discovered later in 1977 [130, 131], 1977 [132] and 1995 [133], respectively.

1475 Following Paul Dirac's formulation of QED [134], Sheldon Glashow [135], Steven  
1476 Weinberg [136] and Abdus Salam [137] managed in 1968 to build a gauge-invariant  
1477 unified theory of the electromagnetic and weak interactions. In order to make the elec-  
1478 troweak theory symmetric under local phase transformations, it required the presence

of four spin-1 massless bosons: two charged particles called  $W^\pm$  bosons and two neutral particles corresponding to the Z boson and photon. But since the weak interactions are short range, it has to be mediated by massive bosons. The addition of mass to the bosons was realized after introducing the spontaneous local breaking of the underlying SU(2) symmetry through the Higgs mechanism [15, 16]. In the following years, Gerardus t’Hooft and Martinus Veltman managed to renormalise the electroweak theory [138, 139], allowing to calculate more precisely the theoretical masses of the weak bosons.

The Z boson was then missing, but a single event was found in the Gargamelle experiment [140], exhibiting a flavour-changing neutral current that could only be mediated by a virtual Z boson ( $\nu_\mu + e^- \rightarrow \nu_\mu + e^-$ ). The experimental study of weak bosons required the development of new particle acceleration technologies. In 1976, Carlo Rubbia, Peter McIntyre and David Cline suggested to transform CERN’s circular proton accelerator, the SPS, into a proton-antiproton collider (Sp̄S) [141]. The upgrade to Sp̄S was made possible thanks to the stochastic cooling technology invented by Simon Van der Meer [142] in 1972, which allowed to cool down and collect anti-protons. Several experiments were built in the Underground Area (UA) to study the proton-antiproton collisions at the Sp̄S. The UA1 and UA2 collaborations observed on-shell W bosons [143, 144] in 1983, via reporting the observation of electrons with large transverse energy and the presence of missing momentum in  $p\bar{p}$  collisions at  $\sqrt{s} = 540 \text{ GeV}$ . And few months later, both collaborations also reported the observation of on-shell Z bosons in the dilepton decay channel [145, 146].

After the major success of the Sp̄S project, CERN constructed in 1983 a new lepton circular collider called the Large Electron-Positron (LEP) collider [147]. LEP was designed to accelerate electrons and positrons to an energy of half the Z-boson mass (45 GeV), in order to perform precision measurements of the Z-boson line-shape. Precise measurements of the W-boson mass [148] were later performed by the experiments in the Fermi National Accelerator Laboratory (FNAL). The FNAL experiments analysed data collected between 1983 and 2011 from the Tevatron [149], a proton-antiproton synchrotron collider that operated at energies up to  $\sqrt{s} = 1.96 \text{ TeV}$ .

The successful programs of LEP and Tevatron produced the most precise measurements of the properties of the electroweak theory, but there was still a missing piece to complete the picture, the Higgs boson. The discovery of the Higgs boson was finally achieved in 2012 by the CMS [17] and ATLAS [18] collaborations at the Large Hadron Collider (LHC).

---

### 1513 3.1.2 The modern electroweak theory

1514 The interactions between elementary particles mediated by the weak and electromagnetic  
 1515 forces are described in the Standard Model using the electroweak theory developed by  
 1516 Glashow, Weinberg and Salam [135–137]. The unification of these two fundamental  
 1517 forces of nature is accomplished mathematically using a non-abelian  $SU(2) \times U(1)_Y$  gauge  
 1518 theory. The electroweak theory requires four massless gauge bosons: three bosons with  
 1519 weak isospin (called  $W_1$ ,  $W_2$  and  $W_3$ ) from  $SU(2)$  and one boson (named  $B$ ) with weak  
 1520 hypercharge from  $U(1)_Y$ .

1521 Since weak bosons have mass, a full description of the electroweak interactions  
 1522 requires the inclusion of massive vector bosons. The problem is that one can not naively  
 1523 add a mass term of the form  $m^2 W^\mu W_\mu$  into the electroweak Lagrangian since this  
 1524 would break gauge invariance making the theory divergent. Thus, this issue is instead  
 1525 solved by spontaneously breaking the  $SU(2) \times U(1)_Y$  electroweak symmetry into a  $U(1)_{EM}$   
 1526 symmetry using the Higgs mechanism [15, 16]. The overall idea is that the electroweak  
 1527 gauge bosons couple to a scalar field called the Higgs field which is present in all space.  
 1528 When this field induces a spontaneous breaking of the gauge symmetry, it is split into  
 1529 one dynamic part corresponding to the Higgs boson, and another constant part called the  
 1530 vacuum expectation value (VEV). The symmetry breaking of  $SU(2) \times U(1)_Y$  to  $U(1)_{EM}$   
 1531 generates three massless Goldstone bosons. The Goldstone bosons are then absorbed  
 1532 by the electroweak gauge bosons producing the  $W^+$ ,  $W^-$  and  $Z$  bosons with masses  
 1533 proportional to the VEV, while the photon remains massless. The  $W^\pm$ ,  $Z$  and  $\gamma$  bosons  
 1534 are correlated with the  $W_1$ ,  $W_2$ ,  $W_3$  and  $B$  gauge bosons in the following way:

$$\begin{aligned} W^\pm &= \frac{1}{\sqrt{2}} (W_1 \pm W_2) \\ \begin{pmatrix} Z \\ \gamma \end{pmatrix} &= \begin{pmatrix} \cos\theta_W & \sin\theta_W \\ -\sin\theta_W & \cos\theta_W \end{pmatrix} \begin{pmatrix} B \\ W_3 \end{pmatrix} \end{aligned} \tag{3.2}$$

1535 where  $\theta_W$  represents the weak mixing angle. In addition, quarks and leptons ac-  
 1536 quire mass through the Yukawa interaction with the Higgs field. Since the quark weak  
 1537 eigenstates are not the same as their mass eigenstates, weak interactions can induce a  
 1538 transition from an up-like quark ( $u$ ,  $c$ ,  $t$ ) to a down-like quark ( $d$ ,  $s$ ,  $b$ ). The strength of the  
 1539 quark-flavour mixing in weak decays is parametrised by the CKM matrix  $V_{CKM}$  via:

$$\begin{pmatrix} d' \\ s' \\ b' \end{pmatrix} = \begin{pmatrix} V_{ud} & V_{us} & V_{ub} \\ V_{cd} & V_{cs} & V_{cb} \\ V_{td} & V_{ts} & V_{tb} \end{pmatrix} \begin{pmatrix} d \\ s \\ b \end{pmatrix} \quad (3.3)$$

where  $(d', s', b')$  are the down-like quark weak eigenstates and  $(d, s, b)$  are the corresponding mass eigenstates. The latest values of the magnitude of the CKM matrix elements are [19]:

$$\begin{pmatrix} |V_{ud}| & |V_{us}| & |V_{ub}| \\ |V_{cd}| & |V_{cs}| & |V_{cb}| \\ |V_{td}| & |V_{ts}| & |V_{tb}| \end{pmatrix} = \begin{pmatrix} 0.97417 & 0.2248 & 0.00409 \\ 0.220 & 0.995 & 0.0405 \\ 0.0082 & 0.04 & 1.009 \end{pmatrix} \quad (3.4)$$

The Lagrangian of the electroweak theory includes several components that describe the interactions between the fermions, electroweak bosons and the Higgs boson. In the case of the Z boson, the term of the Lagrangian that represents the interactions between fermions and neutral-charged electroweak bosons is:

$$L_{NC} = \alpha_{em} \theta_W \sum_{\text{fermions}} \bar{f} \gamma^\mu A_\mu f + \frac{g}{\cos \theta_W} \sum_{\text{fermions}} \bar{f} \gamma^\mu \frac{(g_v^f - g_a^f \gamma^5)}{2} Z_\mu f \quad (3.5)$$

where  $g$  is the coupling constant of  $SU(2)_L$ ,  $f$  is the Dirac spinors of fermions,  $A_\mu$  is the electromagnetic field, and  $g_v^f$  ( $g_a^f$ ) is the fermion vector (axial) weak coupling constants. Eq. (3.5) specify that the Z bosons and photons conserve flavour, always decaying into a fermion and its corresponding anti-fermion. While photons do not distinguish the helicity of particles, the Z-boson couplings are different for left- and right-handed fermions.

Furthermore, the component of the Lagrangian that represents the interaction between W bosons and fermions is given by:

$$L_{CC} = \frac{g}{2\sqrt{2}} \left( (\bar{u}, \bar{c}, \bar{t})_R W_\mu^+ \gamma^\mu V^{\text{CKM}} \begin{pmatrix} d_L \\ s_L \\ b_L \end{pmatrix} + (\bar{\nu}_e, \bar{\nu}_\mu, \bar{\nu}_\tau)_R W_\mu^+ \gamma^\mu \begin{pmatrix} e_L^- \\ \mu_L^- \\ \tau_L^- \end{pmatrix} \right) \quad (3.6)$$

where  $f_L$  correspond to left-handed fermions and  $\bar{f}_R$  represents right-handed anti-fermions. Thus, W bosons only couple to right-handed anti-fermions and left-handed fermions organized in pairs of lepton-neutrino or quark-antiquark, where the electric charge of the of particles differ by one unit. Since the top-quark mass (178 GeV) is larger than the W-boson mass (80 GeV), the W boson can not decay to a virtual top quark.

1559 Figure 3.1 shows the possible decays of weak bosons to fermions. The measured values  
 1560 of the mass, width and couplings of weak vector bosons are summarized in Table 3.1.

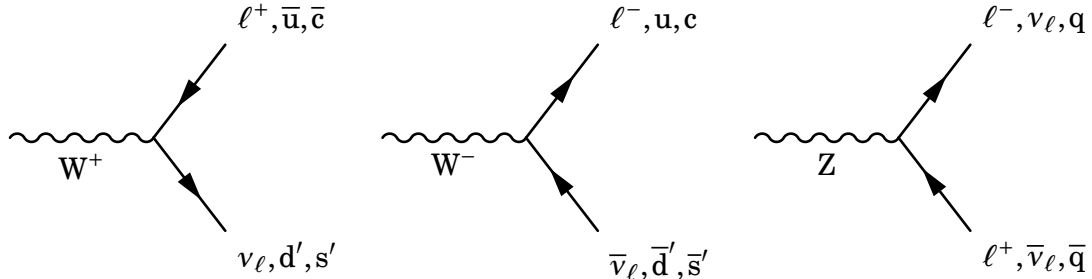


Figure 3.1: Feynman diagram of the decay modes of  $W^+$  (left),  $W^-$  (middle) and  $Z$  (right) bosons to fermions.

Variable	Description	Value
$M_W$	$W$ boson mass	$80.385 \pm 0.015 \text{ GeV}$
$\Gamma_W$	$W$ boson width	$2.085 \pm 0.042 \text{ GeV}$
$\text{BR}(W \rightarrow \ell\nu)$	Branching fraction of $W$ boson semileptonic decays	$(10.86 \pm 0.09)\%$
$\text{BR}(W \rightarrow q\bar{q}')$	Branching fraction of $W$ boson hadronic decays	$(67.41 \pm 0.27)\%$
$M_Z$	$Z$ boson mass	$91.1876 \pm 0.0021 \text{ GeV}$
$\Gamma_Z$	$Z$ boson width	$2.4952 \pm 0.0023 \text{ GeV}$
$\text{BR}(Z \rightarrow \ell^+\ell^-)$	Fraction of $Z$ boson charged-lepton decays	$(3.3658 \pm 0.0023)\%$
$\text{BR}(Z \rightarrow \nu\bar{\nu})$	Fraction of $Z$ boson neutrino decays	$(20.00 \pm 0.06)\%$
$\text{BR}(Z \rightarrow q\bar{q})$	Fraction of $Z$ boson hadronic decays	$(69.91 \pm 0.06)\%$

Table 3.1: Experimental values of the mass, width and branching fractions of weak bosons extracted from the PDG [19].

### 1561 3.1.3 Production of $W$ bosons in p-Pb and decay into muons

1562 In this thesis, the inclusive production of  $W$  bosons is measured in p-Pb collisions through  
 1563 the muonic decay channel, which is represented by the process  $p\text{Pb} \rightarrow W + x \rightarrow \mu + \nu_\mu + x$ .  
 1564 Since the mass of the  $W$  boson is large ( $M_W = 80.385 \text{ GeV}$ ), the  $W$  bosons are formed  
 1565 during the initial hard scatterings between the partons from the incoming proton and  
 1566 those from the nucleons bound in the Pb ion.

1567 The cross section for the inclusive production of  $W$  bosons in p-Pb collisions can be  
 1568 expressed, assuming that the QCD factorisation holds for a nucleus, as:

$$\sigma[pPb \rightarrow W + X] = \sum_{a,i,j} \int dx_p dPb_2 f_i^p(x_p, Q^2) \cdot f_j^{a/Pb}(x_{Pb}, Q^2) \hat{\sigma}[i + j \rightarrow W + X] \quad (3.7)$$

1569 where  $f^{a/Pb}$  are the PDFs of a nucleon  $a$  bound in the Pb ion,  $f^p$  are the PDFs of  
 1570 the incoming proton and  $\hat{\sigma}$  is the partonic cross section. The partonic cross section is  
 1571 evaluated using pQCD by expanding it in terms of  $\alpha_s$ , as given by:

$$\hat{\sigma} = \sum_i (\alpha_s^i \cdot \hat{\sigma}^i) = \hat{\sigma}^{\text{LO}} + \alpha_s \hat{\sigma}^{\text{NLO}} + \dots \quad (3.8)$$

1572 In practice, the expansion of the partonic cross section is truncated at a given order  
 1573 (e.g. NLO). At leading order, the production of W bosons in proton-nucleon collisions is  
 1574 accomplished through the process of quark-antiquark annihilation ( $q + \bar{q} \rightarrow W$ ), as shown  
 1575 in Figure 3.2. On the other hand, the NLO cross section includes contributions from the  
 1576 processes shown in Figure 3.3.

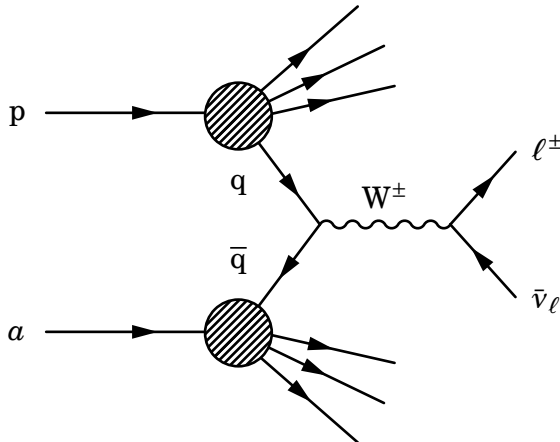


Figure 3.2: Leading order Feynman diagram of W boson production to final state leptons, from a collision between an incoming proton (p) and a bound nucleon (a) in a Pb nucleus.

1577 The total partonic cross section at LO for  $pPb \rightarrow W \rightarrow \mu\nu_\mu$  can be computed using  
 1578 electroweak theory and is given by [19]:

$$\hat{\sigma}^{\text{LO}}[ij \rightarrow W \rightarrow \mu\nu_\mu](Q^2) = \frac{|V_{ij}^{\text{CMK}}|^2}{N_c} \frac{8G_F^2 M_W^4}{16\sqrt{2}\pi} \left( \frac{Q^2}{(Q^2 - M_W^2)^2 + Q^2 \Gamma_W^2} \right) \quad (3.9)$$

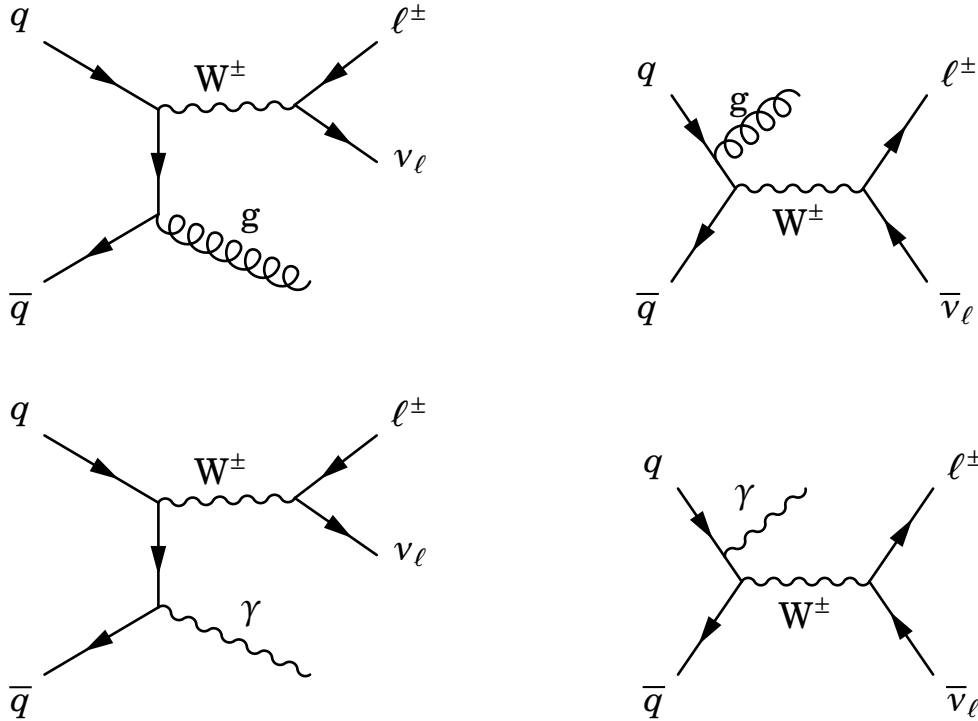


Figure 3.3: Next-to-leading order Feynman diagrams of W boson partonic production to final state leptons.

1579 where  $M_W$  is the mass of the W boson,  $\Gamma_W$  is the width of the W boson,  $N_c = 3$  is the  
 1580 number of colour charges of quarks, and  $|V_{ij}^{\text{CKM}}|$  is the magnitude of the CKM matrix  
 1581 element associated to the interaction between the quarks i and j.

1582 In pPb collisions, the W bosons are mainly produced from interactions between the  
 1583 valence quarks and sea anti-quarks of the proton and nucleons. The dominant production  
 1584 modes of  $W^+$  bosons correspond to up quark and down anti-quark annihilation ( $u\bar{d} \rightarrow W^+$ )  
 1585 while for  $W^-$  bosons correspond to down quark and up anti-quark annihilation ( $d\bar{u} \rightarrow W^-$ ).  
 1586 The next relevant contributions come from  $c\bar{s}$  and  $s\bar{c}$ , while the other quark-antiquark  
 1587 contributions are suppressed according to the off-diagonal CKM matrix elements. Thus,  
 1588 the inclusive W boson cross section measured in p-Pb data is mostly sensitive to the  
 1589 proton and nuclear PDFs of light quarks and anti-quarks.

1590 In addition, the direction of the outgoing muons and anti-muons is different with  
 1591 respect to the scattered quarks. In weak interactions, the  $W^+$  boson couples to left-handed  
 1592 neutrinos while the  $W^-$  boson couples to right-handed anti-neutrinos. As a consequence,  
 1593 in order to conserve helicity, the anti-muons are preferentially produced in the same  
 1594 direction as the  $W^+$  boson while muons are preferentially produced in the opposite

1595 direction, as shown in Figure 3.4.

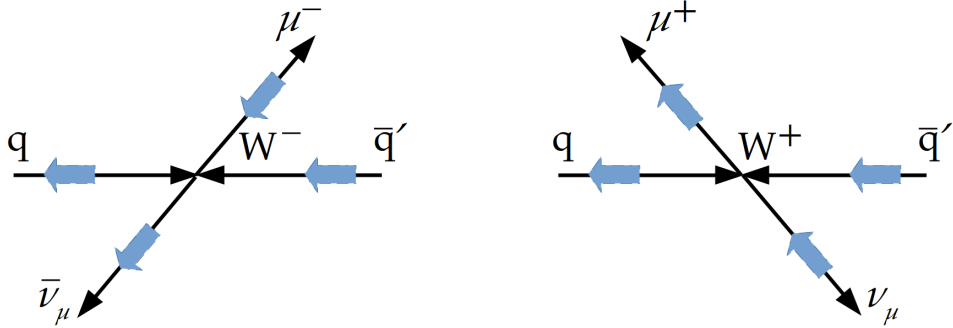


Figure 3.4: Schematic diagram of the production of  $W^-$  (left) and  $W^+$  (right) bosons to muonic decays. The black arrows represent the particle direction of motion whereas the blue arrows correspond to its spin. The spin of the  $W^\pm$  boson points in the direction of the anti-quark.

1596 At LO, the rapidity of  $W$  bosons ( $y_W$ ) is related to the Bjorken- $x$  of the proton and  
1597 Pb nucleon via:

$$x_p = \frac{M_W}{\sqrt{s_{NN}}} e^{y_W} , \quad x_{Pb} = \frac{M_W}{\sqrt{s_{NN}}} e^{-y_W} \quad (3.10)$$

1598 And since the  $W$ -boson rapidity is correlated to the muon  $\eta$ , then the pseudorapidity  
1599 distribution of muons arising from  $W$ -boson decays in p-Pb collisions is sensitive to  
1600 different  $x$  regions of the light quark nuclear PDF that are described in the next section.

### 1601 3.1.4 Nuclear PDFs

1602 The parton distribution functions can not be determined from first principles due to the  
1603 non-perturbative behaviour of the strong interactions. Nevertheless, their dependence  
1604 on  $x$  can be derived by fitting observables (e.g. structure functions or asymmetries) to  
1605 experimental data from different processes since PDFs do not depend on the initial hard  
1606 scattering. The  $Q^2$  dependence of the PDFs is determined using the DGLAP evolution  
1607 equations. The most common processes used to constrain the PDFs correspond to DY,  
1608 DIS, vector boson and jet production, which have been measured by various experiments,  
1609 including data from HERA, SLAC and LHC.

1610 There are several proton PDF global fits currently available. In this thesis we use  
1611 the NLO CT14 PDF sets published in 2016 [150] by the collaboration of theorists and  
1612 experimentalist on QCD (CTEQ). The global fits of CT14 PDFs include data of vector  
1613 bosons and jets from LHC p-p collisions at 7 TeV and 8 TeV, charm quark DIS production

### 3.1. INTRODUCTION

1614 from HERA, and electron charge asymmetry from Tevatron. The  $x$ -dependence of the  
 1615 CT14 PDF is parametrised at low  $Q^2$  by [150]:

$$x f_a(x, Q^2) = x^{c_1} (1-x)^{c_2} P_a(x) \quad (3.11)$$

1616 where  $f_a$  is the PDF of a parton  $a$ ,  $c_i$  are parameters and  $P_a$  is a polynomial function.  
 1617 In total, the CT14 proton PDFs are described by 26 parameters including: 8 parameters  
 1618 for the valence quarks, 5 parameters for the gluon and 13 parameters for the sea  
 1619 quarks [150].

1620 Figure 3.5 presents the CT14 proton PDF results at  $Q = 10\text{ GeV}$  and  $Q = 100\text{ GeV}$ . One  
 1621 can observe that the light valence quarks carry most of the momentum of the proton  
 1622 while the gluons and sea quarks are mainly distributed at low  $x$ . When the energy is  
 1623 increased, the distribution of partons gets significantly enhanced at low  $x$ , predominantly  
 1624 dominated by gluons.

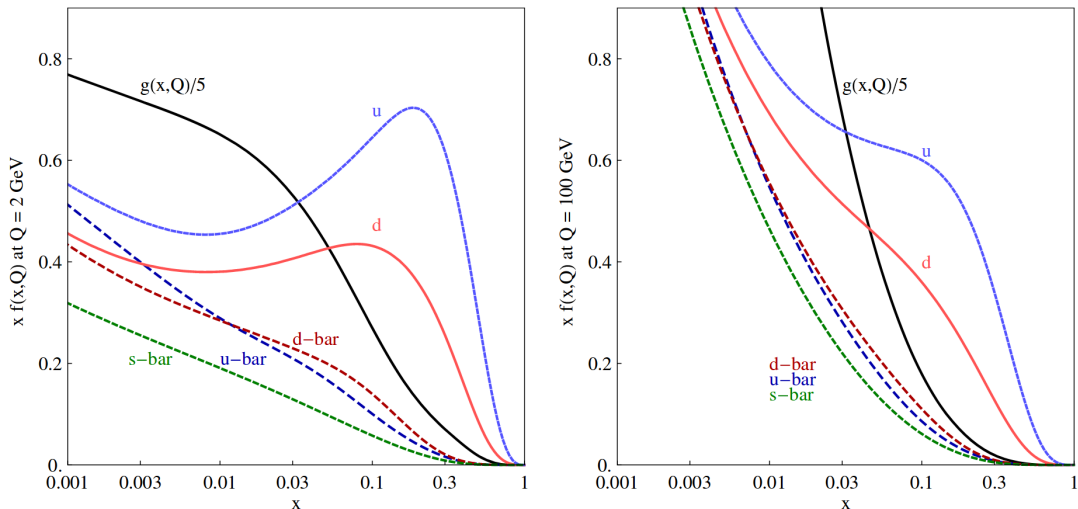


Figure 3.5: Results of the CT14 proton PDFs at NNLO derived at  $Q = 10\text{ GeV}$  (left) and  $Q = 100\text{ GeV}$  (right). Figure taken from Ref. [150].

1625 In heavy-ion collisions, the PDFs of the protons and neutrons bound in the nucleus  
 1626 are modified by the presence of the nuclear medium environment. The PDFs of nuclei  
 1627 were initially analysed in charged-lepton DIS experiments using nuclear targets by  
 1628 measuring the nuclear structure function per nucleon ( $F_2^A$ ) for a heavy-ion target (A)  
 1629 relative to the one for deuterium ( $F_2^D$ )<sup>1</sup> ( $R_{F_2}^A = F_2^A/F_2^D$ ).

1630 The European Muon Collaboration (EMC) measured at CERN the structure function  
 1631 of muon DIS from iron and deuterium targets, and published in 1983 the first observation

<sup>1</sup>Deuterium is approximately considered to be composed of a free proton and a free neutron.

1632 of a depletion of the DIS cross section from iron relative to the one from deuterium in the  
 1633 high  $x$ -region  $0.3 < x < 0.65$  [151], which was named the EMC region. Afterwards, further  
 1634 DIS measurements at CERN and SLAC found a suppression of the nuclear structure  
 1635 function compared to deuterium in the low- $x$  region  $x < 0.1$  and an enhancement in  
 1636 the intermediate  $x$ -region  $0.1 < x < 0.3$ , which are referred as the shadowing and anti-  
 1637 shadowing regions [152]. Moreover, the measurements at SLAC using data at higher  $x$   
 1638 observed an increase of  $R_{F_2}^A$  while approaching  $x = 1$ , which was expected from the motion  
 1639 of nucleons inside the nuclei, called Fermi motion. Figure 3.6 presents an illustration of  
 1640 the different regions of nuclear modifications found experimentally.

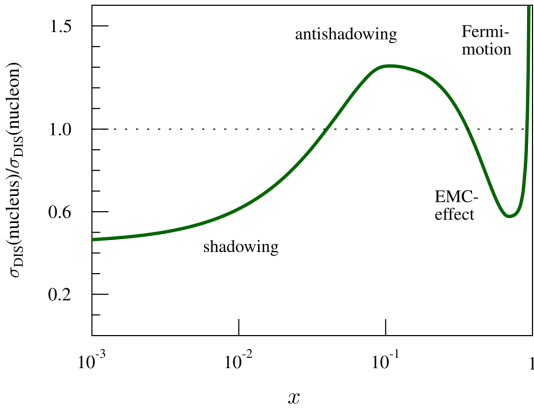


Figure 3.6: Illustration of the different nuclear PDF effects. Figure taken from Ref. [153].

1641 In the case of heavy-ion collisions, the different nuclear modifications can be qualita-  
 1642 tively described as follows:

- 1643 • **Shadowing:** corresponds to the suppression seen in  $x \lesssim 0.1$ , and it arises from  
 1644 the multiple interactions between the scattered partons and the ones from the  
 1645 different nucleons. The multiple parton scatterings shifts the momentum transfer  
 1646  $x$  of the partons towards higher values, effectively reducing the parton densities at  
 1647 low  $x$ .
- 1648 • **Anti-shadowing:** corresponds to an enhancement in  $0.1 \lesssim x \lesssim 0.3$ , and it can be  
 1649 understood as a consequence of the multiple parton scatterings that occur in the  
 1650 nucleus.
- 1651 • **EMC effect:** corresponds to the suppression in  $0.3 \lesssim x \lesssim 0.7$ . Some models have  
 1652 been proposed to explain this phenomenon which consider modifications of the nu-

1653 cleon structure due to the nuclear medium and also due to short-range correlations  
 1654 between nucleons.

- 1655 • **Fermi-motion effect:** corresponds to a enhancement in  $x > 0.7$ , and it is due to  
 1656 the motion of nucleons inside the nucleus.

1657 The first global fit to describe leading-order nuclear effects was the EKS98 nPDF [154],  
 1658 which employed the nuclear DIS data measured at CERN and Fermilab, and the DY  
 1659 dimuon data from Fermilab proton-nucleus collisions. The pion data collected by RHIC  
 1660 was later included in subsequent global nPDF fits, such as EPS08 [155], EPS09 [156]  
 1661 and DSSZ [157], which provided constrains to the gluon nPDF.

1662 The nPDFs or the nuclear modification are defined for protons bound in a nucleus. The  
 1663 bound neutron nPDFs are derived from the bound proton PDFs using isospin symmetry  
 1664 (i.e. by exchanging the up and down quark PDFs). The full nPDFs for a nucleus of  $Z$   
 1665 protons and  $A - Z$  neutrons can be derived using the bound proton nPDFs  $f^{p/A}$  and the  
 1666 bound neutron nPDFs  $f^{n/A}$ , according to:

$$f^A = \frac{Z}{A} f^{p/Pb} + \frac{A-Z}{A} f^{n/Pb} \quad (3.12)$$

1667 From now on, we will focus on the latest nuclear PDF sets: the EPPS16 and nCTE15  
 1668 nPDFs, which are used in this thesis.

1669 **EPPS16 nPDF.** The EPPS16 nuclear PDFs were published in 2017 by Eskola, Paakki-  
 1670 nen, Paukkunen and Salgado (EPPS) [158]. The EPPS16 nPDF calculations updates  
 1671 their previous EPS09 global fits [156].

1672 The EPPS16 global fits includes the same data sets as EPS09 (charged-lepton-nucleus  
 1673 DIS data from SLAC, DY dilepton production from EMC proton-nucleus collisions,  
 1674 and inclusive pion production from RHIC deuteron-nucleus collisions), as well as the  
 1675 CHORUS neutrino-nucleus DIS data, low-mass DY production from RHIC pion-nucleus  
 1676 collisions, and the results using dijet and electroweak boson production in LHC pPb  
 1677 collisions at  $\sqrt{s_{NN}} = 5.02\text{TeV}$ . The addition of the new LHC, RHIC and CHORUS data  
 1678 into the global fit is not in tension with the previous EPS09 data sets, reassuring the  
 1679 validity of the universality of the nuclear PDFs. Moreover, the inclusion of the CMS  
 1680 measurements of dijet production in pPb collisions at  $\sqrt{s_{NN}} = 5.02\text{TeV}$  highly constrained  
 1681 the gluon nPDF. On the other hand, the LHC measurements of the electroweak boson  
 1682 production in pPb data did not significantly constrain the nPDF fits, mostly due to the  
 1683 limited statistical precision, but the the results of the W-boson production from the CMS

1684 collaboration suggested possible differences in the modifications of the quark nPDFs.  
 1685 The measurements of the electroweak boson production in heavy-ion collisions at LHC  
 1686 will be presented in the next subsection.

1687 The EPPS16 includes five additional parameters compared to EPS09, to account for  
 1688 possible flavour dependence of the quark nuclear modifications seen at LHC. The nuclear  
 1689 PDFs are parametrised in EPPS16 as:

$$f_i^{p/A}(x, Q^2) = R_i^A(x, Q^2) f_i^p(x, Q^2) \quad (3.13)$$

1690 where  $f_i^{p/A}$  represents the bound proton nPDF of parton  $i$  in a nucleus A,  $f_i^p$  is the  
 1691 free proton PDF of parton  $i$  and  $R_i^A$  is the corresponding nuclear correction factor. The  
 1692 EPPS16 nuclear modifications are derived using the NLO CT14 PDF as the free proton  
 1693 baseline. The parameters of  $R_i^A$  are determined in three regions: the shadowing region  
 1694  $x \rightarrow 0$ , the anti-shadowing maximum point  $x_a$  and the EMC minimum point  $x_e$  (see  
 1695 Figure 3.6). The dependence on the number of nucleons A is parametrised along the  
 1696 three x regions in the following way:

$$R_i^A(x, Q_0^2) = R_i^{A_{\text{ref}}}(x, Q_0^2) \left( \frac{A}{A_{\text{ref}}} \right)^{\gamma_i [R_i^{A_{\text{ref}}}(x, Q_0^2) - 1]} \quad (3.14)$$

1697 where  $Q_0$  is a parametrisation scale fixed at the charm pole mass (1.3 GeV),  $\gamma_i$  is  
 1698 a positive parameter and  $A_{\text{ref}} = 12$ . The  $Q^2$  dependence above  $Q_0^2$  is determined by  
 1699 solving the DGLAP parton evolution equations. The EPPS16 nuclear modifications are  
 1700 parametrised in total by 20 parameters.

1701 The EPPS16 nuclear correction factors for Pb ions  $R^{\text{Pb}}$  extracted from the global PDF  
 1702 fit are shown in Figure 3.7. The EPPS16 results are compared against a baseline derived  
 1703 by performing the EPPS16 fits on the reduced dataset used in EPS09. The inclusion of  
 1704 these CHORUS, RHIC p-A and LHC data improves the uncertainties of the gluon  $R^A$  at  
 1705 high  $x$  and the strange-quark  $R^{\text{Pb}}$  at low  $x$ .

1706 **nCTEQ15 nPDF.** The nCTEQ15 nuclear PDFs, published by Kovarik et al. in 2016 [159],  
 1707 were derived using the CTEQ framework. The nCTEQ15 nPDF global fits make use of  
 1708 the charged-lepton DIS data, DY dilepton data and RHIC inclusive pion data. In contrast  
 1709 with EPPS16, where the nuclear modification factor  $R_i^{p/A}$  is fitted, the nCTEQ15 global  
 1710 analysis parametrises the nuclear PDF  $f_i^{p/A}$  directly (i.e. no free proton PDF is used as  
 1711 baseline). The nCTEQ nPDFs are parametrised as:

### 3.1. INTRODUCTION

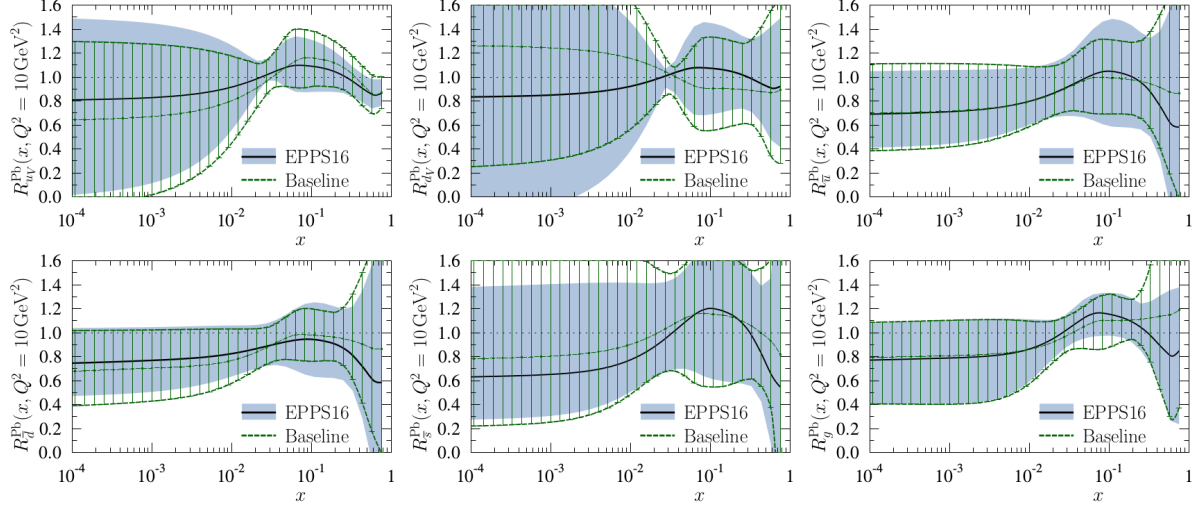


Figure 3.7: Results of the EPPS16 nuclear correction factor  $R^A$  for Pb ions at  $Q^2 = 10 \text{ GeV}^2$ . The black curve represents the central fit while the blue bands shows the total uncertainty of the PDF fit. The results are compared against a baseline made by performing the EPPS16 fits on the same datasets used for EPS09. Figure taken from Ref. [158].

$$xf_a^{p/A}(x, Q_0^2) = c_0 x^{c_1} (1-x)^{c_2} e^{c_3 x} (1 + e^{c_4 x})^{c_5} \\ \frac{\bar{d}(x, Q_0^2)}{\bar{u}(x, Q_0^2)} = c_0 x^{c_1} (1-x)^{c_2} + (1 + c_3 x)(1-x)^{c_4} \quad (3.15)$$

where  $f_a^{p/A}$  is the bound proton nPDF of a parton  $a$  in a nucleus A,  $\bar{d}$  and  $\bar{u}$  are the down and up anti-quark nPDFs, respectively,  $c_i$  are parameters, and the parametrisation scale  $Q_0$  is fixed at  $1.3 \text{ GeV}$ . The strange quark and anti-quark nPDFs are assumed to be the same. The A-dependence of the nPDFs is parametrised in nCTEQ15 using the coefficients  $c_i$ , according to:

$$c_i(A) = c_{i,0} + c_{i,1} (1 - A^{-c_{i,2}}) \quad (3.16)$$

The nCTEQ15 fits are performed using 16 free parameters. In addition, the nCTEQ15 treats the up and down valence quark PDFs independently but it assumes no flavour dependence for nuclear modifications of the up and down anti-quarks.

Figure 3.8 shows the nCTEQ15 results of the full nuclear lead PDFs  $f^{\text{Pb}}$  compared to the results from the EPS09 and HKN07 nPDFs. One can see that at  $x \gtrsim 0.05$  and

1722  $Q^2 = 10 \text{ GeV}^2$  the up and down valence quark nPDFs dominates while at  $x < 0.01$  the sea  
 1723 quarks and the gluons nPDFs becomes dominant.

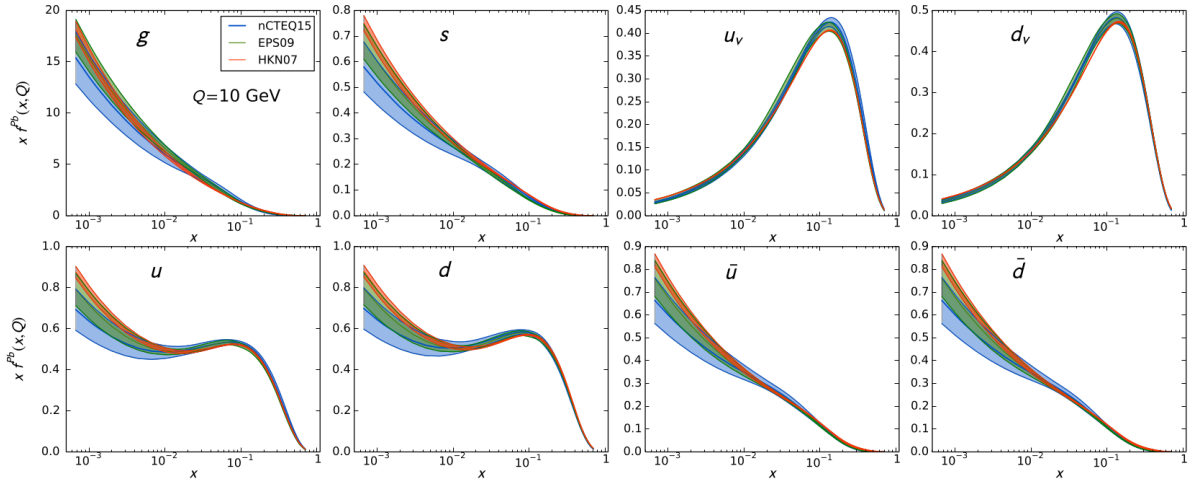


Figure 3.8: Results of the nCTEQ15 full nuclear PDFs for Pb ions  $f^{Pb}$  at  $Q = 10 \text{ GeV}$ .  
 Figure taken from Ref. [159].

1724 A comparison between the results of the nCTEQ15 and EPPS16 nuclear modifications  
 1725 is shown in Figure 3.9. The nCTEQ15 expects more shadowing than EPPS16 for the  
 1726 down valence quarks and light sea quarks, while the opposite trend is observed for  
 1727 up valence quarks. Moreover, the uncertainties of the EPPS16 results are much larger  
 1728 than the nCTEQ15 results because the EPPS16 uses more parameters to fit the nuclear  
 1729 modifications.

1730 The main characteristics of the EPS09, EPPS16 and nCTEQ15 nuclear PDFs are  
 1731 summarized in Table 3.2.

### 1732 3.1.5 Experimental results at LHC

1733 Measurements of the weak boson production in heavy-ion collisions have been performed  
 1734 by the LHC experiments. The latest results have been derived from p-Pb collisions  
 1735 at  $\sqrt{s_{\text{NN}}} = 5.02 \text{ TeV}$  and Pb-Pb collisions at  $\sqrt{s_{\text{NN}}} = 2.56 \text{ TeV}$  and  $\sqrt{s_{\text{NN}}} = 5.02 \text{ TeV}$ . This  
 1736 subsection gives a brief summary on some of the results.

1737 **Pb-Pb results.** The CMS [160, 161] and ATLAS [162, 163] collaboration measured  
 1738 the W- and Z-boson production in Pb-Pb collisions at  $\sqrt{s_{\text{NN}}} = 2.56 \text{ TeV}$  in the lepton  
 1739 decay channel. The ATLAS and CMS measurements were performed in the mid-rapidity

### 3.1. INTRODUCTION

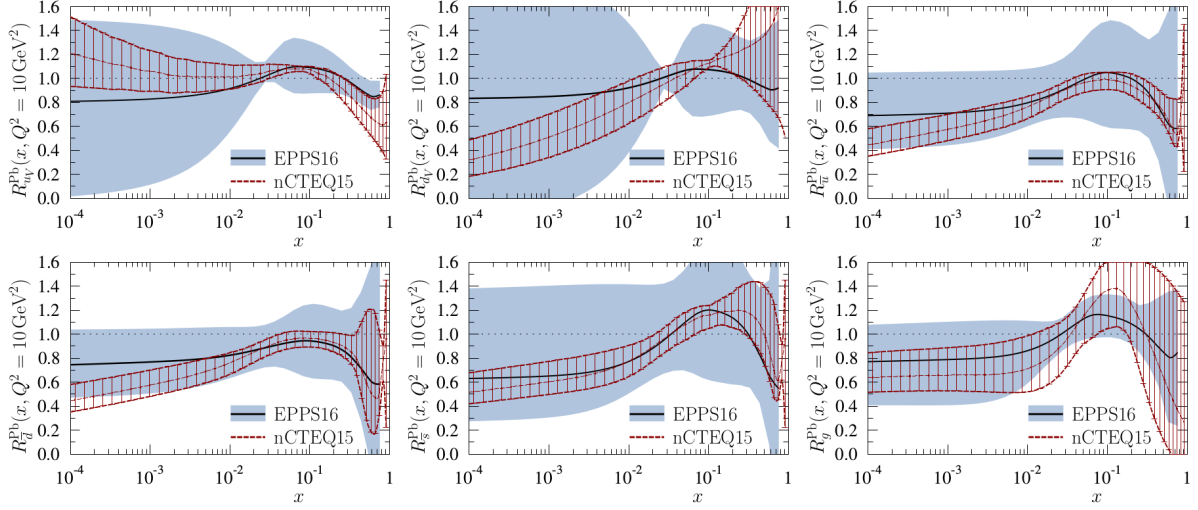


Figure 3.9: Comparison between the EPPS16 (black curve with blue band) and the nCTEQ15 (red curves with hatching) nuclear modifications performed at  $Q^2 = 10 \text{ GeV}^2$ . Figure taken from Ref. [158].

nPDF	EPS09	EPPS16	nCTEQ15
Order	NLO	NLO	NLO
Fit	nuclear modification	nuclear modification	nuclear PDF
Baseline PDF	CTEQ6	CT14	
Free parameters	15	20	17
Data points	929	1811	708
EMC DY dileptons in p-A	Yes	Yes	Yes
RHIC pions in d-A	Yes	Yes	Yes
SLAC $l^\pm$ -A DIS	Yes	Yes	Yes
CHORUS $\nu$ -A DIS	No	Yes	No
RHIC DY in $\pi$ -A	No	Yes	No
LHC dijets in pPb	No	Yes	No
LHC weak bosons in pPb	No	Yes	No

Table 3.2: Summary of the information of EPS09, EPPS16 and nCTEQ15 nuclear PDFs.

1740 region ( $|y| < 2.5$ ). The results are in good agreement with NLO pQCD calculations with  
 1741 and without nuclear PDF corrections. Moreover, the centrality dependence of the weak  
 1742 boson yields is observed to scale with  $N_{\text{coll}}$ , within uncertainties. In the case of W boson,  
 1743 the lepton charge asymmetry of  $W^\pm$ , defined as  $(N_\ell^+ - N_\ell^-)/(N_\ell^+ + N_\ell^-)$ , is found to be  
 1744 different from the results in p-p collisions, but this is understood to be simply associated  
 1745 to the different number of protons and neutrons in the Pb nuclei, the isospin effect. The

statistical precision of the results is not enough to provide significant constraints on the global fits to the PDFs.

Measurements from the ALICE collaboration on the production of Z bosons in Pb-Pb at  $\sqrt{s_{NN}} = 5.20 \text{ TeV}$  complements the forward rapidity region ( $2.5 < y < 4.0$ ). The ALICE results are in good agreement with model calculations including nuclear PDF corrections. On the contrary, the proton PDF calculations assuming only isospin effects deviates from the results by at most 3 standard deviations in the most central Pb-Pb collisions [164], starting to be sensitive to nuclear effects in the forward (low Bjorken-x) region.

**p-Pb results.** The ATLAS collaboration has measured the Z-boson production in p-Pb collisions at  $\sqrt{s_{NN}} = 5.02 \text{ TeV}$ . The Z-boson cross section as a function of the Z-boson rapidity determined in the centre-of-mass frame, is displayed in Figure 3.10. The results are better described by the PDF model calculations including nuclear modifications, although the free-proton PDF calculations are not excluded within the precision of the measurement.

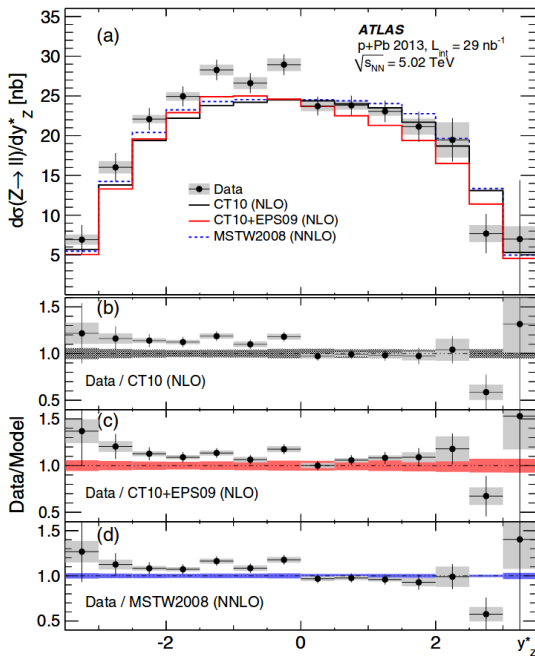


Figure 3.10: Distribution of the production cross section for  $Z \rightarrow \mu^+ \mu^-$  measured as a function of the Z-boson rapidity measured in the centre-of-mass frame. Figure taken from Ref. [165].

The CMS and ALICE collaboration have published results on the production of W bosons in p-Pb collisions at  $\sqrt{s_{NN}} = 5.02 \text{ TeV}$ . The measurements of the W-boson

### 3.1. INTRODUCTION

1762 production cross section performed by the ALICE collaboration, as a function of the  
 1763 lepton rapidity in the centre-of-mass frame, are shown in Figure 3.11. The ALICE results  
 1764 are compared to NLO calculations using the CT10 proton PDF and NNLO calculations  
 1765 using the FEWZ generator and the MSTW200 proton PDF, with and without EPS09  
 1766 nuclear PDF corrections. The cross section results are found to be in good agreement with  
 1767 the NLO model calculations while NNLO calculations without nuclear PDF modifications  
 1768 slightly overestimate the measurement at forward lepton rapidity ( $2.03 < |y_{\text{cms}}| < 3.53$ ).

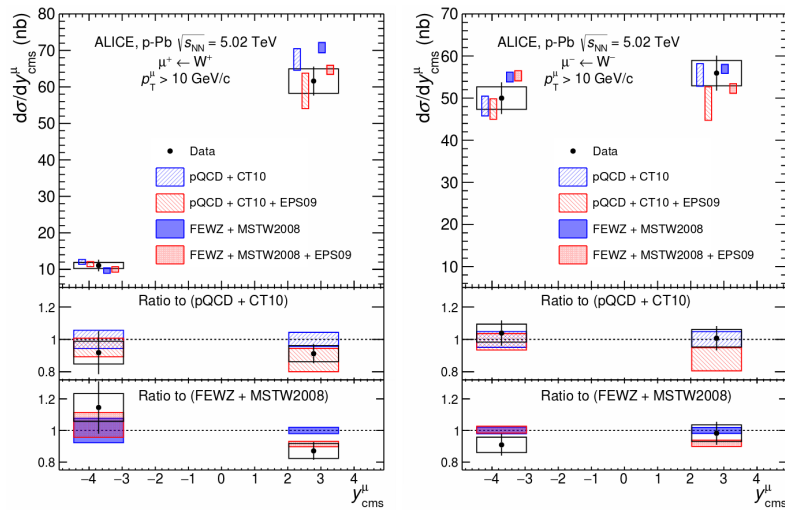


Figure 3.11: Distribution of the production cross section for  $W^- \rightarrow \mu^- \bar{\nu}_\mu$  (left) and  $W^+ \rightarrow \mu^+ \bar{\nu}_\mu$  (right) measured as a function of the muon rapidity in the centre-of-mass frame. Figure taken from Ref. [166].

1769 Finally, the W-boson measurements of CMS are performed in the muon and electron  
 1770 decay channels as a function of the lepton pseudorapidity in the laboratory frame [167].  
 1771 Figure 3.12 shows the measured cross sections for  $W^- \rightarrow \ell^- \bar{\nu}_\ell$  (left) and  $W^+ \rightarrow \ell^+ \nu_\ell$  (mid-  
 1772 dle), and the lepton charge asymmetry (right), compared to the NLO pQCD calculations  
 1773 using the CT10 proton PDF with and without EPS09 nuclear corrections. Both theoret-  
 1774 ical calculations are found to be in good agreement with the measured cross sections  
 1775 within uncertainties, except in the backward region ( $\eta_{\text{lab}} < -1.0$ ) for  $W^-$  bosons, where a  
 1776 small excess is seen in the results. The small deviation is also reflected in the measured  
 1777 lepton charge asymmetry, where the model calculations overestimate the data in the  
 1778 region  $-2.0 < \eta_{\text{lab}} < -1.0$ . It was suggested at the time that the small dis-agreement  
 1779 between the PDF calculations and the data could be due to different flavour dependence  
 1780 between the up and down quark PDFs [167].

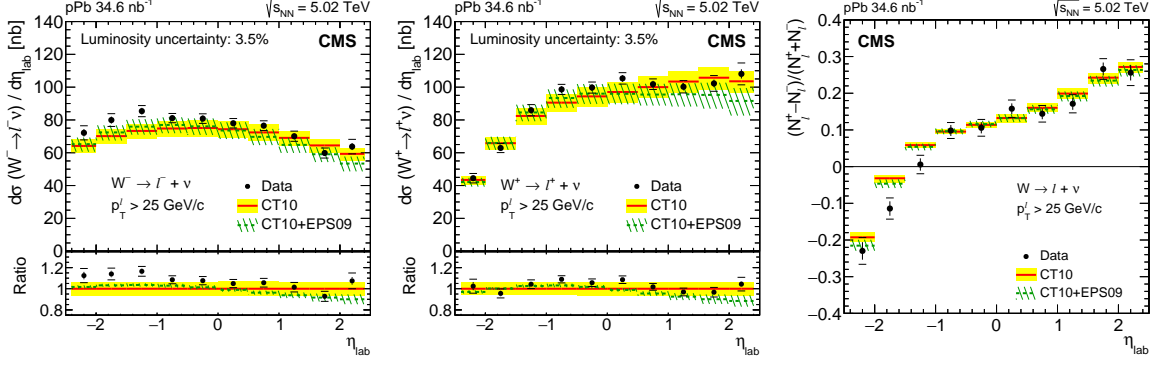


Figure 3.12: Distribution of the production cross section for  $W^- \rightarrow \ell^- \bar{\nu}_\ell$  (left) and  $W^+ \rightarrow \ell^+ \nu_\ell$  (middle), and the lepton charge asymmetry (right) measured as a function of the lepton pseudorapidity in the laboratory frame. The CT10 PDF calculations with EPS09 (green line) and without (red line) nuclear PDF corrections are included. The bottom panels present the ratio of the CT10+EPS09 (green line) and data (black points) normalised to the CT10 baseline. Figure taken from Ref. [167].

## 3.2 Analysis

In this section, the analysis of the W-boson production in p-Pb collisions at  $\sqrt{s_{NN}} = 8.16$  TeV, is described. The measurement is performed in the  $W^\pm \rightarrow \mu^\pm \nu_\mu$  decay channel using data recorded with the CMS detector and the signal event yields are extracted from the missing transverse momentum  $p_T^{\text{miss}}$  distributions. The analysis is currently in the final stage of the internal collaboration review and will be submitted to a peer-review journal in the near future.

The dataset used is introduced in Section 3.2.1, the NLO simulations for the signal and background processes are listed in Section 3.2.2, and the event selection is described in Section 3.2.3. The corrections for the simulated weak boson  $p_T$  and the  $p_T^{\text{miss}}$  are explained in Section 3.2.4 and Section 3.2.5, respectively. The measurement of the signal efficiency is presented in Section 3.2.6 and the extraction of the signal event yields is detailed in Section 3.2.7. The observables of the analysis are introduced in Section 3.2.8. In Section 3.2.9, the different sources of systematic uncertainties and the methods employed to estimate them are presented.

### 3.2.1 Dataset

The production of W bosons is measured in p-Pb collisions using data recorded by the CMS detector at the end of 2016. The dataset employed in this analysis is composed of

1799 events selected by the HLT trigger, requiring the presence of at least one identified muon  
 1800 candidate with  $p_T > 12 \text{ GeV}/c$ . The data were reconstructed with CMSSW 8.0.30 and  
 1801 thoroughly validated by the CMS collaboration. Only sections of the dataset, recorded  
 1802 with all CMS subdetectors operating in optimal conditions, were processed. The total  
 1803 integrated luminosity of the recorded data corresponds to  $173.4 \text{ nb}^{-1}$ , currently known  
 1804 within 3.5% [168].

1805 The p-Pb data-taking period was divided in two parts, as explained in Section 2.1.5.  
 1806 In the first part of the p-Pb run (labelled as Ppb), the proton beam was circulating in the  
 1807 clockwise direction along the LHC ring, while in the second part (referred as pPb), the  
 1808 proton beam was circulating counter-clockwise. The integrated luminosity recorded in  
 1809 the Ppb and pPb runs was  $62.6 \text{ nb}^{-1}$  and  $110.8 \text{ nb}^{-1}$ , respectively.

1810 Since the LHC dipole magnets apply the same magnetic rigidity (i.e. momentum-  
 1811 to-charge ratio) to both beams [169], the energy of the Pb beam is constrained by the  
 1812 energy of the proton beam  $E_p$ , and the number of nucleons ( $A_{\text{Pb}} = 208$ ) and electric  
 1813 charge ( $Z_{\text{Pb}} = 82$ ) of the Pb nucleus. During the entire p-Pb run, the energy of the proton  
 1814 beam was 6.50 TeV and as a result, the energy per nucleon  $E_{\text{Pb}}$  of the Pb beam was then:

$$E_{\text{Pb}} = \frac{Z_{\text{Pb}}}{A_{\text{Pb}}} \times E_p = 2.56 \text{ TeV} \quad (3.17)$$

1815 In addition, the energy of the nucleon-nucleon collisions in the centre-of-mass (CM)  
 1816 frame can be derived in this case using:

$$\sqrt{s_{\text{NN}}} = 2 \sqrt{\frac{Z_{\text{Pb}}}{A_{\text{Pb}}} \times E_p} = 8.16 \text{ TeV} \quad (3.18)$$

1817 Considering that the CMS detector is rapidity-symmetric with respect to the beam  
 1818 orientation, the pPb and Ppb samples are merged in order to maximize the statistics of  
 1819 the data. This is done by first flipping the sign of the pseudorapidity of particles from  
 1820 the Ppb sample measured in the laboratory frame, and then combining them with the  
 1821 events from the pPb sample. The combined samples corresponds to p-Pb collisions with  
 1822 the proton always going toward positive pseudorapidity. From hereafter, all results in  
 1823 this analysis are derived using the combined pPb sample.

1824 Due to the energy difference between the p-Pb colliding beams, the nucleon-pair CM  
 1825 frame is not at rest with respect to the laboratory frame. Massless particles emitted in  
 1826 the CM frame experience a constant longitudinal boost given by:

$$|\Delta\eta| = \frac{1}{2} \times \left| \ln \left( \frac{Z_{\text{Pb}}}{A_{\text{Pb}}} \right) \right| = 0.465 \quad (3.19)$$

1827 As a consequence, the pseudorapidity measured in the CM frame ( $\eta_{\text{CM}}$ ) is derived  
 1828 from the one determined in the laboratory frame ( $\eta_{\text{lab}}$ ), in the following way:

$$\eta_{\text{CM}} = \eta_{\text{lab}} - 0.465 \quad (3.20)$$

### 1829 3.2.2 Next-to-leading order simulations

1830 Fully reconstructed Monte Carlo (MC) simulations are used to describe the W-boson  
 1831 signal, and the top-quark and electroweak background processes. The MC samples were  
 1832 generated at NLO using the PPositive Weight Hardest Emission Generator (POWHEG)  
 1833 version 2 [170–172]. To account for QCD and electroweak theory corrections, the POWHEG-  
 1834 BOX packages  $W_{\text{ew}}\text{-BMMNP}$  [173] and  $Z_{\text{ew}}\text{-BMMNPV}$  [174] were used to generate the  
 1835  $p\bar{p} \rightarrow W \rightarrow \ell\nu_\ell$  and  $p\bar{p} \rightarrow Z/\gamma^* \rightarrow \ell^+\ell^-$  processes, respectively. The  $p\bar{p} \rightarrow t\bar{t}$  was generated  
 1836 using the POWHEG-BOX package hvq [175], which is a heavy flavour quark generator at  
 1837 NLO QCD.

1838 In order to simulate p-Pb collisions, I added to the POWHEG Fortran code a subroutine  
 1839 that modifies the PDFs of one of the incoming particles (referred as the Pb nucleus) by  
 1840 applying the EPPS16 nuclear correction factors derived for  $\text{Pb}^{82+}$  nuclei <sup>2</sup> [158], since  
 1841 the standard POWHEG framework only generates p-p collision events. In this case, the  
 1842 POWHEG event generation starts by evaluating the PDFs associated to both incoming  
 1843 particles (proton and Pb nucleus) using the NLO CT14 PDF set [150]. Afterwards, the  
 1844 PDFs corresponding to the Pb nucleus are modified with my subroutine, following the  
 1845 procedure defined in Ref. [158] and described in the following steps:

1846 1. The EPPS16 nuclear correction factors  $R$  are applied to the PDFs computed by  
 1847 POWHEG, in the following way:

$$\begin{aligned} \hat{f}_p^d &= R_s^d f_p^{\bar{d}} + R_v^d (f_p^d - f_p^{\bar{d}}) & ; \quad \hat{f}_p^{\bar{d}} &= R_s^d f_p^{\bar{d}} \\ \hat{f}_p^u &= R_s^u f_p^{\bar{u}} + R_v^u (f_p^u - f_p^{\bar{u}}) & ; \quad \hat{f}_p^{\bar{u}} &= R_s^u f_p^{\bar{u}} \\ \hat{f}_p^x &= R_s^x f_p^x & ; \quad \hat{f}_p^{\bar{x}} &= R_s^x f_p^{\bar{x}} \quad \text{where } x = \{s, c, b\} \\ \hat{f}_p^g &= R_g^g f_p^g \end{aligned} \quad (3.21)$$

1848 where  $\hat{f}_p$  represent the PDFs of a proton bound in the Pb nucleus,  $f_p$  are the free  
 1849 proton PDFs obtain with NLO CT14, and  $R_s^x$ ,  $R_v^x$  and  $R_g^g$  are the EPPS16 nuclear  
 1850 correction factors for sea quarks, valence quarks and gluons, accordingly.

---

<sup>2</sup>The EPPS16 nuclear correction factors for each nuclei can be found in <https://www.jyu.fi/science/en/physics/research/highenergy/urhic/npdfs/epps16-nuclear-pdfs>

- 1851    2. The bound neutron PDFs ( $\hat{f}_n$ ) are then derived from the bound proton PDFs, by  
 1852    interchanging the up and down (anti-)quark PDFs (isospin symmetry between  
 1853    protons and neutrons), according to:

$$\begin{aligned}\hat{f}_n^d &= \hat{f}_p^u & ; \quad \hat{f}_n^u &= \hat{f}_p^d \\ \hat{f}_n^{\bar{d}} &= \hat{f}_p^{\bar{u}} & ; \quad \hat{f}_n^{\bar{u}} &= \hat{f}_p^{\bar{d}}\end{aligned}\tag{3.22}$$

1854    and assuming the same PDFs ( $\hat{f}_n^i = \hat{f}_p^i$ ) for the other flavours.

- 1855    3. The bound proton and neutron PDFs are combined to form the Pb-nucleus PDFs  
 1856    ( $f_{Pb}$ ), taking into account the number of protons ( $Z_{Pb}$ ) and neutrons ( $N_{Pb} = A_{Pb} -$   
 1857     $Z_{Pb}$ ) in the Pb nucleus, as done in:

$$\begin{aligned}f_{Pb}^d &= \left(\frac{Z_{Pb}}{A_{Pb}}\right) \hat{f}_p^d + \left(\frac{N_{Pb}}{A_{Pb}}\right) \hat{f}_n^d & ; \quad f_{Pb}^{\bar{d}} &= \left(\frac{Z_{Pb}}{A_{Pb}}\right) \hat{f}_p^{\bar{d}} + \left(\frac{N_{Pb}}{A_{Pb}}\right) \hat{f}_n^{\bar{d}} \\ f_{Pb}^u &= \left(\frac{Z_{Pb}}{A_{Pb}}\right) \hat{f}_p^u + \left(\frac{N_{Pb}}{A_{Pb}}\right) \hat{f}_n^u & ; \quad f_{Pb}^{\bar{u}} &= \left(\frac{Z_{Pb}}{A_{Pb}}\right) \hat{f}_p^{\bar{u}} + \left(\frac{N_{Pb}}{A_{Pb}}\right) \hat{f}_n^{\bar{u}} \\ f_{Pb}^i &= \hat{f}_p^i & \text{for other flavours}\end{aligned}\tag{3.23}$$

- 1858    4. The PDFs originally derived by POWHEG are then replaced with the modified PDFs  
 1859    defined in Eq. (3.23), and the rest of the event generation is done with the standard  
 1860    POWHEG framework with no further changes.

1861    The parton showering is performed by hadronizing the POWHEG events with PYTHIA  
 1862    8.212 [176], using the CUETP8M1 underlying event (UE) tune [176, 177]. The full CMS  
 1863    detector response is simulated in all MC samples, based on GEANT4 [178], considering  
 1864    a realistic alignment and calibration of the beam spot and the different subdetectors  
 1865    of CMS, tuned on data. The MC events are reconstructed with the standard CMS p-p  
 1866    reconstruction software used during 2016 data taking.

1867    To consider a more realistic distribution of the underlying environment present in  
 1868    p-Pb collisions, the MC signal events were embedded in a minimum bias (i.e. inelastic  
 1869    hadronic interactions) sample generated with EPOS LHC [179], taking into account both  
 1870    p-Pb boost directions. The EPOS LHC MC samples were tuned to reproduce the global  
 1871    event properties of the p-Pb data such as the charged-hadron transverse momentum  
 1872    spectrum and the particle multiplicity [180]. The list of simulated samples and the cross  
 1873    sections used in this analysis are summarized in Table 3.3. The cross sections of the  
 1874    electroweak processes corresponds to the POWHEG NLO cross sections scaled by  $A_{Pb}$ ,

1875 while the  $t\bar{t}$  cross section is taken from the inclusive cross section measured in pPb  
 1876 collisions at  $\sqrt{s_{NN}} = 8.16 \text{ TeV}$  by the CMS collaboration [181].

Process	Cross section [nb]	Generated events
$p\text{Pb} \rightarrow W^+ \rightarrow \mu^+ \nu_\mu$	1214	982714
$p\text{pb} \rightarrow W^+ \rightarrow \mu^+ \nu_\mu$	1214	981874
$p\text{Pb} \rightarrow W^- \rightarrow \mu^- \bar{\nu}_\mu$	1083	995726
$p\text{pb} \rightarrow W^- \rightarrow \mu^- \bar{\nu}_\mu$	1083	998908
$p\text{Pb} \rightarrow W^+ \rightarrow \tau \nu_\tau$	1147	481125
$p\text{pb} \rightarrow W^+ \rightarrow \tau \bar{\nu}_\tau$	1147	500000
$p\text{Pb} \rightarrow W^- \rightarrow \tau \bar{\nu}_\tau$	1023	495450
$p\text{pb} \rightarrow W^- \rightarrow \tau \bar{\nu}_\tau$	1023	498092
$p\text{Pb} \rightarrow Z/\gamma^* \rightarrow \mu^+ \mu^-$	266	1000000
$p\text{pb} \rightarrow Z/\gamma^* \rightarrow \mu^+ \mu^-$	266	1000000
$p\text{pb} \rightarrow Z/\gamma^* \rightarrow \tau \bar{\tau}$	259	498444
$p\text{Pb} \rightarrow t\bar{t}$	$45 \pm 8$	99578
$p\text{pb} \rightarrow t\bar{t}$	$45 \pm 8$	100000

Table 3.3: Simulated NLO samples used for the W-boson measurement in p-Pb at 8.16 TeV. The listed cross sections are the POWHEG NLO cross sections scaled by  $A_{\text{Pb}} = 208$ , except for the  $t\bar{t}$  production cross section which is taken from the CMS measurement in p-Pb at 8.16 TeV [181].

1877 The pPb and Pbp simulated samples are also combined in the same way as done for  
 1878 data, but the generated events are weighed before merging the samples by applying a  
 1879 global weight, according to their p-Pb boost direction, defined as:

$$w_{\text{MC}} = \frac{\sigma \times \mathcal{L}_{\text{data}}}{N_{\text{gen}}} \quad (3.24)$$

1880 where  $\mathcal{L}_{\text{data}}$  corresponds to the integrated luminosity recorded in each proton-lead  
 1881 run ( $110.8 \text{ nb}^{-1}$  for pPb and  $62.6 \text{ nb}^{-1}$  for Pbp),  $\sigma$  is the cross section associated to the  
 1882 simulated process (listed in Table 3.3) and  $N_{\text{gen}}$  is the total number of generated events.  
 1883 The global weighing is applied to ensure that each MC sample is normalised to the  
 1884 corresponding integrated luminosity of the data.

### 1885 3.2.3 Event selection

1886 The signal events, determined by the process  $W \rightarrow \mu\nu_\mu$ , are characterised by a high-  
 1887  $p_T$  muon and the presence of missing transverse momentum  $p_T^{\text{miss}}$ , originated from  
 1888 the undetected neutrino. Events with similar characteristics can be produced by other

1889 background processes, such as semi-leptonic decays of hadrons formed within jets or  
1890 dilepton decays of Z bosons. This section explain the different selections implemented to  
1891 suppress the background while keeping the signal.

1892 **3.2.3.1 p-Pb global filter**

1893 In order to ensure that the samples are not contaminated by events not originating from  
1894 the inelastic hadronic collisions, a standard p-Pb Global Event Filter (GEF) is applied.  
1895 The different selections included in the p-Pb GEF are described below:

- 1896 • Primary vertex filter: requires the presence of a primary vertex reconstructed from  
1897 at least two tracks, within a longitudinal (transverse) distance of 25 cm (2 cm) of  
1898 the nominal interaction point. This selection reduces the contamination from non-  
1899 collision backgrounds, such as cosmic-ray muons or accelerator-induced particles.
- 1900 • HF coincidence filter: requires at least one tower on each side of the interaction  
1901 point in the Hadron-Forward calorimeter, with an energy deposit per tower of  
1902 at least 3 GeV. This filter rejects events from electronic noise and beam-beam  
1903 electromagnetic interactions.
- 1904 • Beam-scraping filter: requires at least 25% of tracks in the event to be high quality  
1905 tracks. This requirement is used to further suppress the contribution from beam-  
1906 related backgrounds, such as beam-gas interactions and beam-halo events.

1907 The impact of the GEF was checked both in data and simulation. Only 0.08% of  
1908 events in data and 0.06% of events in the  $W \rightarrow \mu\nu_\mu$  simulation, passing all analysis  
1909 selections summarized in Section 3.2.3.5, were removed by the filter.

1910 **3.2.3.2 Trigger**

1911 The events used in this analysis were selected online with the HLT trigger HLT\_PAL3Mu12.  
1912 This trigger requires a fully reconstructed L3 muon with  $p_T > 12$  GeV/c. The HLT trigger  
1913 was seeded with the L1 trigger path L1\_SingleMu7, which pass events with at least  
1914 one L1 muon with  $p_T > 7$  GeV/c. It is to be noted that only muons of  $p_T$  greater than  
1915 25 GeV/c are considered in the offline analysis, and that this trigger is extremely efficient  
1916 for those.

1917 A reconstructed muons is considered matched to the trigger, if it matches the L3  
1918 muon that fired the trigger. The matching criteria between the reconstructed muon and  
1919 the L3 muon requires:

$$\Delta R(\mu_{\text{reco}}, \mu_{\text{HLT}}) = \sqrt{(\eta_{\text{reco}}^\mu - \eta_{\text{HLT}}^\mu)^2 + (\phi_{\text{reco}}^\mu - \phi_{\text{HLT}}^\mu)^2} < 0.1 \quad (3.25)$$

### 3.2.3.3 Muon selection

Muon candidates are identified using a standard *tight* selection, optimised for muons with high  $p_T$ . The tight selection requires muon candidates to be reconstructed globally from hits in the muon stations and the tracker, be identified with the PF algorithm [111] and pass the following criteria:

- The muon track fit has at least a  $\chi^2$  per degree of freedom less than ten, ensuring a minimal fit quality.
- The muon track segments are matched to at least two muon stations, making the selection consistent with the muon trigger logic.
- The transverse impact parameter (longitudinal distance) of the muon track is consistent with the primary vertex within 2 mm (5 mm), to reduce the background from cosmic rays and muon decays in flight (e.g. from pion, kaon and heavy-flavour hadron decays).
- The muon track has at least one hit in the pixel detector to further suppress muons from decays in flight.
- The muon track includes hits in at least six inner-tracker layers to guarantee a good  $p_T$  measurement.

Apart from the *tight* identification criteria, muon candidates are also required to be isolated in order to reduce the proportion of muons coming from jets. Muons are considered isolated if the sum of the  $p_T$  of all PF-identified photons, charged hadrons and neutral hadrons, within a cone of  $\Delta R(\mu, \text{PF}) < 0.3$ , is less than 15% of the muon  $p_T^\mu$ . The muon isolation variable is thus defined as:

$$I^\mu = \left( \sum_{\text{charged hadrons}}^{\Delta R < 0.3} p_T + \sum_{\text{neutral hadrons}}^{\Delta R < 0.3} p_T + \sum_{\text{photons}}^{\Delta R < 0.3} p_T \right) / p_T^\mu \quad (3.26)$$

Finally, muon candidates are required to have  $p_T > 25 \text{ GeV}/c$  and be within  $|\eta_{\text{lab}}| < 2.4$ . If more than one muon is found with  $p_T > 25 \text{ GeV}/c$  and passing the identification criteria in a given event, then the corresponding muon with the highest  $p_T$  is used. This happens in 3% of events in data but are later suppressed down to 0.001% of events with the  $Z/\gamma^* \rightarrow \mu^+ \mu^-$  veto described in the next section.

1947 **3.2.3.4  $Z/\gamma^* \rightarrow \mu^+ \mu^-$  veto**

1948 A veto is applied to suppress the contribution from  $Z/\gamma^* \rightarrow \mu^+ \mu^-$  background events. This  
 1949 veto consists in removing events that contain at least two opposite-sign muons with  
 1950  $p_T > 15$  GeV/c, each passing the muon identification and isolation criteria.

1951 The probability that  $Z/\gamma^* \rightarrow \mu^+ \mu^-$  events survive the veto is checked using simulation.  
 1952 The denominator of the  $Z/\gamma^* \rightarrow \mu^+ \mu^-$  veto efficiency is filled with muons passing the  
 1953 signal selection criteria summarised in the next section, while the numerator is filled  
 1954 with the same muons as long as the event pass the  $Z/\gamma^* \rightarrow \mu^+ \mu^-$  veto. The simulated  
 1955 survival probability is shown in Figure 3.13. As can be observed, most of the  $Z/\gamma^* \rightarrow \mu^+ \mu^-$   
 1956 events that survive the veto mainly contributes in the forward pseudorapidity region,  
 1957 where one of the muons from the  $Z/\gamma^*$ -boson decay escapes the detector.

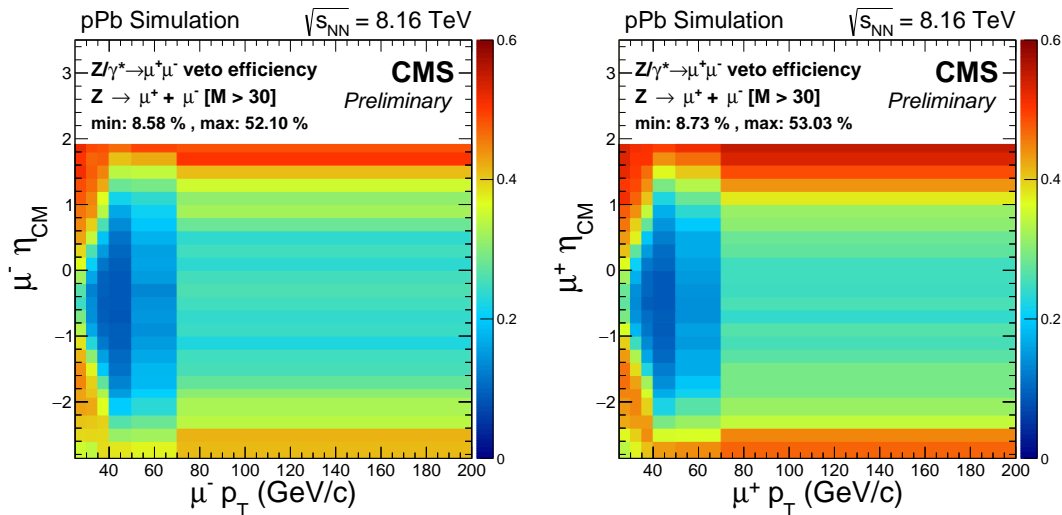


Figure 3.13: Survival probability of single muons from a  $Z/\gamma^* \rightarrow \mu^+ \mu^-$  ( $M > 30$  GeV/c $^2$ ) simulation, as a function of the muon  $\eta_{CM}^\mu$  and  $p_T^\mu$ , separated in negative (left) and positive (right) charged muons. Muons are required to have  $p_T > 25$  GeV/c and  $|\eta| < 2.4$ , match the trigger and pass the isolation and identification criteria.

1958 **3.2.3.5 Event selection summary**

1959 In summary, the signal selection consists of the detection of a high- $p_T$  muon, passing the  
 1960 identification criteria detailed in Section 3.2.3.3. The muon candidate is required to have  
 1961  $p_T > 25$  GeV/c, be isolated and match the trigger (see Section 3.2.3.2). The events entering  
 1962 the signal region are also required to satisfy the p-Pb global event filter (Section 3.2.3.1)  
 1963 and the  $Z/\gamma^* \rightarrow \mu^+ \mu^-$  veto (Section 3.2.3.4).

1964 The other signature of a  $W \rightarrow \mu\nu_\mu$  event is a high- $p_T$  neutrino, estimated through the  
 1965  $p_T^{\text{miss}}$ . No explicit selection is applied on the missing transverse momentum. The  $p_T^{\text{miss}}$  is  
 1966 directly used to extract the event yields by fitting the signal and background components.  
 1967 Apart from the main signal sample, two more samples are used:

- 1968 •  $Z \rightarrow \mu^+ \mu^-$  control sample: selects  $Z \rightarrow \mu^+ \mu^-$  events by reverting the  $Z/\gamma^* \rightarrow \mu^+ \mu^-$   
 1969 veto and selecting  $\mu^+ \mu^-$  pairs with invariant mass within the  $Z$ -boson mass window.  
 1970 Used to derive corrections for the weak boson  $p_T$  (Section 3.2.4) and the  $p_T^{\text{miss}}$   
 1971 (Section 3.2.5).
- 1972 • QCD jet control sample: selects non-isolated muon events by reverting the muon  
 1973 isolation cut. Used to determine the shape of the QCD jet background from data.

1974 The conditions used to define the signal and control regions of interest are illustrated  
 1975 in Figure 3.14.

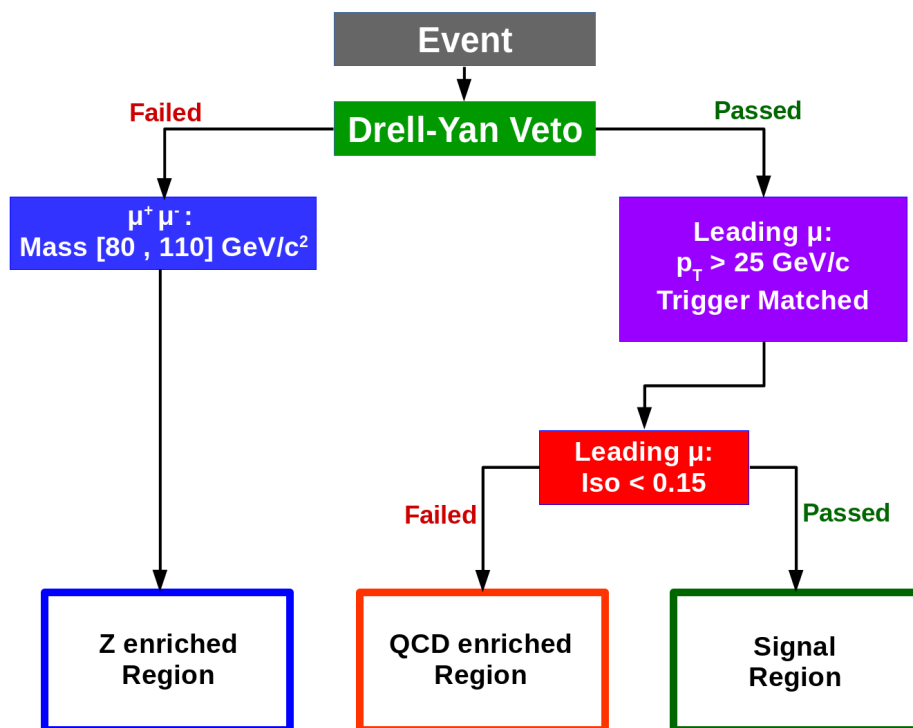


Figure 3.14: Flowchart illustrating the way the events are classified

### 1976 3.2.4 Correction for weak-boson transverse momentum

1977 In a p-Pb collision at high energies, the partons can be described as moving collinearly  
 1978 with the proton or the Pb nucleus, contributing momentum only along the beam axis. As  
 1979 a result, at leading order, W and Z bosons are produced with no transverse momentum.  
 1980 Higher order processes, such as NLO or next-to-NLO, can radiate quarks and gluons  
 1981 that recoil against the weak boson, which acquires transverse momentum in the process.

1982 Since the simulations were produced using the POWHEG NLO generator, the absence  
 1983 of higher order contributions can lead to a mismodelling of the weak boson  $p_T$ , which can  
 1984 then affect the  $p_T$  distribution of the boson decay products (e.g. muon and neutrino). To  
 1985 check this, one can select  $Z \rightarrow \mu^+ \mu^-$  events and compare the  $p_T$  distribution of Z boson  
 1986 candidates from simulation and data.

1987 The  $p_T$  distribution of Z bosons has been measured in an on-going CMS analysis of  
 1988 the Drell–Yan production in pPb collisions at 8.16 TeV<sup>3</sup>, which makes use of the same  
 1989 data and electroweak NLO simulations presented in this chapter. As part of the DY  
 1990 analysis, the measurement of the Z-boson  $p_T$  distribution in the dimuon mass region [60,  
 1991 120] GeV/ $c^2$  was compared, after correcting for acceptance and efficiency, to the generated  
 1992 one from POWHEG and found to disagree by up to 20%. To correct for the disagreement,  
 1993 the ratio between the measured and simulated  $p_T$ -differential  $Z \rightarrow \mu^+ \mu^-$  cross sections  
 1994 was parametrised as a function of the Z-boson  $p_T$ , resulting in:

$$w^Z(p_T) = \frac{\left(\frac{d\sigma[Z \rightarrow \mu^+ \mu^-]}{dp_T}\right)^{\text{data}}}{\left(\frac{d\sigma[Z \rightarrow \mu^+ \mu^-]}{dp_T}\right)^{\text{MC}}} = \frac{1}{1.19 - 0.37 \times p_T^{-0.37}} \quad (3.27)$$

1995 and the generated Z-boson  $p_T$  distribution was then weighed per event using  $w^Z(p_T)$ .

1996 Considering that Z and W bosons have similar production mechanisms and masses,  
 1997  $w^Z(p_T)$  is also used to weigh, on an event-by-event basis, the generated W-boson  $p_T$   
 1998 spectrum. The boson  $p_T$  weighing is applied to the POWHEG simulations of both signal  
 1999 ( $W \rightarrow \mu\nu_\mu$ ) and electroweak backgrounds ( $W \rightarrow \tau\nu_\tau$ ,  $Z/\gamma^* \rightarrow \mu^+ \mu^-$  and  $Z/\gamma^* \rightarrow \tau\bar{\tau}$ ).

2000 The impact of the boson  $p_T$  weighing is checked on a W-boson enhanced sample in  
 2001 data and simulation, made by applying a requirement on the transverse mass, defined  
 2002 as  $M_T = \sqrt{p_T^\mu \cdot p_T^{\text{miss}} \cdot (1 - \cos(\Delta\theta))}$ , where  $\Delta\theta$  is the azimuthal angle between the  $\vec{p}_T^{\text{miss}}$   
 2003 and muon  $\vec{p}_T^\mu$ . The events of the W-boson enhanced sample are selected from the signal  
 2004 region by requiring  $M_T > 60$  GeV/ $c$ , and the corresponding muon  $p_T$  distribution is then

<sup>3</sup>The details of the CMS Drell–Yan analysis can be checked in the private link <http://cms.cern.ch/iCMS/analysisadmin/cadilines?line=HIN-18-003&tp=an&id=2036&ancode=HIN-18-003>

2005 compared before and after applying the boson  $p_T$  weighing in Figure 3.15. The simulated  
 2006 muon  $p_T$  distribution is observed to describe better the data in the high- $p_T$  region  
 2007 ( $p_T^\mu \gtrsim 40$  GeV/c) after weighing the generated W-boson boson  $p_T$  distribution.

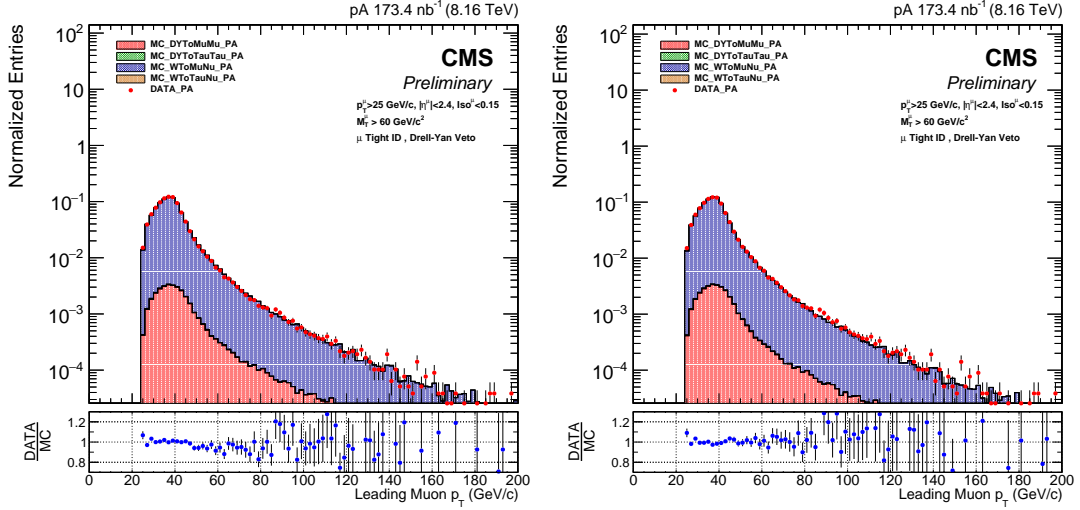


Figure 3.15: Muon  $p_T$  distribution extracted from the W-boson enhanced sample before (left) and after (right) applying the boson  $p_T$  weights. The red points correspond to data, while the blue and red filled areas correspond to events from the  $W \rightarrow \mu\nu_\mu$  and  $Z/\gamma^* \rightarrow \mu^+\mu^-$  simulations, respectively. The bottom panels shows the ratio of data over simulation.

### 3.2.5 Corrections for missing transverse momentum

2009 Since the W-boson analysis relies on  $p_T^{\text{miss}}$  distributions from simulations to extract the  
 2010 signal, it is important that the simulated  $p_T^{\text{miss}}$  describes the data. To achieve this, the  
 2011  $p_T$  distribution of the reconstructed particles, including those recoiling against the weak  
 2012 boson (referred as the recoil), have to be well modelled.

2013 The  $p_T^{\text{miss}}$  vector derived from  $W \rightarrow \mu\nu_\mu$  events can be decomposed, according to  
 2014 Eq. (2.5), in two parts: the  $p_T$  vector of the muon candidate ( $\vec{p}_T^\mu$ ) and the  $p_T$  vector of the  
 2015 recoil ( $\vec{u}_T$ ), as defined in:

$$\vec{p}_T^{\text{miss}} = -(\vec{u}_T + \vec{p}_T^\mu) \quad (3.28)$$

2016 The recoil  $\vec{u}_T$  is measured via the  $\vec{p}_T$  vectorial sum of all particles identified in an  
 2017 event with the PF algorithm *excluding* the muon from the W-boson decay, as given by:

$$\vec{u}_T = \left( \sum_{\text{particles}} \vec{p}_T \right) - \vec{p}_T^\mu \quad (3.29)$$

2018        The recoil is a complex quantity that includes particles from the hard scattering  
 2019 that balances the W-boson  $p_T$  and from the underlying event (e.g. spectator parton  
 2020 interactions and multiple parton scatterings), as well as effects related to the detector  
 2021 (e.g. electronic noise,  $p_T$  resolution, reconstruction efficiency and acceptance) and the  
 2022 accelerator (e.g. beam-beam remnants). As a result, the recoil is difficult to simulate  
 2023 precisely in p-Pb collisions and the mismodelling of the recoil  $u_T$  can affect the signal  
 2024 extraction.

2025        To improve the modelling of the  $p_T^{\text{miss}}$  in the signal region, the  $p_T^{\text{miss}}$  is corrected in  
 2026 two steps. First, the distribution of the simulated event activity measured as a function  
 2027 of the total energy deposited in the HF calorimeter (hereafter referred as the HF energy)  
 2028 is weighed to the level observed in data as detailed in Section 3.2.5.1. Afterwards, the  
 2029 simulated recoil is calibrated following the procedure described in Section 3.2.5.2.

### 2030     3.2.5.1 Event activity weighing

2031        The muon isolation and the  $p_T^{\text{miss}}$  are computed by summing over particles produced in  
 2032 the event. As a consequence, any disagreement in the modelling of the event activity (EA)  
 2033 can impact the muon efficiency and the signal extraction. The disagreement between  
 2034 data and the POWHEG simulations embedded in EPOS minimum bias events can be  
 2035 caused by the presence of hard probes such as W bosons, which bias the event activity  
 2036 towards higher particle multiplicity compared to minimum bias events.

2037        To check if the event activity is well modelled in the simulations, the distribution  
 2038 of the number of tracks per event and the HF energy is compared between data and  
 2039 simulation in a  $Z \rightarrow \mu^+ \mu^-$  control sample. The  $Z \rightarrow \mu^+ \mu^-$  events are selected by requiring  
 2040 a  $\mu^+ \mu^-$  pair within the invariant mass region  $80 < M_{\mu^+ \mu^-} < 110$  GeV/ $c^2$  as detailed in  
 2041 Section 3.2.3.5. The data-simulation comparisons are shown in Figure 3.16, and it is  
 2042 observed that the simulated samples are indeed not able to reproduce the event activity  
 2043 present in p-Pb data.

2044        The modelling of the event activity is improved using a set of weights determined  
 2045 from the ratio of the number of  $Z \rightarrow \mu^+ \mu^-$  events extracted from data and simulation in  
 2046 different bins of HF energy ( $E_{\text{HF}}$ ), as given by:

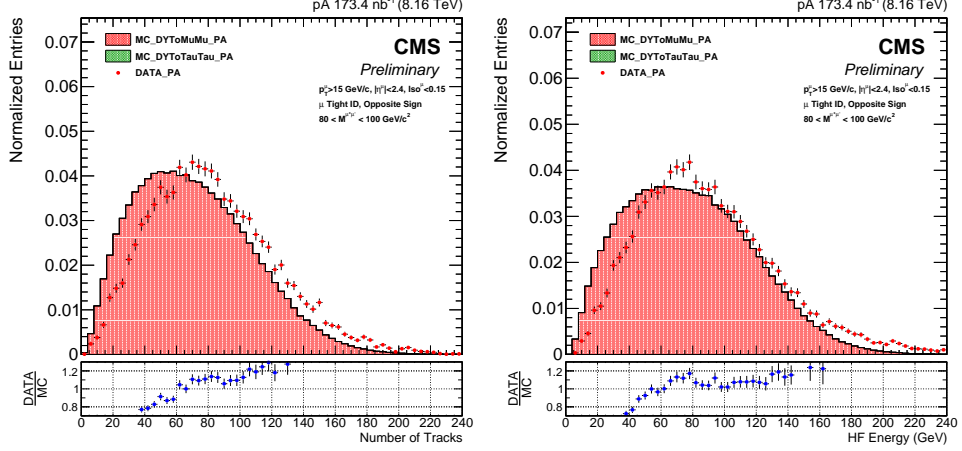


Figure 3.16: Distribution of the number of tracks per event (left) and the total energy deposited in the HF calorimeter (right) in  $Z \rightarrow \mu^+ \mu^-$  events. The red points and filled area correspond to data and  $Z/\gamma^* \rightarrow \mu^+ \mu^-$  simulation, respectively.

$$w^{\text{EA}}(E_{\text{HF}}) = \frac{N_{Z \rightarrow \mu^+ \mu^-}^{\text{data}}[E_{\text{HF}}]}{N_{Z \rightarrow \mu^+ \mu^-}^{\text{MC}}[E_{\text{HF}}]} \quad (3.30)$$

2047      The  $w^{\text{EA}}(E_{\text{HF}})$  weights are used, event-by-event, to weigh the HF energy distribution  
 2048      of the electroweak and  $t\bar{t}$  simulations. Figure 3.17 shows that the HF energy weighing  
 2049      improves the simulation-to-data agreement of the  $p_T^{\text{miss}}$  distribution of  $Z \rightarrow \mu^+ \mu^-$  events.  
 2050      The remaining level of disagreement in the  $p_T^{\text{miss}}$  is then corrected for by calibrating the  
 2051      simulated recoil as explained in the next section.

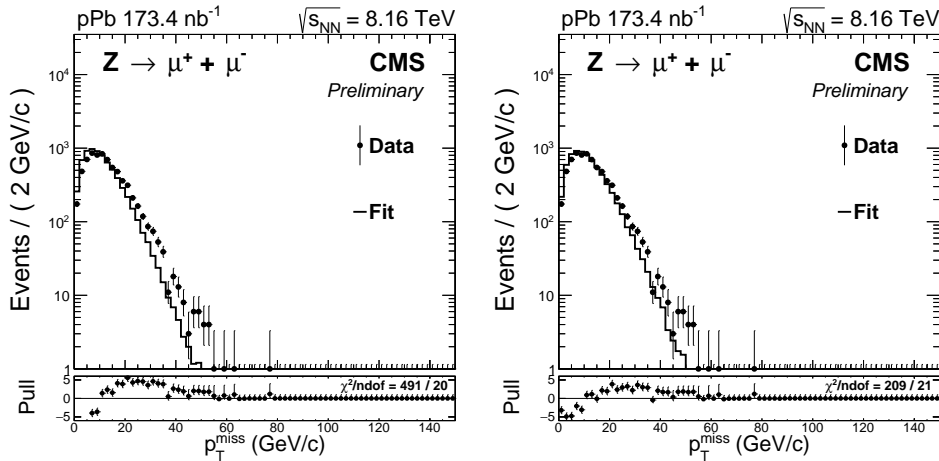


Figure 3.17: Comparison of the  $p_T^{\text{miss}}$  distribution in data and simulation for  $Z \rightarrow \mu^+ \mu^-$  events before (left) and after (right) applying the HF energy weights.

2052 **3.2.5.2 Recoil calibration**

2053 The recoil calibration procedure starts by measuring the recoil in  $Z \rightarrow \mu^+ \mu^-$  events in  
 2054 data and simulation, and then parametrise, in each sample, the components of the recoil  
 2055  $\vec{u}_T$  with respect to the transverse momentum of the  $Z$  boson ( $q_T^Z$ ). Afterwards, these  
 2056 parametrisations are used to scale in each event the simulated  $\vec{u}_T$  components according  
 2057 to the weak boson  $p_T$ , from each electroweak simulation, to match the average recoil  
 2058 distribution measured in data.

2059 The  $Z \rightarrow \mu^+ \mu^-$  control sample employed to extract the recoil calibration is the same  
 2060 as the one used to derive the event activity weights described in the previous section. In  
 2061 addition, the simulated HF energy and the generated  $Z$ -boson  $p_T$  distributions of the  
 2062 control sample have been weighed accordingly.

2063 **Extraction of the recoil scale and resolution.** Since there are no neutrinos pro-  
 2064 duced in the initial hard scattering of  $Z \rightarrow \mu^+ \mu^-$  events, the  $p_T^{\text{miss}}$  spectrum can be  
 2065 used to directly measure the  $p_T^{\text{miss}}$  resolution. Figure 3.18 compares the  $p_T^{\text{miss}}$  spectra  
 2066 extracted from data and simulation in the  $Z \rightarrow \mu^+ \mu^-$  control sample. It is observed that  
 2067 the simulation does not properly describe the  $p_T^{\text{miss}}$  distribution measured in data.

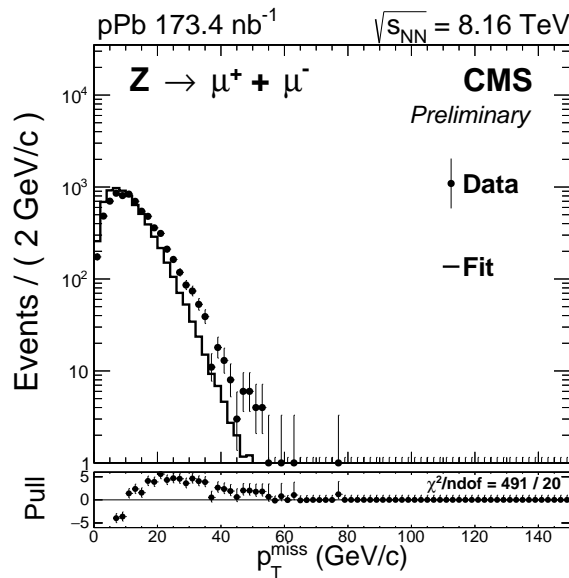


Figure 3.18: Distribution of the  $p_T^{\text{miss}}$  in data and simulation for  $Z \rightarrow \mu^+ \mu^-$  selected events.

2068 In the case of  $Z \rightarrow \mu^+ \mu^-$  events, the recoil  $\vec{u}_T$  is measured by *subtracting* the  $p_T$  vector  
 2069 of the  $Z$ -boson candidate ( $\vec{q}_T^Z = \vec{p}_T^{\mu^+} + \vec{p}_T^{\mu^-}$ ) from the  $\vec{p}_T^{\text{miss}}$ , according to:

$$\vec{u}_T = -\vec{p}_T^{\text{miss}} - \vec{q}_T^Z \quad (3.31)$$

2070 The recoil  $\vec{u}_T$  is then projected along the Z-boson  $\vec{q}_T^Z$  direction. The parallel and  
 2071 perpendicular components of  $\vec{u}_T$ , with respect to the  $\vec{q}_T^Z$ , are labelled as  $u_{\parallel}$  and  $u_{\perp}$ ,  
 2072 respectively. Figure 3.19 shows the components of the recoil in  $Z \rightarrow \mu^+ \mu^-$  events.

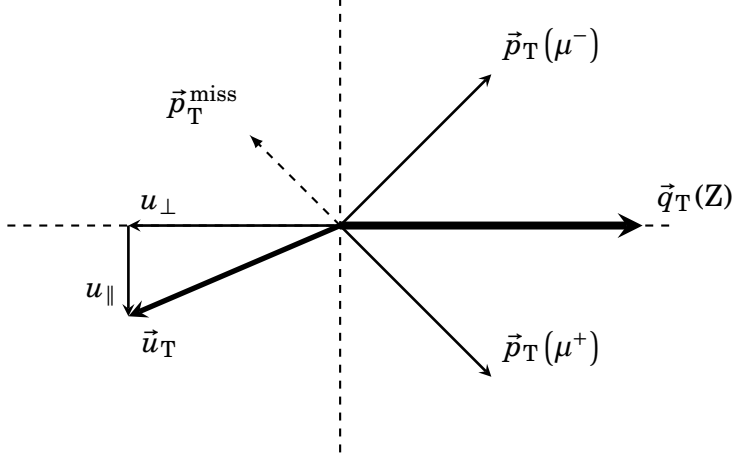


Figure 3.19: Definition and components of the recoil  $\vec{u}_T$  for  $Z \rightarrow \mu^+ \mu^-$  events.

2073 The  $u_{\parallel}$  and  $u_{\perp}$  recoil components are evaluated event-by-event and sorted in 30 bins  
 2074 of  $q_T^Z$  defined within the range  $0 < q_T^Z < 140$  GeV/c. The distributions of  $u_{\parallel}$  and  $u_{\perp}$  from  
 2075 data and simulation are fitted separately in each  $q_T^Z$  bin with a weighed sum of two  
 2076 Gaussian functions, according to:

$$F(u_{\parallel}) = N_{\parallel} \cdot \left( f_{\parallel} \cdot \exp \left[ \frac{(u_{\parallel} - \mu_{\parallel})^2}{2 \cdot \sigma_{\parallel,1}^2} \right] + (1 - f_{\parallel}) \cdot \exp \left[ \frac{(u_{\parallel} - \mu_{\parallel})^2}{2 \cdot \sigma_{\parallel,2}^2} \right] \right) \quad (3.32)$$

$$F(u_{\perp}) = N_{\perp} \cdot \left( f_{\perp} \cdot \exp \left[ \frac{(u_{\perp} - \mu_{\perp})^2}{2 \cdot \sigma_{\perp,1}^2} \right] + (1 - f_{\perp}) \cdot \exp \left[ \frac{(u_{\perp} - \mu_{\perp})^2}{2 \cdot \sigma_{\perp,2}^2} \right] \right)$$

2077 where  $N_{\parallel(\perp)}$  corresponds to the number of events in each  $q_T^Z$  bin,  $f_{\parallel(\perp)}$  is the weight of  
 2078 the Gaussian components,  $\mu_{\parallel(\perp)}$  is the mean of the Gaussian functions, and  $\sigma_{\parallel(\perp),1}$  and  
 2079  $\sigma_{\parallel(\perp),2}$  are the corresponding Gaussian widths. The parameters  $f_{\parallel}$  and  $f_{\perp}$  are fixed to:  
 2080  $f_{\parallel} = f_{\perp} = 0.70$  in data and  $f_{\parallel} = f_{\perp} = 0.45$  in simulation, to obtain a better convergence of  
 2081 the fits. The other parameters are left free.

2082 Examples of the distributions of the parallel and perpendicular recoil components are  
 2083 shown in Figure 3.20 for data and simulation. Also, the fits performed with the weighed  
 2084 combination of Gaussian functions and their pull distributions are presented.

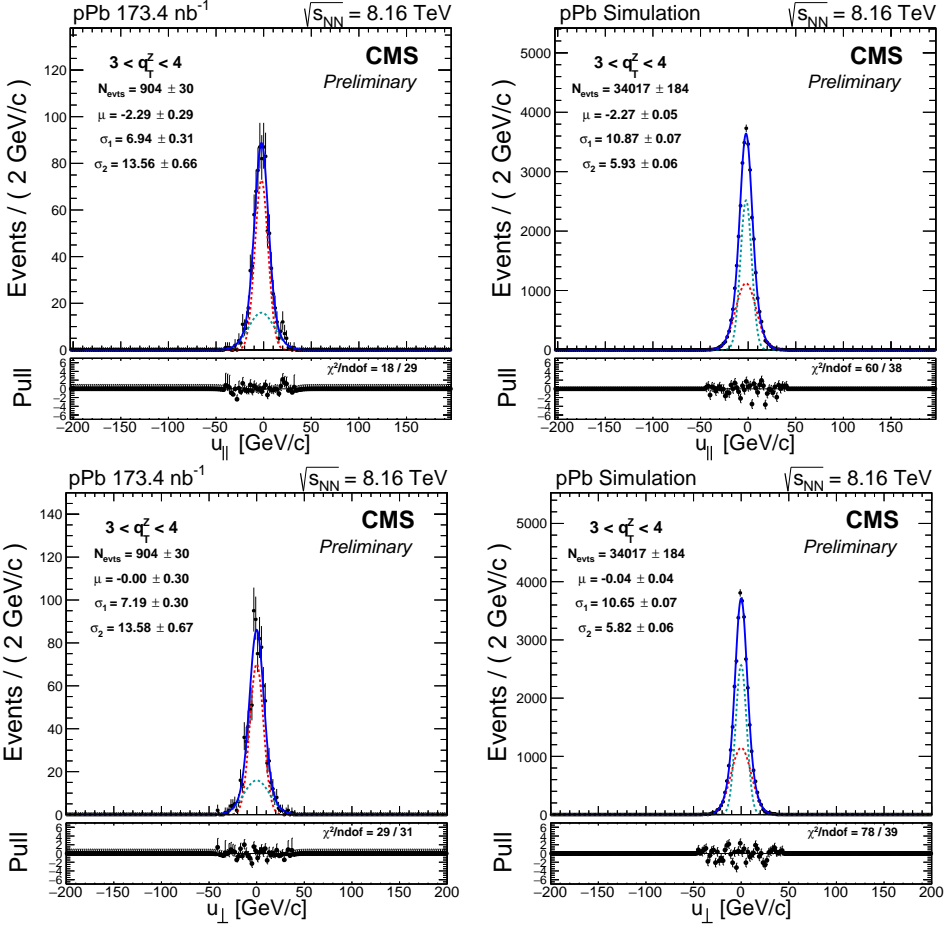


Figure 3.20: Distributions of the  $u_{\parallel}$  (top) and  $u_{\perp}$  (bottom) recoil components in data (left) and simulation (right). The fit function is based on a weighted sum of two Gaussian distributions as defined in Eq. (3.32). The plots correspond to the  $q_T^Z$  bin [3, 4] GeV/c.

2085 **Parameterisation of the recoil scale.** The Gaussian mean parameter  $\mu_{\parallel}$  of the  
 2086 recoil parallel component is extracted in each  $q_T^Z$  bin by fitting the recoil  $u_{\perp}$  distribution  
 2087 as shown in Figure 3.20. The profile of  $\mu_{\parallel}$  as a function of  $q_T^Z$  is then fitted using the  
 2088 following function:

$$\mu_{\parallel}(q_T^Z) = -\left(c_0 + c_1 q_T^Z\right) \left( \frac{1 + \text{Erf}\left[\alpha \cdot (q_T^Z)^{\beta}\right]}{2} \right) \quad (3.33)$$

2089 where  $c_0$ ,  $c_1$ ,  $\alpha$  and  $\beta$  are free parameters, and  $\text{Erf}(x)$  is the Gaussian error function.  
 2090 These fits are shown in Figure 3.21, where the sign of  $\mu_{\parallel}$  has been reversed to plot the  
 2091 results in the positive y-axis. The slope  $c_1$  and intercept  $c_0$  parameters are found to be  
 2092  $c_1 \approx 0.9$  and  $c_0 < 1.0$  GeV/c, which means that the average  $u_{\parallel}$  is roughly 10% lower than

2093  $q_T^Z$  and the contributions at  $q_T^Z = 0$  are negligible. The distributions of the average  $u_{\parallel}$  for  
 2094 data and simulation are observed to be in good agreement.

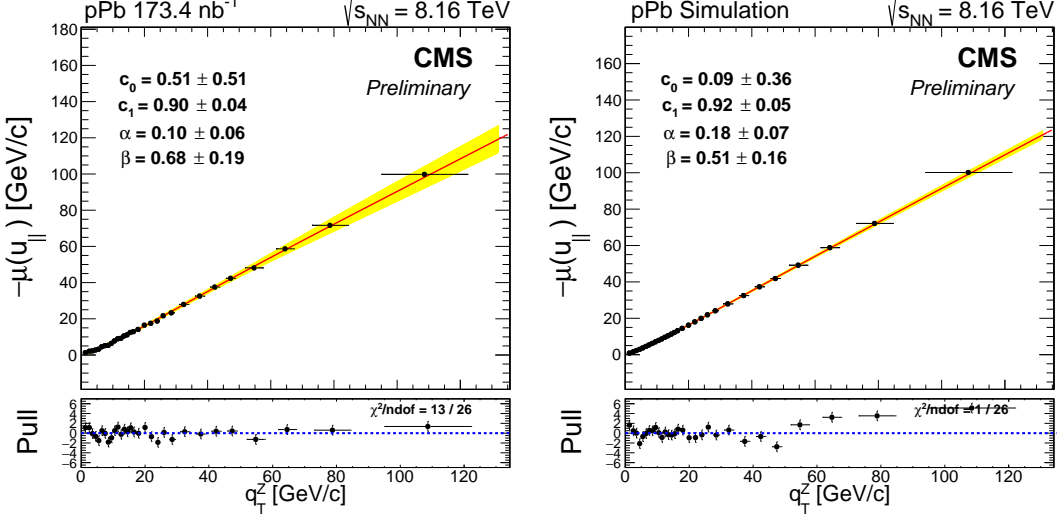


Figure 3.21: Fits of the profile of  $-\mu_{\parallel}$  as a function of  $q_T^Z$ . The results are derived from  $Z \rightarrow \mu^+ \mu^-$  events in data (left) and simulation (right). The yellow band represents the 68% error band of the fit.

2095 In the case of the perpendicular recoil component, the average  $u_{\perp}$  value should be  
 2096 zero based on momentum conservation. To check this, the profile of the Gaussian mean  
 2097 parameter  $\mu_{\perp}$  as a function of  $q_T^Z$  is fitted in data and simulation with a constant function:

$$\mu_{\perp}(q_T^Z) = c_0 \quad (3.34)$$

2098 The outcome of the fits is shown in Figure 3.22. As expected, the  $\mu_{\perp}$  is found to be  
 2099 consistent with zero in simulation and data, showing that there is no bias that affects  
 2100 the average value of the recoil component perpendicular to  $\vec{q}_T^Z$ . From now on,  $\mu_{\perp}$  is fixed  
 2101 to zero.

2102 **Parameterisation of the recoil resolution.** The two Gaussian width parameters  
 2103 ( $\sigma_{\parallel(\perp),1}$  and  $\sigma_{\parallel(\perp),2}$ ) of the parallel (perpendicular) component of the recoil are also ex-  
 2104 tracted from the recoil fits for each  $q_T^Z$  bin. The  $\sigma_{\parallel(\perp),1}$  and  $\sigma_{\parallel(\perp),2}$  parameters of  $u_{\parallel}$  ( $u_{\perp}$ )  
 2105 are parametrised as a function of  $q_T^Z$  using the following formula:

$$\sigma_{1,2}(q_T^Z) = \sqrt{s_0^2 + s_1^2 \cdot q_T^{\alpha}} \quad (3.35)$$

2106 where  $s_0$ ,  $s_1$  and  $\alpha$  are free parameters. The results of the fits to the  $\sigma_1$  and  $\sigma_2$   
 2107 profiles as a function of  $q_T^Z$  are presented in Figure 3.23 for  $u_{\parallel}$  and in Figure 3.24 for  $u_{\perp}$ .

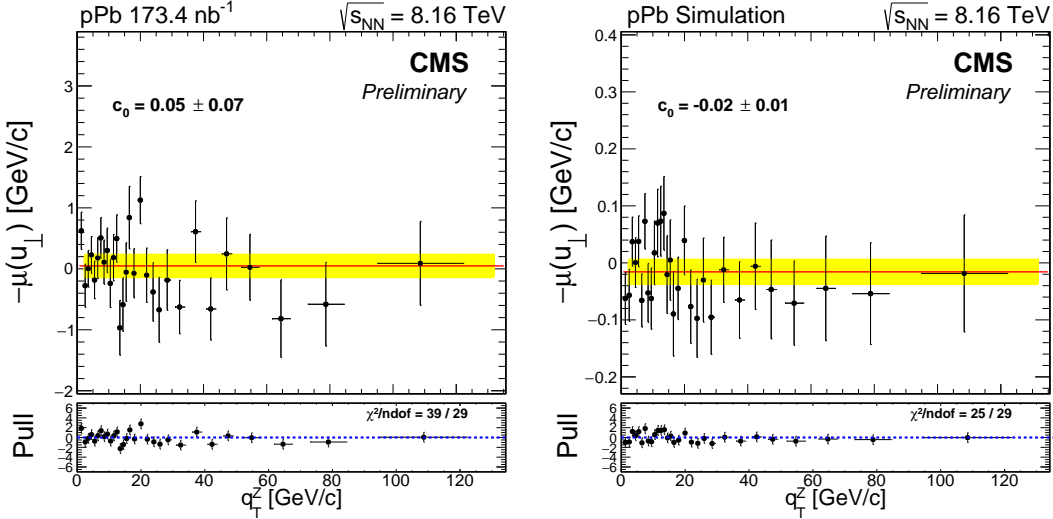


Figure 3.22: Fits of the profile of  $\mu_{\perp}$  as a function of  $q_T^Z$ . The results are derived from  $Z \rightarrow \mu^+ \mu^-$  events in data (left) and simulation (right). The yellow band represents the 68% error band of the fit.

2108 In addition, the profiles of the weighed average of the two Gaussian width parameters,  
2109 given by:

$$\begin{aligned}\sigma_{\perp} &= f_{\perp} \cdot \sigma_{\perp,1} + (1 - f_{\perp}) \cdot \sigma_{\perp,2} \\ \sigma_{\parallel} &= f_{\parallel} \cdot \sigma_{\parallel,1} + (1 - f_{\parallel}) \cdot \sigma_{\parallel,2}\end{aligned}\quad (3.36)$$

2110 are also fitted using Eq. (3.35) and the results are shown in Figure 3.24 and Fig-  
2111 ure 3.23.

2112 It is observed in Figure 3.23 and 3.24, that the recoil resolution increases with  $q_T^Z$ .  
2113 This is expected since high- $p_T$  Z bosons are produced in association with several jets  
2114 from higher order processes, which contributes to the recoil resolution.

2115 Also, the parameter  $s_0$  of the weighed average  $\sigma$ , which measure the recoil resolution  
2116 at  $q_T^Z = 0$  GeV/c, is found to be larger in data than in simulation, which means that the  
2117 modelling of the contributions not originating from the hard scattering (e.g. underlying  
2118 events) are underestimated compared to data. In addition, the contributions to the recoil  
2119 resolution at high  $q_T^Z$  are also larger in data than in simulation.

2120 **Calibration of the simulated recoil.** The recoil corrections are applied to the fol-  
2121 lowing simulated processes:  $W \rightarrow \mu\nu_{\mu}$ ,  $Z/\gamma^* \rightarrow \mu^+ \mu^-$  and  $W \rightarrow \tau\nu_{\tau}$ . The simulated recoil  
2122 distribution is calibrated using the parametric equations obtained in the previous sec-

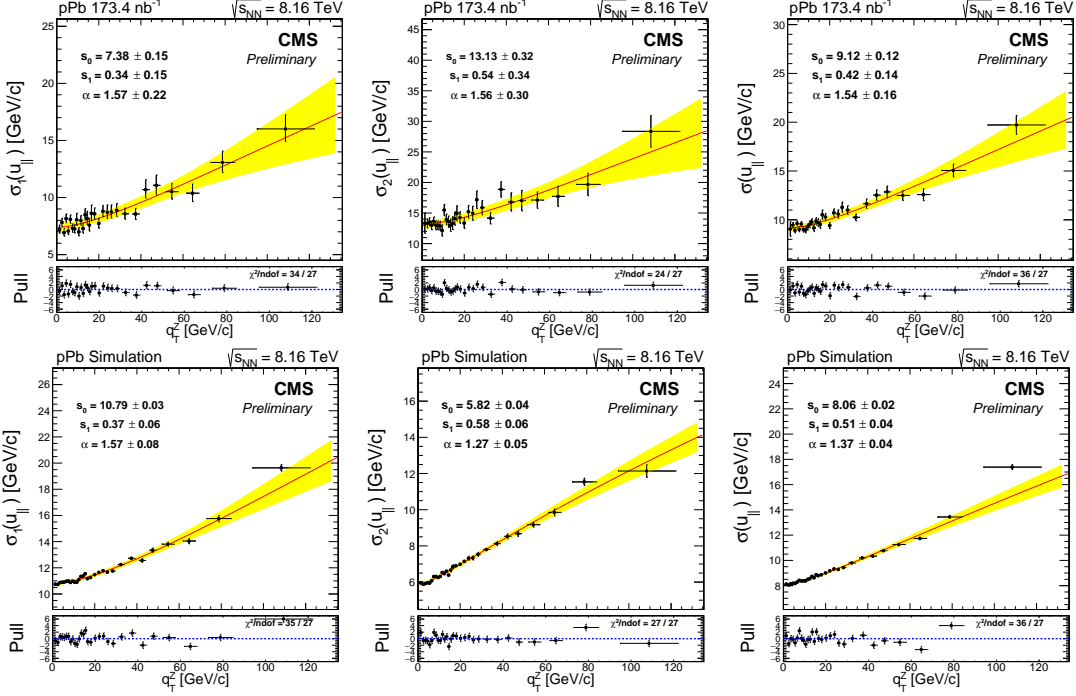


Figure 3.23: Fits to the profile of the  $\sigma_{\parallel,1}$  (left),  $\sigma_{\parallel,2}$  (middle) and weighed average  $\sigma_{\parallel}$  (right) values of the parallel recoil component as a function of  $q_T^Z$ . The results are derived from  $Z \rightarrow \mu^+ \mu^-$  events in data (top) and simulation (bottom).

2123 tions for the Gaussian mean  $\mu(q_T)$  and weighed-average width  $\sigma(q_T)$ . These parametric  
2124 equations are summarised below:

- 2125 • Recoil parametric equations from data:

$$\begin{aligned} \mu_{\parallel}^{\text{data}}(q_T) &= (0.5 + 0.9 \cdot q_T) \left( \frac{1 + \text{Erf}[0.1 \cdot (q_T)^{0.7}]}{2} \right) \\ \sigma_{\parallel}^{\text{data}}(q_T) &= \sqrt{9.1^2 + 0.4^2 \cdot (q_T)^{1.5}} \\ \sigma_{\perp}^{\text{data}}(q_T) &= \sqrt{9.1^2 + 0.4^2 \cdot (q_T)^{1.3}} \end{aligned} \quad (3.37)$$

- 2126 • Recoil parametric equations from simulation:

$$\begin{aligned} \mu_{\parallel}^{\text{MC}}(q_T) &= (0.1 + 0.9 \cdot q_T) \left( \frac{1 + \text{Erf}[0.2 \cdot (q_T)^{0.5}]}{2} \right) \\ \sigma_{\parallel}^{\text{MC}}(q_T) &= \sqrt{8.1^2 + 0.5^2 \cdot (q_T)^{1.4}} \\ \sigma_{\perp}^{\text{MC}}(q_T) &= \sqrt{8.0^2 + 0.8^2 \cdot (q_T)^{0.9}} \end{aligned} \quad (3.38)$$

### 3.2. ANALYSIS

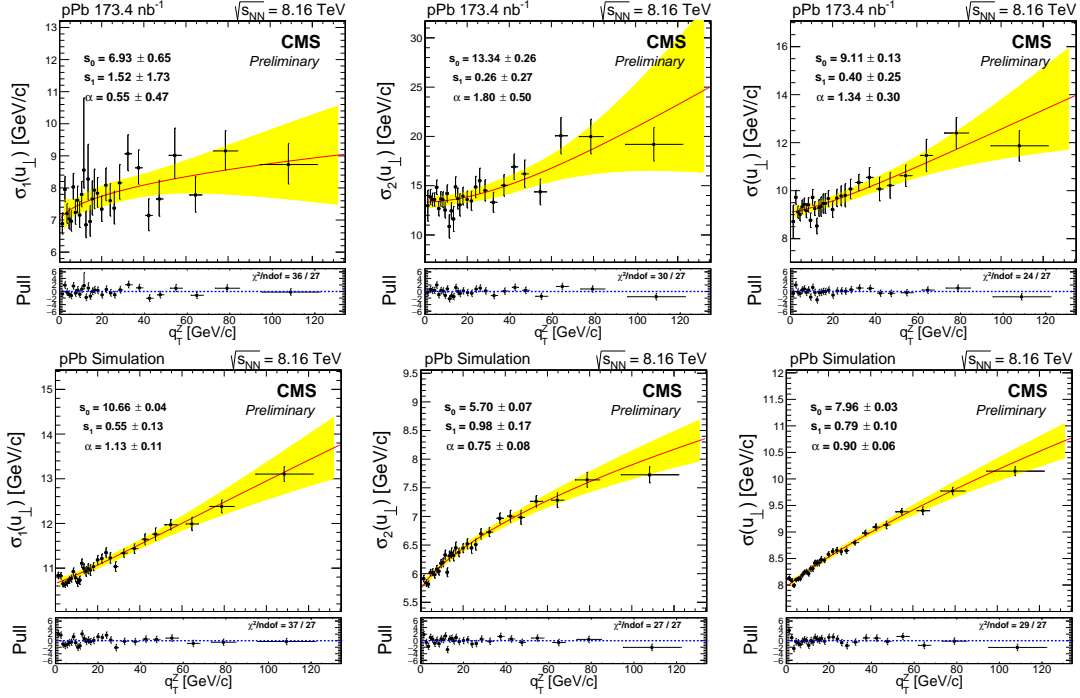


Figure 3.24: Fits for the  $\sigma_{\perp,1}$  (left),  $\sigma_{\perp,2}$  (middle) and weighed average  $\sigma_{\perp}$  (right) values of the recoil perpendicular component as a function of  $q_T$ . The results are derived from  $Z \rightarrow \mu^+ \mu^-$  events in data (top) and simulation (bottom).

2127     The procedure to calibrate the simulated recoil starts by computing the  $p_T$  vector  
 2128     of the boson ( $\vec{q}_T$ ) and simulated recoil ( $\vec{u}_T^{MC}$ ). The boson  $\vec{q}_T$  is determined using the  
 2129     reconstructed muon information whenever possible, as described below:

- 2130     •  $W \rightarrow \mu \nu_\mu$ :  $\vec{q}_T$  is the  $\vec{p}_T$  sum of the reconstructed muon and generated neutrino.  
 2131     •  $W \rightarrow \tau \nu_\tau$ :  $\vec{q}_T$  is the generated  $W$  boson  $p_T$  vector.  
 2132     •  $Z/\gamma^* \rightarrow \mu^+ \mu^-$ : if one of the muons is not reconstructed, then  $\vec{q}_T$  is the  $\vec{p}_T$  sum of the  
 2133     reconstructed muon and the generated-only muon, otherwise  $\vec{q}_T$  is equal to the  $\vec{p}_T$   
 2134     sum of both reconstructed muons ( $\vec{q}_T^{Z/\gamma^*}$ ).

2135     The recoil  $\vec{u}_T^{MC}$  of the simulated event is derived by removing from the  $\vec{p}_T^{\text{miss}}$ , the  
 2136     reconstructed muons from the decay of the weak boson. In other words, for  $W \rightarrow \mu \nu_\mu$   
 2137     events,  $Z/\gamma^* \rightarrow \mu^+ \mu^-$  events with only one reconstructed muon ( $Z/\gamma^* \rightarrow \mu$ ) and  $W \rightarrow$   
 2138      $\tau \nu_\tau$  events, the  $\vec{u}_T^{MC} = -\vec{p}_T^{\text{miss}} - \vec{p}_T^\mu$ , while for  $Z/\gamma^* \rightarrow \mu^+ \mu^-$  events with both muons  
 2139     reconstructed, the  $\vec{u}_T^{MC} = -\vec{p}_T^{\text{miss}} - \vec{q}_T^{Z/\gamma^*}$ .

Once the  $\vec{u}_T^{MC}$  and  $\vec{q}_T$  have been derived for a given event, the  $\vec{u}_T^{MC}$  is then separated in a component parallel ( $u_{\parallel}^{MC}$ ) and perpendicular ( $u_{\perp}^{MC}$ ) to the direction of  $\vec{q}_T$ . The simulated recoil components are then scaled event-by-event, according to:

$$\begin{aligned} u_{\parallel}^{\text{corr}} &= \left( u_{\parallel}^{MC} - \mu_{\parallel}^{MC}(q_T) \right) \cdot \left( \frac{\sigma_{\parallel}^{\text{data}}(q_T)}{\sigma_{\parallel}^{MC}(q_T)} \right) + \mu_{\parallel}^{\text{data}}(q_T) \\ u_{\perp}^{\text{corr}} &= u_{\perp}^{MC} \cdot \left( \frac{\mu_{\perp}^{\text{data}}(q_T)}{\sigma_{\perp}^{MC}(q_T)} \right) \end{aligned} \quad (3.39)$$

Afterwards, the corrected recoil  $\vec{u}_T^{\text{corr}}$  is propagated to the  $p_T^{\text{miss}}$  of the event, as follows:

- For  $W \rightarrow \mu\nu_\mu$ ,  $W \rightarrow \tau\nu_\tau$  and  $Z/\gamma^* \rightarrow \mu$  events:

$$p_T^{\text{miss}} = |u_T^{\text{corr}} + \vec{p}_T^\mu| \quad (3.40)$$

- For fully reconstructed  $Z/\gamma^* \rightarrow \mu^+ \mu^-$  events:

$$p_T^{\text{miss}} = |u_T^{\text{corr}} + \vec{q}_T^{Z/\gamma^*}| \quad (3.41)$$

As an alternative method used to determine the systematic uncertainty associated to the recoil calibration method, the simulated recoil components are smeared, instead of being scaled, by generating a random recoil component per event according to the following Gaussian distribution functions:

$$\begin{aligned} u_{\parallel}^{\text{corr}} &= \text{Gauss} \left( u_{\parallel} - \mu_{\parallel}^{MC}(q_T) + \mu_{\parallel}^{\text{data}}(q_T), \sqrt{\sigma_{\parallel}^{\text{data}}(q_T)^2 - \sigma_{\parallel}^{MC}(q_T)^2} \right) \\ u_{\perp}^{\text{corr}} &= \text{Gauss} \left( u_{\perp}, \sqrt{\sigma_{\perp}^{\text{data}}(q_T)^2 - \sigma_{\perp}^{MC}(q_T)^2} \right) \end{aligned} \quad (3.42)$$

**Closure test.** The recoil calibration is checked using the  $Z \rightarrow \mu^+ \mu^-$  control sample. The  $p_T^{\text{miss}}$  spectrum from data and the corrected one from simulation are shown in Figure 3.25. As can be observed, the agreement between data and simulation is significantly improved after applying the recoil calibration using the scaling method.

**Impact of the recoil calibration in the signal region.** The  $p_T^{\text{miss}}$  distribution in the signal region is compared between data and the simulations. The fit to the data is performed following the signal extraction procedure described in Section 3.2.7. The recoil corrections are applied to the electroweak simulations using both the nominal

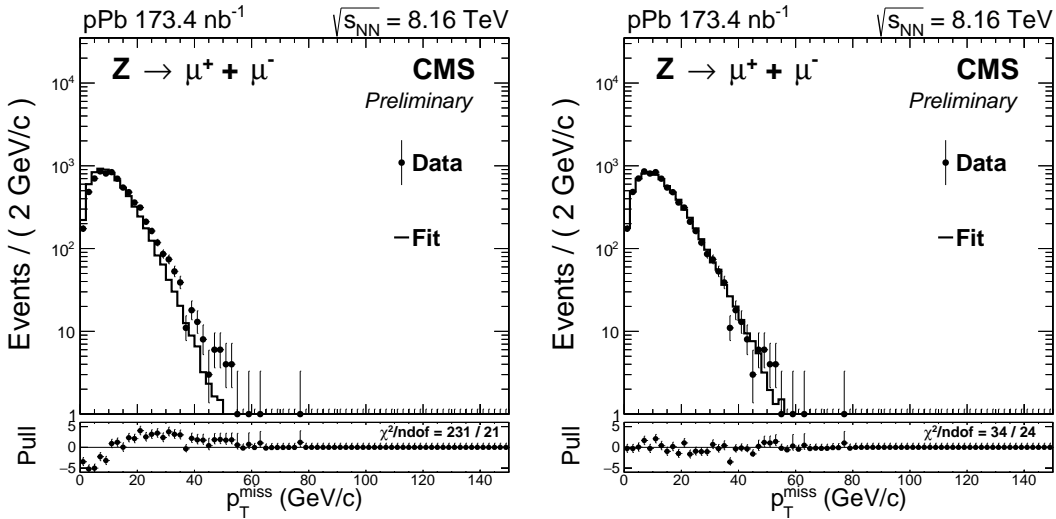


Figure 3.25: A comparison of the  $p_T^{\text{miss}}$  distribution from  $Z \rightarrow \mu^+ \mu^-$  events between data and simulation, before (left) and after (right) calibrating the simulated recoil. The distributions of the simulated HF energy and generated Z-boson  $p_T$  have been weighed.

2159 scaling method and the alternative smearing method, and the results are shown in  
 2160 Figure 3.26. Both the nominal and the alternative recoil calibrations improve significantly  
 2161 the agreement between the  $p_T^{\text{miss}}$  distribution extracted from data and simulations.

### 2162 3.2.6 Signal efficiency

2163 The  $W \rightarrow \mu\nu_\mu$  signal efficiency is defined as the probability for a muon with  $p_T > 25$  GeV/c  
 2164 and  $|\eta_{\text{lab}}^\mu| < 2.4$ , to be reconstructed and pass all the analysis selection criteria. The signal  
 2165 efficiency is obtained from simulation as detailed in Section 3.2.6.1 and then corrected  
 2166 using data-to-MC efficiency ratios derived with the tag-and-probe method as explained  
 2167 in Section 3.2.6.2.

#### 2168 3.2.6.1 Simulated signal efficiency

2169 The signal efficiency is estimated using the  $W \rightarrow \mu\nu_\mu$  simulations since they contain  
 2170 the full history of the signal events, including the generation and reconstruction of the  
 2171 particles. To improve the modelling of the event activity in p-Pb and the W-boson  $p_T$   
 2172 spectrum, the distribution of the generated W-boson  $p_T$  and simulated HF energy is  
 2173 weighed per event as explained in Section 3.2.4 and Section 3.2.5.1, respectively.

2174 A reconstructed muon is considered an offline muon if it satisfies the signal selection  
 2175 requirements. Among the selection criteria, an offline muon is required to satisfy the

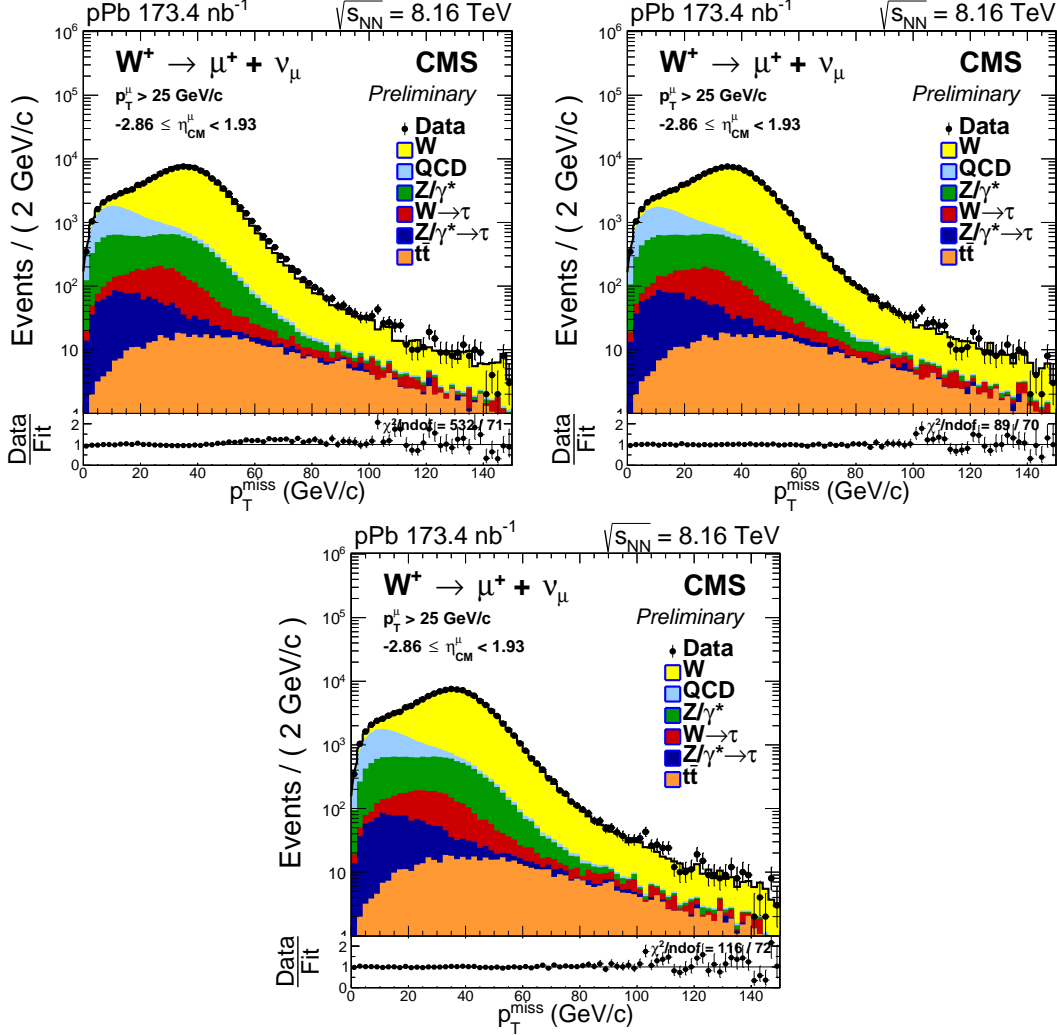


Figure 3.26: Comparison of the  $p_T^{\text{miss}}$  distribution in data and simulation for positive-charged muons in the  $\eta_{\text{CM}}^{\mu}$ -inclusive signal region. The results are shown before (top-left) and after (top-right) applying the recoil calibrations using the nominal scaling method. The result using the alternative smearing method (bottom) is also presented. The distributions of the simulated HF energy and generated Z-boson  $p_T$  have been weighed.

isolation and identification criteria defined in Section 3.2.3.3, match the trigger, have  $p_T^{\mu} > 25 \text{ GeV}/c$  and be within the CMS detector coverage  $|\eta_{\text{lab}}^{\mu}| < 2.4$ .

The signal efficiency of the simulated events is computed as the fraction of *generated* muons matched to an *offline* muon around a cone of  $\Delta R = \sqrt{\Delta\eta^2 + \Delta\phi^2} < 0.05$ . All generated muons are required to be within the analysis kinematic region ( $p_T^{\mu} > 25 \text{ GeV}/c$  and  $|\eta_{\text{lab}}| < 2.4$ ) and come from a W-boson decay. The signal efficiency of the pPb and Pbp

### 3.2. ANALYSIS

2182  $W \rightarrow \mu\nu_\mu$  simulations is derived as a function of the generated muon  $\eta_{\text{lab}}^\mu$ , according to:

$$\epsilon_{\text{pPb(Pbp)}}^{\mu^\pm}(\eta_{\text{CM}}^\mu) = \left( \frac{N_{\text{off}}^{\mu^\pm}[\eta_{\text{lab}}^\mu]}{N_{\text{gen}, p_T > 25}^{\mu^\pm}[\eta_{\text{lab}}^\mu]} \right)_{\text{pPb(Pbp)}} \quad (3.43)$$

2183 where  $N_{\text{off}}$  and  $N_{\text{gen}}$  are the number of offline and generated muons, accordingly.  
 2184 A comparison of the signal efficiencies from the pPb and Pbp simulations is shown in  
 2185 Figure 3.27. A good agreement between the two samples is observed.

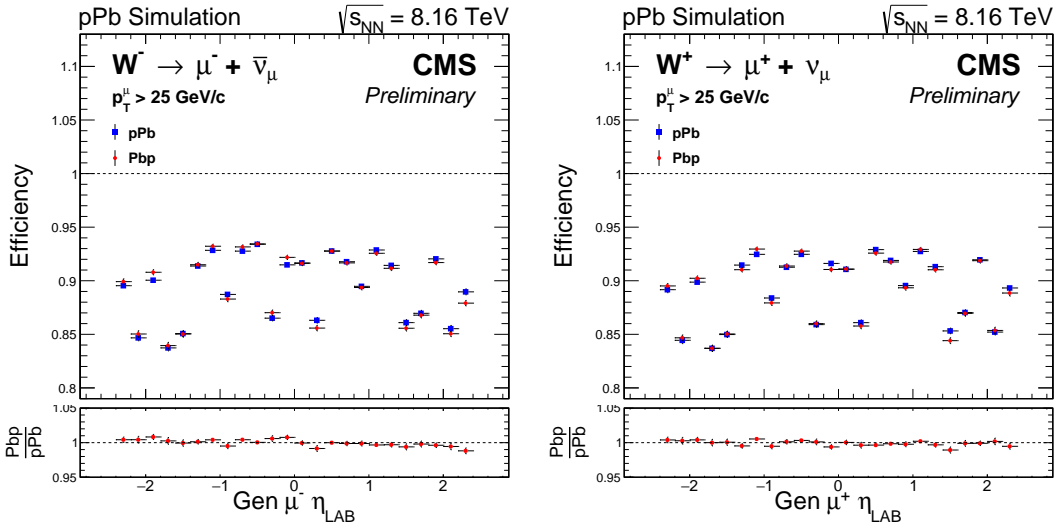


Figure 3.27: Comparison of the signal efficiency derived from the pPb and Pbp  $W \rightarrow \mu\nu_\mu$  simulations as a function of the generated muon  $\eta_{\text{lab}}$ , separated in negative (left) and positive (right) charged muons. The distributions of the simulated HF energy and generated W-boson  $p_T$  have been weighed. The bottom panel shows the ratio of Pbp over pPb signal efficiencies.

2186 The signal efficiencies extracted from the pPb and Pbp  $W \rightarrow \mu\nu_\mu$  simulations are then  
 2187 combined in the centre-of-mass frame, and the final simulated signal efficiency  $\epsilon_{\text{MC}}^{\mu^\pm}$  is  
 2188 obtained as:

$$\epsilon_{\text{MC}}^{\mu^\pm}(\eta_{\text{CM}}^\mu) = \frac{\mathcal{L}_{\text{pPb}} \cdot \epsilon_{\text{pPb}}^{\mu^\pm}(\eta_{\text{CM}}^\mu) + \mathcal{L}_{\text{Pbp}} \cdot \epsilon_{\text{Pbp}}^{\mu^\pm}(\eta_{\text{CM}}^\mu)}{\mathcal{L}_{\text{pPb}} + \mathcal{L}_{\text{Pbp}}} \quad (3.44)$$

2189 where  $\mathcal{L}_{\text{pPb}}$  and  $\mathcal{L}_{\text{Pbp}}$  are the recorded integrated luminosity of each p-Pb run. The re-  
 2190 sults of the  $W \rightarrow \mu\nu_\mu$  efficiency, extracted from the simulations, are shown in Figure 3.28.

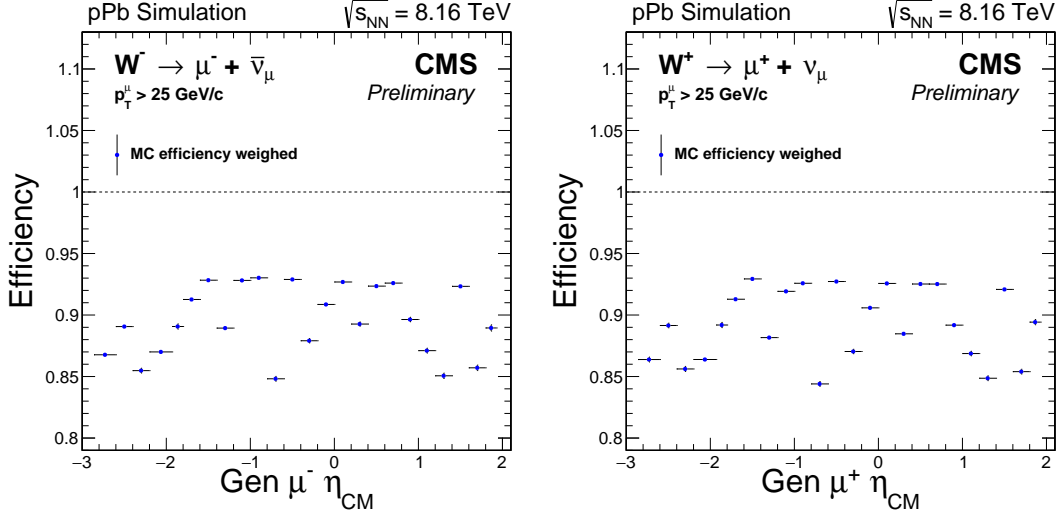


Figure 3.28: Simulated signal efficiency derived from the  $W \rightarrow \mu\nu_\mu$  NLO simulations as a function of the generated muon  $\eta_{CM}$ , separated in negative (left) and positive (right) charged muons. The distributions of the simulated HF energy and generated  $W$ -boson  $p_T$  have been weighed.

### 2191 3.2.6.2 Corrected signal efficiency

2192 The simulation of the CMS detector is very precise but still far from fully describing all  
 2193 the detector conditions observed in real data. In order to compensate for the imperfections  
 2194 in the simulation, a set of data-to-MC corrections provided by the CMS heavy-ion (HIN)  
 2195 group are used to improve the estimation of the signal efficiency. These corrections  
 2196 are derived from the ratio of efficiencies measured in data and simulation using the  
 2197 tag-and-probe (TnP) method.

2198 The tag-and-probe method is a data-driven technique widely used to compute effi-  
 2199 ciencies of physical objects, such as muons, produced from the decay of known mass  
 2200 resonances (e.g. Z bosons). The main advantage of the TnP method is that it can be  
 2201 applied to data and simulation, allowing to asses the differences between the two.

2202 **Definition of the tag-and-probe efficiencies.** To study the different elements that  
 2203 enters in the reconstruction and selection of muons, the total muon efficiency is factorised  
 2204 in five different components, according to:

$$\epsilon^\mu = \epsilon_{STA} \cdot \epsilon_{TRK} \cdot \epsilon_{ID} \cdot \epsilon_{Trig} \cdot \epsilon_{Iso} \quad (3.45)$$

2205 where each efficiency component is defined relative to the previous one, as described

2206 below:

- 2207 •  $\epsilon_{\text{STA}}$  : represents the standalone-muon (STA) reconstruction efficiency. It is probed  
2208 by tracker tracks and is derived by matching the probe to a standalone muon.
- 2209 •  $\epsilon_{\text{trk}}$  : represents the global muon tracking efficiency. It is probed by standalone  
2210 muons and is derived by matching the probe to a global muon.
- 2211 •  $\epsilon_{\text{ID}}$  : represents the muon identification efficiency. It is probed by global muons and  
2212 is determined by requiring that the probe satisfy the tight identification criteria  
2213 defined in Section 3.2.3.3.
- 2214 •  $\epsilon_{\text{trig}}$  : represents the muon trigger efficiency. It is probed by global muons passing  
2215 the identification criteria, and it is determined by requiring that the probe is  
2216 matched to the muon trigger.
- 2217 •  $\epsilon_{\text{iso}}$  : represents the muon isolation efficiency. It is probed by global muons pass-  
2218 ing the identification criteria and matched to the trigger, and it is computed by  
2219 requiring that the probe pass the muon isolation requirement ( $I^{\mu} < 0.15$ ).

2220 **Extraction of the tag-and-probe efficiencies.** For high- $p_{\text{T}}$  muons ( $p_{\text{T}} > 15 \text{ GeV}/c$ ),  
2221 the dimuon decay of Z bosons is used to create a clean sample. In each event, a high-  
2222 quality muon, called the *tag*, is combined with the *probe* of the efficiency being measured,  
2223 to form a tag-probe pair within the Z-boson mass window. The tag and the probe are  
2224 required to have  $p_{\text{T}} > 15 \text{ GeV}/c$  and be inside the acceptance of CMS ( $|\eta_{\text{lab}}| < 2.4$ ). In  
2225 addition, the tag is also required to satisfy the muon isolation and identification criteria,  
2226 and be matched to the trigger.

2227 The tag-probe pairs are separated into two samples depending on whether the  
2228 probe pass the selection criteria under study. The efficiency is then determined by  
2229 performing a simultaneous unbinned maximum likelihood fit to the tag-probe invariant  
2230 mass distribution ( $m_{\text{TP}}$ ) for failing and passing probes. The  $Z \rightarrow \mu^+ \mu^-$  signal distributions  
2231 are parametrised with a Voigt profile [182] and the background distributions with an  
2232 exponential. The same procedure is performed for all efficiencies measured in data and  
2233 simulation.

2234 As an example, the fits to the tag-probe invariant mass distribution for passing  
2235 and failing probes, used to measure the STA reconstruction efficiency, are shown in  
2236 Figure 3.29.

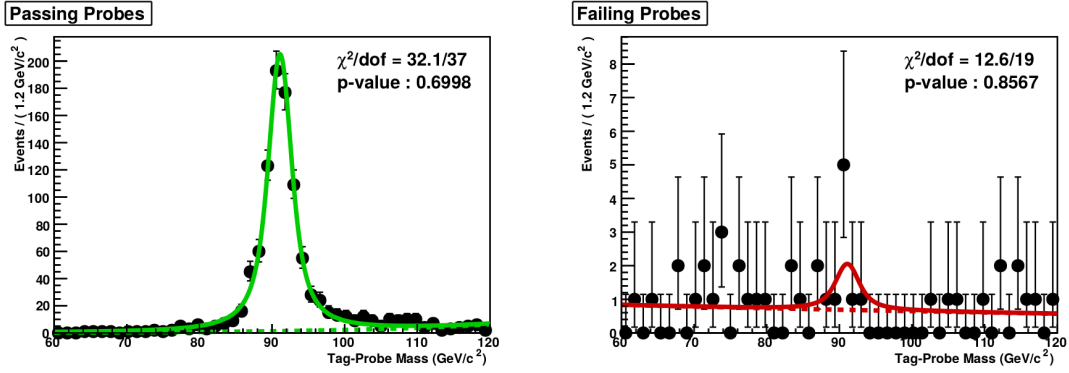


Figure 3.29: Fits to the tag-probe invariant mass distribution for passing (left) and failing (right) probes, used to measure the STA reconstruction efficiency. The results correspond to the probe kinematic region:  $|\eta_{\text{lab}}| < 2.4$  and  $50 < p_T < 80$  GeV/c. Figures taken from the private Ref. [183].

**Results of the tag-and-probe efficiencies.** The STA reconstruction  $\epsilon_{\text{STA}}$  and global muon tracking  $\epsilon_{\text{trk}}$  efficiencies are found to be in very good agreement between data and simulation, and no correction is required for the simulated  $W \rightarrow \mu\nu_\mu$  efficiency.

In the case of the muon identification  $\epsilon_{\text{ID}}$  and isolation  $\epsilon_{\text{iso}}$  efficiencies, the results obtained from simulation are observed to disagree with those from data, as shown in Figure 3.30. As a result, the efficiencies measured in data and simulation, as a function of the probed  $p_T$ , are fitted with: a linear function ( $f_{\text{ID}}(p_T) = a \cdot p_T + b$ ) for muon identification and a displaced error function ( $f_{\text{iso}}(p_T) = a \cdot \text{Erf}[(p_T - c)/b] + d$ ) for muon isolation. The fits to the efficiencies are performed in three regions of probe  $\eta_{\text{lab}}$ , corresponding to:  $|\eta_{\text{lab}}^\mu| < 1.2$ ,  $1.2 < |\eta_{\text{lab}}^\mu| < 2.1$  and  $2.1 < |\eta_{\text{lab}}^\mu| < 2.4$ . The ratio of the fitted functions extracted from the data and simulation efficiencies, for muon identification ( $w_{\text{ID}} = f_{\text{ID}}^{\text{data}}/f_{\text{ID}}^{\text{MC}}$ ) and for muon isolation ( $w_{\text{iso}} = f_{\text{iso}}^{\text{data}}/f_{\text{iso}}^{\text{MC}}$ ), are used as TnP corrections for the simulated  $W \rightarrow \mu\nu_\mu$  efficiency.

The muon trigger efficiency  $\epsilon_{\text{trig}}$  extracted from the simulation is seen to disagree with the results from data as a function of the probe  $\eta_{\text{lab}}$ , as presented in Figure 3.31. In this case, the ratio of the measured efficiency extracted from data and simulation ( $w_{\text{trig}} = \epsilon_{\text{ID}}^{\text{data}}/\epsilon_{\text{ID}}^{\text{MC}}$ ), in each bin of probe  $\eta_{\text{lab}}$ , is used to correct the simulated  $W \rightarrow \mu\nu_\mu$  efficiency.

**Correction of the signal efficiency.** The simulated signal efficiency is recomputed by weighing the offline muon yield per event using the TnP corrections provided by the CMS HIN group, for muon identification  $w_{\text{ID}}$ , trigger  $w_{\text{trig}}$  and isolation  $w_{\text{iso}}$ , according

### 3.2. ANALYSIS

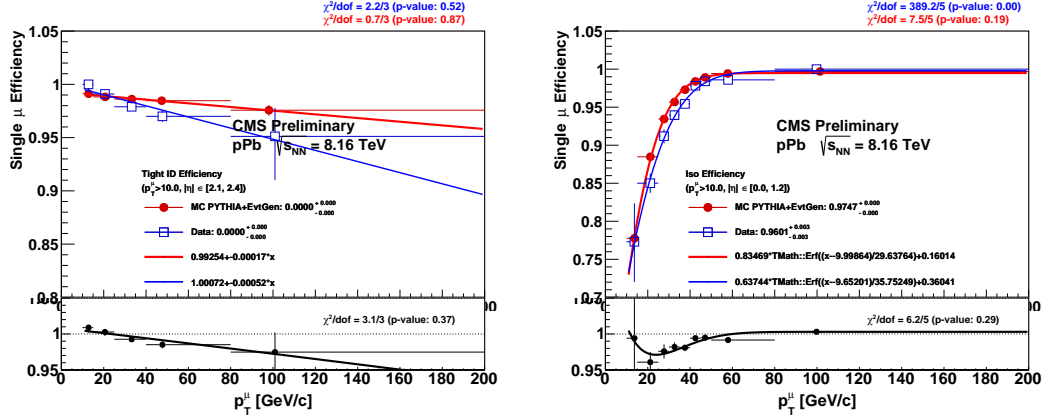


Figure 3.30: Muon identification (left) and isolation (right) efficiencies extracted from data (blue) and simulation (red) using the TnP method, as a function of the probe  $p_T$ . The bottom panels show the data-to-simulation efficiency ratio. The results of the fits to the efficiencies are also shown. Figures taken from the private Ref. [183].

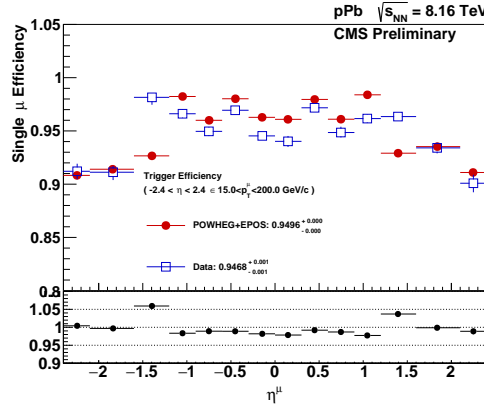


Figure 3.31: Muon trigger efficiency extracted from data (blue) and simulation (red) using the TnP method, as a function of the probe  $\eta_\text{lab}$ . The bottom panel shows the data-to-simulation efficiency ratio. Figure taken from the private Ref. [183].

2258 to:

$$\epsilon_{\text{corr}}^{\mu^\pm} = \frac{\left[ \sum_{i=1}^{N_{\text{off}}^{\mu^\pm}} w_{\text{ID}}(p_T^\mu, |\eta_\text{lab}|) \cdot w_{\text{trig}}(\eta_\text{lab}) \cdot w_{\text{iso}}(p_T^\mu, |\eta_\text{lab}|) \right]}{N_{\text{gen}, p_T > 25}^{\mu^\pm}} \quad (3.46)$$

2259 where the TnP corrections are evaluated with the offline muon  $p_T$  and  $\eta_\text{lab}$  in each  
2260 event, and the sum is performed over the simulated signal events.

2261 **Uncertainties of the tag-and-probe corrections.** The uncertainties associated to  
2262 the TnP corrections are driven by the larger background and lower statistics present in  
2263 data. As a result, only the uncertainties associated to the data efficiencies are propagated  
2264 to the TnP corrections, while the simulation efficiencies are fixed. The statistical and  
2265 systematic components of the TnP correction uncertainties are estimated by performing  
2266 the following set of variations:

- 2267 • (A) Statistical uncertainty for muon ID and isolation: estimated by generating  
2268 a hundred sets of TnP corrections using pseudo-experiments. For each pseudo-  
2269 experiment, the data efficiency points are randomly varied based on a Gaussian  
2270 distribution of width equal to the statistical uncertainty of the efficiency points.  
2271 The varied data efficiencies are then refitted providing new TnP corrections.
- 2272 • (B) Statistical uncertainty for muon trigger: estimated with two sets of TnP correc-  
2273 tions, determined by varying the data efficiency points up and down according to  
2274 their statistical uncertainty.
- 2275 • (C) Systematic uncertainty of the efficiency extraction: derived by refitting the  
2276 tag-probe invariant mass distributions after varying the signal and background  
2277 functional forms, and by extending the range of the Z-boson mass window. These  
2278 uncertainties are then propagated to the TnP corrections by varying the data  
2279 efficiency points up and down by one standard deviation, producing two sets of TnP  
2280 corrections.
- 2281 • (D) Systematic uncertainty of the efficiency parametrisation for muon ID and  
2282 isolation: estimated by using the ratio of the efficiency points from data and  
2283 simulation ( $w = \epsilon^{\text{data}} / \epsilon^{\text{MC}}$ ), instead of the fitted efficiency curves.

2284 In addition, an uncertainty of 0.34% is included to account for the impact of the differ-  
2285 ent level of event activity present in data and simulation. This is derived by comparing  
2286 the simulated muon isolation efficiency before and after applying the HF energy weigh-  
2287 ing. Moreover, an uncertainty of 0.6% is also added to account for possible mismodelling  
2288 of the STA reconstruction efficiency, determined from the maximum difference between  
2289 data and simulation.

2290 The uncertainties of the TnP corrections are propagated to the signal efficiency in  
2291 two ways:

- For the hundred TnP corrections described in (A): the signal efficiency is recomputed with each of the TnP corrections and the RMS of the hundred signal efficiencies obtained is then taken as the uncertainty on the signal efficiency.
- For the up and down variations used in (B), (C) and (D): the uncertainty on the signal efficiency is determined from the maximum difference between the signal efficiency recomputed with the nominal and each of the varied TnP corrections.

The total uncertainty on the signal efficiency due to TnP corrections, is obtained by summing in quadrature the uncertainties from (A), (B), (C) and (D). The additional relative uncertainties of 0.34% and 0.6% are also included.

**Results of the signal efficiency correction.** The corrected signal efficiency is shown in Figure 3.32, including the uncertainties due to TnP correction.

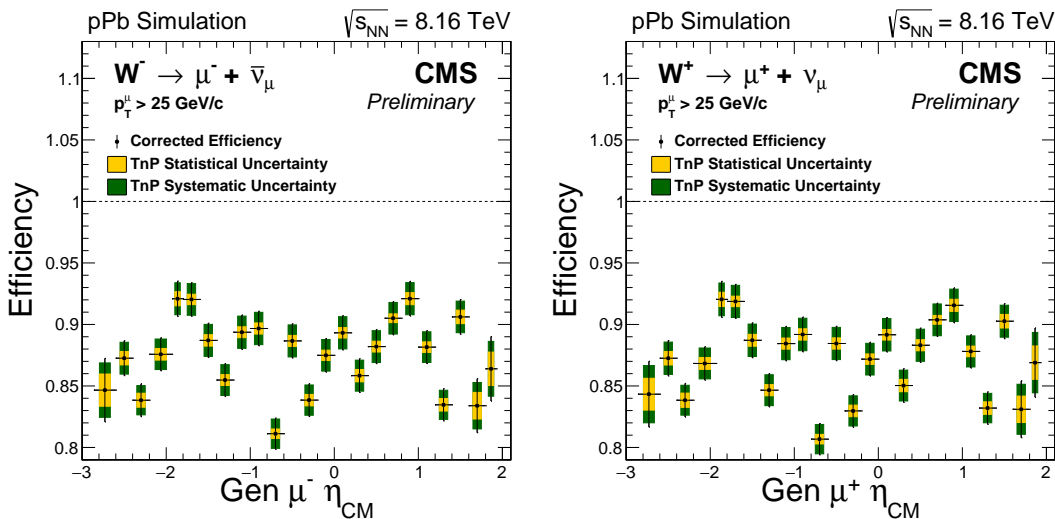


Figure 3.32: Corrected signal efficiency as a function of the generated muon  $\eta_{CM}$ , separated in negative (left) and positive (right) charged muons. The yellow and green boxes represent the uncertainty on the signal efficiency due to the TnP statistics and systematics, respectively.

The relative difference between the corrected and the simulated signal efficiencies ( $(\epsilon_{corr} - \epsilon_{MC})/\epsilon_{MC}$ ), is presented in Table 3.4 as a function of the generated  $\eta_{CM}$ . The largest variation due to the TnP corrections is found to be 4.7%.

$\eta_{CM}^\mu$ Range	$\mu^- \frac{\epsilon_{corr} - \epsilon_{MC}}{\epsilon_{MC}} [\%]$	$\mu^+ \frac{\epsilon_{corr} - \epsilon_{MC}}{\epsilon_{MC}} [\%]$
-2.86 , -2.60	-2.4	-2.4
-2.60 , -2.40	-2.0	-2.1
-2.40 , -2.20	-1.9	-2.1
-2.20 , -1.93	0.7	0.5
-1.93 , -1.80	3.4	3.2
-1.80 , -1.60	0.8	0.6
-1.60 , -1.40	-4.4	-4.5
-1.40 , -1.20	-3.9	-4.0
-1.20 , -1.00	-3.7	-3.8
-1.00 , -0.80	-3.6	-3.7
-0.80 , -0.60	-4.4	-4.4
-0.60 , -0.40	-4.6	-4.6
-0.40 , -0.20	-4.6	-4.7
-0.20 , +0.00	-3.7	-3.8
+0.00 , +0.20	-3.6	-3.7
+0.20 , +0.40	-3.8	-3.9
+0.40 , +0.60	-4.5	-4.6
+0.60 , +0.80	-2.3	-2.3
+0.80 , +1.00	2.7	2.7
+1.00 , +1.20	1.2	1.1
+1.20 , +1.40	-1.9	-2.0
+1.40 , +1.60	-1.9	-2.0
+1.60 , +1.80	-2.7	-2.7
+1.80 , +1.93	-2.9	-2.8

Table 3.4: Relative difference between the corrected and simulated signal efficiencies as a function of the generated muon  $\eta_{CM}$ , separated in negative and positive charged muons.

### 3.2.7 Signal extraction

The signal and background event yields are extracted by fitting the  $p_T^{\text{miss}}$  distribution from data. The background events correspond to high- $p_T$  muons that satisfy the signal selection criteria and are not produced from a direct decay of a W boson. A brief description of the background sources considered in this analysis is given below:

- QCD jet: constitute high- $p_T$  muons produced from semi-leptonic decays of heavy-flavour hadrons formed within jets. Such muons are generally surrounded by a large hadronic activity and their contribution is significantly suppressed by selecting isolated muons ( $I^\mu < 0.15$ ). However, muons from hadron decays can

sometimes pass the isolation criteria and thus, a small fraction of the QCD jet background remains in the signal region.

- $Z/\gamma^* \rightarrow \mu^+ \mu^-$ : a high- $p_T$  muon produced from a Z-boson decay or Drell–Yan. The contribution from this process is suppressed by applying the  $Z/\gamma^* \rightarrow \mu^+ \mu^-$  veto, which excludes events containing at least one pair of well-identified isolated muons, each with  $p_T > 15$  GeV/ $c$ . The  $Z/\gamma^* \rightarrow \mu^+ \mu^-$  events, in which one of the two muons is produced outside of the CMS coverage ( $|\eta_{\text{lab}}| < 2.4$ ) or does not satisfy the muon selection criteria, survive the veto. Such events are expected to contribute more in the CMS endcap regions ( $|\eta| > 2.0$ ), where one of the muons from the  $Z/\gamma^* \rightarrow \mu^+ \mu^-$  decay escape the detector producing a large  $p_T^{\text{miss}}$ .
- $t\bar{t} \rightarrow \mu\nu_\mu + X$ : a high- $p_T$  muon from semi-leptonic decays of top (anti-)quarks. The inclusive cross section of top-quark pair production in pPb at  $\sqrt{s_{\text{NN}}} = 8.16$  TeV, has been measured by the CMS collaboration to be  $\sigma_{t\bar{t}} = 45 \pm 8$  nb $^{-1}$  [181]. The  $t\bar{t}$  process is expected to have a very small impact in the signal region due its small inclusive cross section and its branching ratio (13.4%) to muons [19].
- $W \rightarrow \tau\nu_\tau \rightarrow \mu\nu_\mu + X$ : consists of the leptonic decay of a W boson into a  $\tau$  lepton, which then decays into a high- $p_T$  muon.
- $Z/\gamma^* \rightarrow \tau\bar{\tau} \rightarrow \mu\nu_\mu + X$ : corresponds to a ditau decay of a Z boson or virtual photon, where one of the  $\tau$  leptons then decays into a high- $p_T$  muon.

The largest source of background in the signal region correspond to QCD jets which represents approximately 18% of events in data. Among the electroweak background processes, the dominant one is the  $Z/\gamma^* \rightarrow \mu^+ \mu^-$  background. The electroweak background amounts to roughly 12% of the events in the signal region, divided as:  $Z/\gamma^* \rightarrow \mu^+ \mu^-$  (9%),  $W \rightarrow \tau\nu_\tau$  (2%) and  $Z/\gamma^* \rightarrow \tau\bar{\tau}$  (1%). The  $t\bar{t}$  background contributes roughly 0.5% of events. Other electroweak processes such as double boson decays (WW, WZ and ZZ) have been checked to contribute less than 0.03%, so they are not considered.

The shape of the QCD jet background is modelled using a functional form derived from data as explained in Section 3.2.7.1 and the shapes of the signal,  $t\bar{t}$  background and electroweak background are estimated using the  $p_T^{\text{miss}}$  distribution from simulations, as described in Section 3.2.7.2. Section 3.2.7.3 introduces the model used to extract the signal. The event yields obtained from the fits are presented in Section 3.2.7.4 and corrected for efficiency in Section 3.2.7.5.

### 3.2.7.1 Modelling of the QCD jet background

The QCD jet background cannot be simulated reliably in p-Pb collisions due to the imprecise knowledge of the production cross sections and nuclear modifications of hadrons, and the inaccurate modelling of the event activity. Thus, a data-driven approach is used to determine the QCD jet shape.

The overall procedure consist of the following steps: first parametrise the  $p_T^{\text{miss}}$  shape of the QCD jet background in a region dominated by non-isolated muons, then determine the dependence of the QCD jet functional form with respect to the muon isolation and finally extrapolate the QCD jet shape to low muon isolation values, namely in the signal region.

The shape of the QCD jet background is parametrised by a modified Rayleigh distribution, defined as:

$$f_{\text{QCD}}(p_T^{\text{miss}}) = p_T^{\text{miss}} \cdot \exp \left( -\frac{(p_T^{\text{miss}})^2}{2(\sigma_0 + \sigma_1 \cdot p_T^{\text{miss}} + \sigma_2 \cdot (p_T^{\text{miss}})^2)^2} \right) \quad (3.47)$$

where  $\sigma_0$ ,  $\sigma_1$ , and  $\sigma_2$  are free parameters extracted by performing an unbinned maximum-likelihood fit to the  $p_T^{\text{miss}}$  distribution in a control sample from data. The events in the control sample are selected by applying all signal selection requirements, except the muon isolation cut. The fits are performed separately for positive and negative charged muon events.

To derive the muon isolation dependence of the QCD jet background parameters, the  $p_T^{\text{miss}}$  spectrum in the control sample is fitted with the QCD jet functional form, in five bins of the muon isolation variable with the following boundaries: [ 0.4 , 0.5 , 0.6 , 0.7 , 0.8 , 0.9 ]. Lower muon isolation values ( $I^\mu < 0.4$ ) are discarded, due to the large contamination from weak boson decays. The results of the QCD jet background fits, corresponding to the lowest and highest muon isolation regions, are shown in Figure 3.33.

The QCD background parameters  $\sigma_0$ ,  $\sigma_1$ , and  $\sigma_2$ , are extracted from the fits to the  $p_T^{\text{miss}}$  spectrum in each muon isolation bin, and their profile as a function of  $I^\mu$  is observed to be well described by a linear function, given by:

$$\sigma_i(I^\mu) = \hat{\sigma}_i + s_i \cdot I^\mu \quad (3.48)$$

where  $\hat{\sigma}_i$  and  $s_i$  are free parameters extracted separately for each QCD background parameter. The outcome of the linear fits is shown in Figure 3.34.

### 3.2. ANALYSIS

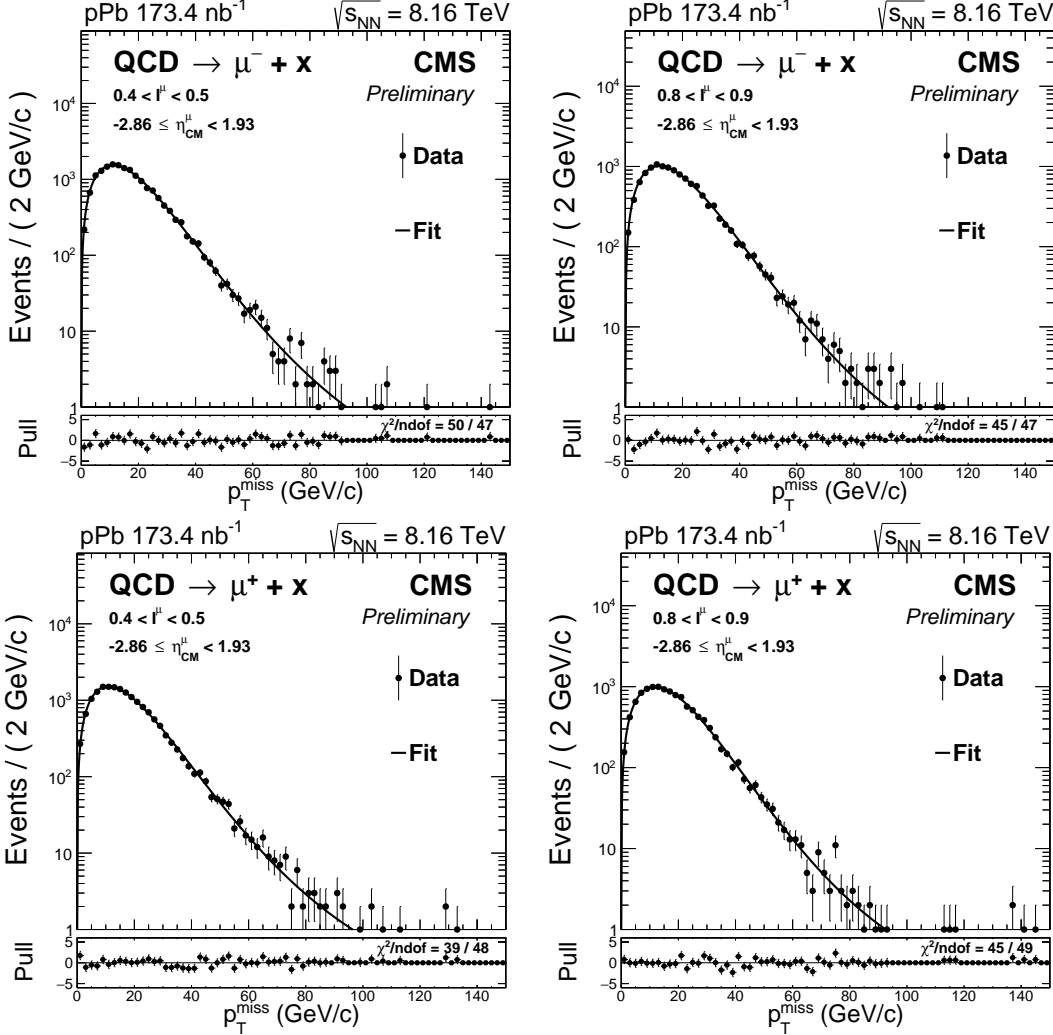


Figure 3.33: QCD jet background fits to the  $p_T^{\text{miss}}$  distribution in a control sample of non-isolated muon events corresponding to the muon isolation bins:  $0.4 < I^\mu < 0.5$  (left) and  $0.8 < I^\mu < 0.9$  (right). The results are shown for positive (top) and negative (bottom) charged muons separately.

2375     The  $\sigma_0$ ,  $\sigma_1$ , and  $\sigma_2$  parameters are extrapolated to the signal region (average muon  
 2376     isolation of 0.03) using the parametrisation as a function of  $I^\mu$  extracted from the linear  
 2377     fits. The values of the QCD background parameters derived from the extrapolation are  
 2378     presented in Table 3.5.

2379     The dependence of the extrapolated QCD jet shape on the muon  $\eta_{\text{CM}}^\mu$  is checked by  
 2380     splitting the control sample in different  $\eta_{\text{CM}}^\mu$  bins, and then repeating the QCD jet shape  
 2381     extraction procedure for each  $\eta_{\text{CM}}^\mu$  bin. The results of the extrapolated values of  $\sigma_0$ ,  $\sigma_1$ ,  
 2382     and  $\sigma_2$ , determined for each  $\eta_{\text{CM}}^\mu$  bin, are compared in Figure 3.35 to the results obtained

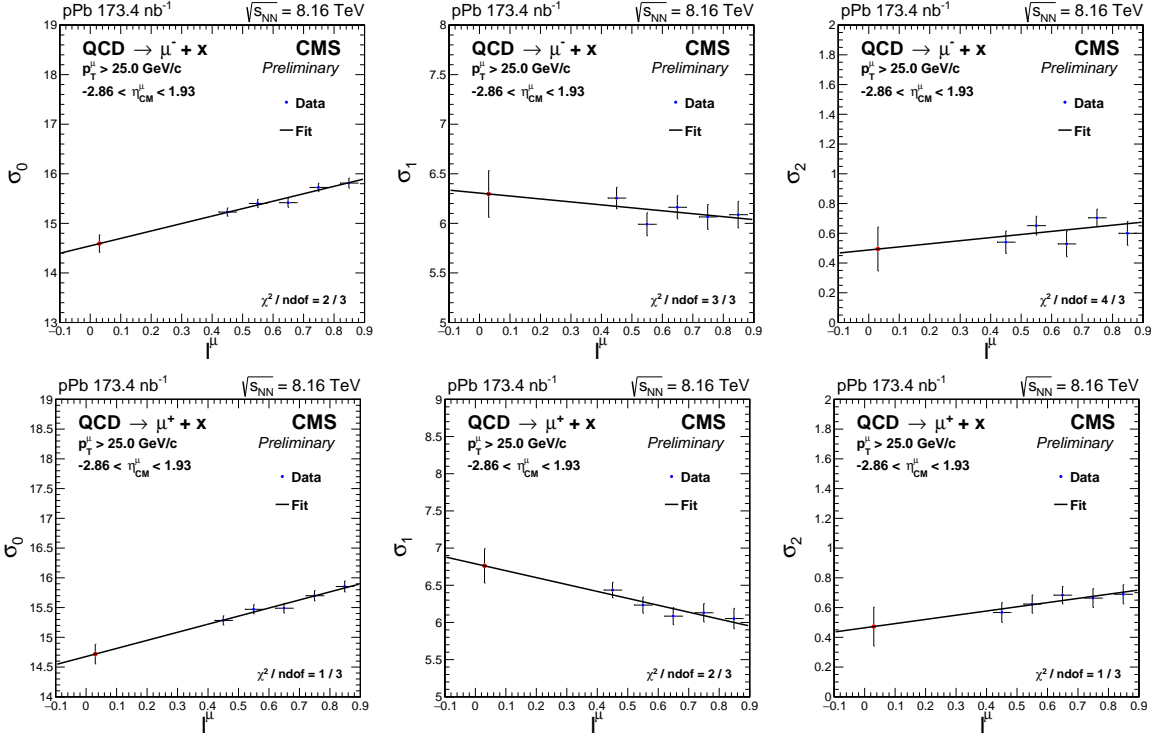


Figure 3.34: Linear fits to the profile of the QCD background parameters:  $\sigma_0$  (left),  $\sigma_1$  (middle) and  $\sigma_2$  (right), with respect to the muon isolation variable  $I^\mu$ . The results are shown for negative (top) and positive (bottom) charged muons in the  $\eta_{CM}^\mu$ -inclusive range. The red points represent the value obtained by linearly extrapolating to  $I^\mu = 0.03$ .

Parameter	QCD jet $\rightarrow \mu^-$	QCD jet $\rightarrow \mu^+$
$\sigma_0$	$14.6 \pm 0.2$	$14.7 \pm 0.2$
$\sigma_1$	$6.3 \pm 0.2$	$6.8 \pm 0.2$
$\sigma_2$	$0.5 \pm 0.2$	$0.5 \pm 0.1$

Table 3.5: QCD background parameters extrapolated to  $I^\mu = 0.03$ . The results are presented for positive and negative charged muons in the  $\eta_{CM}^\mu$ -inclusive range.

2383 in the  $\eta_{CM}^\mu$ -inclusive range.

2384 It is observed that the  $\sigma_0$ ,  $\sigma_1$ , and  $\sigma_2$  parameters, extrapolated to low muon isolation,  
 2385 do not vary significantly with respect to  $\eta_{CM}^\mu$  and are found to be consistent with the  
 2386 corresponding values obtained in the  $\eta_{CM}^\mu$ -inclusive range. As a result, the extrapolated  
 2387 parameters derived in the  $\eta_{CM}^\mu$ -inclusive range for  $\mu^+$  and  $\mu^-$ , are used to fix the QCD jet  
 2388 background shape when fitting the signal.

### 3.2. ANALYSIS

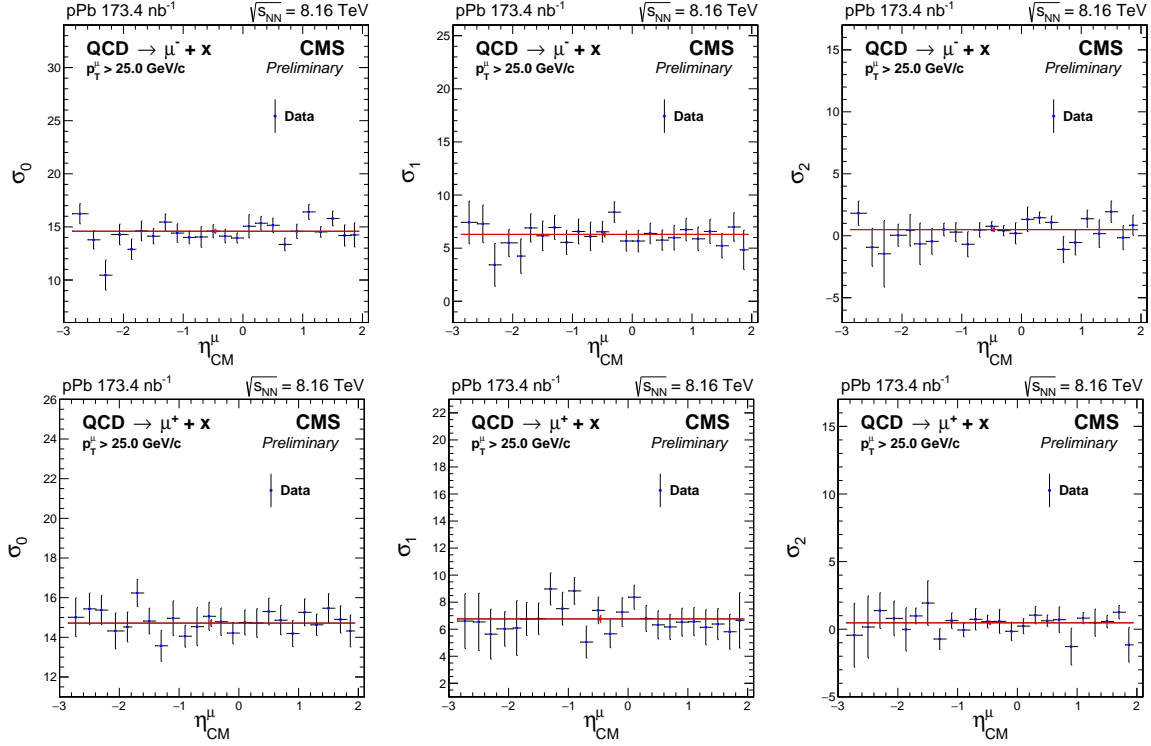


Figure 3.35: Muon  $\eta_{\text{CM}}^{\mu}$  dependence of  $\sigma_0$  (left),  $\sigma_1$  (middle) and  $\sigma_2$  (right) parameters extrapolated to  $I^{\mu} = 0.03$ . The results are shown for negative (top) and positive (bottom) charged muons. The red line corresponds to the QCD jet parameter extrapolated in the  $\eta_{\text{CM}}^{\mu}$ -inclusive range.

#### 2389 3.2.7.2 Modelling of the signal, $t\bar{t}$ and electroweak backgrounds

2390 The  $p_{\text{T}}^{\text{miss}}$  distribution of the signal, as well as, the  $t\bar{t}$  and electroweak background events,  
 2391 are estimated using the corresponding POWHEG simulations mentioned in Section 3.2.2.  
 2392 The simulated events for each process are required to satisfy the signal selection criteria  
 2393 summarised in Section 3.2.3.5.

2394 In order to improve the description of the data, several corrections are applied to  
 2395 the simulations. First, the simulated HF energy distribution is weighed as explained in  
 2396 Section 3.2.5.1. Then, the generated weak boson  $p_{\text{T}}$  distribution from the  $W \rightarrow \mu\nu_{\mu}$ ,  $W \rightarrow$   
 2397  $\tau\nu_{\tau}$ ,  $Z/\gamma^* \rightarrow \mu^+\mu^-$  and  $Z/\gamma^* \rightarrow \tau\bar{\tau}$  simulations, is weighed as described in Section 3.2.4  
 2398 And finally, the recoil of  $W \rightarrow \mu\nu_{\mu}$ ,  $W \rightarrow \tau\nu_{\tau}$  and  $Z/\gamma^* \rightarrow \mu^+\mu^-$  events is calibrated as  
 2399 detailed in Section 3.2.5.2, improving the agreement of the  $p_{\text{T}}^{\text{miss}}$  distribution between  
 2400 data and simulation.

2401 Once the simulations have been corrected, the  $p_{\text{T}}^{\text{miss}}$  shape of the signal,  $t\bar{t}$  background  
 2402 and electroweak background, is determined by building a template histogram of the

2403 simulated  $p_T^{\text{miss}}$  distribution (2 GeV/c bin width). These template histograms are then  
 2404 used in the fitting procedure described in the next section.

### 2405 3.2.7.3 Fit model

2406 The number of  $W \rightarrow \mu\nu_\mu$  signal events is obtained by performing an unbinned maximum-  
 2407 likelihood fit of the observed  $p_T^{\text{miss}}$  distribution in different muon  $\eta_{\text{CM}}^\mu$  regions. The fits  
 2408 are done using a combination of template histograms and a functional form. The data  
 2409 analysis framework RooFit v3.60 [184] is used to make the fits.

2410 The total fit model includes six contributions: the signal  $W \rightarrow \mu\nu_\mu$  template ( $\mathcal{T}_W$ ), the  
 2411 electroweak background templates  $Z/\gamma^* \rightarrow \mu^+\mu^-$  ( $\mathcal{T}_{Z\mu}$ ),  $W \rightarrow \tau\nu_\tau$  ( $\mathcal{T}_{W\tau}$ ) and  $Z/\gamma^* \rightarrow \tau\bar{\tau}$   
 2412 ( $\mathcal{T}_{Z\tau}$ ), the  $t\bar{t}$  background template ( $\mathcal{T}_{t\bar{t}}$ ), and the QCD jet background functional form  
 2413 ( $\mathcal{F}_{\text{QCD}}$ ). The model used to fit the data is:

$$N_W \cdot (\mathcal{T}_W + r_{Z\mu} \cdot \mathcal{T}_{Z\mu} + r_{W\tau} \cdot \mathcal{T}_{W\tau} + r_{Z\tau} \cdot \mathcal{T}_{Z\tau} + r_{t\bar{t}} \cdot \mathcal{T}_{t\bar{t}}) + N_{\text{QCD}} \cdot \mathcal{F}_{\text{QCD}} \quad (3.49)$$

2414 where  $N_W$  and  $N_{\text{QCD}}$  are the normalisation factors of the  $W \rightarrow \mu\nu_\mu$  signal and QCD  
 2415 jet background,  $r_{t\bar{t}}$  represents the ratio of  $t\bar{t}$  background events over the number of signal  
 2416 events ( $N_{t\bar{t}}/N_W$ ), and  $r_{Z\mu}$ ,  $r_{Z\tau}$  and  $r_{W\tau}$  are the corresponding ratios for the  $Z/\gamma^* \rightarrow \mu^+\mu^-$ ,  
 2417  $Z/\gamma^* \rightarrow \tau\bar{\tau}$  and  $W \rightarrow \tau\nu_\tau$  background processes, respectively.

2418 The shapes of the signal,  $t\bar{t}$  background and electroweak background processes are  
 2419 defined based on template histograms extracted from simulations. Being very small and  
 2420 with a moderately discriminating shape, the electroweak and  $t\bar{t}$  background components  
 2421 cannot be directly and independently fitted on data. Instead, we take advantage that  
 2422 their nuclear modification should be small and close to the one of the  $W$ -boson signal.  
 2423 Thus, the ratios of  $Z/\gamma^* \rightarrow \mu^+\mu^-$ ,  $Z/\gamma^* \rightarrow \tau\bar{\tau}$ ,  $W \rightarrow \tau\nu_\tau$  and  $t\bar{t}$  events over the number of  
 2424  $W \rightarrow \mu\nu_\mu$  events, are fixed to the results from simulations after having normalised all the  
 2425 MC samples to the recorded integrated luminosity of data as detailed in Section 3.2.2  
 2426 and applied all analysis corrections and selection criteria.

2427 The QCD jet background contribution is taken into account by means of a functional  
 2428 form depending on three parameters. For the fits to the  $p_T^{\text{miss}}$  distribution in the signal  
 2429 region, the  $\sigma_0$ ,  $\sigma_1$  and  $\sigma_2$  parameters are fixed to the extrapolated values mentioned in  
 2430 Table 3.5, and the normalisation is left free.

2431 The  $p_T^{\text{miss}}$  distribution is fitted separately for  $W^+ \rightarrow \mu^+\nu_\mu$  and  $W^- \rightarrow \mu^-\bar{\nu}_\mu$  events.  
 2432 Only the signal ( $N_W$ ) and the QCD jet background ( $N_{\text{QCD}}$ ) normalisation factors are left  
 2433 free when fitting the signal region in data. The fits are done in the  $\eta_{\text{CM}}^\mu$ -inclusive range  
 2434 and in bins of muon  $\eta_{\text{CM}}^\mu$ . The results of the fits performed in the  $\eta_{\text{CM}}^\mu$ -inclusive range

2435 are shown in Figure 3.36 and those performed in the other muon  $\eta_{\text{CM}}^{\mu}$  bins are presented  
 2436 in Appendix A.

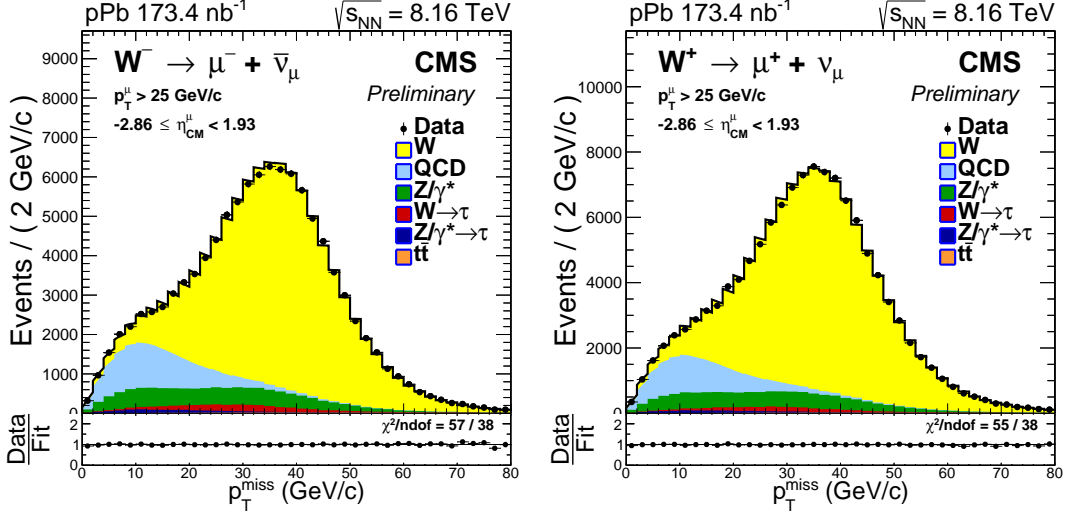


Figure 3.36: The  $p_T^{\text{miss}}$  distribution for  $W^- \rightarrow \mu^- \bar{\nu}_\mu$  (left) and  $W^+ \rightarrow \mu^+ \nu_\mu$  (right) events within the  $\eta_{\text{CM}}^{\mu}$ -inclusive range, shown in linear scale. Unbinned fits to the data (black points) are performed with six contributions, stacked from top to bottom:  $W \rightarrow \mu\nu_\mu$  (yellow), QCD jet (light blue),  $Z/\gamma^* \rightarrow \mu^+\mu^-$  (green),  $W \rightarrow \tau\nu_\tau$  (red),  $Z/\gamma^* \rightarrow \tau\bar{\tau}$  (dark blue) and  $t\bar{t}$  (orange). The lower panel, on each figure, display the ratio of the measurements over the result of the fit. The  $\chi^2$  test value over the number of degrees of freedom is also shown.

#### 2437 3.2.7.4 Extracted event yields

2438 The results of the fits to the data in each of the different muon  $\eta_{\text{CM}}$  bins are summarized  
 2439 in Table 3.6 and Table 3.7 for  $W^- \rightarrow \mu^- \bar{\nu}_\mu$  and  $W^+ \rightarrow \mu^+ \nu_\mu$  events, respectively.

#### 2440 3.2.7.5 Corrected event yields

2441 The signal event yields extracted from the fits are corrected by taking into account the  
 2442 efficiency of the detector, according to:

$$N_{\mu}^{\pm}(\eta_{\text{CM}}^{\mu}) = \frac{N_{\mu,\text{raw}}^{\pm}(\eta_{\text{CM}}^{\mu})}{\epsilon_{\text{corr}}^{\pm}(\eta_{\text{CM}}^{\mu})} \quad (3.50)$$

2443 where  $N_{\mu,\text{raw}}$  is the number of signal events extracted from the fits,  $N_{\mu}$  is the number  
 2444 of signal events after correcting for efficiency and  $\epsilon_{\text{corr}}^{\pm}$  is the signal efficiency corrected

$\eta_{\text{CM}}^\mu$ Range	Total	Signal	$Z/\gamma^* \rightarrow \mu^+ \mu^-$	$W \rightarrow \tau \nu_\tau$	$Z/\gamma^* \rightarrow \tau \bar{\tau}$	$t\bar{t}$	QCD
-2.86 , -2.60	5210	$4041 \pm 65$	$560 \pm 9$	$135 \pm 2$	$45 \pm 1$	$3.1 \pm 0.1$	$427 \pm 40$
-2.60 , -2.40	4308	$3395 \pm 60$	$461 \pm 8$	$102 \pm 2$	$36 \pm 1$	$4.0 \pm 0.1$	$310 \pm 37$
-2.40 , -2.20	4273	$3276 \pm 59$	$449 \pm 8$	$100 \pm 2$	$36 \pm 1$	$5.9 \pm 0.1$	$407 \pm 38$
-2.20 , -1.93	6423	$4920 \pm 74$	$654 \pm 10$	$156 \pm 2$	$62 \pm 1$	$12.9 \pm 0.2$	$617 \pm 48$
-1.93 , -1.80	3140	$2419 \pm 52$	$303 \pm 6$	$79 \pm 2$	$28 \pm 1$	$8.4 \pm 0.2$	$302 \pm 34$
-1.80 , -1.60	4822	$3672 \pm 64$	$435 \pm 8$	$117 \pm 2$	$45 \pm 1$	$15.2 \pm 0.3$	$537 \pm 43$
-1.60 , -1.40	4727	$3631 \pm 64$	$390 \pm 7$	$117 \pm 2$	$39 \pm 1$	$18.8 \pm 0.3$	$533 \pm 43$
-1.40 , -1.20	4521	$3590 \pm 64$	$340 \pm 6$	$109 \pm 2$	$45 \pm 1$	$21.6 \pm 0.4$	$416 \pm 40$
-1.20 , -1.00	4626	$3666 \pm 65$	$306 \pm 5$	$118 \pm 2$	$48 \pm 1$	$25.2 \pm 0.4$	$463 \pm 42$
-1.00 , -0.80	4722	$3762 \pm 66$	$277 \pm 5$	$119 \pm 2$	$45 \pm 1$	$32 \pm 1$	$488 \pm 43$
-0.80 , -0.60	4198	$3425 \pm 63$	$238 \pm 4$	$102 \pm 2$	$46 \pm 1$	$32 \pm 1$	$355 \pm 39$
-0.60 , -0.40	4648	$3738 \pm 66$	$245 \pm 4$	$119 \pm 2$	$54 \pm 1$	$35 \pm 1$	$456 \pm 43$
-0.40 , -0.20	4344	$3478 \pm 64$	$226 \pm 4$	$111 \pm 2$	$50 \pm 1$	$36 \pm 1$	$443 \pm 41$
-0.20 , +0.00	4474	$3510 \pm 65$	$260 \pm 5$	$113 \pm 2$	$43 \pm 1$	$39 \pm 1$	$509 \pm 43$
+0.00 , +0.20	4643	$3654 \pm 65$	$309 \pm 6$	$114 \pm 2$	$47 \pm 1$	$42 \pm 1$	$477 \pm 43$
+0.20 , +0.40	4638	$3533 \pm 64$	$335 \pm 6$	$111 \pm 2$	$50 \pm 1$	$42 \pm 1$	$567 \pm 44$
+0.40 , +0.60	4718	$3528 \pm 63$	$390 \pm 7$	$114 \pm 2$	$46 \pm 1$	$39 \pm 1$	$601 \pm 44$
+0.60 , +0.80	4552	$3375 \pm 62$	$446 \pm 8$	$103 \pm 2$	$48 \pm 1$	$37 \pm 1$	$544 \pm 43$
+0.80 , +1.00	4637	$3325 \pm 61$	$489 \pm 9$	$103 \pm 2$	$43 \pm 1$	$37 \pm 1$	$640 \pm 44$
+1.00 , +1.20	4612	$3265 \pm 60$	$539 \pm 10$	$105 \pm 2$	$45 \pm 1$	$29 \pm 1$	$630 \pm 44$
+1.20 , +1.40	4053	$2769 \pm 55$	$517 \pm 10$	$78 \pm 2$	$38 \pm 1$	$23.8 \pm 0.5$	$627 \pm 42$
+1.40 , +1.60	4251	$2917 \pm 56$	$620 \pm 12$	$96 \pm 2$	$39 \pm 1$	$21.5 \pm 0.4$	$557 \pm 42$
+1.60 , +1.80	3844	$2506 \pm 51$	$611 \pm 12$	$78 \pm 2$	$35 \pm 1$	$15.4 \pm 0.3$	$599 \pm 41$
+1.80 , +1.93	2640	$1719 \pm 42$	$439 \pm 11$	$54 \pm 1$	$22 \pm 1$	$9.6 \pm 0.2$	$397 \pm 33$

Table 3.6: Event yields of  $W^- \rightarrow \mu^- \bar{\nu}_\mu$  and background processes, extracted from the fits to the  $p_T^{\text{miss}}$  distribution in each muon  $\eta_{\text{CM}}^\mu$  region. All analysis selection criteria are applied including the muon  $p_T > 25$  GeV/c. All uncertainties shown are statistical only.

2445 with the TnP corrections. The statistical uncertainty of the corrected signal yields are  
 2446 computed based on error propagation with:

$$\delta N_\mu^\pm = \frac{\delta N_{\mu,\text{raw}}^\pm(\eta_{\text{CM}}^\mu)}{\epsilon_{\text{corr}}^\pm(\eta_{\text{CM}}^\mu)} \quad (3.51)$$

2447 where  $\delta N_{\mu,\text{raw}}^\pm$  is the uncertainty of the signal event yield determined from the fits  
 2448 to the data. The results of the corrected signal event yields for each muon  $\eta_{\text{CM}}^\mu$  range  
 2449 are summarized in Table 3.8 and Table 3.9 for  $W^- \rightarrow \mu^- \bar{\nu}_\mu$  and  $W^+ \rightarrow \mu^+ \nu_\mu$  events,  
 2450 accordingly.

$\eta_{\text{CM}}^\mu$	Range	Total	Signal	$Z/\gamma^* \rightarrow \mu^+ \mu^-$	$W \rightarrow \tau \nu_\tau$	$Z/\gamma^* \rightarrow \tau \bar{\tau}$	$t\bar{t}$	QCD
-2.86 , -2.60		4465	$3358 \pm 59$	$583 \pm 10$	$67 \pm 1$	$44 \pm 1$	$3.3 \pm 0.1$	$409 \pm 38$
-2.60 , -2.40		4234	$3247 \pm 58$	$526 \pm 9$	$65 \pm 1$	$35 \pm 1$	$4.2 \pm 0.1$	$358 \pm 36$
-2.40 , -2.20		4377	$3351 \pm 60$	$500 \pm 9$	$61 \pm 1$	$36 \pm 1$	$6.5 \pm 0.1$	$423 \pm 38$
-2.20 , -1.93		6847	$5257 \pm 76$	$714 \pm 10$	$101 \pm 1$	$53 \pm 1$	$14.3 \pm 0.2$	$706 \pm 49$
-1.93 , -1.80		3592	$2762 \pm 55$	$385 \pm 7$	$56 \pm 1$	$29 \pm 1$	$8.5 \pm 0.2$	$400 \pm 36$
-1.80 , -1.60		5421	$4299 \pm 69$	$488 \pm 8$	$94 \pm 2$	$50 \pm 1$	$16.0 \pm 0.3$	$471 \pm 43$
-1.60 , -1.40		5343	$4375 \pm 70$	$446 \pm 7$	$96 \pm 2$	$45 \pm 1$	$18.0 \pm 0.3$	$364 \pm 42$
-1.40 , -1.20		5129	$4182 \pm 69$	$375 \pm 6$	$98 \pm 2$	$41 \pm 1$	$23.4 \pm 0.4$	$405 \pm 43$
-1.20 , -1.00		5382	$4465 \pm 72$	$339 \pm 5$	$100 \pm 2$	$53 \pm 1$	$28.3 \pm 0.5$	$395 \pm 43$
-1.00 , -0.80		5467	$4485 \pm 73$	$306 \pm 5$	$100 \pm 2$	$50 \pm 1$	$32 \pm 1$	$491 \pm 45$
-0.80 , -0.60		4738	$3960 \pm 68$	$244 \pm 4$	$89 \pm 2$	$42 \pm 1$	$29 \pm 1$	$373 \pm 41$
-0.60 , -0.40		5349	$4435 \pm 73$	$255 \pm 4$	$99 \pm 2$	$49 \pm 1$	$38 \pm 1$	$473 \pm 45$
-0.40 , -0.20		5027	$4146 \pm 70$	$238 \pm 4$	$88 \pm 1$	$46 \pm 1$	$37 \pm 1$	$468 \pm 43$
-0.20 , +0.00		5161	$4269 \pm 71$	$268 \pm 4$	$99 \pm 2$	$45 \pm 1$	$39 \pm 1$	$439 \pm 43$
+0.00 , +0.20		5473	$4352 \pm 72$	$308 \pm 5$	$100 \pm 2$	$52 \pm 1$	$39 \pm 1$	$621 \pm 47$
+0.20 , +0.40		5175	$4179 \pm 70$	$337 \pm 6$	$99 \pm 2$	$48 \pm 1$	$37 \pm 1$	$475 \pm 44$
+0.40 , +0.60		5482	$4334 \pm 71$	$399 \pm 7$	$93 \pm 2$	$43 \pm 1$	$36 \pm 1$	$576 \pm 46$
+0.60 , +0.80		5722	$4469 \pm 72$	$469 \pm 8$	$99 \pm 2$	$51 \pm 1$	$38 \pm 1$	$595 \pm 47$
+0.80 , +1.00		6061	$4652 \pm 72$	$561 \pm 9$	$99 \pm 2$	$48 \pm 1$	$37 \pm 1$	$664 \pm 48$
+1.00 , +1.20		5814	$4404 \pm 70$	$595 \pm 9$	$102 \pm 2$	$41 \pm 1$	$33 \pm 1$	$639 \pm 47$
+1.20 , +1.40		5365	$4050 \pm 67$	$570 \pm 9$	$87 \pm 1$	$35 \pm 1$	$23.9 \pm 0.4$	$596 \pm 45$
+1.40 , +1.60		5768	$4308 \pm 68$	$674 \pm 11$	$92 \pm 1$	$39 \pm 1$	$21.5 \pm 0.3$	$633 \pm 46$
+1.60 , +1.80		5320	$3969 \pm 65$	$662 \pm 11$	$81 \pm 1$	$34 \pm 1$	$16.1 \pm 0.3$	$557 \pm 44$
+1.80 , +1.93		3600	$2654 \pm 53$	$450 \pm 9$	$63 \pm 1$	$19.8 \pm 0.4$	$9.3 \pm 0.2$	$404 \pm 36$

Table 3.7: Event yields of  $W^+ \rightarrow \mu^+ \nu_\mu$  and background processes, extracted from the fits to the  $p_T^{\text{miss}}$  distribution in each muon  $\eta_{\text{CM}}^\mu$  region. All analysis selection criteria are applied including the muon  $p_T > 25$  GeV/c. All uncertainties shown are statistical only.

### 3.2.8 Observables

The main motivation behind measuring the W-boson production in p-Pb collisions is to probe the nuclear modifications of the PDFs. To accomplish this, the efficiency-corrected  $W \rightarrow \mu \nu_\mu$  event yields are combined to measure three kinds of observables: cross sections, muon charge asymmetry and forward-backward ratios.

**W  $\rightarrow \mu \nu_\mu$  cross sections.** The  $W^\pm \rightarrow \mu^\pm \nu_\mu$  differential cross sections are computed as a function of  $\eta_{\text{CM}}^\mu$ , according to:

$$\frac{d\sigma(W^\pm \rightarrow \mu^\pm \nu_\mu)}{d\eta_{\text{CM}}^\mu}(\eta_{\text{CM}}^\mu) = \frac{N_\mu^\pm(\eta_{\text{CM}}^\mu)}{\mathcal{L} \cdot \Delta\eta_{\text{CM}}^\mu} \quad (3.52)$$

$\eta_{\text{CM}}^\mu$ Range	Extracted yield	Efficiency (%)	Corrected yield
-2.86 , -2.60	$4041 \pm 65$	$84.7 \pm 0.2$	$4773 \pm 77$
-2.60 , -2.40	$3395 \pm 60$	$87.3 \pm 0.2$	$3891 \pm 69$
-2.40 , -2.20	$3276 \pm 59$	$83.8 \pm 0.2$	$3907 \pm 71$
-2.20 , -1.93	$4920 \pm 74$	$87.6 \pm 0.2$	$5619 \pm 84$
-1.93 , -1.80	$2419 \pm 52$	$92.1 \pm 0.2$	$2627 \pm 56$
-1.80 , -1.60	$3672 \pm 64$	$92.0 \pm 0.1$	$3990 \pm 70$
-1.60 , -1.40	$3631 \pm 64$	$88.7 \pm 0.2$	$4093 \pm 72$
-1.40 , -1.20	$3590 \pm 64$	$85.5 \pm 0.2$	$4200 \pm 75$
-1.20 , -1.00	$3666 \pm 65$	$89.4 \pm 0.2$	$4102 \pm 73$
-1.00 , -0.80	$3762 \pm 66$	$89.7 \pm 0.2$	$4195 \pm 74$
-0.80 , -0.60	$3425 \pm 63$	$81.1 \pm 0.2$	$4222 \pm 78$
-0.60 , -0.40	$3738 \pm 66$	$88.7 \pm 0.2$	$4216 \pm 75$
-0.40 , -0.20	$3478 \pm 64$	$83.8 \pm 0.2$	$4148 \pm 76$
-0.20 , +0.00	$3510 \pm 65$	$87.5 \pm 0.2$	$4012 \pm 74$
+0.00 , +0.20	$3654 \pm 65$	$89.3 \pm 0.2$	$4091 \pm 73$
+0.20 , +0.40	$3533 \pm 64$	$85.8 \pm 0.2$	$4116 \pm 74$
+0.40 , +0.60	$3528 \pm 63$	$88.2 \pm 0.2$	$4000 \pm 72$
+0.60 , +0.80	$3375 \pm 62$	$90.5 \pm 0.2$	$3729 \pm 68$
+0.80 , +1.00	$3325 \pm 61$	$92.1 \pm 0.2$	$3610 \pm 66$
+1.00 , +1.20	$3265 \pm 60$	$88.2 \pm 0.2$	$3704 \pm 68$
+1.20 , +1.40	$2769 \pm 55$	$83.5 \pm 0.2$	$3318 \pm 65$
+1.40 , +1.60	$2917 \pm 56$	$90.6 \pm 0.2$	$3219 \pm 61$
+1.60 , +1.80	$2506 \pm 51$	$83.4 \pm 0.2$	$3005 \pm 61$
+1.80 , +1.93	$1719 \pm 42$	$86.4 \pm 0.3$	$1990 \pm 48$

Table 3.8: Corrected event yields of  $W^- \rightarrow \mu^- \bar{\nu}_\mu$ , given for each muon  $\eta_{\text{CM}}^\mu$  bin. All analysis selection criteria are applied including the muon  $p_T > 25$  GeV/c. The muon efficiency has been corrected by applying the tag-and-probe corrections, HF energy weights and vector boson  $p_T$  weights, event by event. All uncertainties shown are statistical only.

where  $\mathcal{L} = 173.4 \pm 6.1$  nb $^{-1}$  is the recorded integrated luminosity,  $\Delta\eta_{\text{CM}}^\mu$  is the width of the  $\eta_{\text{CM}}^\mu$  range in which the measurement is performed and  $N_\mu(\eta_{\text{CM}}^\mu)$  is the number of signal events after correcting for efficiency.

**Muon charge asymmetry.** The muon charge asymmetry measures the difference between the event yields of the  $W^- \rightarrow \mu^- \bar{\nu}_\mu$  and  $W^+ \rightarrow \mu^+ \nu_\mu$  processes, which is sensitive to the number of protons and neutrons in the nucleus (isospin effect), and to the flavour dependence of the nuclear modifications of the PDFs. It is defined in the following way:

$\eta_{\text{CM}}^\mu$ Range	Extracted yield	Efficiency (%)	Corrected yield
-2.86 , -2.60	$3358 \pm 59$	$84.3 \pm 0.2$	$3982 \pm 70$
-2.60 , -2.40	$3247 \pm 58$	$87.3 \pm 0.2$	$3721 \pm 66$
-2.40 , -2.20	$3351 \pm 60$	$83.8 \pm 0.2$	$3997 \pm 71$
-2.20 , -1.93	$5257 \pm 76$	$86.8 \pm 0.2$	$6055 \pm 87$
-1.93 , -1.80	$2762 \pm 55$	$92.0 \pm 0.2$	$3001 \pm 60$
-1.80 , -1.60	$4299 \pm 69$	$91.9 \pm 0.1$	$4679 \pm 75$
-1.60 , -1.40	$4375 \pm 70$	$88.7 \pm 0.2$	$4931 \pm 79$
-1.40 , -1.20	$4182 \pm 69$	$84.7 \pm 0.2$	$4940 \pm 82$
-1.20 , -1.00	$4465 \pm 72$	$88.4 \pm 0.2$	$5049 \pm 81$
-1.00 , -0.80	$4485 \pm 73$	$89.2 \pm 0.2$	$5029 \pm 82$
-0.80 , -0.60	$3960 \pm 68$	$80.7 \pm 0.2$	$4908 \pm 85$
-0.60 , -0.40	$4435 \pm 73$	$88.5 \pm 0.2$	$5015 \pm 83$
-0.40 , -0.20	$4146 \pm 70$	$83.0 \pm 0.2$	$4996 \pm 85$
-0.20 , +0.00	$4269 \pm 71$	$87.2 \pm 0.2$	$4897 \pm 81$
+0.00 , +0.20	$4352 \pm 72$	$89.2 \pm 0.2$	$4881 \pm 81$
+0.20 , +0.40	$4179 \pm 70$	$85.0 \pm 0.2$	$4915 \pm 82$
+0.40 , +0.60	$4334 \pm 71$	$88.3 \pm 0.2$	$4908 \pm 81$
+0.60 , +0.80	$4469 \pm 72$	$90.4 \pm 0.2$	$4944 \pm 79$
+0.80 , +1.00	$4652 \pm 72$	$91.6 \pm 0.2$	$5081 \pm 79$
+1.00 , +1.20	$4404 \pm 70$	$87.8 \pm 0.2$	$5016 \pm 80$
+1.20 , +1.40	$4050 \pm 67$	$83.2 \pm 0.2$	$4867 \pm 80$
+1.40 , +1.60	$4308 \pm 68$	$90.3 \pm 0.2$	$4773 \pm 76$
+1.60 , +1.80	$3969 \pm 65$	$83.1 \pm 0.2$	$4776 \pm 78$
+1.80 , +1.93	$2654 \pm 53$	$86.9 \pm 0.2$	$3054 \pm 61$

Table 3.9: Corrected event yields of  $W^+ \rightarrow \mu^+ \nu_\mu$ , given for each muon  $\eta_{\text{CM}}^\mu$ . All analysis selection criteria are applied including the muon  $p_T > 25 \text{ GeV}/c$ . The muon efficiency has been corrected by applying the tag-and-probe corrections, HF energy weights and vector boson  $p_T$  weights, event by event. All uncertainties shown are statistical only.

$$\mathcal{A}_\mu(\eta_{\text{CM}}^\mu) = \frac{N_\mu^+(\eta_{\text{CM}}^\mu) - N_\mu^-(\eta_{\text{CM}}^\mu)}{N_\mu^+(\eta_{\text{CM}}^\mu) + N_\mu^-(\eta_{\text{CM}}^\mu)} \quad (3.53)$$

where  $N_\mu^-$  and  $N_\mu^+$  represents the efficiency-corrected number of  $W^- \rightarrow \mu^- \bar{\nu}_\mu$  and  $W^+ \rightarrow \mu^+ \nu_\mu$  events, respectively.

**Forward-backward ratios.** To probe the modification of the PDFs between different pseudorapidity regions, the signal event yields measured in the forward region ( $\eta_{\text{CM}}^\mu > 0$ ) are combined with those measured in the backward region ( $\eta_{\text{CM}}^\mu < 0$ ), to derive forward-

2470 backward ratios. These ratios are computed separately for  $W^+ \rightarrow \mu^+ \nu_\mu$  and  $W^- \rightarrow \mu^- \bar{\nu}_\mu$   
 2471 events in the following way:

$$R_{FB}^\pm(\eta_{CM}^\mu) = \frac{N_\mu^\pm(+\eta_{CM}^\mu)}{N_\mu^\pm(-\eta_{CM}^\mu)} \quad (3.54)$$

2472 A forward-backward ratio is also derived for all  $W \rightarrow \mu \nu_\mu$  events, by combining the  
 2473 yields of the  $W^- \rightarrow \mu^- \bar{\nu}_\mu$  and  $W^+ \rightarrow \mu^+ \nu_\mu$  processes, according to:

$$R_{FB}(\eta_{CM}^\mu) = \frac{N_\mu^+ (+\eta_{CM}^\mu) + N_\mu^- (+\eta_{CM}^\mu)}{N_\mu^+ (-\eta_{CM}^\mu) + N_\mu^- (-\eta_{CM}^\mu)} \quad (3.55)$$

### 2474 3.2.9 Systematic uncertainties

2475 This section presents the different sources and the procedure employed to determine  
 2476 the systematic uncertainties in the measurement of the W-boson production in p-Pb  
 2477 collisions.

#### 2478 3.2.9.1 Luminosity

2479 The recorded integrated luminosity of the 2016 p-Pb data sample is  $173.4 \text{ nb}^{-1}$ , and is  
 2480 known with a precision of 3.5% [168]. Since the integrated luminosity cancels in forward-  
 2481 backward ratios and in the muon charge asymmetry, it only affects the measurement of  
 2482 the  $W \rightarrow \mu \nu_\mu$  differential cross sections. In this case, this 3.5% systematic uncertainty is  
 2483 global and the bin-to-bin correlations is 100%. This uncertainty is the dominant one on  
 2484 the  $W \rightarrow \mu \nu_\mu$  differential cross sections.

#### 2485 3.2.9.2 Signal efficiency

2486 The dominant systematic uncertainty on the forward-backward ratios and muon charge  
 2487 asymmetry are due to the estimation of the signal efficiency. Since the signal efficiencies  
 2488 are computed from simulations and corrected using the TnP corrections, two sources  
 2489 of systematic uncertainties are considered. The first one corresponds to the theoretical  
 2490 modelling of the simulated signal, which takes into account the uncertainty on the  
 2491 nuclear PDFs and the impact of the renormalisation and factorisation scales. The second  
 2492 source corresponds to the TnP correction uncertainties, which derives from the  $Z \rightarrow \mu^+ \mu^-$   
 2493 control sample used to extract the TnP data efficiencies.

2494 **Theoretical modelling.** The NLO model used to generate the simulations can impact  
2495 the measurement of the signal efficiencies. The main sources of theoretical uncertainties  
2496 include the choice of the nuclear parton distribution function (EPPS16+CT14), and the  
2497 renormalisation and factorisation scales.

2498 Since the PDFs are not calculable from first principles but are determined experi-  
2499 mentally, in particular by the measurements reported here, the inclusion of any PDF  
2500 introduces an additional systematic uncertainty. Thus, it is important to determine  
2501 the impact of a change of PDF on the signal efficiencies. The procedure to derive the  
2502 theoretical uncertainties of the PDF variations consist of reweighing the simulations  
2503 event-by-event using weights derived from POWHEG after applying various PDF sets. The  
2504 PDF sets are accessed through the LHAPDF6 [185] framework and consist of 56 CT14  
2505 PDFs and 40 EPPS16 nuclear corrections. Once the simulations are reweighed with each  
2506 PDF set, the efficiencies are recomputed and used to recalculate all the observables. The  
2507 nPDF uncertainty is determined by combining the EPPS16+CT14 PDF variations of the  
2508 observables using the Hessian approach, as recommended by the EPPS16 authors [158].

Moreover, the uncertainty due to the renormalisation ( $\mu_R$ ) and factorisation ( $\mu_F$ ) scales is computed by varying these two scales in POWHEG using the following six combinations:

$$(\mu_R, \mu_F) = [ (0.5, 0.5), (1.0, 0.5), (0.5, 1.0), (1.0, 2.0), (2.0, 1.0), (2.0, 2.0) ]$$

2509 The simulations are reweighed event by event using the POWHEG weights produced  
2510 with each set of scales, then the efficiencies are recomputed and the observables are  
2511 recalculated for each varied efficiency. The variations on the observables are combined  
2512 by taking the envelope (i.e. the maximum variation in each  $\eta_{\text{CM}}^\mu$  range).

2513 The systematic uncertainties from the PDF and scale variations are summed in  
2514 quadrature, and amount to 0.1%. Thus, the theoretical uncertainties have negligible  
2515 impact on the signal efficiencies.

2516 **Tag-and-probe correction.** The main source of systematic uncertainty in the mea-  
2517 surement of the signal efficiency arises from the application of the TnP corrections. As  
2518 mentioned in Section 3.2.6.2, the statistical and systematic uncertainties of the TnP  
2519 corrections are derived from the muon identification, isolation and trigger efficiencies  
2520 measured in data.

2521 It is crucial to consider the correlation between the different TnP uncertainties  
2522 as a function of muon pseudorapidity and its charge, since they could cancel in the

2523 forward-backward ratios and muon charge asymmetry. The statistical TnP variations  
2524 are uncorrelated between the different  $\eta_{\text{lab}}$  ranges in which they were derived. The sys-  
2525 tematic TnP variations are considered to be fully correlated as a function of muon charge  
2526 since the detector response is the same for muons and anti-muons, and uncorrelated  
2527 between the different  $\eta_{\text{CM}}$  ranges (spanning different detectors).

2528 To compute the uncertainties, the muon charge asymmetry and the forward-backward  
2529 ratios are recalculated for each efficiency derived by varying the TnP corrections. The TnP  
2530 uncertainties are then determined by taking the difference between the value obtained  
2531 with the varied TnP correction and its nominal value, combining the uncertainties as  
2532 explained in Section 3.2.6.2. If the source of TnP correction is correlated in muon charge  
2533 or pseudorapidity, the corresponding signal yields are varied at the same time. Moreover,  
2534 for the  $W^\pm$  differential cross sections, the statistical and systematic TnP uncertainties  
2535 are calculated by propagating the uncertainties on the corrected signal efficiency.

2536 The systematic uncertainty due to the TnP corrections amounts to 3.2% and the  
2537 dominant TnP uncertainties are derived from the TnP systematic variations of the muon  
2538 isolation (2.5%) and trigger (1.1%) components.

### 2539 3.2.9.3 QCD jet background

2540 The systematic uncertainty in the QCD jet background originates from the uncertainty  
2541 in the modelling of the QCD jet  $p_T^{\text{miss}}$  distribution in the signal region. The nominal  
2542 procedure consists in fixing the parameters of the modified Rayleigh distribution from  
2543 the fits extrapolated from data as explained in Section 3.2.7.1. In order to estimate the  
2544 uncertainty of the mismodelling of the QCD jet background shape, both the parameters  
2545 and the functional form are varied.

2546 **QCD jet background parameters.** The first source of systematic uncertainty reflects  
2547 the possible mismodelling of the QCD jet background shape due to the  $\eta_{\text{CM}}^\mu$  dependence  
2548 of the QCD background parameters. In order to check this, the parameters of the nominal  
2549 QCD jet model are set free but constrained to be near their nominal values by using a  
2550 Gaussian penalty. The width of the penalty Gaussian function is fixed, for a given QCD  
2551 background parameter, to the root mean square (RMS) of the set of extrapolated results  
2552 along all  $\eta_{\text{CM}}^\mu$  ranges, shown in Figure 3.35. The RMS values used in the Gaussian  
2553 penalty for the  $\sigma_0$ ,  $\sigma_1$  and  $\sigma_2$  parameters are presented in Table 3.10. The difference  
2554 between the number of signal events extracted from the Gaussian-constrained fits and  
2555 the nominal fits is taken as the systematic uncertainty, which is then propagated to all

observables. This source of uncertainty is considered to be fully uncorrelated since the  $p_T^{\text{miss}}$  distribution in each  $\eta_{\text{CM}}^\mu$  range is fitted separately.

Parameter	RMS	
	$QCD \rightarrow \mu^-$	$QCD \rightarrow \mu^+$
$\sigma_0$	1.0	0.5
$\sigma_1$	0.9	0.9
$\sigma_2$	0.7	0.6

Table 3.10: The RMS of the set of QCD background parameters extrapolated along all  $\eta_{\text{CM}}^\mu$  regions.

Another systematic variation consists of changing the muon isolation point used to extrapolate the QCD background parameters. In the nominal case, the isolation point of 0.03 is determined from the average muon isolation value in data within the signal region. As an alternative case, the muon isolation distribution is checked in a QCD PYTHIA simulated sample satisfying the signal selection criteria, and the average isolation value is determined to be approximately 0.08. As a result, the QCD background parameters are recomputed by extrapolating them to an isolation point of  $I^\mu = 0.08$ , and the fits are redone by fixing the QCD background parameters to the extrapolated values in the  $\eta_{\text{CM}}^\mu$ -inclusive range as in the nominal case. The difference between the number of signal events extracted from the fits using the varied QCD background shape and the nominal results is taken as the systematic uncertainty. This uncertainty is propagated to all observables. The QCD background parameters extrapolated to  $I^\mu = 0.08$  are listed in Table 3.11. Since the result in each  $\eta_{\text{CM}}^\mu$  range varies independently, the uncertainty is considered to be fully uncorrelated.

Parameter	$QCD \rightarrow \mu^-$	$QCD \rightarrow \mu^+$
$\sigma_0$	14.67	14.79
$\sigma_1$	6.28	6.71
$\sigma_2$	0.50	0.49

Table 3.11: QCD shape parameters extrapolated to the average muon isolation point iso = 0.08.

The systematic uncertainty associated to the  $\eta_{\text{CM}}^\mu$  dependence of the QCD background parameters amounts to 1.1%, while the uncertainty corresponding to the change of extrapolation point represents 0.2%.

2575 **QCD jet background functional form.** To assign a systematic uncertainty due to  
2576 the assumed functional form for modelling the QCD jet background  $p_T^{\text{miss}}$  distribution,  
2577 the shape of the QCD jet background is described using a different model. The alternative  
2578  $p_T^{\text{miss}}$  functional form employed, taken from Ref.[167], is given by:

$$f_{\text{QCD}}(p_T^{\text{miss}}) = (p_T^{\text{miss}} + x_0)^{\alpha} \cdot \exp\left(\beta \cdot \sqrt{p_T^{\text{miss}} + x_0}\right) \quad (3.56)$$

2579 The extrapolation procedure explained in Section 3.2.7.1 is redone using the alterna-  
2580 tive model. All the fits are remade using the alternative QCD background functional form  
2581 fixed to the parameters extrapolated in the  $\eta_{\text{CM}}^{\mu}$ -inclusive range. The difference between  
2582 the number of signal events measured using the alternative QCD background model and  
2583 the nominal results is taken as the systematic uncertainty due to mismodelling of the  
2584 QCD jet background shape. This systematic uncertainty is propagated to all observables  
2585 and amounts to 0.6%. The bin-to-bin correlation is taken to be fully uncorrelated.

### 2586 3.2.9.4 Electroweak and $t\bar{t}$ backgrounds

2587 The  $t\bar{t}$  background and the different sources of electroweak background are described  
2588 using template histograms derived from simulations. The simulated samples are scaled  
2589 to the recorded integrated luminosity of data using the NLO POWHEG cross sections for  
2590 the electroweak processes and the CMS measured cross section for the  $t\bar{t}$  production.  
2591 Since for each these background sources, the ratio of background over signal events is  
2592 fixed to simulation when performing the fits, a systematic uncertainty is assigned to each  
2593 source by varying up and down their cross sections as explained below. The systematic  
2594 uncertainty in each  $\eta_{\text{CM}}^{\mu}$  range is derived by taking the maximum difference between  
2595 the nominal and the up/down variations. The bin-to-bin correlations in muon charge and  
2596 pseudorapidity are considered correlated since the total cross section is used to normalise  
2597 all simulated events.

2598 **Z/ $\gamma^*$   $\rightarrow \mu^+ \mu^-$  background.** The uncertainty on the ratio of Z/W total cross sections is  
2599 estimated using the Monte Carlo for FeMtobarn processes (MCFM) program [186] at  
2600 NLO with the CT14+EPPS16 nuclear PDFs. A relative uncertainty of 0.8% for  $Z/W^-$  and  
2601 1.3% for  $Z/W^+$  cross-section ratios is determined with MCFM taking into account the  
2602 PDF uncertainties. Since the cross sections in the muon channel depend on the branching  
2603 ratio associated to each process, their uncertainty has to also be taken into account.  
2604 The values of the branching ratios correspond to  $\text{BR}(Z \rightarrow \mu^+ \mu^-) = (3.366 \pm 0.007)\%$  and  
2605  $\text{BR}(W \rightarrow \mu \nu_\mu) = (10.63 \pm 0.15)\%$  [19], which gives a relative uncertainty on the ratio of

2606 Z/W branching ratios of 1.4%. Summing in quadrature the MCFM uncertainties with the  
 2607 ones derived from the branching ratios, one gets a total relative uncertainty for  $Z/W^+$   
 2608 of 1.6% and for  $Z/W^-$  of 1.9%. To be conservative the systematic variation is fixed to  
 2609 2% overall. The systematic uncertainty is then determined by varying the  $Z/\gamma^* \rightarrow \mu^+ \mu^-$   
 2610 cross section by 2% up and down when performing the fits, yielding a change of 0.3% in  
 2611 the measured  $W \rightarrow \mu \nu_\mu$  cross sections.

2612  **$Z/\gamma^* \rightarrow \tau \bar{\tau}$  background.** The uncertainty on the ratio of  $Z/\gamma^* \rightarrow \tau \bar{\tau}$  background over  
 2613 signal events is considered to be the same as the 2% uncertainty determined for the  
 2614  $Z/\gamma^* \rightarrow \mu^+ \mu^-$  background. Hence, the  $Z/\gamma^* \rightarrow \tau \bar{\tau}$  cross section is varied by 2% up and  
 2615 down when performing the fits. The impact of this systematic uncertainty is negligible  
 2616 and modifies the  $W \rightarrow \mu \nu_\mu$  cross sections by 0.01%.

2617  **$W \rightarrow \tau \nu_\tau$  background.** The values of the W-boson leptonic branching ratios correspond  
 2618 to  $\text{BR}(W \rightarrow \mu \nu_\mu) = (10.63 \pm 0.15)\%$  and  $\text{BR}(W \rightarrow \tau \nu_\tau) = (11.38 \pm 0.21)\%$  [19], which gives a  
 2619 relative uncertainty on the ratio of  $W \rightarrow \tau \nu_\tau$  over  $W \rightarrow \mu \nu_\mu$  cross sections of 2.3%. Thus,  
 2620 the systematic uncertainty is estimated by varying the ratio of  $W \rightarrow \tau \nu_\tau$  to signal events  
 2621 up and down by  $\pm 2.3\%$ . The impact of this systematic uncertainty on the  $W \rightarrow \mu \nu_\mu$  cross  
 2622 sections is found to be 0.04%.

2623  **$t \bar{t}$  background.** The  $t \bar{t}$  simulation is normalized using the CMS measured total cross  
 2624 section  $\sigma_{t \bar{t}} = 45 \pm 8 \text{ nb}^{-1}$  [181]. The systematic related to the  $t \bar{t}$  background normalization  
 2625 is computed by varying up and down the  $t \bar{t}$  cross section by its measured relative  
 2626 uncertainty ( $\pm 18\%$ ). This systematic uncertainty amounts to 0.2%.

### 2627 3.2.9.5 Weak boson $p_T$

2628 The modelling of the weak boson  $p_T$  in the signal and electroweak background simula-  
 2629 tions is corrected by weighing event-by-event the generated weak boson  $p_T$  distribution  
 2630 following the procedure described in Section 3.2.4. To determine the impact of the  
 2631 modelling of the weak boson  $p_T$ , the boson  $p_T$  corrections are removed and both the  
 2632 efficiency and the fits to the  $p_T^{\text{miss}}$  distribution are remade. The systematic uncertainty is  
 2633 determined in each  $\eta_{\text{CM}}^\mu$  range from the difference between the nominal results and the  
 2634 results obtained without weighing the generated boson  $p_T$  distribution. This uncertainty  
 2635 amounts to 0.5% and it is considered to be correlated with respect to muon charge and  
 2636 pseudorapidity.

**3.2.9.6 Event activity**

The modelling of the event activity present in p-Pb collisions is improved by weighing the distribution of the total HF energy, as explained in Section 3.2.5.1. The event activity is also correlated with other global variables, such as the number of tracks per event. Since the pseudorapidity coverage of the tracker ( $|\eta| < 2.5$ ) and the HF calorimeter ( $3.0 < |\eta| < 5.4$ ) is different, the HF energy and the track multiplicity are sensitive to different kinematic regions of the event activity. Thus, the systematic uncertainty on the modelling of the event activity is determined by weighing instead the distribution of the simulated track multiplicity following the same procedure as the one used for the HF energy. The fits to the  $p_T^{\text{miss}}$  distribution and the signal efficiency are recomputed after weighing the simulated track multiplicity distribution. The difference between the varied and nominal observables is assigned as the systematic uncertainty in each muon  $\eta_{\text{CM}}^\mu$  range. This uncertainty is considered correlated in muon charge and pseudorapidity, and it amounts to 0.6%.

**3.2.9.7 Recoil calibration**

The uncertainties due to the recoil calibration are of different nature: statistical and systematic. The statistical component arises from the uncertainties associated to the recoil scale and resolution derived from the fits to the recoil distributions from data. The systematic components arise from the following sources:

- The recoil calibration method employed to correct the simulated  $p_T^{\text{miss}}$  distribution;
- The choice of functional form used to fit the recoil distributions in each  $q_T^Z$  range;
- The parametrisation of the  $q_T$  dependence of the recoil scale and resolution.

**Statistical component.** In order to estimate the uncertainty associated to the recoil resolution, the weighed average Gaussian widths of the perpendicular and parallel recoil components, defined in Eq. (3.36), are randomly smeared in each  $q_T^Z$  range using a Gaussian distribution centred on the parameter value and with a width equal to the parameter uncertainty. The  $q_T$  dependence is parametrised again using the nominal functions presented in Eq. (3.35). The procedure is repeated a hundred times, and the recoil calibrations are applied to the simulated  $p_T^{\text{miss}}$  distributions, redoing the measurements every time. The RMS of the number of signal events extracted from the fits using each variation of the recoil calibration, is used to determine the statistical

2668 uncertainty of the recoil calibration. This uncertainty is propagated to all observables  
2669 and amounts to 0.09%. It is considered fully uncorrelated.

2670 **Systematic components.** The fit function used to parametrise the  $q_T$  dependence  
2671 of the recoil scale and resolution, is varied in both data and simulation to determine  
2672 the associated uncertainty. Instead of using the nominal functions for the Gaussian  
2673 mean (Eq. (3.33)) and Gaussian widths (Eq. (3.35)), a second order polynomial is used to  
2674 parametrise the Gaussian parameters with respect to  $q_T^Z$ . The varied recoil calibration  
2675 is applied to the simulated  $p_T^{\text{miss}}$  distributions, which are then used to extract the  
2676 signal from the data. The difference between the observables measured using the varied  
2677 recoil calibration and the nominal observables, in each  $\eta_{\text{CM}}^\mu$ , is assigned as a systematic  
2678 uncertainty.

2679 The uncertainty on the shape of the recoil distributions in each  $q_T^Z$  range is estimated  
2680 by varying the recoil fit model. Instead of using a sum of two Gaussian functions, the  
2681 recoil distributions are parametrised with a sum of a Breit-Wigner and a Gaussian  
2682 distribution, in both data and simulation (varied at the same time). The resulting  
2683  $q_T$  dependence of the recoil scale and resolution is determined following the nominal  
2684 procedure and the measurements are performed again. The systematic uncertainty is  
2685 determined as the variation between the observables derived with the varied recoil  
2686 calibration and the nominal ones.

2687 Moreover, the uncertainty associated to the method used to apply the recoil calibration  
2688 is determined by smearing the recoil distributions as described in Eq. (3.42), instead of  
2689 scaling them as done in the nominal case. The difference between the varied and nominal  
2690 observables in each  $\eta_{\text{CM}}^\mu$  is assigned as a systematic uncertainty.

2691 The largest source of systematic uncertainty in this case is the one associated to  
2692 the shape of the recoil distribution, which amounts to 0.3%. The uncertainty related  
2693 to the recoil calibration represents 0.2%, while the uncertainty corresponding to the  
2694  $q_T$  dependence of the recoil scale and resolution is determined to be 0.06%. These  
2695 uncertainties are considered correlated both in muon charge and pseudorapidity.

2696 **3.2.9.8 W-boson POWHEG BOX**

2697 The  $W \rightarrow \mu\nu_\mu$  simulations were generated using the POWHEG-BOX package `W_ew-BMMNP` [173],  
2698 in which electroweak NLO corrections are implemented. In order to asses the impact of  
2699 these NLO corrections on the final results, the  $W \rightarrow \mu\nu_\mu$  simulations were remade instead

2700 using the standard POWHEG-BOX package  $W$  [187], which does not include electroweak  
 2701 NLO corrections, following the same procedure described in Section 3.2.2.

2702 To determine the systematic uncertainty, the signal efficiencies and the template  
 2703 histograms for the signal were recomputed using the  $W \rightarrow \mu\nu_\mu$  simulations without elec-  
 2704 troweak NLO corrections. Then, the fits to the  $p_T^{\text{miss}}$  distribution in data were performed  
 2705 again, and the difference between the observables measured using the varied signal  
 2706 templates and the nominal results is assigned as a systematic uncertainty in each  $\eta_{\text{CM}}^\mu$   
 2707 range. This uncertainty amounts to 0.9% and it is considered to be fully correlated.

2708 **3.2.9.9 Summary of systematic uncertainties**

2709 The largest systematic uncertainty for each category among all  $\eta_{\text{CM}}^\mu$  ranges is sum-  
 2710 marised in Table 3.12. The systematic uncertainties are shown for each observable, in-  
 2711 cluding the  $W \rightarrow \mu\nu_\mu$  cross sections, muon charge asymmetry and the forward-backward  
 2712 ratios. The uncertainties presented for the cross sections are relative while those for the  
 2713 forward-backward ratios and the muon charge asymmetry are absolute.

Systematic Variation	$\sigma(W^- \rightarrow \mu^-\bar{\nu}_\mu)$ [%]	$\sigma(W^+ \rightarrow \mu^+\nu_\mu)$ [%]	$R_{\text{FB}}^-$	$R_{\text{FB}}^+$	$R_{\text{FB}}$	$\mathcal{A}_\mu$
Luminosity	3.5	3.5	0.000	0.000	0.000	0.000
Signal efficiency	3.0	3.2	0.026	0.037	0.030	0.011
QCD jet background	1.2	0.7	0.016	0.007	0.009	0.006
Electroweak and $t\bar{t}$ backgrounds	0.4	0.3	0.002	0.001	0.001	0.000
Weak boson $p_T$	0.5	0.4	0.001	0.001	0.001	0.001
Event activity	0.6	0.4	0.002	0.002	0.001	0.002
Recoil calibration	0.2	0.3	0.002	0.004	0.002	0.002
W-boson POWHEG-BOX	0.9	0.5	0.007	0.004	0.006	0.003
Total systematic uncertainty	4.8	4.8	0.030	0.038	0.031	0.013
Statistical uncertainty	2.4	2.0	0.026	0.029	0.019	0.015

Table 3.12: Maximum uncertainty of the measured observables determined for each category. The uncertainties of the  $W \rightarrow \mu\nu_\mu$  differential cross sections are relative while for the forward-backward ratios and muon charge asymmetry are absolute.

2714 The uncertainties of the measurements are shown in Figure 3.37 as a function of  
 2715  $\eta_{\text{CM}}^\mu$ . They are observed to be similar between the different  $\eta_{\text{CM}}^\mu$  ranges, except for the  
 2716 most backward and forward regions, which are driven by the systematic uncertainty  
 2717 on the signal efficiency. It is also seen that the systematic uncertainties dominates on  
 2718 the  $W^\pm \rightarrow \mu^\pm\nu_\mu$  differential cross sections and the forward-backward ratios in all  $\eta_{\text{CM}}^\mu$   
 2719 ranges. In the case of the muon charge asymmetry, most of the systematic uncertainties  
 2720 are found to be suppressed due to the correlations in muon charge, and as a result, the  
 2721 statistical uncertainties dominates in most of the  $\eta_{\text{CM}}^\mu$  ranges.

### 3.2. ANALYSIS

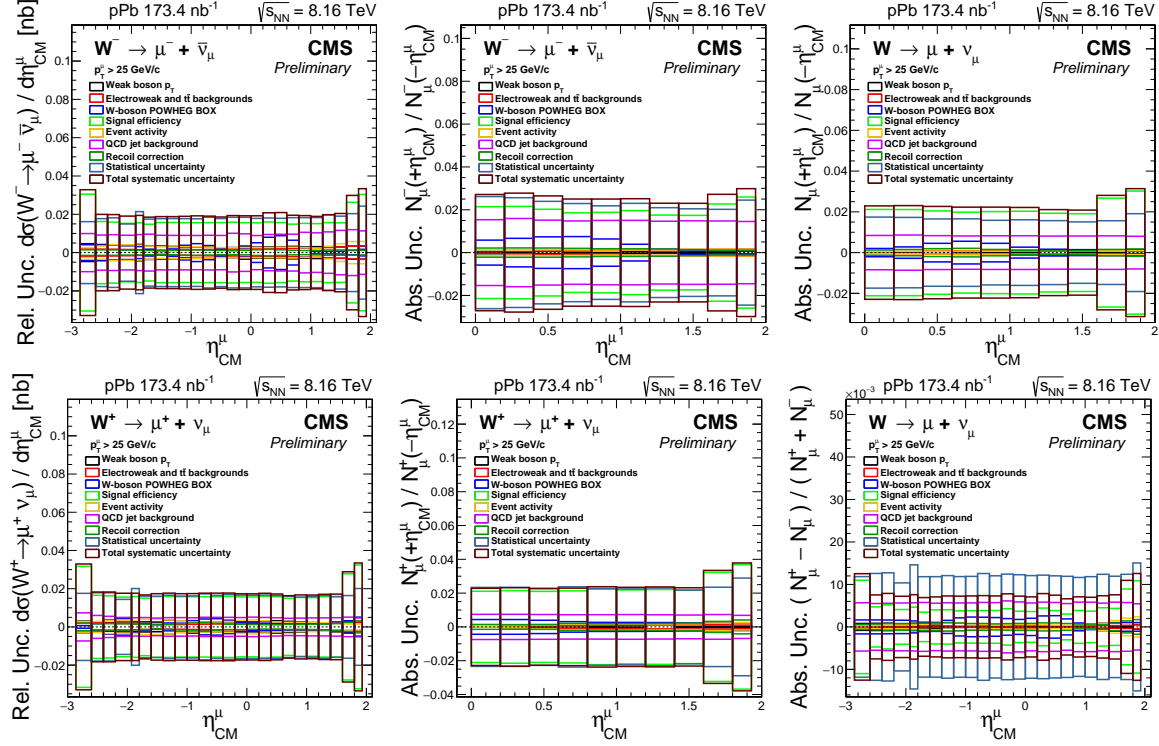


Figure 3.37: Uncertainty corresponding to each category as function of the muon  $\eta_{\text{CM}}$ . The plots are divided as:  $W^- \rightarrow \mu^- \bar{\nu}_\mu$  (top-left) and  $W^+ \rightarrow \mu^+ \nu_\mu$  (bottom-left) differential cross sections,  $W^- \rightarrow \mu^- \bar{\nu}_\mu$  (top-middle) and  $W^+ \rightarrow \mu^+ \nu_\mu$  (bottom-middle) forward-backward ratios, and finally the charge-summed forward-backward ratio (top-right) and muon charge asymmetry (bottom-right). The uncertainties of the cross sections are relative while for the forward-backward ratios and muon charge asymmetry are absolute. The global luminosity uncertainty of 3.5% is not included.

#### 3.2.9.10 Covariance matrix

The covariance matrices of the  $W \rightarrow \mu\nu_\mu$  differential cross sections, the forward-backward ratios and the muon charge asymmetry are computed by taking into account the measurements extracted in each  $\eta_{\text{CM}}^\mu$  range. In the case of the  $W^\pm \rightarrow \mu^\pm \nu_\mu$  differential cross sections and the  $W^\pm \rightarrow \mu^\pm \nu_\mu$  forward-backward ratios, the matrices are made of 48x48 entries (24 muon  $\eta_{\text{CM}}^\mu$  ranges times two muon charge measurements), while for the muon charge asymmetry and the charge-summed forward-backward ratio, only 24x24 entries are considered.

For a given (i,j) entry of the covariance matrix, the covariance is calculated as the uncertainty in bin i times the uncertainty in bin j. If the uncertainty is uncorrelated, the off-diagonal elements are set to zero. The total covariance matrix of each observable is

2733 determined by summing the covariance matrix of the statistical uncertainty together  
2734 with the covariance matrices of all the systematic uncertainties.

2735 The covariance matrix of the statistical uncertainty corresponds to a fully diagonal  
2736 matrix where each (i, i) element in the diagonal is the square of the statistical uncer-  
2737 tainty of bin i. On the other hand, the covariance matrix of each systematic uncertainty  
2738 is computed by taking into account the bin-to-bin correlations in muon charge and  
2739 pseudorapidity.

2740 The total correlation matrix of each observable is derived from the total covariance  
2741 matrix, using the following formula:

$$\text{corr}(i, j) = \frac{\text{cov}(i, j)}{\sqrt{\text{cov}(i, i) * \text{cov}(j, j)}} \quad (3.57)$$

2742 The corresponding correlation matrices are shown in Figure 3.38. The black lines  
2743 are used to distinguish the different bins in muon charge, which are ordered in a given  
2744 plot from top to bottom as: Minus-Minus, Minus-Plus, Plus-Minus and Plus-Plus. The  
2745 large correlation observed in the  $W \rightarrow \mu\nu_\mu$  differential cross sections arise from the  
2746 luminosity uncertainty. On the other hand, the anti-correlation seen in the muon charge  
2747 asymmetry derive from the TnP corrections for muon isolation and identification, which  
2748 are applied as a function of  $|\eta_{\text{lab}}|$  and thus, introduces correlations between the backward  
2749 and forward pseudorapidity regions.

### 2750 3.3 Results

2751 This section presents the analysis results of the W-boson production in pPb collisions at  
2752  $\sqrt{s_{\text{NN}}} = 8.16 \text{ TeV}$ . The W-boson yields are extracted in the muon kinematic region defined  
2753 by  $p_T^\mu > 25 \text{ GeV}/c$  and  $|\eta_{\text{lab}}^\mu| < 2.4$ . The  $W \rightarrow \mu\nu_\mu$  differential cross sections, the muon  
2754 charge asymmetry, and the forward-backward ratios are measured as a function of muon  
2755  $\eta_{\text{CM}}^\mu$ . The measurements are compared to PDF calculations with and without including  
2756 nuclear modifications.

#### 2757 3.3.1 W-boson production in p-Pb at 8.16 TeV

2758 The  $W^\pm \rightarrow \mu^\pm \nu_\mu$  differential cross sections are derived using Eq. (3.52). The results of the  
2759 differential cross sections of  $W^+ \rightarrow \mu^+ \nu_\mu$  and  $W^- \rightarrow \mu^- \bar{\nu}_\mu$  are shown as a function muon  
2760  $\eta_{\text{CM}}^\mu$  in Figure 3.39. The vertical error bars represent the statistical uncertainties from  
2761 the number of  $W \rightarrow \mu\nu_\mu$  events measured in each  $\eta_{\text{CM}}^\mu$  range, while the brackets show

### 3.3. RESULTS

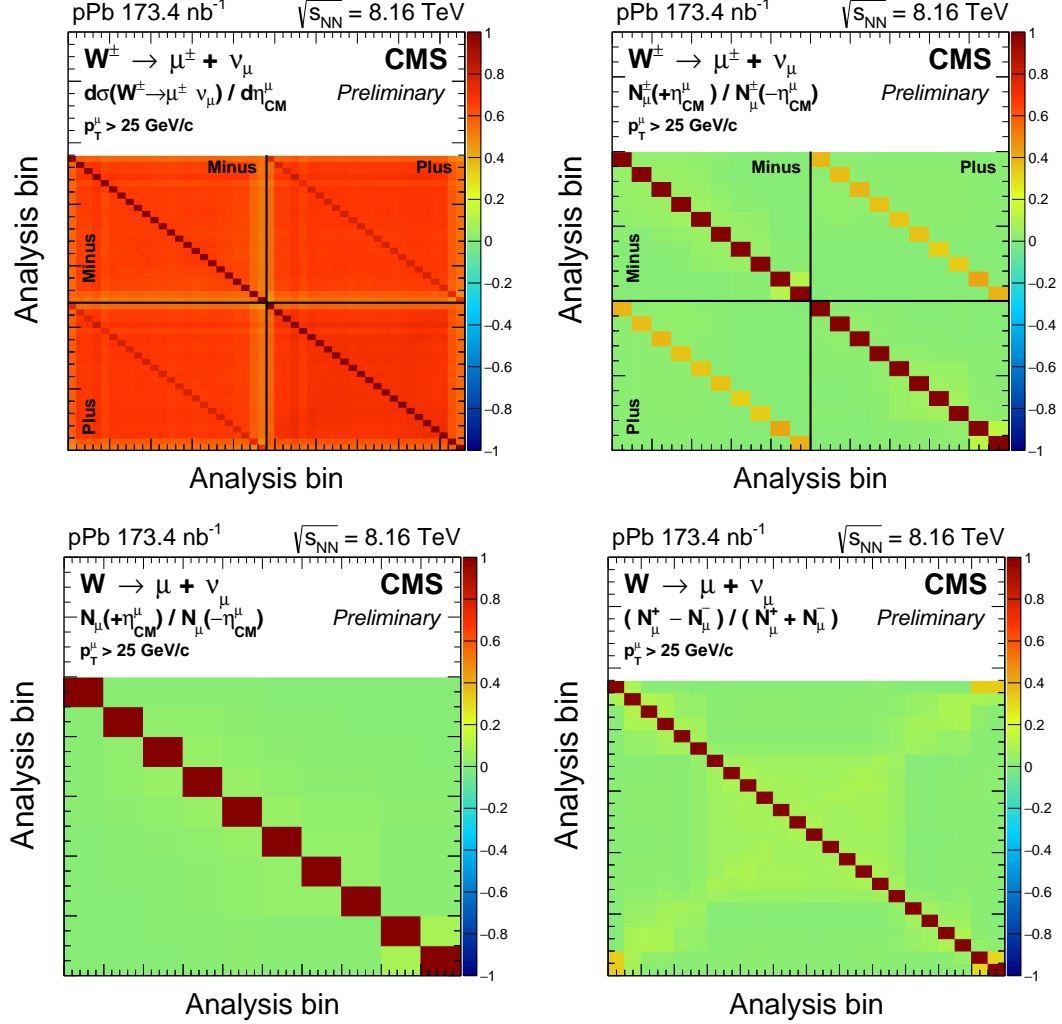


Figure 3.38: Correlation matrices for:  $W^\pm$  cross section (top-left),  $W^\pm R_{FB}$  (top-right), charge-inclusive  $R_{FB}$  (bottom-left), and charge asymmetry (bottom-right). The lines in the top plots are used to separate the different muon charge bins.

2762 the statistical and total systematic uncertainties summed in quadrature. The global  
2763 integrated luminosity uncertainty of 3.5% [168] is not shown in the figures.

2764 The opposite trend seen between the  $W^+ \rightarrow \mu^+ \nu_\mu$  and  $W^- \rightarrow \mu^- \bar{\nu}_\mu$  differential cross  
2765 sections as a function of  $\eta_{CM}^\mu$  is expected from parity violation of the electroweak interac-  
2766 tion. The  $W^+$  bosons decay to a right-handed anti-muon boosted in the opposite direction,  
2767 while the  $W^-$  bosons decay to a left-handed muon along the direction of the  $W^-$  boson.

2768 The muon charge asymmetry is determined from the efficiency-corrected signal event  
2769 yields using Eq. (3.53). The measured muon charge asymmetry is shown in Figure 3.40  
2770 as a function muon  $\eta_{CM}^\mu$ .

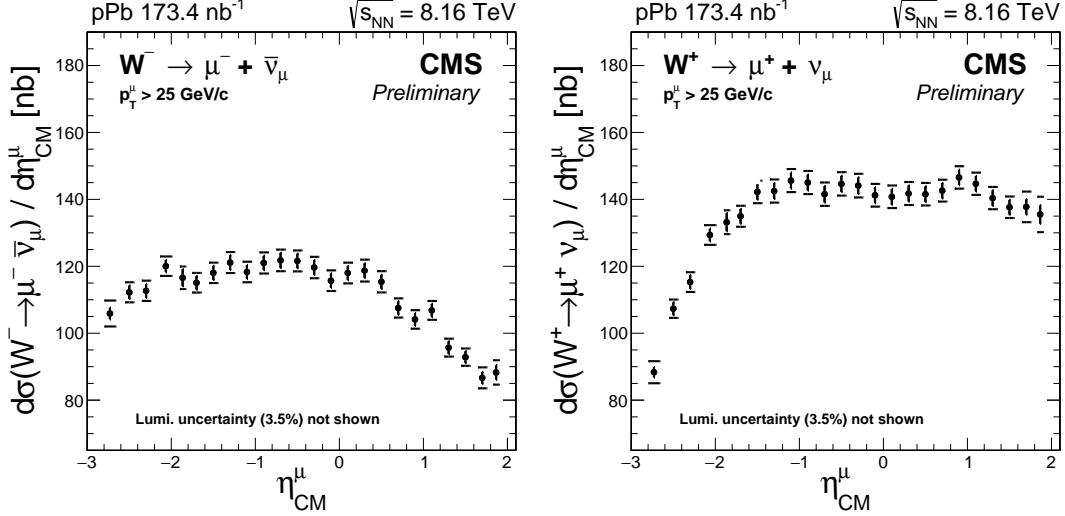


Figure 3.39: Differential production cross sections for  $W^+ \rightarrow \mu^+ \nu_\mu$  (left) and  $W^- \rightarrow \mu^- \bar{\nu}_\mu$  (right), as a function of the muon pseudorapidity in the center-of-mass frame. The brackets represent the statistical and systematic uncertainties summed in quadrature, while the error bars show the statistical uncertainties only. The global luminosity uncertainty of 3.5% [168] is not shown.

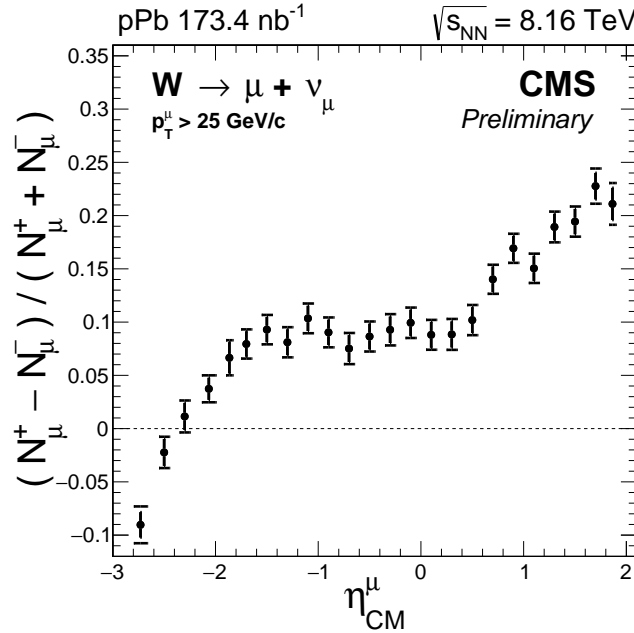


Figure 3.40: Muon charge asymmetry as a function of the muon pseudorapidity in the center-of-mass frame. The brackets represent the statistical and systematic uncertainties summed in quadrature, while the error bars show the statistical uncertainties only.

### 3.3. RESULTS

2771 The  $W^+ \rightarrow \mu^+ \nu_\mu$  and  $W^- \rightarrow \mu^- \bar{\nu}_\mu$  forward-backward ratios are computed using  
 2772 Eq. (3.54), while the charge-summed forward-backward ratio is determined using Eq. (3.55).  
 2773 As mentioned in Section 3.2.1, the forward region ( $\eta_{CM}^\mu > 0$ ) is defined on the proton-going  
 2774 direction while the backward region corresponds to the Pb-going direction. The results of  
 2775 the muon forward-backward ratios are shown in Figure 3.41.

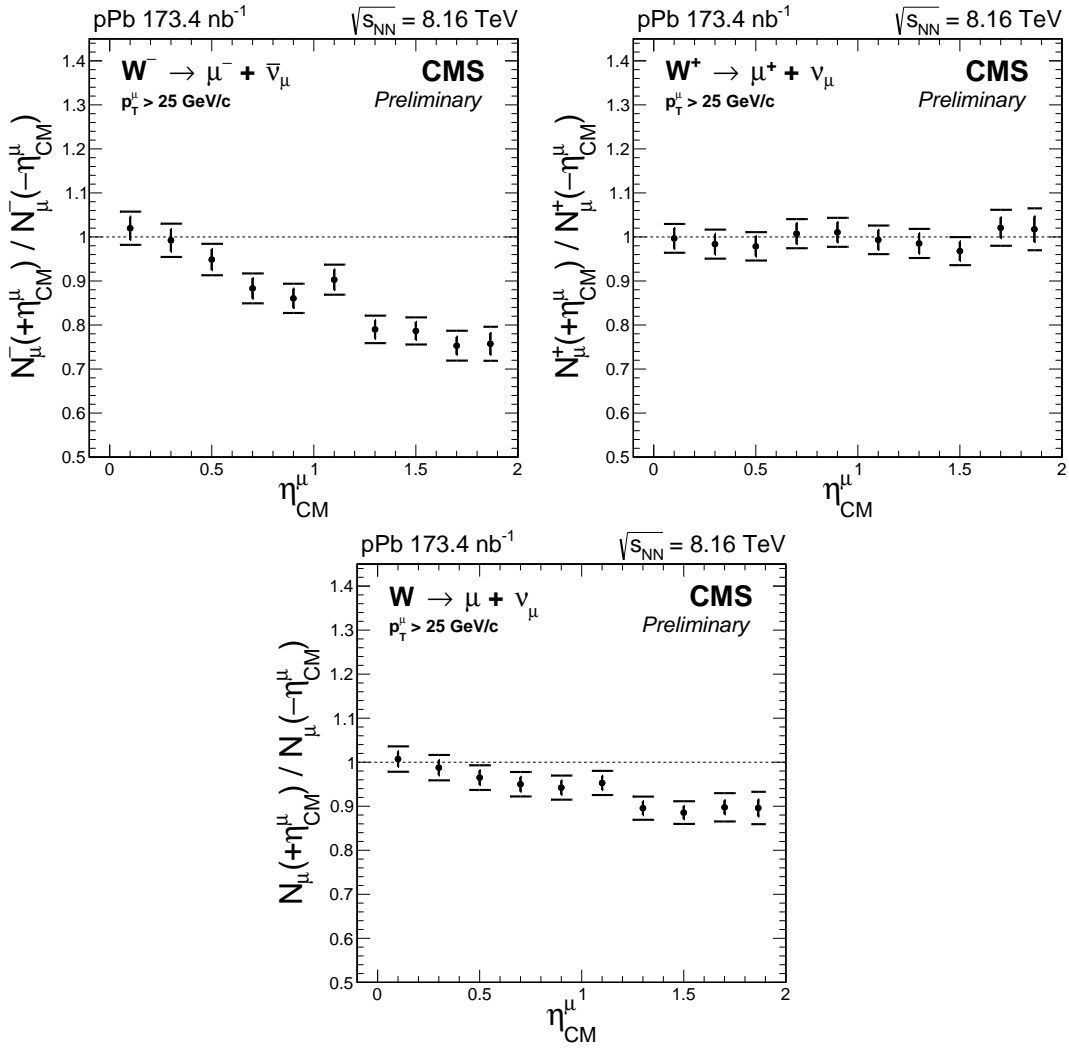


Figure 3.41: Forward-backward ratios, for the positive (top-left), negative (top-right) and all (bottom) charged muons. The brackets represent the statistical and systematic uncertainties summed in quadrature, while the error bars show the statistical uncertainties only.

**3.3.2 Comparison with theoretical models**

The measurements of the W-boson production in p-Pb collisions at 8.16 TeV are compared to three NLO PDF calculations. In all three PDF calculations, the isospin effect is taking into account for the Pb nucleus. A description of each PDF model is provided below:

- CT14: this model assumes no nuclear modifications and uses the NLO CT14 proton PDF for both the incoming proton and Pb-ion.
- CT14+EPPS16: this PDF model employs the CT14 PDF for the incoming proton and apply the EPPS16 nuclear corrections on the CT14 PDF for the incoming Pb-ion.
- CT14+nCTEQ15: this PDF model makes use of the CT14 PDF for the incoming proton and the nCTEQ15 nuclear PDF for the incoming Pb-ion.

The results of the PDF models are derived using the parton-level Monte Carlo program MCFM [186]. The comparison between the PDF calculations and the data are shown in Figure 3.42 for the  $W \rightarrow \mu\nu_\mu$  differential cross sections, in Figure 3.43 for the muon charge asymmetry and in Figure 3.44 for the forward-backward ratios. In all figures, the results of the CT14 PDF model calculations are shown using continuous lines, while the CT14+EPPS16 and CT14+nCTEQ15, are shown with green and brown dashed lines, respectively.

As can be seen in Figure 3.42, the  $W \rightarrow \mu\nu_\mu$  cross section measurements at forward rapidity favour the PDF calculations including nuclear modifications, while at backward rapidity all three PDF calculations are in good agreement with the data. Moreover, in the case of the muon charge asymmetry shown in Figure 3.43, the results of the theory calculations derived using the CT14 proton PDF only, and those including the EPPS16 nuclear modifications, are in good agreement with the measurements, while the nCTEQ15 nPDF calculations expect a slightly larger muon charge asymmetry in the most backward  $\eta_{CM}^\mu$  range. Finally, from the ratios of the signal event yields at forward-over-backward  $\eta_{CM}^\mu$  displayed in Figure 3.44, the nuclear PDF calculations describe much better the data compared to the free-nucleon PDF calculation.

In order to quantify the level of agreement between each PDF calculation and the measurements of the W-boson production in p-Pb collisions, a  $\chi^2$  test is performed according to:

### 3.3. RESULTS

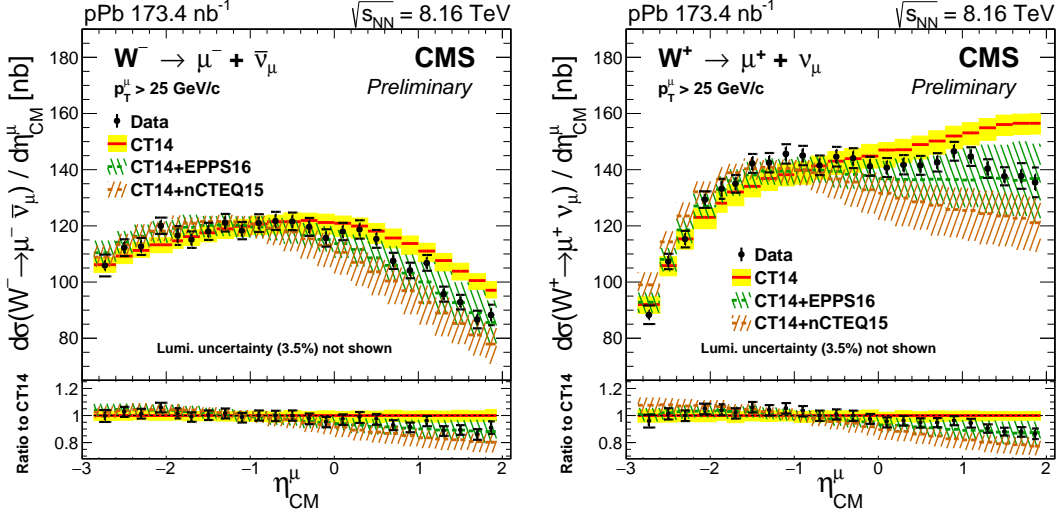


Figure 3.42: Differential cross sections for  $W^+ \rightarrow \mu^+ \nu_\mu$  (left) and  $W^- \rightarrow \mu^- \bar{\nu}_\mu$  (right), as a function of the muon  $\eta_\mu^{\text{CM}}$ . Errors bars represent the statistical uncertainties, while the brackets represent the statistical and systematic uncertainties summed in quadrature. The global luminosity uncertainty of 3.5% is not displayed. Theoretical predictions with (CT14+EPPS16 shown in dashed green line and CT14+nCTEQ15 shown in dashed brown line) and without (CT14, solid red line) PDF nuclear modifications are also shown, with the uncertainty bands include the PDF uncertainties.

$$\chi^2 = \sum_i \sum_j \left[ (t(i) - d(i)) \cdot (\text{COV}_{\text{data}} + \text{COV}_{\text{theory}})^{-1} [i, j] \cdot (t(j) - d(j)) \right] \quad (3.58)$$

where  $t(i)$  is the value of the observable derived from the PDF calculation in bin  $i$ ,  $d(j)$  is the value of the observable measured in data in bin  $j$ , and  $(\text{COV}_{\text{data}} + \text{COV}_{\text{theory}})^{-1}$  is the inverse of the sum of the covariance matrices extracted from the data and PDF calculations. This approach takes into account the bin-to-bin correlations in both muon charge and pseudorapidity.

The outcome of the  $\chi^2$  statistical test derived using the CT14 PDF, CT14+EPPS16 nPDF and CT14+nCTEQ15 nPDF calculations are summarized in Table 3.13. The results of the CT14 PDF calculations are significantly disfavoured by the measurements, while the PDF calculations including nuclear modifications are in good agreement. In addition, the measurements tend to favour the nPDF calculations of the CT14+EPPS16 model over the ones from the CT14+nCTEQ15 model.

Considering the smaller size of the uncertainties of the measurements compared to those from the PDF models, the measurements have the potential to constrain the parametrisations of the EPPS16 nuclear modifications and the nCTEQ15 nuclear PDFs.

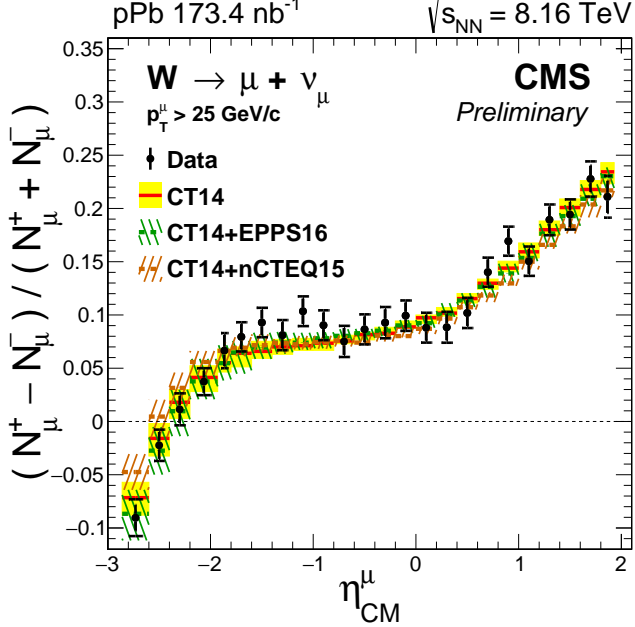


Figure 3.43: Muon charge asymmetry of  $W \rightarrow \mu\nu_\mu$ , given for each muon  $\eta_{\text{CM}}^\mu$  range. Errors bars represent the statistical uncertainties, while the brackets represent the statistical and systematic uncertainties summed in quadrature. Theoretical predictions with (CT14+EPPS16 shown in dashed green line and CT14+nCTEQ15 shown in dashed brown line) and without (CT14, solid red line) PDF nuclear modifications are also shown, with the uncertainty bands. All theory uncertainty bands include the PDF uncertainties.

Observable	CT14			CT14+EPPS16			CT14+nCTEQ15		
	$\chi^2$	ndf	Prob.(%)	$\chi^2$	ndf	Prob.(%)	$\chi^2$	ndf	Prob.(%)
$d\sigma(W^\pm \rightarrow \mu^\pm \nu_\mu) / d\eta_{\text{CM}}^\mu$	135	48	$3 \times 10^{-8}$	32	48	96	40	48	79
$(N_\mu^+ - N_\mu^-) / (N_\mu^+ + N_\mu^-)$	23	24	54	18	24	80	29	24	23
$N_\mu^\pm (+\eta_{\text{CM}}^\mu) / N_\mu^\pm (-\eta_{\text{CM}}^\mu)$	98	20	$3 \times 10^{-10}$	11	20	95	14	20	83
$N_\mu (+\eta_{\text{CM}}^\mu) / N_\mu (-\eta_{\text{CM}}^\mu)$	87	10	$2 \times 10^{-12}$	3	10	99	5	10	90

Table 3.13: Results of the  $\chi^2$  statistical test between the measurements and the theory calculations from the CT14 PDF, CT14+EPPS16 nPDF and CT14+nCTEQ15 nPDF models. The value of the  $\chi^2$ , the number of degrees of freedom (ndf) and the  $\chi^2$  probability (Prob.), are presented for the  $W^\pm \rightarrow \mu^\pm \nu_\mu$  differential cross sections, the muon charge asymmetry, the  $W^\pm \rightarrow \mu^\pm \nu_\mu$  forward-backward ratios, and the charge-summed forward-backward ratio, respectively.

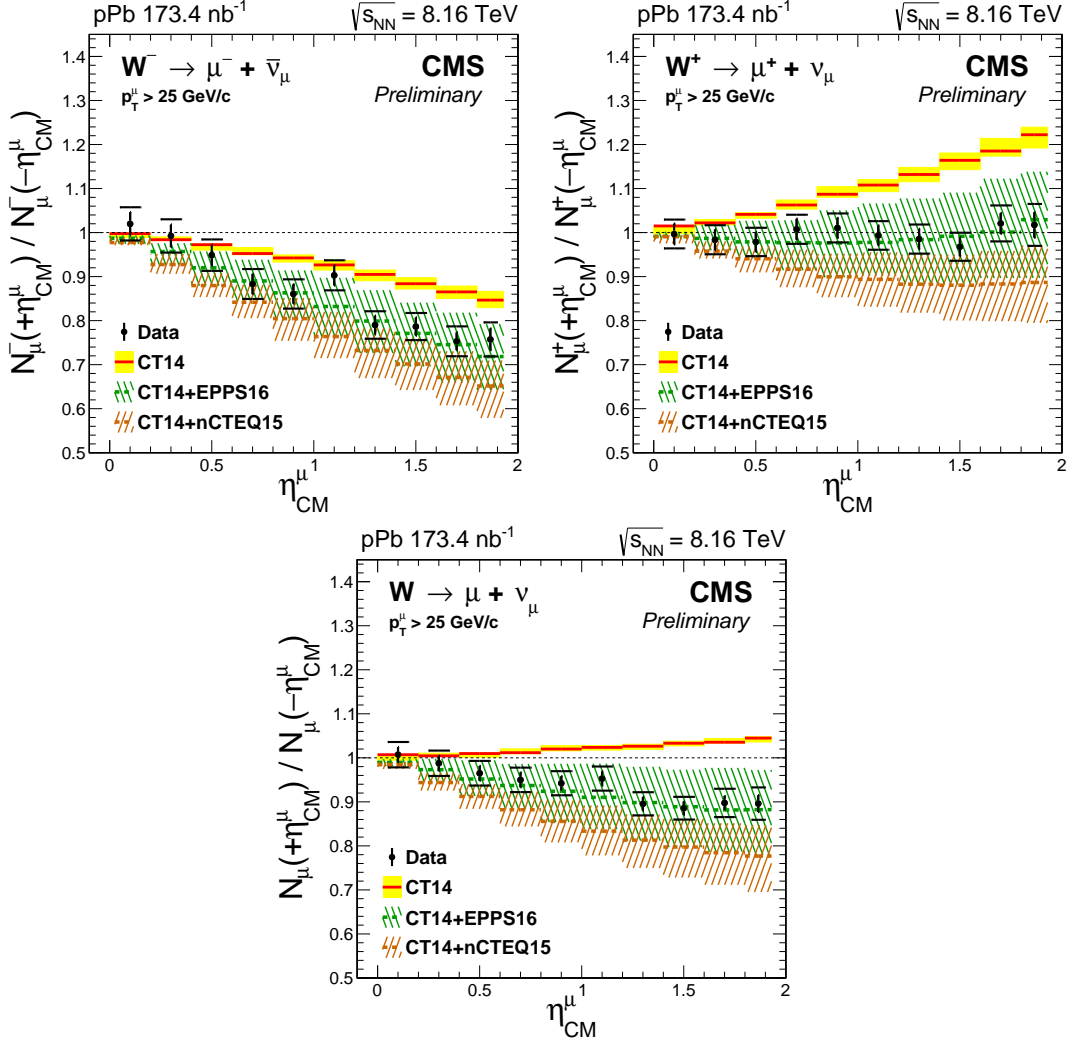


Figure 3.44: Forward-backward ratio of  $W \rightarrow \mu\nu_{\mu}$ , given for each muon  $\eta_{CM}^{\mu}$  range separated in negative (top-left), positive (top-right) and all (bottom) charged muons. Errors bars represent the statistical uncertainties, while the brackets represent the statistical and systematic uncertainties summed in quadrature. Theoretical predictions with (CT14+EPPS16 shown in dashed green line and CT14+nCTEQ15 shown in dashed brown line) and without (CT14, solid red line) PDF nuclear modifications are also shown, with the uncertainty bands include the PDF uncertainties.



2821

C H A P T E R



2822

## CHARMONIA

2823      **T**his chapter reports the measurement of the production of  $J/\psi$  and  $\psi(2S)$  mesons  
2824      in lead-lead (Pb-Pb) collisions compared to p-p collisions at  $\sqrt{s_{\text{NN}}} = 5.02 \text{ TeV}$ . A  
2825      brief introduction to the theory of charmonium physics in heavy-ion collisions  
2826      and an summary of some of the latest measurements of charmonium production in Pb-Pb  
2827      collisions are presented in Section 4.1. The charmonia analysis is then described in  
2828      detailed in Section 4.2. Section 4.3 presents the results of the charmonia analysis and  
2829      compares them to the latest charmonium measurements at LHC.

2830 **4.1 Theory**

2831 **4.1.1 Charmonium hadronic production**

2832 **4.1.1.1 Colour singlet model**

2833 **4.1.1.2 Colour evaporation model**

2834 **4.1.1.3 Nonrelativistic QCD**

2835 **4.1.1.4 Nonprompt charmonium production**

2836 **4.1.2 Cold nuclear matter effects**

2837 **4.1.3 Hot nuclear matter effects**

2838 **4.1.4 Experimental results in Pb-Pb collisions at LHC**

## 4.2. ANALYSIS

**4.2 Analysis****4.2.1 Dataset and simulated samples****4.2.1.1 Dataset****4.2.1.2 Simulations****4.2.2 Event selection****4.2.2.1 Global event filter****4.2.2.2 Trigger****4.2.2.3 Centrality determination****4.2.2.4 Muon selection****4.2.2.5 Muon kinematic cut****4.2.2.6  $\text{J}/\psi$  meson selection****4.2.3  $\text{J}/\psi$ -meson yield extraction****4.2.3.1 Invariant mass parameterisation****Parameterisation of  $\text{J}/\psi$ -meson  $m_{\mu^+\mu^-}$  distribution****Parameterisation of background  $m_{\mu^+\mu^-}$  distribution****4.2.3.2 Pseudo-proper decay length parameterisation****Parameterisation of  $\sigma_\ell$  distribution****Parameterisation of  $\ell_{\text{J}/\psi}$  resolution****Parameterisation of  $\ell_{\text{J}/\psi}$  distribution of nonprompt  $\text{J}/\psi$  mesons****Parameterisation of background  $\ell_{\text{J}/\psi}$  distribution****4.2.3.3 Two-dimensional fit of  $m_{\mu^+\mu^-}$  and  $\ell_{\text{J}/\psi}$** **4.2.4 Signal acceptance and efficiency****4.2.4.1  $\text{J}/\psi$  meson acceptance****4.2.4.2  $\text{J}/\psi$  meson efficiency****4.2.4.3 Corrected  $\text{J}/\psi$  meson efficiency<sup>148</sup>****4.2.5 Systematic uncertainties****Variation of  $\text{J}/\psi$ -meson invariant mass parameters**

2875 **4.3 Results**



## CONCLUSION





## RESULTS OF THE FITS FOR THE W BOSON ANALYSIS

The results of the fits to the  $p_T^{\text{miss}}$  distribution in data are shown in Figure A.1 for  $W^- \rightarrow \mu^- \bar{\nu}_\mu$  events, in Figure A.2 for  $W^+ \rightarrow \mu^+ \nu_\mu$  events, and in Figure A.3 for the  $\eta_{\text{CM}}^\mu$ -inclusive range.

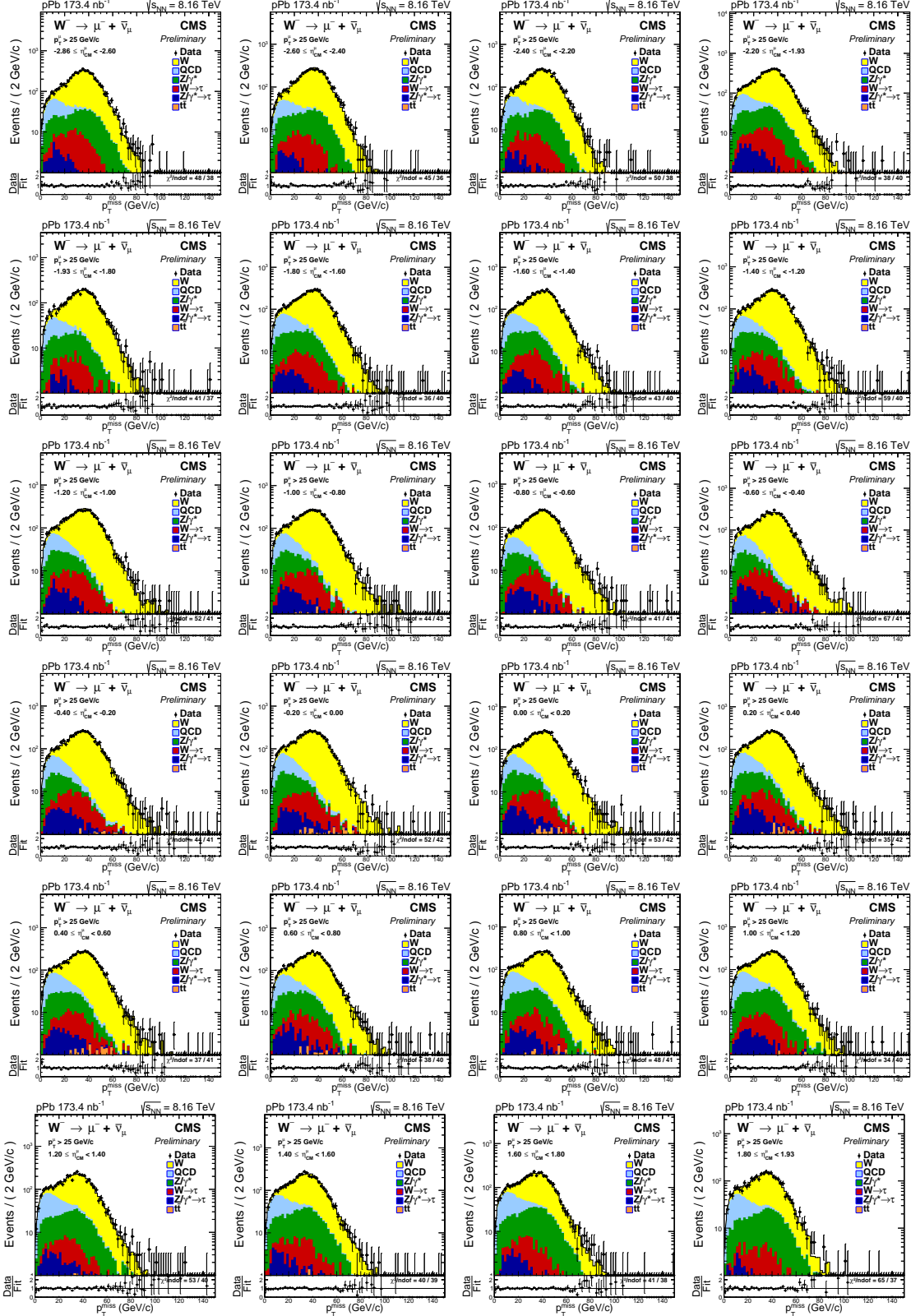


Figure A.1: The  $p_T^{\text{miss}}$  distribution for  $W^- \rightarrow \mu^- \bar{\nu}_\mu$  events within each fitted  $\eta_{\text{CM}}^\mu$  range, shown in logarithmic scale. Unbinned fits to the data (black points) are performed with six contributions, stacked from top to bottom:  $W^+ \rightarrow \mu^+ \nu_\mu$  (yellow), QCD multijet (light blue),  $Z/\gamma^* \rightarrow \mu^+ \mu^-$  (green),  $W^+ \rightarrow \bar{\tau} \nu_\tau$  (red),  $Z/\gamma^* \rightarrow \tau \bar{\tau}$  (dark blue) and  $t\bar{t}$  (orange). Error bars represent statistical uncertainties. The lower panels display the data divided by the result of the fit, for each  $\eta_{\text{CM}}^\mu$  range. The  $\chi^2$  test value over the number of degrees of freedom is also shown.

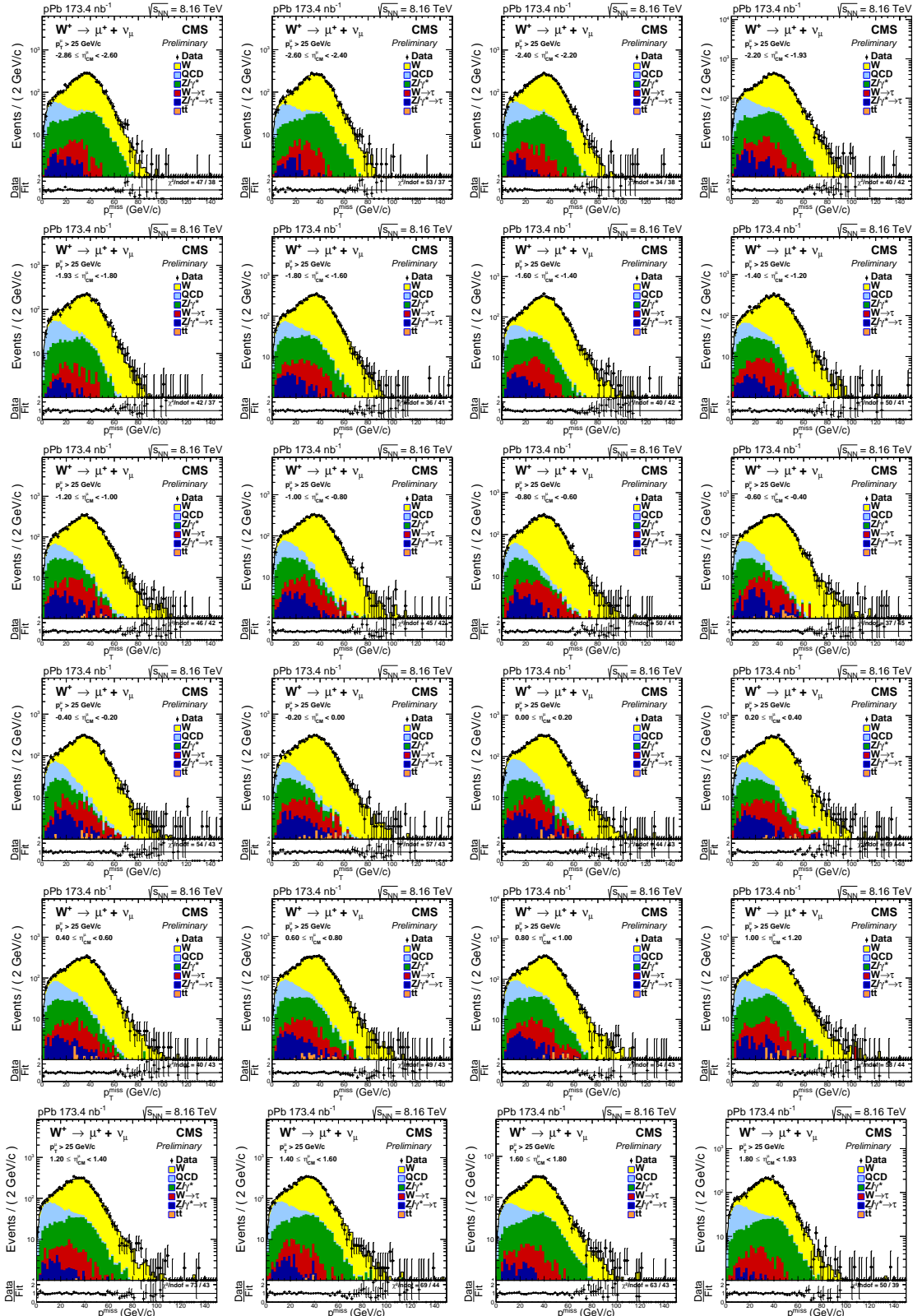


Figure A.2: The  $p_T^{\text{miss}}$  distribution for  $W^+ \rightarrow \mu^+ \nu_\mu$  events within each fitted  $\eta_{\text{CM}}^\mu$  range, shown in logarithmic scale. Unbinned fits to the data (black points) are performed with six contributions, stacked from top to bottom:  $W^+ \rightarrow \mu^+ \nu_\mu$  (yellow), QCD multijet (light blue),  $Z/\gamma^* \rightarrow \mu^+ \mu^-$  (green),  $W^+ \rightarrow \bar{\tau} \nu_\tau$  (red),  $Z/\gamma^* \rightarrow \tau \bar{\tau}$  (dark blue) and  $t\bar{t}$  (orange). Error bars represent statistical uncertainties. The lower panels display the data divided by the result of the fit, for each  $\eta_{\text{CM}}^\mu$  range. The  $\chi^2$  test value over the number of degrees of freedom is also shown.

APPENDIX A. RESULTS OF THE FITS FOR THE W BOSON ANALYSIS

---

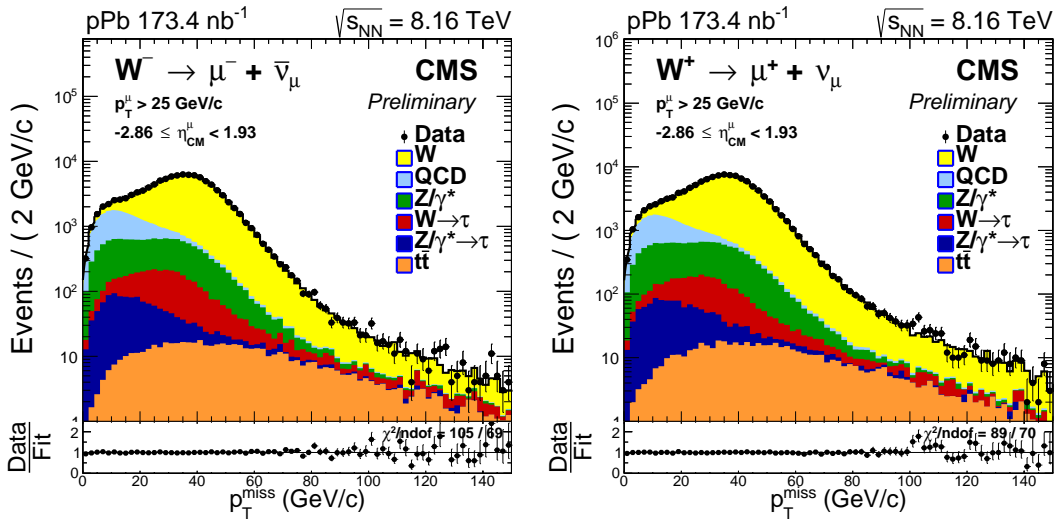


Figure A.3: The  $p_T^{\text{miss}}$  distribution for  $W^+ \rightarrow \mu^+ \nu_\mu$  (left) and  $W^- \rightarrow \mu^- \bar{\nu}_\mu$  (right) events within the  $\eta_{CM}^\mu$ -inclusive range, shown in logarithmic scale. Unbinned fits to the data (black points) are performed with six contributions, stacked from top to bottom:  $W \rightarrow \mu \nu_\mu$  (yellow), QCD multijet (light blue),  $Z/\gamma^* \rightarrow \mu^+ \mu^-$  (green),  $W \rightarrow \tau \nu_\tau$  (red),  $Z/\gamma^* \rightarrow \tau \bar{\tau}$  (dark blue) and  $t\bar{t}$  (orange). Error bars represent statistical uncertainties. The lower panels display the data divided by the result of the fit, for each  $\eta_{CM}^\mu$  range. The  $\chi^2$  test value over the number of degrees of freedom is also shown.

## BIBLIOGRAPHY

- [1] A. G. Stahl Leiton, “nPDF studies with electroweak bosons in pPb collisions at 8.16 TeV with the CMS detector”, XXVII International Conference on Ultrarelativistic Nucleus-Nucleus Collisions (Quark Matter 2018): Venice, Italy, May 14-19, 2018, 2018, unpublished. [[Cited on page 2.](#)]
- [2] A. G. Stahl Leiton, “nPDF studies with electroweak bosons in pPb collisions with the CMS detector”, XXXIX International Conference on High Energy Physics (ICHEP 2018): Seoul, Korea, July 4-11, 2018, 2018, unpublished. [[Cited on page 2.](#)]
- [3] CMS Collaboration, “Constraints on nuclear parton distributions from W boson production in pPb collisions at  $\sqrt{s_{NN}} = 8.16 \text{ TeV}$ ”, Tech. Rep. CMS-PAS-HIN-17-007, CERN, Geneva, 2018. [[Cited on page 2.](#)]
- [4] CMS Collaboration, A. M. Sirunyan *et al.*, “Relative Modification of Prompt  $\psi(2S)$  and  $J/\psi$  Yields from pp to PbPb Collisions at  $\sqrt{s_{NN}} = 5.02 \text{ TeV}$ ”, *Phys. Rev. Lett.* **118** (2017), no. 16, 162301, arXiv:1611.01438. [[Cited on page 2.](#)]
- [5] CMS Collaboration, A. M. Sirunyan *et al.*, “Measurement of prompt and nonprompt charmonium suppression in PbPb collisions at 5.02 TeV”, *Eur. Phys. J. C* **78** (2018), no. 6, 509, arXiv:1712.08959. [[Cited on page 2.](#)]
- [6] CMS Collaboration, A. G. Stahl, “Charmonium production in pp, pPb and PbPb collisions with CMS”, in “Proceedings, Hot Quarks 2016: Workshop for Young Scientists on the Physics of Ultrarelativistic Nucleus-Nucleus Collisions (HQ2016): South Padre Island, Texas, September 12-17, 2016”, vol. 832, p. 012031. 2017. [[Cited on page 2.](#)]
- [7] CMS Collaboration, A. G. Stahl Leiton, “Charmonium production in pPb and PbPb collisions at 5.02 TeV with CMS”, in “Proceedings, 2017 European Physical

## BIBLIOGRAPHY

---

- Society Conference on High Energy Physics (EPS-HEP 2017): Venice, Italy, July 5-12, 2017”, p. 196. 2017. [Cited on page 2.]
- [8] E. Fermi, “Sulla quantizzazione del gas perfetto monoatomico”, *Rendiconti Lincei* **3** (1926) 145. [Cited on page 4.]
- [9] P. A. M. Dirac, “On the theory of quantum mechanics”, *Proceedings of the Royal Society of London A: Mathematical, Physical and Engineering Sciences* **112** (1926), no. 762, 661,  
<http://rspa.royalsocietypublishing.org/content/112/762/661.full.pdf>.  
[Cited on page 4.]
- [10] W. Pauli, “”, *Zeitschrift für Physik* **31** (1925), no. 1, 765. [Cited on page 4.]
- [11] S. N. Bose, “Plancks Gesetz und Lichtquantenhypothese”, *Zeitschrift für Physik* **26** (1924), no. 1, 178. [Cited on page 4.]
- [12] A. Einstein, “Quantentheorie des einatomigen idealen Gases”, *Sitzungber. Kgl. Akad. Wiss.*, 1924 261. [Cited on page 4.]
- [13] **Belle** Collaboration, A. Bondar *et al.*, “Observation of two charged bottomonium-like resonances in Y(5S) decays”, *Physical Review Letters* **108** (2012), no. 6, 122001, arXiv:1110.2251. [Cited on page 5.]
- [14] **LHCb** Collaboration, R. Aaij *et al.*, “Observation of  $J/\psi p$  Resonances Consistent with Pentaquark States in  $\Lambda_b^0 \rightarrow J/\psi K^- p$  Decays”, *Phys. Rev. Lett.* **115** (2015) 072001, arXiv:1507.03414. [Cited on page 5.]
- [15] P. W. Higgs, “Broken Symmetries and the Masses of Gauge Bosons”, *Phys. Rev. Lett.* **13** (1964) 367. [Cited on pages 5, 68, and 69.]
- [16] F. Englert and R. Brout, “Broken Symmetry and the Mass of Gauge Vector Mesons”, *Phys. Rev. Lett.* **13** (1964) 321. [Cited on pages 5, 68, and 69.]
- [17] **CMS** Collaboration, S. Chatrchyan *et al.*, “Observation of a new boson at a mass of 125 GeV with the CMS experiment at the LHC”, *Phys. Lett. B* **716** (2012) 30, arXiv:1207.7235. [Cited on pages 5 and 68.]
- [18] **ATLAS** Collaboration, G. Aad *et al.*, “Observation of a new particle in the search for the Standard Model Higgs boson with the ATLAS detector at the LHC”, *Phys. Lett. B* **716** (2012) 1, arXiv:1207.7214. [Cited on pages 5 and 68.]

- [19] **Particle Data Group** Collaboration, C. Patrignani *et al.*, “Review of Particle Physics”, *Chin. Phys. C* **40** (2016) 100001. [[Cited on pages 6, 8, 9, 70, 71, 72, 115, 130, 131, 175, and 177.](#)]
- [20] M. Gell-Mann, “The Eightfold Way: A Theory of strong interaction symmetry”, 1961. [[Cited on page 5.](#)]
- [21] Y. Ne’eman, “Derivation of strong interactions from a gauge invariance”, *Nucl. Phys.* **26** (1961) 222, [,34(1961)]. [[Cited on page 5.](#)]
- [22] M. Gell-Mann, “A Schematic Model of Baryons and Mesons”, *Phys. Lett.* **8** (1964) 214. [[Cited on page 5.](#)]
- [23] G. Zweig, “An SU(3) model for strong interaction symmetry and its breaking. Version 2”, *Developments in the Quark Theory of Hadrons* **1** (1964) 22. [[Cited on page 5.](#)]
- [24] O. W. Greenberg, “Spin and Unitary Spin Independence in a Paraquark Model of Baryons and Mesons”, *Phys. Rev. Lett.* **13** (1964) 598. [[Cited on page 5.](#)]
- [25] H. Fritzsch, M. Gell-Mann, and H. Leutwyler, “Advantages of the Color Octet Gluon Picture”, *Phys. Lett. B* **47** (1973) 365. [[Cited on page 5.](#)]
- [26] G. ’t Hooft and M. J. G. Veltman, “Regularization and Renormalization of Gauge Fields”, *Nucl. Phys. B* **44** (1972) 189. [[Cited on page 7.](#)]
- [27] J. L. Kneur and A. Neveu, “ $\Lambda_{\text{MS}}^{\text{QCD}}$  from Renormalization Group Optimized Perturbation”, *Phys. Rev. D* **85** (2012) 014005, arXiv:1108.3501. [[Cited on pages 8 and 14.](#)]
- [28] D. J. Gross and F. Wilczek, “Ultraviolet Behavior of Nonabelian Gauge Theories”, *Phys. Rev. Lett.* **30** (1973) 1343, [,271(1973)]. [[Cited on page 8.](#)]
- [29] H. D. Politzer, “Reliable Perturbative Results for Strong Interactions?”, *Phys. Rev. Lett.* **30** (1973) 1346, [,274(1973)]. [[Cited on page 8.](#)]
- [30] L. V. P. R. de Broglie, “Recherches sur la théorie des quanta”, *Annals Phys.* **2** (1925) 22. [[Cited on page 9.](#)]
- [31] M. N. Chernodub, “Background magnetic field stabilizes QCD string against breaking”, arXiv:1001.0570. [[Cited on pages 10 and 177.](#)]

## BIBLIOGRAPHY

---

- [32] J. D. Bjorken, “CURRENT ALGEBRA AT SMALL DISTANCES”, *Conf. Proc.* **670717** (1967) 55. [[Cited on page 10.](#)]
- [33] J. C. Collins, D. E. Soper, and G. F. Sterman, “Factorization of Hard Processes in QCD”, *Adv. Ser. Direct. High Energy Phys.* **5** (1989) 1, arXiv:hep-ph/0409313. [[Cited on page 11.](#)]
- [34] G. Altarelli and G. Parisi, “Asymptotic Freedom in Parton Language”, *Nucl. Phys. B* **126** (1977) 298. [[Cited on page 11.](#)]
- [35] Y. L. Dokshitzer, “Calculation of the Structure Functions for Deep Inelastic Scattering and e+ e- Annihilation by Perturbation Theory in Quantum Chromodynamics.”, *Sov. Phys. JETP* **46** (1977) 641, [Zh. Eksp. Teor. Fiz.73,1216(1977)]. [[Not cited.](#)]
- [36] V. N. Gribov and L. N. Lipatov, “Deep inelastic e p scattering in perturbation theory”, *Sov. J. Nucl. Phys.* **15** (1972) 438, [Yad. Fiz.15,781(1972)]. [[Cited on page 11.](#)]
- [37] ZEUS Collaboration, S. Chekanov *et al.*, “A ZEUS next-to-leading-order QCD analysis of data on deep inelastic scattering”, *Phys. Rev. D* **67** (2003) 012007, arXiv:hep-ex/0208023. [[Cited on pages 12, 13, and 177.](#)]
- [38] R. Hagedorn, “Statistical thermodynamics of strong interactions at high energies”, *Nuovo Cimento, Suppl.* **3** (1965) 147. [[Cited on page 13.](#)]
- [39] N. R. Council, “Nuclear physics: Exploring the heart of matter”, The National Academies Press, Washington, DC, 2013. [[Cited on pages 15, 18, and 177.](#)]
- [40] M. G. Alford, A. Schmitt, K. Rajagopal, and T. Schäfer, “Color superconductivity in dense quark matter”, *Rev. Mod. Phys.* **80** (2008) 1455, arXiv:0709.4635. [[Cited on page 14.](#)]
- [41] H.-T. Ding, “Recent lattice QCD results and phase diagram of strongly interacting matter”, *Nucl. Phys. A* **931** (2014) 52, arXiv:1408.5236. [[Cited on page 14.](#)]
- [42] A. Bazavov *et al.*, “Equation of state and QCD transition at finite temperature”, *Phys. Rev. D* **80** (2009) 014504, arXiv:0903.4379. [[Cited on page 14.](#)]
- [43] W. Scheid, H. Muller, and W. Greiner, “Nuclear Shock Waves in Heavy-Ion Collisions”, *Phys. Rev. Lett.* **32** (1974) 741. [[Cited on page 15.](#)]

- [44] E. J. Lofgren, “ACCELERATOR DIVISION ANNUAL REPORTS, 1 JULY 1972 12/31/1974”, Tech. Rep. LBL-3835, Lawrence Berkeley Laboratory, United States, 1975. [[Cited on page 16.](#)]
- [45] V. R. Pandharipande, D. Pines, and R. A. Smith, “Neutron star structure: theory, observation, and speculation.”, *Astrophys. J.* **208** (1976) 550. [[Cited on page 16.](#)]
- [46] T. L. Ainsworth, E. Baron, G. E. Brown, J. Cooperstein, and M. Prakash, “Equation of State of Dense Nuclear Matter”, *Nucl. Phys. A* **464** (1987) 740. [[Cited on page 16.](#)]
- [47] CERN, “New State of Matter created at CERN”, 2000. [Online; accessed June 11, 2018]. [[Cited on page 16.](#)]
- [48] W. Fischer, “Run overview of the Relativistic Heavy Ion collider”, 2000. [Online; accessed July 28, 2018]. [[Cited on page 16.](#)]
- [49] **BRAHMS** Collaboration, I. Arsene *et al.*, “Quark gluon plasma and color glass condensate at RHIC? The Perspective from the BRAHMS experiment”, *Nuclear Physics A* **757** (2005) 1, arXiv:nucl-ex/0410020. [[Cited on page 17.](#)]
- [50] **PHENIX** Collaboration, K. Adcox *et al.*, “Formation of dense partonic matter in relativistic nucleus-nucleus collisions at RHIC: Experimental evaluation by the PHENIX collaboration”, *Nuclear Physics A* **757** (2005) 184, arXiv:nucl-ex/0410003. [[Not cited.](#)]
- [51] **STAR** Collaboration, J. Adams *et al.*, “Experimental and theoretical challenges in the search for the quark gluon plasma: The STAR Collaboration’s critical assessment of the evidence from RHIC collisions”, *Nuclear Physics A* **757** (2005) 102, arXiv:nucl-ex/0501009. [[Not cited.](#)]
- [52] B. B. Back *et al.*, “The PHOBOS perspective on discoveries at RHIC”, *Nuclear Physics A* **757** (2005) 28, arXiv:nucl-ex/0410022. [[Cited on page 17.](#)]
- [53] M. L. Miller, K. Reygers, S. J. Sanders, and P. Steinberg, “Glauber modeling in high energy nuclear collisions”, *Annual Review of Nuclear and Particle Science* **57** (2007) 205, arXiv:nucl-ex/0701025. [[Cited on pages 18 and 19.](#)]
- [54] U. W. Heinz, “The Strongly coupled quark-gluon plasma created at RHIC”, *J. Phys. A* **42** (2009) 214003, arXiv:0810.5529. [[Cited on pages 22 and 177.](#)]

## BIBLIOGRAPHY

---

- [55] R. Snellings, “Elliptic Flow: A Brief Review”, *New J. Phys.* **13** (2011) 055008, arXiv:1102.3010. [[Cited on pages 22 and 23.](#)]
- [56] P. Kovtun, D. T. Son, and A. O. Starinets, “Viscosity in strongly interacting quantum field theories from black hole physics”, *Phys. Rev. Lett.* **94** (2005) 111601, arXiv:hep-th/0405231. [[Cited on page 23.](#)]
- [57] J.-Y. Ollitrault, “Relativistic hydrodynamics for heavy-ion collisions”, *Eur. J. Phys.* **29** (2008) 275, arXiv:0708.2433. [[Cited on page 23.](#)]
- [58] P. Braun-Munzinger and J. Stachel, “The quest for the quark-gluon plasma”, *Nature* **448** (2007) 302. [[Cited on pages 23, 24, and 177.](#)]
- [59] **CMS** Collaboration, V. Khachatryan *et al.*, “”, *Journal of High Energy Physics* **09** (2010) 091, arXiv:1009.4122. [[Cited on pages 23, 25, and 178.](#)]
- [60] **PHOBOS** Collaboration, B. Alver *et al.*, “System size dependence of cluster properties from two-particle angular correlations in Cu+Cu and Au+Au collisions at  $\sqrt{s_{NN}} = 200$  GeV”, *Physical Review C* **81** (2010) 024904, arXiv:0812.1172. [[Cited on page 24.](#)]
- [61] J. Rafelski and R. Hagedorn, “From Hadron Gas to Quark Matter. 2.”, in “International Symposium on Statistical Mechanics of Quarks and Hadrons Bielefeld, Germany, August 24-31, 1980”, p. 253. 1980. [[Cited on page 25.](#)]
- [62] A. Capella, “Strangeness enhancement in heavy ion collisions”, *Phys. Lett. B* **364** (1995) 175, arXiv:hep-ph/9501331. [[Cited on pages 25 and 26.](#)]
- [63] K. Safarik, “Strangeness production at CERN SPS”, in “Strangeness in quark matter. Proceedings, 5th International Conference, Strangeness 2000, Berkeley, USA, July 20-25, 2000”, vol. 27, pp. 579–583. 2001. [[Cited on page 25.](#)]
- [64] **NA49** Collaboration, A. Mischke *et al.*, “Lambda production in central Pb + Pb collisions at CERN SPS energies”, *J. Phys. G* **28** (2002) 1761–1768, arXiv:nucl-ex/0201012. [[Cited on page 25.](#)]
- [65] **STAR** Collaboration, B. I. Abelev *et al.*, “Enhanced strange baryon production in Au+Au collisions compared to p+p at  $\sqrt{s_{NN}} = 200$  GeV”, *Physical Review C* **77** (2008) 044908, arXiv:0705.2511. [[Cited on pages 25, 26, and 178.](#)]

- [66] **ALICE** Collaboration, J. Adam *et al.*, “Enhanced production of multi-strange hadrons in high-multiplicity proton-proton collisions”, *Nature Phys.* **13** (2017) 535, arXiv:1606.07424. [[Cited on pages 26 and 178.](#)]
- [67] M. Cacciari, G. P. Salam, and G. Soyez, “The Anti-k(t) jet clustering algorithm”, *JHEP* **04** (2008) 063, arXiv:0802.1189. [[Cited on page 27.](#)]
- [68] J. D. Bjorken, “Energy Loss of Energetic Partons in Quark - Gluon Plasma: Possible Extinction of High p(t) Jets in Hadron - Hadron Collisions”, 1982. [[Cited on page 27.](#)]
- [69] A. P. S. . A. Stonebraker, “Sketch of jet production in proton-proton and heavy-ion collisions”, 2014. [Online; accessed June 8, 2018]. [[Cited on pages 27 and 178.](#)]
- [70] **PHENIX** Collaboration, A. Adare *et al.*, “Centrality dependence of low-momentum direct-photon production in Au+Au collisions at  $\sqrt{s_{NN}} = 200 \text{ GeV}$ ”, *Phys. Rev. C* **91** (2015), no. 6, 064904, arXiv:1405.3940. [[Cited on page 28.](#)]
- [71] B. Betz, “Jet Quenching in Heavy-Ion Collisions - The Transition Era from RHIC to LHC”, *The European Physical Journal A* **48** (2012) 164, arXiv:1211.5897. [[Cited on pages 29 and 178.](#)]
- [72] **ATLAS** Collaboration, G. Aad *et al.*, “Observation of a Centrality-Dependent Dijet Asymmetry in Lead-Lead Collisions at  $\sqrt{s_{NN}} = 2.76 \text{ TeV}$  with the ATLAS Detector at the LHC”, *Physical Review Letters* **105** (2010) 252303, arXiv:1011.6182. [[Cited on pages 28, 30, and 178.](#)]
- [73] **CMS** Collaboration, S. Chatrchyan *et al.*, “Observation and studies of jet quenching in PbPb collisions at nucleon-nucleon center-of-mass energy  $\sqrt{s_{NN}} = 2.76 \text{ TeV}$ ”, *Physical Review C* **84** (2011) 024906, arXiv:1102.1957. [[Cited on page 28.](#)]
- [74] H. S. Chung, J. Lee, and D. Kang, “Cornell Potential Parameters for S-wave Heavy Quarkonia”, *J. Korean Phys. Soc.* **52** (2008) 1151, arXiv:0803.3116. [[Cited on page 29.](#)]
- [75] T. Matsui and H. Satz, “ $J/\psi$  Suppression by Quark-Gluon Plasma Formation”, *Phys. Lett. B* **178** (1986) 416. [[Cited on page 30.](#)]

## BIBLIOGRAPHY

---

- [76] **CMS** Collaboration, A. M. Sirunyan *et al.*, “Suppression of Excited  $\Upsilon$  States Relative to the Ground State in Pb-Pb Collisions at  $\sqrt{s_{NN}}=5.02\text{TeV}$ ”, *Phys. Rev. Lett.* **120** (2018), no. 14, 142301, arXiv:1706.05984. [[Cited on pages 30, 31, and 178.](#)]
- [77] **LHCb** Collaboration, R. Aaij *et al.*, “Study of  $\chi_b$  meson production in p p collisions at  $\sqrt{s} = 7$  and 8 TeV and observation of the decay  $\chi_b(3P) \rightarrow \Upsilon(3S)\gamma$ ”, *Eur. Phys. J. C* **74** (2014), no. 10, 3092, arXiv:1407.7734. [[Cited on page 31.](#)]
- [78] **NA50** Collaboration, M. C. Abreu *et al.*, “Anomalous  $J/\psi$  suppression in Pb-Pb interactions at 158 GeV/c per nucleon”, *Phys. Lett. B* **410** (1997) 337. [[Cited on page 31.](#)]
- [79] **NA50** Collaboration, B. Alessandro *et al.*, “A New measurement of  $J/\psi$  suppression in Pb-Pb collisions at 158-GeV per nucleon”, *Eur. Phys. J. C* **39** (2005) 335, arXiv:hep-ex/0412036. [[Cited on page 31.](#)]
- [80] **PHENIX** Collaboration, A. Adare *et al.*, “ $J/\psi$  Production vs Centrality, Transverse Momentum, and Rapidity in Au+Au Collisions at  $\sqrt{s_{NN}} = 200$  GeV”, *Physical Review Letters* **98** (2007) 232301, arXiv:nucl-ex/0611020. [[Cited on page 31.](#)]
- [81] P. Braun-Munzinger and J. Stachel, “(Non)thermal aspects of charmonium production and a new look at  $J/\psi$  suppression”, *Phys. Lett. B* **490** (2000) 196, arXiv:nucl-th/0007059. [[Cited on page 32.](#)]
- [82] L. Yan, P. Zhuang, and N. Xu, “Competition between  $J/\psi$  suppression and regeneration in quark-gluon plasma”, *Phys. Rev. Lett.* **97** (2006) 232301, arXiv:nucl-th/0608010. [[Cited on page 32.](#)]
- [83] R. Vogt, “Systematics of heavy quark production at RHIC”, arXiv:hep-ph/0203151. [[Cited on page 32.](#)]
- [84] **ALICE** Collaboration, B. B. Abelev *et al.*, “Centrality, rapidity and transverse momentum dependence of  $J/\psi$  suppression in Pb-Pb collisions at  $\sqrt{s_{NN}}=2.76$  TeV”, *Phys. Lett. B* **734** (2014) 314, arXiv:1311.0214. [[Cited on pages 33 and 179.](#)]
- [85] **CMS** Collaboration, S. Chatrchyan *et al.*, “Study of Z production in PbPb and pp collisions at  $\sqrt{s_{NN}} = 2.76$  TeV in the dimuon and dielectron decay channels”, *JHEP* **03** (2015) 022, arXiv:1410.4825. [[Cited on pages 33, 34, and 179.](#)]

- [86] A. D. Rosso, “Particle kickers. Aiguiller les particules”, Jun 2014. [[Cited on pages 38 and 179.](#)]
- [87] **ALICE** Collaboration, K. Aamodt *et al.*, “The ALICE experiment at the CERN LHC”, *Journal of Instrumentation* **3** (2008), no. 8, 08002. [[Cited on page 37.](#)]
- [88] **ATLAS** Collaboration, G. Aad *et al.*, “The ATLAS Experiment at the CERN Large Hadron Collider”, *Journal of Instrumentation* **3** (2008), no. 8, 08003. [[Cited on page 38.](#)]
- [89] **CMS** Collaboration, S. Chatrchyan *et al.*, “The CMS Experiment at the CERN LHC”, *Journal of Instrumentation* **3** (2008), no. 8, 08004. [[Cited on pages 38, 41, 45, 46, 47, 53, 179, and 180.](#)]
- [90] **LHCb** Collaboration, A. A. Alves, Jr. *et al.*, “The LHCb Detector at the LHC”, *Journal of Instrumentation* **3** (2008), no. 8, 08005. [[Cited on page 38.](#)]
- [91] J. Jowett *et al.*, “The 2015 Heavy-Ion Run of the LHC”, in “Proceedings, 7th International Particle Accelerator Conference (IPAC 2016): Busan, Korea, May 8-13, 2016”, vol. TUPMW027. 2016. [[Cited on pages 40, 41, and 179.](#)]
- [92] J. Jowett *et al.*, “The 2016 Proton-Nucleus Run of the LHC”, in “Proceedings, 8th International Particle Accelerator Conference (IPAC 2017): Copenhagen, Denmark, May 14-19, 2017”, vol. TUPVA014. 2017. [[Cited on pages 42 and 179.](#)]
- [93] J. M. Jowett, “Colliding Heavy Ions in the LHC”, in “Proceedings, 9th International Particle Accelerator Conference (IPAC 2018): Vancouver, BC, Canada, April 29 - May 4, 2018”, vol. TUXGBD2. 2018. [[Cited on pages 42 and 175.](#)]
- [94] T. Sakuma and T. McCauley, “Detector and Event Visualization with SketchUp at the CMS Experiment”, in “Proceedings, 20th International Conference on Computing in High Energy and Nuclear Physics (CHEP 2013): Amsterdam, The Netherlands, October 14-18, 2013”, vol. 513, p. 022032. 2014. [[Cited on pages 43 and 179.](#)]
- [95] C. Battilana, “The CMS muon system: status and upgrades for LHC Run-2 and performance of muon reconstruction with 13 TeV data”, in “Proceedings, 14th Topical Seminar on Innovative Particle and Radiation Detectors (IPRD16): Siena, Italy, Oct 3-6, 2016”, vol. 12, p. 01048. 2017. [[Cited on page 45.](#)]

## BIBLIOGRAPHY

---

- [96] **CMS** Collaboration, J. Mans, J. Anderson, B. Dahmes, P. de Barbaro, J. Freeman, T. Grassi, E. Hazen, J. Mans, R. Ruchti, I. Schimdt, *et al.*, “CMS Technical Design Report for the Phase 1 Upgrade of the Hadron Calorimeter”, 2012. [[Cited on pages 45, 49, and 179.](#)]
- [97] **CMS** Collaboration, A. Tapper and D. Acosta, “CMS Technical Design Report for the Level-1 Trigger Upgrade”, tech. rep., 2013. [[Cited on pages 45 and 56.](#)]
- [98] **CMS** Collaboration, A. Benaglia, “The CMS ECAL performance with examples”, in “Proceedings, 13th Topical Seminar on Innovative Particle and Radiation Detectors (IPRD13): Siena, Italy, October 7-10, 2013”, vol. 9, p. 02008. 2014. [[Cited on pages 47 and 179.](#)]
- [99] G. Abbiendi, “The CMS muon system in Run2: preparation, status and first results”, in “Proceedings, 2015 European Physical Society Conference on High Energy Physics (EPS-HEP 2015): Vienna, Austria, July 22-29, 2015”, vol. 234, p. 237. 2016. [[Cited on pages 51 and 179.](#)]
- [100] **CMS** Collaboration, S. Chatrchyan *et al.*, “Performance of the CMS Drift Tube Chambers with Cosmic Rays”, *Journal of Instrumentation* **5** (2010), no. 3, 03015. [[Cited on pages 52 and 180.](#)]
- [101] M. Abbrescia *et al.*, “Beam test results on double-gap resistive plate chambers proposed for CMS experiment”, *Nuclear Instruments and Methods in Physics Research Section A: Accelerators, Spectrometers, Detectors and Associated Equipment* **414** (1998), no. 2, 135. [[Cited on pages 53 and 180.](#)]
- [102] C. Collaboration, “Resistive Plate Chambers”, 2011. [Online; accessed July 7, 2018]. [[Cited on pages 53 and 180.](#)]
- [103] **CMS** Collaboration, V. Khachatryan *et al.*, “The CMS trigger system”, *Journal of Instrumentation* **12** (2017), no. 1, 01020. [[Cited on pages 54 and 55.](#)]
- [104] J. J. Brooke, D. G. Cussans, R. Frazier, G. Heath, D. Machin, and D. Newbold, “The New Global Muon Trigger of the CMS Experiment”, in “Proceedings, 9th Workshop on Electronics for LHC Experiments, Amsterdam, The Netherlands, 29 Sep - 3 Oct 2003”, p. 226. 2003. [[Cited on pages 55 and 180.](#)]
- [105] A. Zabi *et al.*, “Triggering on electrons, jets and tau leptons with the CMS upgraded calorimeter trigger for the LHC RUN II”, in “Proceedings, Topical

Workshop on Electronics for Particle Physics (TWEPP15): Lisbon, Portugal, September 28 - October 02, 2015”, vol. 11, p. 02008. 2016. [[Cited on page 57.](#)]

- [106] J. Fulcher, J. Lingemann, D. Rabady, T. Reis, and H. Sakulin, “The New Global Muon Trigger of the CMS Experiment”, in “Proceedings, 20th IEEE-NPSS Real Time Conference (RT2016): Padua, Italy, June 5-10, 2016”, vol. 64, p. 1467. 2017. [[Cited on page 57.](#)]
- [107] J.-M. André *et al.*, “Performance of the new DAQ system of the CMS experiment for run-2”, in “Proceedings, 2016 IEEE-NPSS Real Time Conference (RT): Padua, Italy, June 6-10, 2016”, p. 1. 2016. [[Cited on page 58.](#)]
- [108] R. Fruhwirth, “Application of Kalman filtering to track and vertex fitting”, *Nuclear Instruments and Methods in Physics Research Section A: Accelerators, Spectrometers, Detectors and Associated Equipment* **262** (1987), no. 2, 444. [[Cited on pages 59 and 60.](#)]
- [109] **CMS** Collaboration, A. M. Sirunyan *et al.*, “Performance of the CMS muon detector and muon reconstruction with proton-proton collisions at  $\sqrt{s} = 13$  TeV”, *Journal of Instrumentation* **13** (2018), no. 6, 06015. [[Cited on page 60.](#)]
- [110] D. Barney, “CMS Detector Slice”, CMS Collection., Jan 2016, unpublished. [[Cited on pages 61 and 180.](#)]
- [111] **CMS** Collaboration, A. M. Sirunyan *et al.*, “Particle-flow reconstruction and global event description with the CMS detector”, *JINST* **12** (2017), no. 10, P10003, arXiv:1706.04965. [[Cited on pages 63 and 90.](#)]
- [112] C. Collaboration, “Performance of missing transverse momentum in pp collisions at  $\text{sqrt}(s)=13$  TeV using the CMS detector”, Tech. Rep. CMS-PAS-JME-17-001, CERN, Geneva, 2018. [[Cited on page 63.](#)]
- [113] **CMS** Collaboration, V. Khachatryan *et al.*, “Performance of the CMS missing transverse momentum reconstruction in pp data at  $\sqrt{s} = 8$  TeV”, *Journal of Instrumentation* **10** (2015), no. 2, 02006. [[Cited on page 63.](#)]
- [114] E. Rutherford, “Uranium radiation and the electrical conduction produced by it”, *Philos. Mag.* **47** (1899) 109. [[Cited on page 66.](#)]

## BIBLIOGRAPHY

---

- [115] J. Chadwick, “Intensitätsverteilung im magnetischen Spektrum von  $\beta$ -Strahlen von Radium B+C”, *Verhandlungen der deutschen physikalischen Gesellschaft* **16** (1914) 383. [[Cited on page 66.](#)]
- [116] J. Chadwick and C. D. Ellis, “A Preliminary Investigation of the Intensity Distribution in the  $\beta$ -Ray Spectra of Radium B and C”, *Proceedings of the Cambridge Philosophical Society* **21** (1922) 274. [[Cited on page 66.](#)]
- [117] W. Pauli, “Fünf Arbeiten zum Ausschliessungsprinzip und zum Neutrino”, Wissenschaftliche Buchgesellschaft, [Abt. Verlag], 1977. [[Cited on page 66.](#)]
- [118] K. Winter, “Neutrino physics”, Cambridge University Press, 1991. [[Cited on page 66.](#)]
- [119] J. Chadwick, “Possible Existence of a Neutron”, *Nature* **129** (1932) 312. [[Cited on page 66.](#)]
- [120] E. Fermi, “Collected Papers of Enrico Fermi”, University of Chicago Press, 1965. [[Cited on page 66.](#)]
- [121] E. Fermi, “Versuch einer Theorie der  $\beta$ -Strahlen. I”, *Zeitschrift für Physik* **88** (1934) 161. [[Cited on page 66.](#)]
- [122] T. D. Lee and C. N. Yang, “Question of Parity Conservation in Weak Interactions”, *Phys. Rev.* **104** (1956) 254. [[Cited on pages 66 and 67.](#)]
- [123] C. S. Wu, E. Ambler, R. W. Hayward, D. D. Hoppes, and R. P. Hudson, “Experimental Test of Parity Conservation in Beta Decay”, *Phys. Rev.* **105** (1957) 1413. [[Cited on page 67.](#)]
- [124] M. Goldhaber, L. Grodzins, and A. W. Sunyar, “Helicity of Neutrinos”, *Phys. Rev.* **109** (1958) 1015. [[Cited on page 67.](#)]
- [125] E. C. G. Sudarshan and R. E. Marshak, “Origin of the Universal VÄA theory”, *AIP Conf. Proc.* **300** (1994) 110, [,0001(1984)]. [[Cited on page 67.](#)]
- [126] J. H. Christenson, J. W. Cronin, V. L. Fitch, and R. Turlay, “Evidence for the  $2\pi$  Decay of the  $K_2^0$  Meson”, *Phys. Rev. Lett.* **13** (1964) 138. [[Cited on page 67.](#)]
- [127] M. Kobayashi and T. Maskawa, “CP Violation in the Renormalizable Theory of Weak Interaction”, *Prog. Theor. Phys.* **49** (1973) 652. [[Cited on page 67.](#)]

- [128] N. Cabibbo, “Unitary Symmetry and Leptonic Decays”, *Phys. Rev. Lett.* **10** (1963) 531, [,648(1963)]. [[Cited on page 67.](#)]
- [129] S. L. Glashow, J. Iliopoulos, and L. Maiani, “Weak Interactions with Lepton-Hadron Symmetry”, *Phys. Rev. D* **2** (1970) 1285. [[Cited on page 67.](#)]
- [130] **E598** Collaboration, J. J. Aubert *et al.*, “Experimental Observation of a Heavy Particle  $J$ ”, *Phys. Rev. Lett.* **33** (1974) 1404. [[Cited on page 67.](#)]
- [131] **SLAC-SP-017** Collaboration, J. E. Augustin *et al.*, “Discovery of a Narrow Resonance in  $e^+e^-$  Annihilation”, *Phys. Rev. Lett.* **33** (1974) 1406. [[Cited on page 67.](#)]
- [132] S. W. Herb *et al.*, “Observation of a Dimuon Resonance at 9.5-GeV in 400-GeV Proton-Nucleus Collisions”, *Phys. Rev. Lett.* **39** (1977) 252. [[Cited on page 67.](#)]
- [133] **CDF** Collaboration, F. Abe *et al.*, “Observation of top quark production in  $\bar{p}p$  collisions”, *Phys. Rev. Lett.* **74** (1995) 2626, arXiv:hep-ex/9503002. [[Cited on page 67.](#)]
- [134] P. A. M. Dirac, “The Principles of Quantum Mechanics”, Clarendon Press, 1930. [[Cited on page 67.](#)]
- [135] S. L. Glashow, “The renormalizability of vector meson interactions”, *Nucl. Phys.* **10** (1959) 107. [[Cited on pages 67 and 69.](#)]
- [136] S. Weinberg, “A Model of Leptons”, *Phys. Rev. Lett.* **19** (1967) 1264. [[Cited on page 67.](#)]
- [137] A. Salam, “Weak and Electromagnetic Interactions”, *Conf. Proc. C* **680519** (1968) 367. [[Cited on pages 67 and 69.](#)]
- [138] G. t. Hooft, “Renormalizable Lagrangians for massive Yang-Mills fields”, *Nuclear Physics B* **35** (1971) 167. [[Cited on page 68.](#)]
- [139] G. t. Hooft and M. Veltman, “Regularization and renormalization of gauge fields”, *Nuclear Physics B* **44** (1972) 189. [[Cited on page 68.](#)]
- [140] **Gargamelle Neutrino** Collaboration, F. J. Hasert *et al.*, “Observation of Neutrino Like Interactions without Muon or Electron in the Gargamelle Neutrino Experiment”, *Nucl. Phys. B* **73** (1974) 1. [[Cited on page 68.](#)]

## BIBLIOGRAPHY

---

- [141] C. Rubbia, P. McIntyre, and D. Cline, *Producing Massive Neutral Intermediate Vector Bosons with Existing Accelerators*, p. 683. Vieweg+Teubner Verlag, Wiesbaden, 1977. [[Cited on page 68.](#)]
- [142] S. van der Meer, “Stochastic damping of betatron oscillations in the ISR”, Tech. Rep. CERN-ISR-PO-72-31. ISR-PO-72-31, CERN, Geneva, Aug 1972. [[Cited on page 68.](#)]
- [143] G. Arnison *et al.*, “Experimental observation of isolated large transverse energy electrons with associated missing energy at  $\sqrt{s}=540$  GeV”, *Phys. Lett. B* **122** (1983) 103. [[Cited on page 68.](#)]
- [144] M. Banner *et al.*, “Observation of single isolated electrons of high transverse momentum in events with missing transverse energy at the CERN pp collider”, *Phys. Lett. B* **122** (1983) 476. [[Cited on page 68.](#)]
- [145] **UA1** Collaboration, G. Arnison *et al.*, “Experimental Observation of Lepton Pairs of Invariant Mass Around 95-GeV/c\*\*2 at the CERN SPS Collider”, *Phys. Lett. B* **126** (1983) 398, [,7.55(1983)]. [[Cited on page 68.](#)]
- [146] **UA2** Collaboration, P. Bagnaia *et al.*, “Evidence for  $Z_0 \rightarrow e^+ e^-$  at the CERN anti-p p Collider”, *Phys. Lett. B* **129** (1983) 130, [,7.69(1983)]. [[Cited on page 68.](#)]
- [147] S. Myers, “The LEP Collider, from design to approval and commissioning”, CERN, Geneva, 1991. Delivered at CERN, 26 Nov 1990. [[Cited on page 68.](#)]
- [148] **DØ Collaboration** Collaboration, V. M. Abazov *et al.*, “Improved  $W$  boson mass measurement with the DØ detector”, *Phys. Rev. D* **66** Jul (2002) 012001. [[Cited on page 68.](#)]
- [149] R. R. Wilson, “The Tevatron”, *Phys. Today* **30** (1977) 23. [[Cited on page 68.](#)]
- [150] S. Dulat, T.-J. Hou, J. Gao, M. Guzzi, J. Huston, P. Nadolsky, J. Pumplin, C. Schmidt, D. Stump, and C. P. Yuan, “New parton distribution functions from a global analysis of quantum chromodynamics”, *Phys. Rev. D* **93** (2016) 033006, arXiv:1506.07443. [[Cited on pages 74, 75, 86, and 180.](#)]
- [151] **European Muon** Collaboration, J. J. Aubert *et al.*, “The ratio of the nucleon structure functions  $F_{2n}$  for iron and deuterium”, *Phys. Lett. B* **123** (1983) 275–278. [[Cited on page 76.](#)]

- [152] **European Muon** Collaboration, M. Arneodo *et al.*, “Shadowing in Deep Inelastic Muon Scattering from Nuclear Targets”, *Phys. Lett. B* **211** (1988) 493. [[Cited on page 76.](#)]
- [153] H. Paukkunen, “Nuclear PDFs in the beginning of the LHC era”, *Nucl. Phys. A* **926** (2014) 24, arXiv:1401.2345. [[Cited on pages 76 and 180.](#)]
- [154] K. J. Eskola, V. J. Kolhinen, and C. A. Salgado, “The Scale dependent nuclear effects in parton distributions for practical applications”, *Eur. Phys. J. C* **9** (1999) 61, arXiv:hep-ph/9807297. [[Cited on page 77.](#)]
- [155] K. J. Eskola, H. Paukkunen, and C. A. Salgado, “An Improved global analysis of nuclear parton distribution functions including RHIC data”, *JHEP* **07** (2008) 102, arXiv:0802.0139. [[Cited on page 77.](#)]
- [156] K. J. Eskola, H. Paukkunen, and C. A. Salgado, “EPS09: A New Generation of NLO and LO Nuclear Parton Distribution Functions”, *JHEP* **04** (2009) 065, arXiv:0902.4154. [[Cited on page 77.](#)]
- [157] D. de Florian, R. Sassot, P. Zurita, and M. Stratmann, “Global Analysis of Nuclear Parton Distributions”, *Phys. Rev. D* **85** (2012) 074028, arXiv:1112.6324. [[Cited on page 77.](#)]
- [158] K. J. Eskola, P. Paakkinen, H. Paukkunen, and C. A. Salgado, “EPPS16: Nuclear parton distributions with LHC data”, *Eur. Phys. J. C* **77** (2017) 163, arXiv:1612.05741. [[Cited on pages 77, 79, 81, 86, 127, and 180.](#)]
- [159] K. Kovarik *et al.*, “nCTEQ15 - Global analysis of nuclear parton distributions with uncertainties in the CTEQ framework”, *Phys. Rev. D* **93** (2016), no. 8, 085037, arXiv:1509.00792. [[Cited on pages 78, 80, and 180.](#)]
- [160] **CMS** Collaboration, S. Chatrchyan *et al.*, “Study of  $W$  boson production in PbPb and  $pp$  collisions at  $\sqrt{s_{NN}} = 2.76$  TeV”, *Phys. Lett. B* **715** (2012) 66, arXiv:1205.6334. [[Cited on page 80.](#)]
- [161] **CMS** Collaboration, S. Chatrchyan *et al.*, “Study of  $Z$  boson production in PbPb collisions at  $\sqrt{s_{NN}} = 2.76$  TeV”, *Phys. Rev. Lett.* **106** (2011) 212301, arXiv:1102.5435. [[Cited on page 80.](#)]

## BIBLIOGRAPHY

---

- [162] **ATLAS** Collaboration, G. Aad *et al.*, “Measurement of the production and lepton charge asymmetry of  $W$  bosons in Pb+Pb collisions at  $\sqrt{s_{\text{NN}}} = 2.76$  TeV with the ATLAS detector”, *Eur. Phys. J. C* **75** (2015), no. 1, 23, arXiv:1408.4674. [[Cited on page 80.](#)]
- [163] **ATLAS** Collaboration, G. Aad *et al.*, “Measurement of  $Z$  boson Production in Pb+Pb Collisions at  $\sqrt{s_{\text{NN}}} = 2.76$  TeV with the ATLAS Detector”, *Phys. Rev. Lett.* **110** (2013), no. 2, 022301, arXiv:1210.6486. [[Cited on page 80.](#)]
- [164] **ALICE** Collaboration, S. Acharya *et al.*, “Measurement of  $Z^0$ -boson production at large rapidities in Pb-Pb collisions at  $\sqrt{s_{\text{NN}}} = 5.02$  TeV”, *Phys. Lett. B* **780** (2018) 372, arXiv:1711.10753. [[Cited on page 82.](#)]
- [165] **ATLAS** Collaboration, G. Aad *et al.*, “ $Z$  boson production in p+Pb collisions at  $\sqrt{s_{\text{NN}}} = 5.02$  TeV measured with the ATLAS detector”, *Phys. Rev. C* **92** (2015), no. 4, 044915, arXiv:1507.06232. [[Cited on pages 82 and 181.](#)]
- [166] **ALICE** Collaboration, J. Adam *et al.*, “ $W$  and  $Z$  boson production in p-Pb collisions at  $\sqrt{s_{\text{NN}}} = 5.02$  TeV”, *JHEP* **02** (2017) 077, arXiv:1611.03002. [[Cited on pages 83 and 181.](#)]
- [167] **CMS** Collaboration, V. Khachatryan *et al.*, “Study of  $W$  boson production in pPb collisions at  $\sqrt{s_{\text{NN}}} = 5.02$  TeV”, *Phys. Lett. B* **750** (2015) 565, arXiv:1503.05825. [[Cited on pages 83, 84, 130, and 181.](#)]
- [168] CMS Collaboration, “CMS luminosity measurement using 2016 proton-nucleus collisions at nucleon-nucleon center-of-mass energy of 8.16 TeV”, Tech. Rep. CMS-PAS-LUM-17-002, CERN, Geneva, 2018. [[Cited on pages 85, 126, 137, 138, and 184.](#)]
- [169] C. A. Salgado *et al.*, “Proton-Nucleus Collisions at the LHC: Scientific Opportunities and Requirements”, *Journal of Physics G: Nuclear and Particle Physics* **39** (2012), no. 1, 015010, arXiv:1105.3919. [[Cited on page 85.](#)]
- [170] S. Frixione, P. Nason, and C. Oleari, “Matching NLO QCD computations with Parton Shower simulations: the POWHEG method”, *JHEP* **11** (2007) 070, arXiv:0709.2092. [[Cited on page 86.](#)]
- [171] P. Nason, “A New method for combining NLO QCD with shower Monte Carlo algorithms”, *JHEP* **11** (2004) 040, arXiv:hep-ph/0409146. [[Not cited.](#)]

- [172] S. Alioli, P. Nason, C. Oleari, and E. Re, “A general framework for implementing NLO calculations in shower Monte Carlo programs: the POWHEG BOX”, *JHEP* **06** (2010) 043, arXiv:1002.2581. [[Cited on page 86.](#)]
- [173] L. Barze, G. Montagna, P. Nason, O. Nicrosini, and F. Piccinini, “Implementation of electroweak corrections in the POWHEG BOX: single W production”, *JHEP* **04** (2012) 037, arXiv:1202.0465. [[Cited on pages 86 and 133.](#)]
- [174] L. Barze, G. Montagna, P. Nason, O. Nicrosini, F. Piccinini, and A. Vicini, “Neutral-current Drell–Yan with combined QCD and electroweak corrections in the POWHEG BOX”, *Eur. Phys. J. C* **73** (2013) 2474, arXiv:1302.4606. [[Cited on page 86.](#)]
- [175] S. Frixione, P. Nason, and G. Ridolfi, “A Positive-Weight Next-to-Leading-Order Monte Carlo for Heavy Flavour Hadroproduction”, *JHEP* **09** (2007) 126, arXiv:0707.3088. [[Cited on page 86.](#)]
- [176] T. Sjöstrand, S. Ask, J. R. Christiansen, R. Corke, N. Desai, P. Ilten, S. Mrenna, S. Prestel, C. O. Rasmussen, and P. Z. Skands, “An Introduction to PYTHIA 8.2”, *Comput. Phys. Commun.* **191** (2015) 159, arXiv:1410.3012. [[Cited on page 87.](#)]
- [177] **CMS** Collaboration, S. Chatrchyan *et al.*, “Study of the underlying event at forward rapidity in pp collisions at  $\sqrt{s} = 0.9, 2.76$ , and  $7$  TeV”, *JHEP* **04** (2013) 072, arXiv:1302.2394. [[Cited on page 87.](#)]
- [178] **GEANT4** Collaboration, S. Agostinelli *et al.*, “GEANT4: A Simulation toolkit”, *Nucl. Instrum. Meth. A* **506** (2003) 250. [[Cited on page 87.](#)]
- [179] T. Pierog, I. Karpenko, J. M. Katzy, E. Yatsenko, and K. Werner, “EPOS LHC: Test of collective hadronization with data measured at the CERN Large Hadron Collider”, *Phys. Rev. C* **92** (2015) 034906, arXiv:1306.0121. [[Cited on page 87.](#)]
- [180] **CMS** Collaboration, A. M. Sirunyan *et al.*, “Pseudorapidity distributions of charged hadrons in proton-lead collisions at  $\sqrt{s_{\text{NN}}} = 5.02$  and  $8.16$  TeV”, *JHEP* **01** (2018) 045, arXiv:1710.09355. [[Cited on page 87.](#)]
- [181] **CMS** Collaboration, A. M. Sirunyan *et al.*, “Observation of top quark production in proton-nucleus collisions”, *Phys. Rev. Lett.* **119** (2017) 242001, arXiv:1709.07411. [[Cited on pages 88, 115, 131, and 175.](#)]

## BIBLIOGRAPHY

---

- [182] B. H. Armstrong, “Spectrum line profiles: The Voigt function”, *J. Quant. Spectrosc. Radiat. Transfer* **7** (1967) 61. [[Cited on page 109.](#)]
- [183] CMS Collaboration, “Muon performance studies in 2016 pPb data”, Tech. Rep. CMS-HIN-AN-17-137, CERN, Geneva, 2017. [[Cited on pages 110, 111, 182, and 183.](#)]
- [184] W. Verkerke and D. P. Kirkby, “The RooFit toolkit for data modeling”, *eConf C* **0303241** (2003) 186, arXiv:physics/0306116. [[Cited on page 120.](#)]
- [185] A. Buckley, J. Ferrando, S. Lloyd, K. Nordström, B. Page, M. Rüfenacht, M. Schönher, and G. Watt, “LHAPDF6: parton density access in the LHC precision era”, *Eur. Phys. J. C* **75** (2015) 132, arXiv:1412.7420. [[Cited on page 127.](#)]
- [186] R. Boughezal, J. M. Campbell, R. K. Ellis, C. Focke, W. Giele, X. Liu, F. Petriello, and C. Williams, “Color singlet production at NNLO in MCFM”, *Eur. Phys. J. C* **77** (2017) 7, arXiv:1605.08011. [[Cited on pages 130 and 140.](#)]
- [187] S. Alioli, P. Nason, C. Oleari, and E. Re, “NLO vector-boson production matched with shower in POWHEG”, *JHEP* **07** (2008) 060, arXiv:0805.4802. [[Cited on page 134.](#)]

## LIST OF TABLES

1.1 Basic properties of quarks, leptons and bosons from the SM. The table includes the mass, electric charge, spin and type of interactions of each particle. The values are taken from Ref. [19]. . . . .	6
2.1 LHC beam parameters during the highest luminosity physics fills. The luminosity values are averages for CMS. Information extracted from Ref. [93]. . . . .	42
3.1 Experimental values of the mass, width and branching fractions of weak bosons extracted from the PDG [19]. . . . .	71
3.2 Summary of the information of EPS09, EPPS16 and nCTEQ15 nuclear PDFs. . . . .	81
3.3 Simulated NLO samples used for the W-boson measurement in p-Pb at 8.16 TeV. The listed cross sections are the POWHEG NLO cross sections scaled by $A_{\text{Pb}} = 208$ , except for the $t\bar{t}$ production cross section which is taken from the CMS measurement in p-Pb at 8.16 TeV [181]. . . . .	88
3.4 Relative difference between the corrected and simulated signal efficiencies as a function of the generated muon $\eta_{CM}$ , separated in negative and positive charged muons. . . . .	114
3.5 QCD background parameters extrapolated to $I^\mu = 0.03$ . The results are presented for positive and negative charged muons in the $\eta_{CM}^\mu$ -inclusive range. . . . .	118
3.6 Event yields of $W^- \rightarrow \mu^- \bar{\nu}_\mu$ and background processes, extracted from the fits to the $p_T^{\text{miss}}$ distribution in each muon $\eta_{CM}^\mu$ region. All analysis selection criteria are applied including the muon $p_T > 25$ GeV/c. All uncertainties shown are statistical only. . . . .	122
3.7 Event yields of $W^+ \rightarrow \mu^+ \nu_\mu$ and background processes, extracted from the fits to the $p_T^{\text{miss}}$ distribution in each muon $\eta_{CM}^\mu$ region. All analysis selection criteria are applied including the muon $p_T > 25$ GeV/c. All uncertainties shown are statistical only. . . . .	123

LIST OF TABLES

---

3.8	Corrected event yields of $W^- \rightarrow \mu^- \bar{\nu}_\mu$ , given for each muon $\eta_{CM}^\mu$ bin. All analysis selection criteria are applied including the muon $p_T > 25$ GeV/c. The muon efficiency has been corrected by applying the tag-and-probe corrections, HF energy weights and vector boson $p_T$ weights, event by event. All uncertainties shown are statistical only. . . . .	124
3.9	Corrected event yields of $W^+ \rightarrow \mu^+ \nu_\mu$ , given for each muon $\eta_{CM}^\mu$ . All analysis selection criteria are applied including the muon $p_T > 25$ GeV/c. The muon efficiency has been corrected by applying the tag-and-probe corrections, HF energy weights and vector boson $p_T$ weights, event by event. All uncertainties shown are statistical only. . . . .	125
3.10	The RMS of the set of QCD background parameters extrapolated along all $\eta_{CM}^\mu$ regions. . . . .	129
3.11	QCD shape parameters extrapolated to the average muon isolation point $iso = 0.08$ . . . . .	129
3.12	Maximum uncertainty of the measured observables determined for each category. The uncertainties of the $W \rightarrow \mu \nu_\mu$ differential cross sections are relative while for the forward-backward ratios and muon charge asymmetry are absolute. . . . .	134
3.13	Results of the $\chi^2$ statistical test between the measurements and the theory calculations from the CT14 PDF, CT14+EPPS16 nPDF and CT14+nCTEQ15 nPDF models. The value of the $\chi^2$ , the number of degrees of freedom (ndf) and the $\chi^2$ probability (Prob.), are presented for the $W^\pm \rightarrow \mu^\pm \nu_\mu$ differential cross sections, the muon charge asymmetry, the $W^\pm \rightarrow \mu^\pm \nu_\mu$ forward-backward ratios, and the charge-summed forward-backward ratio, respectively. . . . .	142

TABLE	Page
-------	------

## LIST OF FIGURES

1.1 Feynman diagrams of the QCD vertices for quark-gluon coupling (left), triple-gluon self-coupling (middle) and quadri-gluon self-coupling (right). . . . .	7
1.2 Feynman diagrams of 1-loop contributions to pQCD. . . . .	8
1.3 Summary of measurements of $\alpha_s$ as a function of the energy scale $Q$ . Figure taken from the PDG [19] . . . . .	9
1.4 Sketch of the gluon string breaking between a quark $Q$ and an anti-quark $\bar{Q}$ due to $q\bar{q}$ pair creation. Figure taken from Ref. [31]. . . . .	10
1.5 Feynman diagram of deep inelastic scattering of electrons against protons. .	12
1.6 Next-to-leading order QCD fits to the to the ZEUS $F_2$ structure function data from 1996, 1997 and proton fixed-target at HERA. The error bands of the fit represent the total experimental uncertainty from both correlated and uncorrelated sources. Figure taken from Ref. [37]. . . . .	13
1.7 Feynman diagram of the Drell-Yan process. . . . .	13
1.8 Sketch of the QCD phase diagram for nuclear matter. The solid lines show the phase boundaries and the solid circle represents the critical point. Figure taken from Ref. [39]. . . . .	15
1.9 Illustration of two nucleus with impact parameter $b$ before (left) and after (right) colliding. Figure taken from Ref. [39]. . . . .	18
1.10 Schematic representation of the optical Glauber model geometry. . . . .	19
1.11 Sketch of the evolution of a relativistic heavy-ion collision. . . . .	20
1.12 Sketch of the elliptic flow produced in non-central heavy-ion collisions. Figure taken from Ref. [54]. . . . .	22
1.13 Elliptic flow distribution of as a function of transverse momentum for $\pi^\pm$ mesons, $K_s^0$ mesons, antiprotons and $\Lambda$ baryons measured by STAR collaboration in Au-Au collisions at $\sqrt{s_{NN}} = 200$ GeV. The results are compared with relativistic hydrodynamic calculations. Figure taken from Ref. [58]. . . . .	24

1.14 3D display of the $\Delta\eta$ - $\Delta\phi$ correlation function between two charged particles with $1 \text{ GeV}/c < p_T < 3 \text{ GeV}/c$ , measured by the CMS collaboration in high multiplicity ( $N \geq 110$ ) p-p collisions at $\sqrt{s} = 7 \text{ TeV}$ . Figure taken from Ref. [59].	25
1.15 Left: Distribution of the yield of inclusive protons and strange baryons, measured by the STAR collaboration in Au-Au collisions at $\sqrt{s_{\text{NN}}} = 200 \text{ GeV}$ (solid symbols) and by the NA57 collaboration in Pb-Pb collisions at $\sqrt{s_{\text{NN}}} = 17.3 \text{ GeV}$ (empty symbols), relative to the corresponding yield in p-p (at RHIC) or p-Be (at SPS) collisions scaled by $N_{\text{part}}$ . Figure from Ref. [65]. Right: Distribution of the $p_T$ -integrated yield ratios of strange hadrons to pions as a function of the average charged-particle multiplicity measured in $ \eta  < 0.5$ by the ALICE collaboration in p-p, p-Pb and Pb-Pb collisions at $\sqrt{s} = 7 \text{ TeV}$ , $\sqrt{s_{\text{NN}}} = 5.02 \text{ TeV}$ and $\sqrt{s_{\text{NN}}} = 2.56 \text{ TeV}$ , respectively. Figure from Ref. [66].	26
1.16 Sketch of the production mechanism of two jets in proton-proton (top) and heavy-ions (bottom) collisions. Figure taken from Ref. [69].	27
1.17 Distribution of the nuclear modification factor $R_{\text{AA}}$ of direct photons, pions, $\eta$ mesons and charged hadrons, measured at RHIC in central Au-Au collisions at $\sqrt{s_{\text{NN}}} = 200 \text{ GeV}$ . Theoretical predictions of radiative parton energy loss are also included. Figure taken from Ref. [71].	29
1.18 Dijet asymmetry measured by the ATLAS collaboration in lead-lead collisions at $\sqrt{s_{\text{NN}}} = 2.76 \text{ TeV}$ (points) and proton-proton collisions at $\sqrt{s} = 7 \text{ TeV}$ (open circles). The top panel shows the dijet asymmetry distributions and unquenched HIJING with superimposed PYTHIA dijets (solid yellow histograms), as a function of collision centrality. The bottom panel shows the distribution of the azimuthal angle between the two jets $\Delta\phi$ , for data and HIJING+PYTHIA, also as a function of centrality. Figure taken from Ref. [72].	30
1.19 Dimuon invariant mass distribution measured by the CMS collaboration in Pb-Pb collisions at $\sqrt{s_{\text{NN}}} = 5.02 \text{ TeV}$ . The total fit (solid blue line), the background component (dot-dashed blue line) and the individual $\Upsilon(1S)$ , $\Upsilon(2S)$ and $\Upsilon(3S)$ mass peaks (dotted gray lines) are shown. The dashed red line represents the p-p signal shapes added on top of the Pb-Pb background and normalised to the $\Upsilon(1S)$ mass peak in Pb-Pb. Figure taken from Ref. [76].	31

1.20 Nuclear modification factor of $J/\psi$ meson as a function of transverse momentum measured by the ALICE collaboration in the 0% – 20% most central Pb-Pb collisions at $\sqrt{s_{\text{NN}}} = 2.76$ TeV compared to results from the PHENIX collaboration measured in the 0% – 20% most central Au-Au collisions at $\sqrt{s_{\text{NN}}} = 200$ GeV. Figure taken from Ref. [84]. . . . .	33
1.21 Nuclear modification factor $R_{\text{AA}}$ of $Z \rightarrow e^+e^-$ (blue squares) and $Z \rightarrow \mu^+\mu^-$ (red circles) events as a function of $N_{\text{part}}$ measured by the CMS collaboration in Pb-Pb collisions at $\sqrt{s_{\text{NN}}} = 2.56$ TeV. The open points represent the centrality-integrated $R_{\text{AA}}$ and the vertical lines (boxes) correspond to statistical (systematic) uncertainties. Figure taken from Ref. [85]. . . . .	34
2.1 Schematic diagram of the LHC injection chain for protons and Pb nuclei. The proton and Pb ion trajectories are indicated with red and blue arrows, accordingly. The location of each LHC detector is also included. . . . .	36
2.2 Schematic diagram of the LHC layout. Figure taken from Ref. [86]. . . . .	38
2.3 Integrated nucleon-pair luminosity delivered by the LHC to each experiment during Pb-Pb collisions at $\sqrt{s_{\text{NN}}} = 5.02$ TeV. The integrated luminosity of p-Pb collisions at $\sqrt{s_{\text{NN}}} = 5.02$ TeV and Pb-Pb collisions at $\sqrt{s_{\text{NN}}} = 2.76$ TeV are included for comparison. Figure taken from Ref. [91]. . . . .	41
2.4 Integrated proton-nucleus luminosity delivered by the LHC to each experiment during p-Pb collisions at $\sqrt{s_{\text{NN}}} = 8.16$ TeV (solid lines). The integrated luminosity of p-Pb collisions at $\sqrt{s_{\text{NN}}} = 5.02$ TeV (dashed lines) is included for comparison. Figure taken from Ref. [92]. . . . .	42
2.5 Cutaway view of the CMS detector in its configuration used during 2015 and 2016. Labels and basic details of each subdetector are included. [94] . . . . .	43
2.6 Schematic diagram of the coordinate system used in the CMS experiment. . .	44
2.7 View of the CMS tracker in the $r$ - $z$ plane. Each line represents a detector module. Figure taken from Ref. [89]. . . . .	46
2.8 Schematic layout [89] (left) of the CMS electromagnetic calorimeter, and its corresponding one-quarter geometric view [98] (right). . . . .	47
2.9 Geometric view of one quarter of the CMS detector, displaying the subdetectors of the hadron calorimeter: HB, HE, HF and HO. Figure taken from Ref. [96].	49
2.10 Geometric view of one quadrant the CMS detector in the $r$ - $z$ plane. Each chamber of the muon system is shown in blue (RPC), green (CSC) and orange (DT). Figure taken from Ref. [99]. . . . .	51

2.11 Schematic layout of a DT cell (left) and a DT chamber (right). Figures taken from [100]. . . . .	52
2.12 Schematic layout of a CSC. Figure taken from [89]. . . . .	53
2.13 Cross section view (left) [101] and exploded view (right) [102] of a RPC module. . . . .	53
2.14 Diagram of the legacy L1 trigger of CMS. Figure taken from Ref. [104]. . . . .	55
2.15 Diagram of the CMS L1 trigger used in 2016. . . . .	57
2.16 Cross section view of the CMS detector showing how particles interact in the CMS. The different types of muon tracks are indicated by boxes. Figure taken from Ref. [110]. . . . .	61
3.1 Feynman diagram of the decay modes of $W^+$ (left), $W^-$ (middle) and $Z$ (right) bosons to fermions. . . . .	71
3.2 Leading order Feynman diagram of $W$ boson production to final state leptons, from a collision between an incoming proton ( $p$ ) and a bound nucleon ( $a$ ) in a $Pb$ nucleus. . . . .	72
3.3 Next-to-leading order Feynman diagrams of $W$ boson partonic production to final state leptons. . . . .	73
3.4 Schematic diagram of the production of $W^-$ (left) and $W^+$ (right) bosons to muonic decays. The black arrows represent the particle direction of motion whereas the blue arrows correspond to its spin. The spin of the $W^\pm$ boson points in the direction of the anti-quark. . . . .	74
3.5 Results of the CT14 proton PDFs at NNLO derived at $Q = 10\text{ GeV}$ (left) and $Q = 10\text{ GeV}$ (right). Figure taken from Ref. [150]. . . . .	75
3.6 Illustration of the different nuclear PDF effects. Figure taken from Ref. [153]. . . . .	76
3.7 Results of the EPPS16 nuclear correction factor $R^A$ for $Pb$ ions at $Q^2 = 10\text{ GeV}^2$ . The black curve represents the central fit while the blue bands shows the total uncertainty of the PDF fit. The results are compared against a baseline made by performing the EPPS16 fits on the same datasets used for EPS09. Figure taken from Ref. [158]. . . . .	79
3.8 Results of the nCTEQ15 full nuclear PDFs for $Pb$ ions $f^{Pb}$ at $Q = 10\text{ GeV}$ . Figure taken from Ref. [159]. . . . .	80
3.9 Comparison between the EPPS16 (black curve with blue band) and the nCTEQ15 (red curves with hatching) nuclear modifications performed at $Q^2 = 10\text{ GeV}^2$ . Figure taken from Ref. [158]. . . . .	81

3.10 Distribution of the production cross section for $Z \rightarrow \mu^+ \mu^-$ measured as a function of the Z-boson rapidity measured in the centre-of-mass frame. Figure taken from Ref. [165]. . . . .	82
3.11 Distribution of the production cross section for $W^- \rightarrow \mu^- \bar{\nu}_\mu$ (left) and $W^+ \rightarrow \mu^+ \nu_\mu$ (right) measured as a function of the muon rapidity in the centre-of-mass frame. Figure taken from Ref. [166]. . . . .	83
3.12 Distribution of the production cross section for $W^- \rightarrow \ell^- \bar{\nu}_\ell$ (left) and $W^+ \rightarrow \ell^+ \nu_\ell$ (middle), and the lepton charge asymmetry (right) measured as a function of the lepton pseudorapidity in the laboratory frame. The CT10 PDF calculations with EPS09 (green line) and without (red line) nuclear PDF corrections are included. The bottom panels present the ratio of the CT10+EPS09 (green line) and data (black points) normalised to the CT10 baseline. Figure taken from Ref. [167]. . . . .	84
3.13 Survival probability of single muons from a $Z/\gamma^* \rightarrow \mu^+ \mu^-$ ( $M > 30$ GeV/c $^2$ ) simulation, as a function of the muon $\eta_{CM}^\mu$ and $p_T^\mu$ , separated in negative (left) and positive (right) charged muons. Muons are required to have $p_T > 25$ GeV/c and $ \eta  < 2.4$ , match the trigger and pass the isolation and identification criteria. . . . .	91
3.14 Flowchart illustrating the way the events are classified . . . . .	92
3.15 Muon $p_T$ distribution extracted from the W-boson enhanced sample before (left) and after (right) applying the boson $p_T$ weights. The red points correspond to data, while the blue and red filled areas correspond to events from the $W \rightarrow \mu \nu_\mu$ and $Z/\gamma^* \rightarrow \mu^+ \mu^-$ simulations, respectively. The bottom panels shows the ratio of data over simulation. . . . .	94
3.16 Distribution of the number of tracks per event (left) and the total energy deposited in the HF calorimeter (right) in $Z \rightarrow \mu^+ \mu^-$ events. The red points and filled area correspond to data and $Z/\gamma^* \rightarrow \mu^+ \mu^-$ simulation, respectively. . . . .	96
3.17 Comparison of the $p_T^{\text{miss}}$ distribution in data and simulation for $Z \rightarrow \mu^+ \mu^-$ events before (left) and after (right) applying the HF energy weights. . . . .	96
3.18 Distribution of the $p_T^{\text{miss}}$ in data and simulation for $Z \rightarrow \mu^+ \mu^-$ selected events. . . . .	97
3.19 Definition and components of the recoil $\vec{u}_T$ for $Z \rightarrow \mu^+ \mu^-$ events. . . . .	98
3.20 Distributions of the $u_{  }$ (top) and $u_{\perp}$ (bottom) recoil components in data (left) and simulation (right). The fit function is based on a weighted sum of two Gaussian distributions as defined in Eq. (3.32). The plots correspond to the $q_T^Z$ bin [3, 4] GeV/c. . . . .	99

3.21	Fits of the profile of $-\mu_{\parallel}$ as a function of $q_T^Z$ . The results are derived from $Z \rightarrow \mu^+ \mu^-$ events in data (left) and simulation (right). The yellow band represents the 68% error band of the fit. . . . .	100
3.22	Fits of the profile of $\mu_{\perp}$ as a function of $q_T^Z$ . The results are derived from $Z \rightarrow \mu^+ \mu^-$ events in data (left) and simulation (right). The yellow band represents the 68% error band of the fit. . . . .	101
3.23	Fits to the profile of the $\sigma_{\parallel,1}$ (left), $\sigma_{\parallel,2}$ (middle) and weighed average $\sigma_{\parallel}$ (right) values of the parallel recoil component as a function of $q_T^Z$ . The results are derived from $Z \rightarrow \mu^+ \mu^-$ events in data (top) and simulation (bottom). . . . .	102
3.24	Fits for the $\sigma_{\perp,1}$ (left), $\sigma_{\perp,2}$ (middle) and weighed average $\sigma_{\perp}$ (right) values of the recoil perpendicular component as a function of $q_T$ . The results are derived from $Z \rightarrow \mu^+ \mu^-$ events in data (top) and simulation (bottom). . . . .	103
3.25	A comparison of the $p_T^{\text{miss}}$ distribution from $Z \rightarrow \mu^+ \mu^-$ events between data and simulation, before (left) and after (right) calibrating the simulated recoil. The distributions of the simulated HF energy and generated Z-boson $p_T$ have been weighed. . . . .	105
3.26	Comparison of the $p_T^{\text{miss}}$ distribution in data and simulation for positive-charged muons in the $\eta_{\text{CM}}^{\mu}$ -inclusive signal region. The results are shown before (top-left) and after (top-right) applying the recoil calibrations using the nominal scaling method. The result using the alternative smearing method (bottom) is also presented. The distributions of the simulated HF energy and generated Z-boson $p_T$ have been weighed. . . . .	106
3.27	Comparison of the signal efficiency derived from the pPb and Pbp $W \rightarrow \mu\nu_{\mu}$ simulations as a function of the generated muon $\eta_{\text{lab}}$ , separated in negative (left) and positive (right) charged muons. The distributions of the simulated HF energy and generated W-boson $p_T$ have been weighed. The bottom panel shows the ratio of Pbp over pPb signal efficiencies. . . . .	107
3.28	Simulated signal efficiency derived from the $W \rightarrow \mu\nu_{\mu}$ NLO simulations as a function of the generated muon $\eta_{\text{CM}}$ , separated in negative (left) and positive (right) charged muons. The distributions of the simulated HF energy and generated W-boson $p_T$ have been weighed. . . . .	108
3.29	Fits to the tag-probe invariant mass distribution for passing (left) and failing (right) probes, used to measure the STA reconstruction efficiency. The results correspond to the probe kinematic region: $ \eta_{\text{lab}}  < 2.4$ and $50 < p_T < 80$ GeV/c. Figures taken from the private Ref. [183]. . . . .	110

3.30 Muon identification (left) and isolation (right) efficiencies extracted from data (blue) and simulation (red) using the TnP method, as a function of the probe $p_T$ . The bottom panels show the data-to-simulation efficiency ratio. The results of the fits to the efficiencies are also shown. Figures taken from the private Ref. [183]. . . . .	111
3.31 Muon trigger efficiency extracted from data (blue) and simulation (red) using the TnP method, as a function of the probe $\eta_{\text{lab}}$ . The bottom panel shows the data-to-simulation efficiency ratio. Figure taken from the private Ref. [183]. . .	111
3.32 Corrected signal efficiency as a function of the generated muon $\eta_{\text{CM}}$ , separated in negative (left) and positive (right) charged muons. The yellow and green boxes represents the uncertainty on the signal efficiency due to the TnP statistics and systematics, respectively. . . . .	113
3.33 QCD jet background fits to the $p_T^{\text{miss}}$ distribution in a control sample of non-isolated muon events corresponding to the muon isolation bins: $0.4 < I^\mu < 0.5$ (left) and $0.8 < I^\mu < 0.9$ (right). The results are shown for positive (top) and negative (bottom) charged muons separately. . . . .	117
3.34 Linear fits to the profile of the QCD background parameters: $\sigma_0$ (left), $\sigma_1$ (middle) and $\sigma_2$ (right), with respect to the muon isolation variable $I^\mu$ . The results are shown for negative (top) and positive (bottom) charged muons in the $\eta_{\text{CM}}^\mu$ -inclusive range. The red points represents the value obtained by linearly extrapolating to $I^\mu = 0.03$ . . . . .	118
3.35 Muon $\eta_{\text{CM}}^\mu$ dependence of $\sigma_0$ (left), $\sigma_1$ (middle) and $\sigma_2$ (right) parameters extrapolated to $I^\mu = 0.03$ . The results are shown for negative (top) and positive (bottom) charged muons. The red line corresponds to the QCD jet parameter extrapolated in the $\eta_{\text{CM}}^\mu$ -inclusive range. . . . .	119
3.36 The $p_T^{\text{miss}}$ distribution for $W^- \rightarrow \mu^- \bar{\nu}_\mu$ (left) and $W^+ \rightarrow \mu^+ \nu_\mu$ (right) events within the $\eta_{\text{CM}}^\mu$ -inclusive range, shown in linear scale. Unbinned fits to the data (black points) are performed with six contributions, stacked from top to bottom: $W \rightarrow \mu \nu_\mu$ (yellow), QCD jet (light blue), $Z/\gamma^* \rightarrow \mu^+ \mu^-$ (green), $W \rightarrow \tau \nu_\tau$ (red), $Z/\gamma^* \rightarrow \tau \bar{\tau}$ (dark blue) and $t \bar{t}$ (orange). The lower panel, on each figure, display the ratio of the measurements over the result of the fit. The $\chi^2$ test value over the number of degrees of freedom is also shown. . . . .	121

3.37 Uncertainty corresponding to each category as function of the muon $\eta_{\text{CM}}$ . The plots are divided as: $W^- \rightarrow \mu^- \bar{\nu}_\mu$ (top-left) and $W^+ \rightarrow \mu^+ \nu_\mu$ (bottom-left) differential cross sections, $W^- \rightarrow \mu^- \bar{\nu}_\mu$ (top-middle) and $W^+ \rightarrow \mu^+ \nu_\mu$ (bottom-middle) forward-backward ratios, and finally the charge-summed forward-backward ratio (top-right) and muon charge asymmetry (bottom-right). The uncertainties of the cross sections are relative while for the forward-backward ratios and muon charge asymmetry are absolute. The global luminosity uncertainty of 3.5% is not included. . . . .	135
3.38 Correlation matrices for: $W^\pm$ cross section (top-left), $W^\pm R_{FB}$ (top-right), charge-inclusive $R_{FB}$ (bottom-left), and charge asymmetry (bottom-right). The lines in the top plots are used to separate the different muon charge bins. . . . .	137
3.39 Differential production cross sections for $W^+ \rightarrow \mu^+ \nu_\mu$ (left) and $W^- \rightarrow \mu^- \bar{\nu}_\mu$ (right), as a function of the muon pseudorapidity in the center-of-mass frame. The brackets represent the statistical and systematic uncertainties summed in quadrature, while the error bars show the statistical uncertainties only. The global luminosity uncertainty of 3.5% [168] is not shown. . . . .	138
3.40 Muon charge asymmetry as a function of the muon pseudorapidity in the center-of-mass frame. The brackets represent the statistical and systematic uncertainties summed in quadrature, while the error bars show the statistical uncertainties only. . . . .	138
3.41 Forward-backward ratios, for the positive (top-left), negative (top-right) and all (bottom) charged muons. The brackets represent the statistical and systematic uncertainties summed in quadrature, while the error bars show the statistical uncertainties only. . . . .	139
3.42 Differential cross sections for $W^+ \rightarrow \mu^+ \nu_\mu$ (left) and $W^- \rightarrow \mu^- \bar{\nu}_\mu$ (right), as a function of the muon $\eta_{\text{CM}}^\mu$ . Errors bars represent the statistical uncertainties, while the brackets represent the statistical and systematic uncertainties summed in quadrature. The global luminosity uncertainty of 3.5% is not displayed. Theoretical predictions with (CT14+EPPS16 shown in dashed green line and CT14+nCTEQ15 shown in dashed brown line) and without (CT14, solid red line) PDF nuclear modifications are also shown, with the uncertainty bands. All theory uncertainty bands include the PDF uncertainties. . . . .	141

- 3.43 Muon charge asymmetry of  $W \rightarrow \mu\nu_\mu$ , given for each muon  $\eta_{\text{CM}}^\mu$  range. Errors bars represent the statistical uncertainties, while the brackets represent the statistical and systematic uncertainties summed in quadrature. Theoretical predictions with (CT14+EPPS16 shown in dashed green line and CT14+nCTEQ15 shown in dashed brown line) and without (CT14, solid red line) PDF nuclear modifications are also shown, with the uncertainty bands. All theory uncertainty bands include the PDF uncertainties. . . . . 142
- 3.44 Forward-backward ratio of  $W \rightarrow \mu\nu_\mu$ , given for each muon  $\eta_{\text{CM}}^\mu$  range separated in negative (top-left), positive (top-right) and all (bottom) charged muons. Errors bars represent the statistical uncertainties, while the brackets represent the statistical and systematic uncertainties summed in quadrature. Theoretical predictions with (CT14+EPPS16 shown in dashed green line and CT14+nCTEQ15 shown in dashed brown line) and without (CT14, solid red line) PDF nuclear modifications are also shown, with the uncertainty bands. All theory uncertainty bands include the PDF uncertainties. . . . . 143
- A.1 The  $p_T^{\text{miss}}$  distribution for  $W^- \rightarrow \mu^-\bar{\nu}_\mu$  events within each fitted  $\eta_{\text{CM}}^\mu$  range, shown in logarithmic scale. Unbinned fits to the data (black points) are performed with six contributions, stacked from top to bottom:  $W^+ \rightarrow \mu^+\nu_\mu$  (yellow), QCD multijet (light blue),  $Z/\gamma^* \rightarrow \mu^+\mu^-$  (green),  $W^+ \rightarrow \tau\nu_\tau$  (red),  $Z/\gamma^* \rightarrow \tau\bar{\tau}$  (dark blue) and  $t\bar{t}$  (orange). Error bars represent statistical uncertainties. The lower panels display the data divided by the result of the fit, for each  $\eta_{\text{CM}}^\mu$  range. The  $\chi^2$  test value over the number of degrees of freedom is also shown. 154
- A.2 The  $p_T^{\text{miss}}$  distribution for  $W^+ \rightarrow \mu^+\nu_\mu$  events within each fitted  $\eta_{\text{CM}}^\mu$  range, shown in logarithmic scale. Unbinned fits to the data (black points) are performed with six contributions, stacked from top to bottom:  $W^+ \rightarrow \mu^+\nu_\mu$  (yellow), QCD multijet (light blue),  $Z/\gamma^* \rightarrow \mu^+\mu^-$  (green),  $W^+ \rightarrow \tau\nu_\tau$  (red),  $Z/\gamma^* \rightarrow \tau\bar{\tau}$  (dark blue) and  $t\bar{t}$  (orange). Error bars represent statistical uncertainties. The lower panels display the data divided by the result of the fit, for each  $\eta_{\text{CM}}^\mu$  range. The  $\chi^2$  test value over the number of degrees of freedom is also shown. 155

## LIST OF FIGURES

